Geosynthetic Reinforcement in Asphalt Overlays for Increased Roadway Structural Capacity

V. Vinay Kumar
Gholam H. Roodi
Subramanian Sankaranarayanan
Ashray Saxena
Calvin Blake
Jorge G. Zornberg

Technical Report Documentation Page

1. Report No. FHWA/TX-25/0-7002-1	2. Government Accession No.	3. Recipient's Catalog No.
4. Title and Subtitle Geosynthetic reinforcement in asphalt overlays for increased roadway structural capacity		5. Report Date Submitted: 08-2024; Published: 11-2024
		6. Performing Organization Code
7. Author(s) V. Vinay Kumar, PhD., Gholam H. Roodi, Ph.D., Subramanian Sankaranarayanan, Ph.D., Ashray Saxena, Calvin Blake, Ph.D., and Jorge Zornberg. PhD, PE, BC.GE. (ORCID: 0000-0002-6307-1047)		8. Performing Organization Report No. 0-7002-1
9. Performing Organization Name and Address Center for Transportation Research The University of Texas at Austin 3925 W. Braker Lane, 4th Floor Austin, TX 78759		10. Work Unit No. (TRAIS)
		11. Contract or Grant No. 0-7002
12. Sponsoring Agency Name and Address Texas Department of Transportation Research and Technology Implementation Division 125 E. 11th Street, Austin, TX 78701		13. Type of Report and Period Covered Technical Report May 2021 – August 2024
		14. Sponsoring Agency Code
15. Supplementary Notes Project performed in cooperation with the Texas Department of Transportation and the Federal Highway Administration.		
16. Abstract A comprehensive full-scale field monitoring program involving different types of geosynthetic reinforcement products was successfully implemented. The monitoring system included asphalt strain gauges, thermocouples, geophones, and moisture sensors. The monitoring results indicate that all asphalt overlay sections reinforced with geosynthetic reinforcements performed better than the control section in minimizing tensile strains under controlled traffic loads, thereby improving the roadway structural capacity. The tensile strains decreased with increasing asphalt overlay thickness, irrespective of the presence or absence of geosynthetic reinforcements below the asphalt overlays. The benefit of incorporating geosynthetic reinforcements below the asphalt overlays was comparatively higher in thin asphalt overlays than in thick asphalt overlays. Tensile strains increased with increasing ambient air temperatures, irrespective of the presence or absence of geosynthetic reinforcements below the asphalt overlays. The benefit of incorporating geosynthetic reinforcements below the asphalt overlays was higher in conditions involving hot temperatures than in cold temperatures. The tensile strains increased with increasing time since construction (i.e., asphalt aging and degradation), irrespective of the presence or absence of geosynthetic reinforcements below the asphalt overlays. The benefit from incorporating geosynthetic reinforcements below the asphalt overlays was significantly higher as asphalt ages and degraded compared to a fresh asphalt layer. The reductions in tensile strains with the inclusion of geosynthetic reinforcements suggest an increase in the roadway structural capacity. The design could incorporate such benefits via two alternative approaches: Increased apparent asphalt modulus and reduced fatigue damage. The two design approaches would eventually lead to increased service life (ESALs) and decreased asphalt thickness.		
17. Key Words Geosynthetic, interlayers, structural capacity, reflective cracking, field monitoring, strain gages, geophones, geogrids.		18. Distribution Statement No restrictions. This document is available to the public through the National Technical Information Service, Alexandria, Virginia 22312; www.ntis.gov.
19. Security Classif. (of report) Unclassified	20. Security Classif. (of this page) Unclassified	21. No. of pages TBD [Total count excl. cover] 22. Price

Form DOT F 1700.7 (8-72) Reproduction of completed page authoriz

THE UNIVERSITY OF TEXAS AT AUSTIN
CENTER FOR TRANSPORTATION RESEARCH

Geosynthetic reinforcement in asphalt overlays for increased roadway structural capacity

V. Vinay Kumar, PhD
Gholam H. Roodi, Ph.D.,
Subramanian Sankaranarayanan, Ph.D.,
Ashray Saxena,
Calvin Blake, Ph.D., and
Jorge G. Zornberg, PhD, PE, BC.GE.

Center for Transportation Research
The University of Texas at Austin
3925 W. Braker Lane, 4th floor
Austin, TX 78759

http://ctr.utexas.edu/

Disclaimers

Author's Disclaimer: The contents of this report reflect the views of the authors, who are responsible for the facts and the accuracy of the data presented herein. The contents do not necessarily reflect the official view or policies of the Federal Highway Administration or the Texas Department of Transportation (TxDOT). This report does not constitute a standard, specification, or regulation.

Patent Disclaimer: There was no invention or discovery conceived or first actually reduced to practice in the course of or under this contract, including any art, method, process, machine manufacture, design or composition of matter, or any new useful improvement thereof, or any variety of plant, which is or may be patentable under the patent laws of the United States of America or any foreign country.

Engineering Disclaimer

NOT INTENDED FOR CONSTRUCTION, BIDDING, OR PERMIT PURPOSES.

Project Engineer: Jorge G. Zornberg, Ph.D., P.E., BC.GE.
Professional Engineer License State and Number: Texas No. 149473; California No. C 056325
P.E. Designation: Research Supervisor

Acknowledgments

Table of Contents

List of Tables

List of Figures

13

18

19

20

21

Chapter 1. Introduction

1.1. Motivation

Geosynthetics in the form of geogrids, geotextiles, geocells, geomembranes, and geonets can be incorporated into the different layers of pavement systems to enhance their performance through functions such as separation, filtration, reinforcement, stiffening, barrier, drainage and protection (e.g., Zornberg 2017). Specifically, the enhanced pavement performance can be achieved through applications such as reflective crack minimization in asphalt overlays (e.g., Khodaii et al. 2009; Saride and Kumar 2017, 2019), base layer stabilization (e.g., Holtz et al. 1998; Perkins 2002; Roodi and Zornberg 2020; Zornberg and Roodi 2020) and soft subgrade stabilization (e.g., Abu-Farsakh et al. 2016; Kumar and Saride 2016). Among the applications entailing the use of geosynthetics in hot mix asphalt layers, the mitigation of reflective cracks using paving geotextiles correspond to one of the earliest uses of geosynthetics in roadways (Sudarsanan et al. 2015). Reflective cracking can be defined as the reflection of cracks and ruts from the pre-existing asphalt layer on to the new asphalt overlay due to repeated traffic and temperature loads (Cleveland et al. 2002; Saride and Kumar 2017). Specifically, repeated traffic loads induce bending and shear stresses, while temperature variations induce tensile stresses in the vicinity of pre-existing cracks, accelerating crack growth into the overlay (Lytton 1989). Paving interlayers such as geotextiles, geogrids, and geocomposites have been employed to minimize the development and progression of reflective cracks into overlays, thereby extending the pavement service life.

The main mechanisms involved in applications aimed at retarding reflective cracking include tension development and stress relief (Zornberg 2017). The tension development mechanism results in stress redistribution within the asphalt overlay while maintaining confinement of the pre-existing asphalt layer. As shown in Figure 1.1a, the effectiveness of this mechanism mainly depends on developing adequate interface bond strength between the geosynthetic and adjacent asphalt layers, including the pre-existing asphalt and the new overlay. On the other hand, the stress relief mechanism involves development of horizontal deformations leading to controlled interface debonding in the vicinity of pre-existing cracks. As shown in Figure 1.1b, through controlled debonding, potential reflective cracks are intersected and diverted sideways. The tension development mechanism involves the reinforcement function of geosynthetics, which can be achieved by geogrids and geocomposites that have been manufactured by products such as polyester and fiberglass. On the other hand, the stress relief mechanism typically involves use of bitumen-impregnated nonwoven paving geotextiles, placed at the interface between pre-existing and new asphalt layers.

Specifically, paving interlayers generally involving geotextile products have been reported to minimize reflective cracking by providing a separation function between the pre-existing and new asphalt layers through a stress-relief mechanism (Lytton 1989; Zornberg 2017; Solatiyan et al., 2020). Instead, paving interlayers generally involving geogrid products have been reported to minimize reflective cracking by providing a reinforcement function to reduce the stress concentration that triggers reflective cracks (Zornberg 2017; Solatiyan et al., 2020; Kumar et al., 2021a). Finally, paving interlayers involving geocomposites have been reported to behave similar to geogrids in minimizing reflective cracks but often also provide a barrier function (Pasquini et al., 2014; Zornberg 2017; Solatiyan et al., 2020). Some paving fabrics are also expected to provide the barrier function along with separation (Lytton 1989; Farshad 2005). While the original motivation for the development of the various paving interlayer products has been to mitigate reflective crack development, preliminary investigations conducted by Correia and Zornberg (2016, 2018) and Kumar et al. (2021b) suggest that the reinforcement mechanisms developed by geogrids may also lead to an increased structural capacity of the reinforced overlays. Specifically, the inclusion of geogrid reinforcements below the asphalt overlay may minimize the accumulation of permanent deformations and critical tensile strains under repeated traffic and environmental loads. While such increased structural capacity would be highly beneficial, the lack of field monitoring results that quantify such structural benefit has precluded the incorporation of added capacity in roadway design.
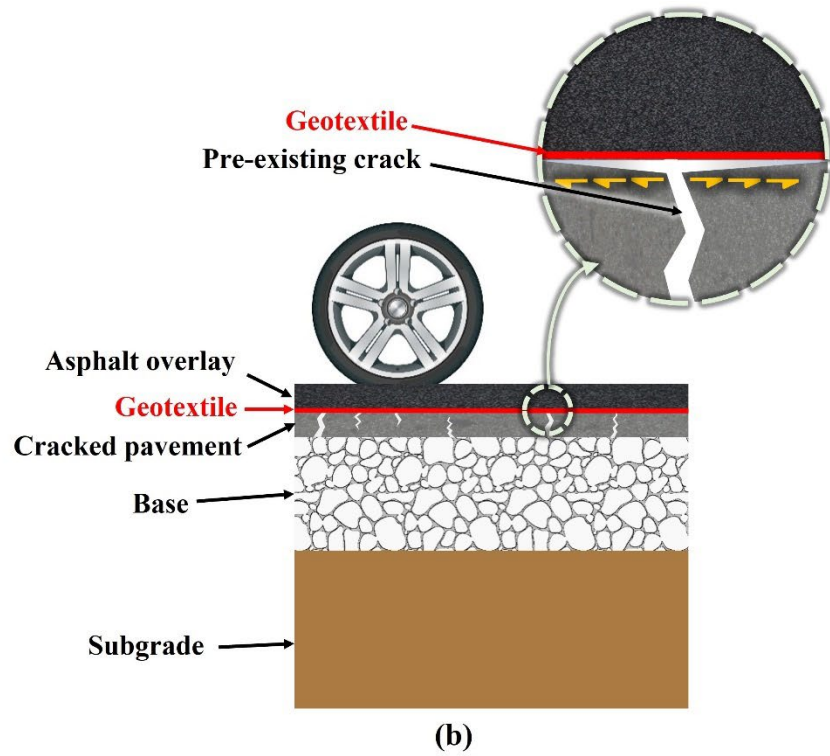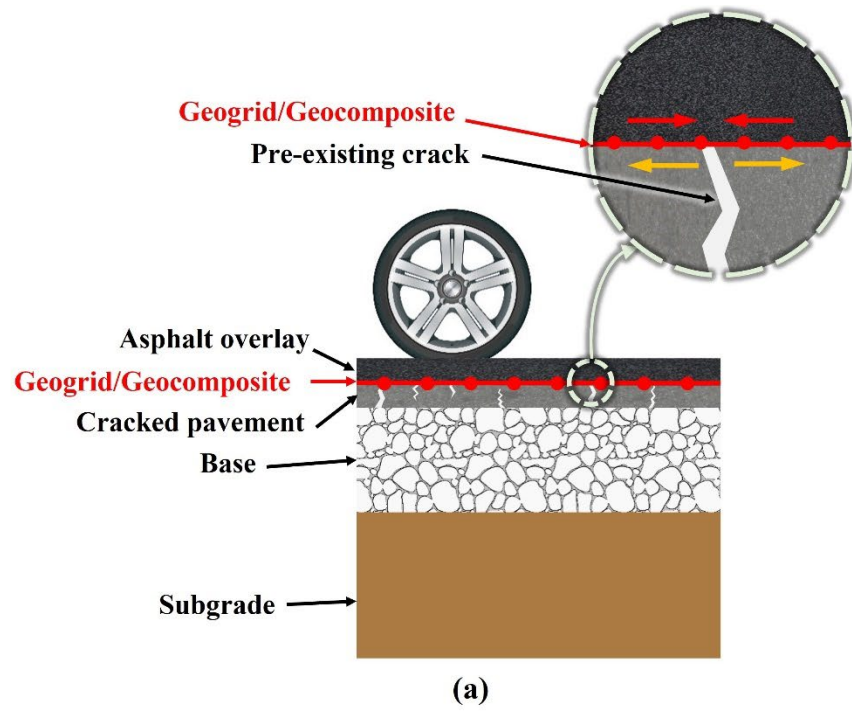
Figure 1.1. Reflective crack mitigation mechanisms using geosynthetics: (a) tension development mechanism; and (b) stress-relief mechanism (Kumar et al. 2023).

The efficacy of various types of geosynthetic interlayers in enhancing the overlay performance against reflective cracking has been evaluated by several researchers (Lytton 1989; Cleveland et al., 2002; Virgili et al., 2009; Zamora-Barraza et al., 2011; Pasquini et al., 2014; Gonzalez-Torre et al., 2015; Kumar and Saride 2017; Sudarsanan et al., 2019). A wide range of experimental procedures have been adopted to quantify the crack development in the laboratory, including conducting flexural beam fatigue tests (e.g., Virgili et al., 2009; Kumar and Saride 2017; Saride and Kumar 2017, 2019; Solatiyan et al., 2021), bond strength tests (e.g., West et al., 2005; Roodi et al., 2017; Saride and Kumar 2017; Solatiyan et al., 2021; Spadoni et al., 2021; Canestrari et al., 2022), and pavement model tests (e.g., Sanders 2001; Siriwardane et al., 2010; Correia and Zornberg 2016; Saride and Kumar 2019; Kumar et al., 2021b). Complementing the insight gained from experimental research, field investigations involving both unreinforced and geosynthetic-reinforced asphalt overlays have also been performed to evaluate the efficacy of geosynthetic interlayers to control reflective cracking (e.g., Laurinavicius and Oginskas 2006; Buhler 2007; Graziani et al., 2014; Imjai et al., 2019; Kumar et al., 2021c). Finally, a number of researchers have resorted to numerical simulations such as the finite element method (FEM) to evaluate the efficacy of geosynthetics in minimizing reflective cracks (e.g., Wathugala et al., 1996; Kwon et al., 2005; Abdesssemed et al., 2015; Correia et al., 2018; Kazimierowicz-Frankowska 2020). However, the results from various laboratory scale tests, pavement model tests, field trials, and numerical simulations reveal consensus on the benefits, but not on the mechanisms by which geosynthetic interlayers minimize the development of reflective cracks in the asphalt overlays. In summary, and in spite of the possible lack of consensus on the relevant mechanisms, previous research on geosynthetic-reinforced asphalt overlays is available, but it has emphasized quantifying their ability to restrict reflective cracks into the asphalt overlays. On the other hand, limited experimental research has been generated on the potential structural benefits of incorporating geosynthetic reinforcements within the asphaltic layers (e.g., Correia and Zornberg 2016, 2018; Kumar et al., 2021b). In addition, a few full-scale field studies have been conducted that report on the structural benefits of incorporating the geosynthetics between the asphalt overlays (e.g., Laurinavicius and Oginskas 2006; Graziani et al., 2014; Imjai et al., 2019). However, the field evaluations conducted by Laurinavicius and Oginskas (2006) did not include any sensors, while field evaluations conducted by Graziani et al. (2014) and Imjai et al. (2019) included sensors (i.e., asphalt strain gages, and pressure sensors), but the geosynthetic interlayers were installed within new asphalt layers instead of a typical geosynthetic installation viz. below an asphalt overlay. Also, none of the previous full-scale field studies have evaluated the influence of different asphalt thicknesses on the structural performance of geosynthetic-reinforced asphalt overlays. Consequently, a research program involving evaluation of the structural performance of full-scale instrumented field sections was implemented in this study to quantify the structural benefits expected from geosynthetics placed below the asphalt overlay, but not necessarily benefits against reflective cracking.

1.2. Objectives

The main objective of this research study is to evaluate the efficacy of adopting different types of geosynthetic reinforcements (i.e., paving interlayers that provide reinforcement function via tension development mechanism) below the asphalt overlay to increase the roadway structural capacity and thereby extend the roadway service life and minimize overlay thickness. Increased roadway structural capacity provided by geosynthetic reinforcements would be quantified in terms of reductions in settlement and strains under traffic loads. Eventually, quantification of such increased structural capacity may be incorporated into future pavement design to reduce asphalt thickness and extend the pavement service life.

To accomplish the objectives of this research study, seven heavily instrumented full-scale asphalt overlay sections including six different geosynthetic reinforcement products were designed and constructed along with several non-instrumented sections that included nine different geosynthetic reinforcement products, during the rehabilitation of the in-service Texas State Highway 21. Subsequently, the pavement response under different field-testing activities were assessed with the help of various sensors instrumented within the pavement system. Additionally, such responses would be recorded and monitored over a period of at least five years from construction, mainly to evaluate the efficacy of various geosynthetic reinforcement products in enhancing the roadway structural capacity and eventually, quantify such increased roadway structural capacity.

1.3. Organization of the Report

This report is organized into 10 chapters.

Chapter 1 describes the motivation and objectives of the research project along with a brief description of the organization of the report.

Chapter 2 provides a brief description of the research background including the previous experiences of TxDOT and other DOTs and agencies on the use of geosynthetic interlayers in hot mix asphalt layers.

Chapter 3 explains the design of SH21 field monitoring program. Specifically, it includes the design of experimental test sections (both sensor- and non-instrumented) and the design of sensor instrumentation for the experimental test sections.

Chapter 4 explains the characterization of materials in SH21 test sections, which includes the preexisting pavement materials (e.g., subgrade soil, base and subbase materials, and preexisting asphalt layer) as well as the materials used for the asphalt overlay construction (e.g., geosynthetic reinforcements, tack coat, asphalt overlay).

Chapter 5 details the procurement and installation of various sensors including moisture sensors, geophones, asphalt strain gauges and thermocouples in SH21 experimental test sections.

Chapter 6 summarizes the various forms of field-testing activities conducted before, during, and after the construction of asphalt overlays. The field-testing activities included the in-situ stiffness characterization using FWD and static plate load tests; a passive evaluation conducted using GPR to assess the asphalt overlay uniformity; and total station surveys for surface movements. Finally, the active loading campaigns designed to assess the response of the installed sensors under controlled traffic loading are also covered.

Chapter 7 details the passive monitoring of the installed sensors to assess the long-term performance of the sensor-instrumented and non-instrumented experimental test sections. The various sensors from which the long-term data was collected and the status of data collection from these sensors are summarized.

Chapter 8 describes the synthesis and analysis of the data collected from the sensors under controlled traffic loading campaigns. Specifically, the influence of asphalt type and thickness, ambient air temperature, and time after construction on the performance of geosynthetic-reinforced asphalt and quantification of increased roadway structural capacity has been discussed. Additionally, design charts developed for geosynthetic-reinforced asphalt layers have been presented and discussed.

Chapter 9 summarizes the characterization of milling, reusing, and recycling of geosynthetic-reinforced asphalt.

Chapter 10 outlines key conclusions drawn from this research study.

Chapter 2. Research Background

2.1. Introduction

This chapter reports the activities that have been completed in Task 1 of TxDOT Project 0-7002. The main aim of this task was to collect, review and assess the relevant TxDOT and other agencies experiences on various types of geogrid-reinforced Hot Mix Asphalt (HMA) overlay projects. Specifically, the evaluation of field trials and/or test sections consisting of asphalt layers reinforced with different types of geosynthetic interlayers.

The evaluation of previous experiences with geosynthetic-interlayers could be summarized under the following parts:

Previous experience by TxDOT on the use of geosynthetic-interlayers in asphalt layers

Previous experience by other Departments of Transportation (DOTs) and agencies in the US and overseas, on the use of geosynthetic-interlayers in asphalt layers

2.2. Previous Experience by TxDOT on the Use of Geosynthetic Interlayers

2.2.1. TxDOT Experience in Odessa District: IH-20, Reeves County, 1970

This project involved construction of four different overlay designs along IH20 located in Reeves County, TX. Figure 2.1 shows the various test section profiles constructed in this project. Figure 2.2 presents the plan layout of the various test sections constructed in this project.
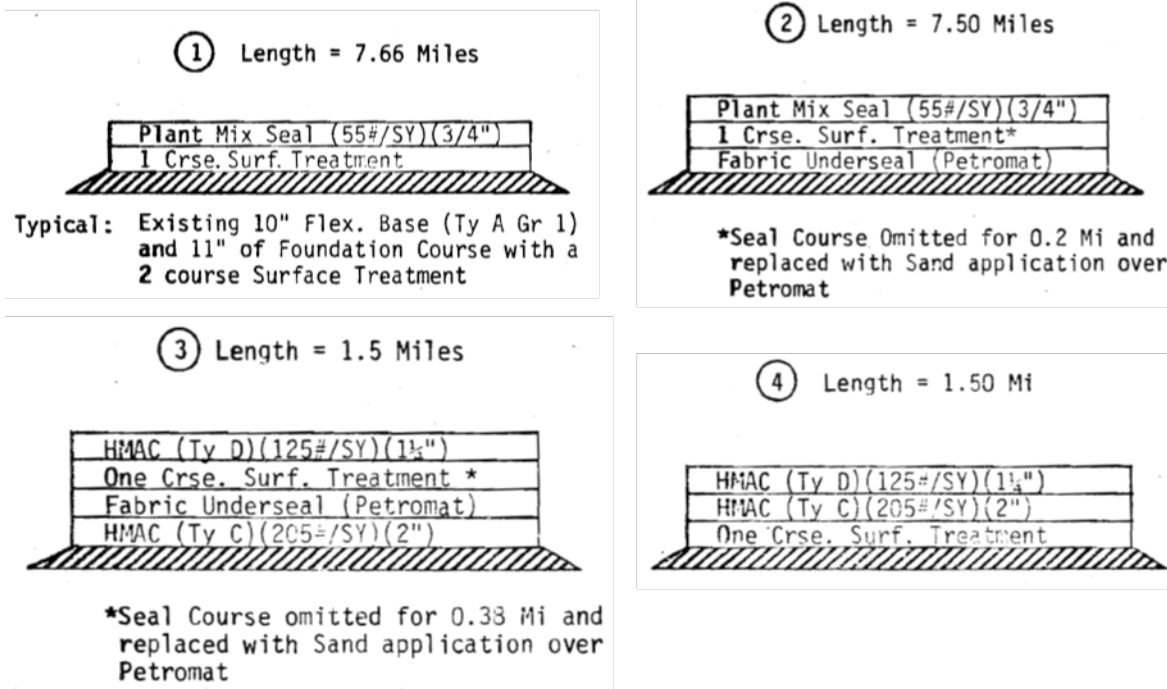
Figure 2.2. Section profiles in IH20 construction (Huffman 1978).
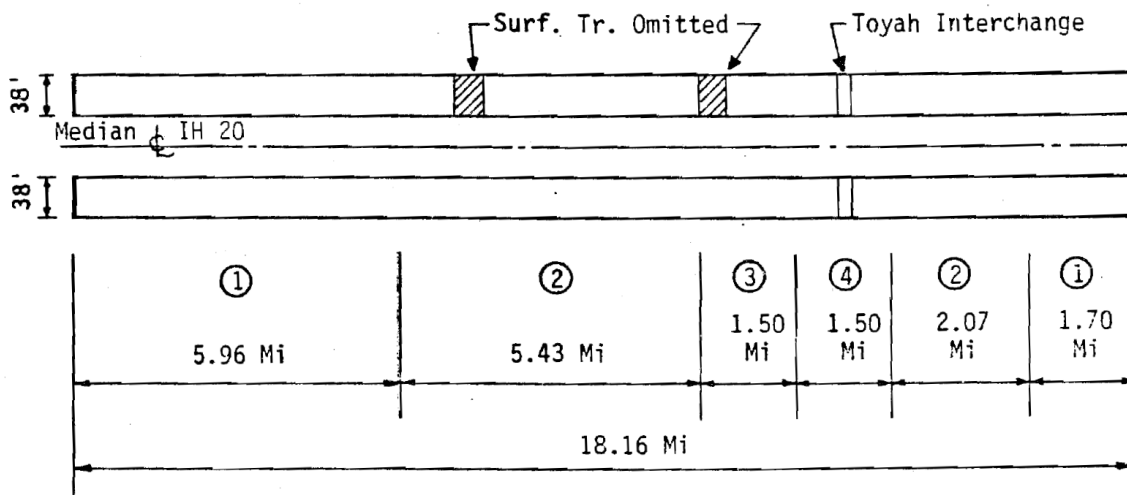
Figure 2.3. Plan layout for test sections in IH20 construction (Huffman 1978).

Section 1 consisted of a one-course surface treatment overlain by a ¾" thick overlay from Plant Mix Seal. This design was used along a 7.5-mile-long stretch of the road. Section 2 involved laying a Petromat layer overlain by one course of surface treatment and a ¾" thick overlay from Plant Mix Seal. The length of this section was also 7.5 miles. Section 3 consisted of a 2" course of Type C HMA, overlain by a layer of Petromat fabric and a one-course surface treatment, and 1 1/4" course of Type D HMA. This section was extended for 1.5 miles. The control section

29

(Section 4) consisted of a one-course surface treatment under seal, 2" of Type C HMA, overlain by a 1 1/4" course of Type D wearing HMA course. This section was also 1.5-mile long.

The test sections were subjected to a severe winter, hot summer, and, at the time of reporting, back into winter again. They observed that the control section and Sections 3 outperformed Sections 1 and 2. Between Sections 1 and 2, the section with the Petromat fabric (Section 2) was found to have less cracks than the section without the Petromat fabric (i.e., Section 1). However, the control section (Section 4) was judged by the district to perform the best (Huffman 1978).

2.2.2. TxDOT Experience in Amarillo District: IH-40, Potter County, 1970

The objective of the Amarillo district in this project was to evaluate surface sealing systems involving seals coats and poly-fab underseals. Specifically, the project aimed at evaluating the performance of Petromat material (referred to in this project as the Poly-fab layer) in reducing the reflective cracking. The project was extended along IH40 located in the Oldham and Potter counties. The project location was approximately 18 miles west of Amarillo at an elevation of 3,900 ft and with a gentle sloping ranging from 1% to 3%. Evaluation of the performance of the surface sealing systems in retarding reflective cracking was of special interest in this project.

The climate in the project area classified as dry and cold. According to Day (1978): "The average rainfall is 18.23 in with an average of 13 inches of snow. The mean annual temperature is 590 Fahrenheit with an average minimum temperature of 20.90 Fahrenheit in January. The lowest recorded temperature is -80 Fahrenheit and daily variations of 300 to 400 are common. Drops of 600 are not uncommon with passages of "Northers" during the winter. Hard freezes for three or four days with rapid thaws are not unusual."

In this project, TxDOT incorporated four different design concepts as follows:

Design (I) consisted of a seal coat on top of the existing asphalt, overlain by level-up and a final course of HMA. The seal coat that used in this design consisted of 0.35 gal/SY of asphalt and Type A Grade 3 Aggregate applied at a rate of 1 CY per 85 SY (Figure 2.3).
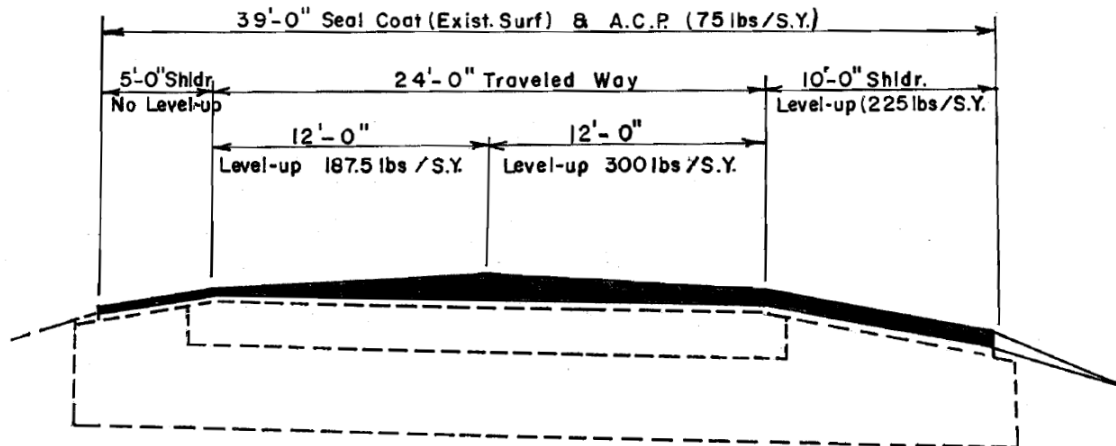
Figure 2.4. Design I in IH40 rehabilitation project in Potter County (Day 1978).

Design (II) involved placing HMA and Poly-fab underseal on top of the existing pavement. Then, a seal coat layer was constructed overlain by level-up and a final course of HMA. The seal coat that used in this design consisted of 0.25 gal/SY of asphalt and Type A Grade 5 Aggregate applied at a rate of 1 CY per 120 SY (Figure 2.4).
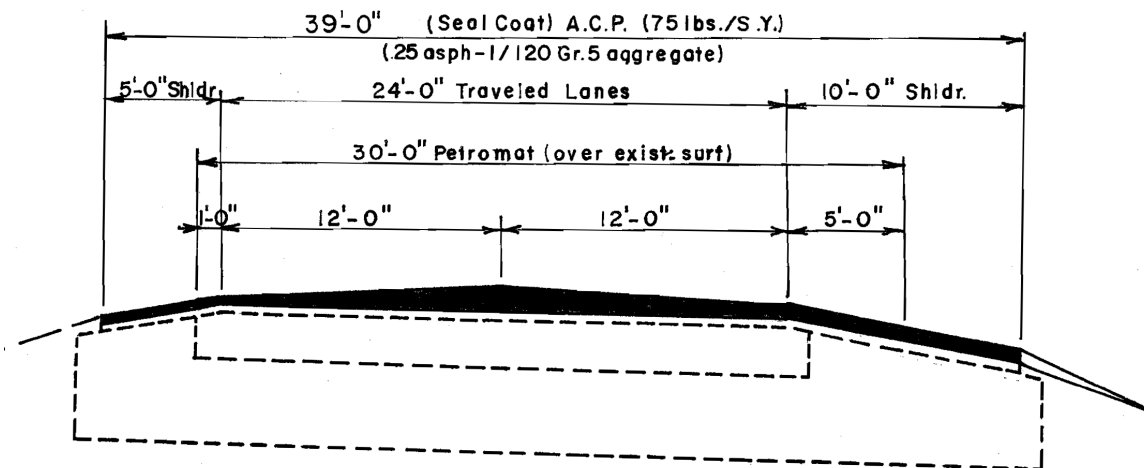
Figure 2.5. Design II in IH40 rehabilitation project in Potter County (Day 1978).

Design III involved a level-up course of HMA placed directly on top of the existing pavement. An HMA layer and Poly-fab underseal were then placed on top of the level-up. A final course average at 75 lb/SY was then placed on top of the Poly-fab layer (Figure 2.5).
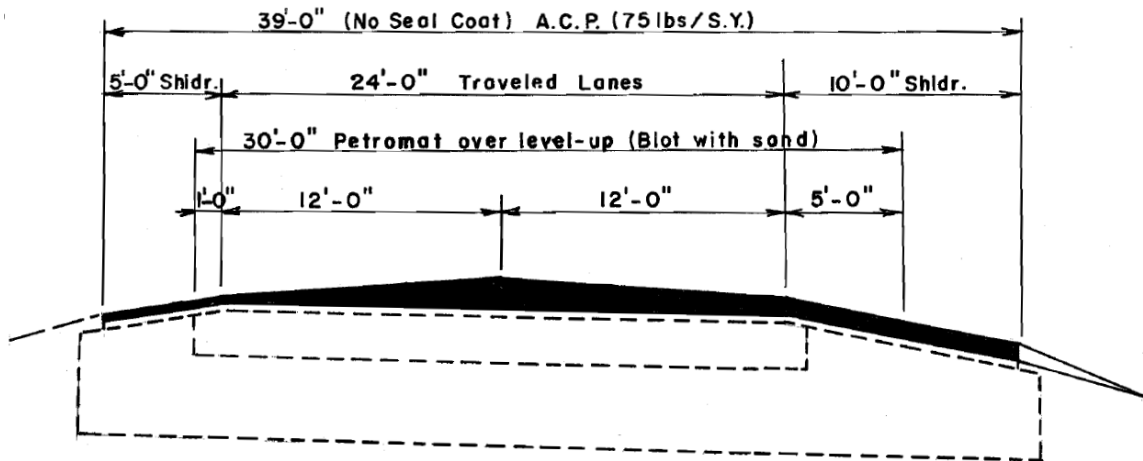
Figure 2.6. Design III in IH40 rehabilitation project in Potter County (Day 1978).

In the last design (Design IV), HMA and Poly-fab underseal were placed directly on top of the existing pavement. The surface was then blotted with sand and overlaid using a level-up course and a final HMA course (Figure 2.6).
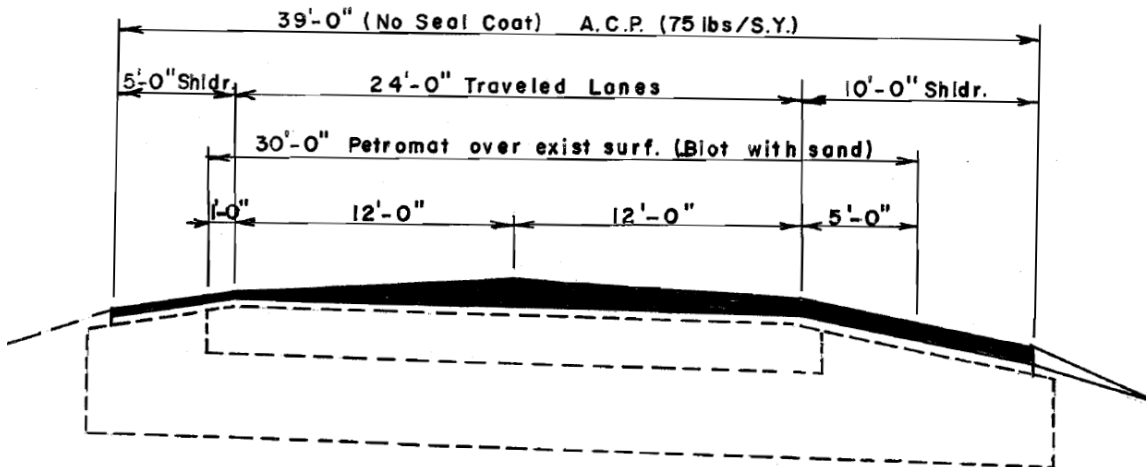
Figure 2.7. Design IV in IH40 rehabilitation project in Potter County (Day 1978).

The cost-effectiveness of using a Petromat layer was also evaluated in IH40 rehabilitation project. Specifically, the total cost of construction for Design 1, which was constructed without a Petromat, was estimated at $2.69 per square yard. On the other hand, the total cost of construction for Designs I, II and III, which were constructed using a Petromat, was estimated at $3.64, $3.30 and $3.30 per square yard, respectively.

Performance of the test section was evaluated by condition surveys and taking pictures at set reference points. By the time of reporting the evaluation results, although a record-cold winter

had past and the rain, sleet and snow amount was well above average, no crack was observed in any of the section.

2.2.3. TxDOT Experience in San Angelo, Amarillo, Tyler and Pharr Districts, 1979 to 1989

In 1979, TxDOT installed a wide range of geotextile interlayer materials at four projects that were spread along different geographic and climate regions of the state. Figure 2.7 shows the locations of the four projects. The projects were located in Ozona (Crockett County, San Angelo District) located in a dry-warm climate region, Edinburg (Hidalgo County, Pharr District) located in a dry-warm climate region, Amarillo (Potter County, Amarillo District) located in a dry-cold climate region, and Tyler (Smith County, Tyler District) located in a wet-cold climate region.
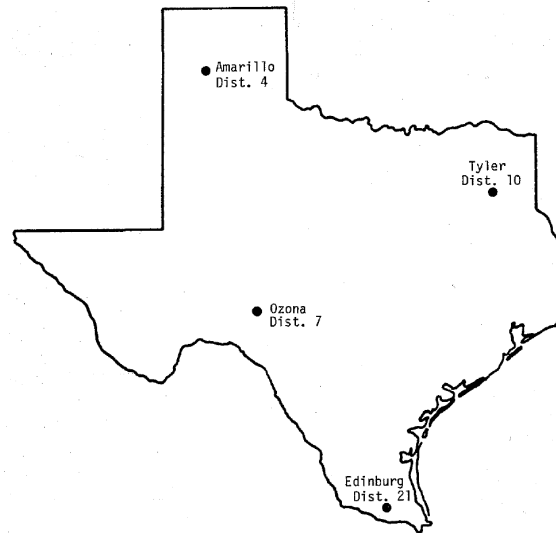
Figure 2.8. Location of four projects used for evaluation of geotextile interlayers in 1979 (Button 1989).

A total of 10 different fabrics with the mass per unit area ranging from 3 to 8 oz/SY were used in the test sections spread between the four locations. The tack coat rate that was used to cover the fabrics ranged from 0.2 to 0.4 gallons/SY. Table 2.1 summarizes the main characteristics of the four projects. Characteristics of the fabrics and their mechanical properties tested by TxDOT are also presented in Table 2.2 and Table 2.3, respectively.

Table 2.1. Characteristics of four projects involving geotextile interlayer materials (Button and Epps 1982).

Item	West of Ozona	West of Amarillo	Edinburg	East of Tyler	
Highway Designation	IH-10	IH-40	US 281 & SH 107	IH 20	
No. of Lanes each Direction	2	2	2	2	
Existing Pavement					
Layer 1 (top)	3" HMAC	1" HMAC (Type D)	1" HMAC*	8" CRCP	
Layer 2	15" Flex Base	2" HMAC (Type A)	12" Flex Base	RC-2 membrane	
Layer 3	Subbase	12" Flex Base	Subgrade	6" Soil Cement	
Layer 4	--	6" lime Tr.Subgr.	--	Subgrade	
Date of Overlay Construction	Aug-Sept 1979	Sept 1979	Feb 1980	July 1981	
Materials Evaluated	Chipseal (Control)	Control	Control	Control	
	Bidim C-22	Bidim C-22	Bidim C-22	Old Petromat	
	Bidim C-34	Bidim C-34	Bidim C-34	New petromat	
	Old Petromat	Old Petromat	Old Petromat	Reepav - 3 oz	
	New Petromat	New Petromat	New Petromat	Reepav - 4 oz	
	Petromat 8 oz	Petromat 8 oz	Petromat 8 oz	Crown-Zellerbach	
			Bidim C-28	Mirafi 900x	
HMAC Overlay				Type B	Type D
Asphalt Type & Grade	Type D	Type D	Type D	AC-20	AC-20
Asphalt Source	AC-10	AC-10	AC-10	Refinery 6	Refinery 24
Aggregate Type	Refinery 4	Refinery 15	Refinery 15	Crsh Limestone	Lt wt +conc.
	Crsh Limestone + Field Sand	Crsh Limestone + Field Sand + Blow Sand	River Gravel + Sand	+ Field Sand	Sand + Fld Sand
Asphalt Additives	None	None	None	TexEmuls M-200	Pavebond AP
Thickness	1 3/4-inch	1 1/4-inch	1.6-inch	2-inch	1 1/2-inch
Traffic Data (1980)			(US 281) (SH 107)		
ADT	3,400	7,900	19,500 13,000	14,000	
Percent Trucks	24.1	23.8	3.4 18.2	22	
Equivalent 18D axle loads	5,983	15,468	19,043 1,476	--	
Percent Tandem Axles	90	20	90 40	40	

Table 2.2. Characteristics of geotextile interlayer materials (Button and Epps 1982).

Fabric I.D.	Nominal Weight, oz/yd$_2$	Nominal Thickness, mils	Material	Type Construction	Type Filament	Fiber Bonding
Bidim C-22	4	60	Polyester	Nonwoven	Continuous	Needle-punched
Bidim C-34	8	90	Polyester	Nonwoven	Continuous	Needle-punched
Old Petromat	4	--	Polypropylene	Nonwoven	Staple	Needle-punched and heat bonded on both sides
New Petromat	4	--	Polypropylene	Nonwoven	Staple	Needle-punched and heat bonded on one side
Petromat - 8 oz.	8	--	Polyproprylene	Nonwoven	Staple	Needle-punched and heat bonded on one side
Bidim C-28	6	75	Polyester	Nonwoven	Continuous	Needle-punched
Reepav - 3 oz.	3	15	Polyester	Nonwoven	Continuous	Spunbonded and heat bonded
Reepav - 4 oz.	4	17	Polyester	Nonwoven	Continuous	Spunbounded and heat bonded
Crown-Zellerbach	5	60	Polypropylene	Nonwoven	Continuous	Spunbounded and needle-punched
Mirafi 900 X	5	--	Polyester and Polypropylene	Woven	Continuous	Woven

Table 2.3. Mechanical properties of geotextile interlayer materials (Button and Epps 1982).

34

Test Pavement Location	Fabric I.D.	Average Fabric Weight, oz/yd²	Machine Direction[4]		Cross Machine[4]		Asphalt Retention,[2] oz/ft²	Change in Area,[3] percent
			Elongation, percent	Break, pounds	Elongation, percent	Break, pounds		
Ozona	Bidim C-22[1]	4.4	85	148	84	128	4.2	0
	Bidim C-34[1]	7.1	91	215	108	211	5.2	0
	Old Petromat[1]	4.2	103	75	65	92	2.2	-2
	New Petromat[1]	4.2	76	121	67	154	3.6	-5
	Petromat - 8 oz.	8.6	78	300+	97	300+	4.9	0
Amarillo	Bidim C-22	--	--	--	--	--	--	--
	Bidim C-34	--	--	--	--	--	--	--
	Old Petromat	4.3	84	91	71	112	2.2	-2.0
	New Petromat	4.3	69	115	82.9	133	3.6	-4.8
	Petromat - 8 oz.[1]	8.4	71	300+	71	300+	4.2	0
Edinburg	Bidim C-22	4.9	95	113	99.8	116	3.6	-2.3
	Bidim C-34	--	--	--	--	--	--	--
	Old Petromat	--	--	--	--	--	--	--
	New Petromat	4.6	104	124	91	186	4.0	-9.0
	Petromat - 8 oz.	--	--	--	--	--	--	--
	Bidim C-28	6.5	83	162	91	113	3.8	0
Tyler	Old Petromat	4.6	90	154	79	110	3.4[1]	0[1]
	New Petromat	4.5	94	81	76	118	2.3[1]	0[1]
	Reepave - 3 oz.	3.0	50	89	59	73	--	--
	Reepave - 4 oz.	4.1	52	116	57	96	1.6	0
	Crown-Zellerbach	5.1	140	117	161	112	3.9[1]	0[1]
	Mirafi 900 X	4.9	58	102	47	76	--	--

[1] Only one sample tested.
[2] Asphalt required to saturate fabric.
[3] Change in area (shrinkage upon exposure to asphalt at 275° F for 60 minutes.
[4] Grab tensile test, ASTM D1682

Evaluation of the performance of all the test sections for 10 years from 1979 to 1989 indicated that the geotextile materials were "not consistently cost-effective methods to address reflective cracking. However, limited evidence indicated that geotextiles reduce "pumping after cracking dose occur" (Button 1989).

2.2.4. TxDOT Experience in Waco, Amarillo and Pharr Districts, 1999 to 2009

As part of TxDOT Project 1-7777, a large number of test sections were constructed in three different regions of Texas that had significantly different climate and geographical characteristics. That included Marlin (located in Waco District), northeast of Amarillo city (located in Amarillo District), and McAllen (located in Pharr District). General characteristics of the project locations are summarized in Table 2.4. Test sections in Amarillo city and McAllen were constructed on an existing flexible pavement while the test sections at Marlin were constructed on an existing jointed rigid pavement. Section profiles for the test sections at each location is presented in Table 2.5.

A wide range of interlayer materials were used in construction of the test sections including the three main types of polymeric interlayers (geotextiles (fabrics), geogrids, and geocomposites), glass grid materials and wire mesh. The plan layout of the test sections constructed in the three districts is presented in Figure 2.8, Figure 2.9, and Figure 2.10.

Table 2.4. General characteristic of project sites in Waco, Amarillo and Pharr Districts (2009).

District	Highway Name	Pavement Type	Average Daily Temperature Range (°F)	Elevation (ft)	Annual Rainfall/ Precipitation (inch)	Traffic (2005)	
						AADT	ESAL
Amarillo	SH 136	Flexible	23 – 92	3585.0	18.0	4000	1933
Pharr	FM 1926	Flexible	48 – 96	100.0	24.0	27500	1279
Waco	BUS 6	Flexible over jointed concrete	34 - 97	388.0	36.0	3100	791

Table 2.5. Section profile of test sections at project sites in Waco, Amarillo and Pharr Districts (2009).

Test Pavement	Layer	Description
Amarillo	Layer 1	2.0-inch Type D HMA
	Layer 2	Geosynthetic/grid/mesh
	Layer 3	0.75-inch to 1.0-inch Type D leveling course
	Layer 4	2.25- to 2.5-inch HMA
	Layer 5	3.5- to 4.0-inch ASB
	Layer 6	12.0-inch flexible base
	Layer 7	Subgrade (treatment status unknown)
Waco	Layer 1	1.75 to 2.0-inch HMA
	Layer 2	Geosynthetic/grid/mesh
	Layer 3	1.0-inch HMA level up
	Layer 4	0.2-inch to 0.25-inch seal coat with TR
	Layer 5	6.0-inch jointed concrete 20-ft spacing
	Layer 6	Subgrade (treatment status unknown)
Pharr	Layer 1	2.0-inch Type D HMA
	Layer 2	Geosynthetic/grid/mesh
	Layer 3	Type D ACP (1.0-inch inside, milled to zero thickness at outside)
	Layer 4	14-inch flexible base (2% lime stabilized)
	Layer 5	12-inch subgrade (3% lime stabilized)

Figure 2.9. Plan layout of Waco District test sections (2005).
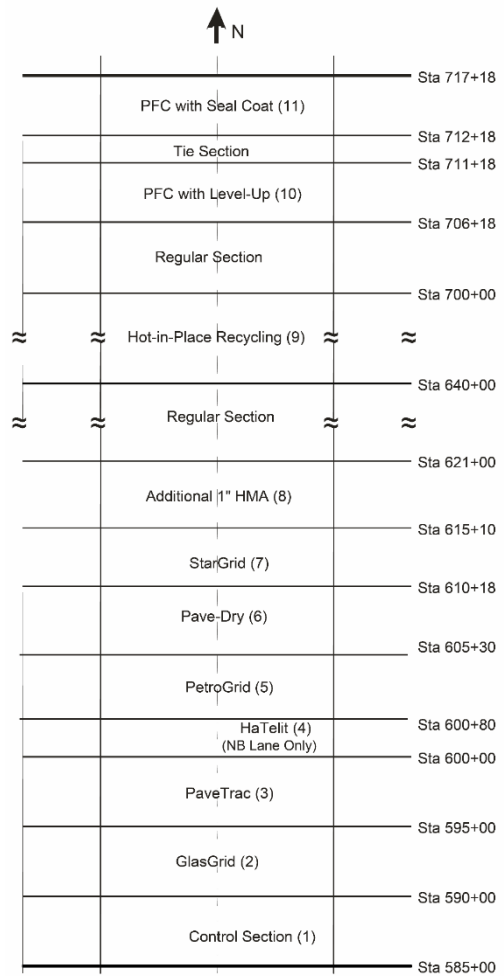
Figure 2.10. Plan layout of Amarillo District test sections (2005).

37

	Northbound Lanes	Turn Lane	Southbound Lanes	
Sta 81+00				Control
Sta 86+00				GlasGrid 8501
Sta 91+00				HaTelit C40/17
Sta95+85				
Sta 96+00				PaveDry 381
Sta 101+00				Control with 1-inch Thicker Section
Sta 106+00				StarGrid GPS
Sta 111+00				
Sta 112+50				Bitutex
Sta 116+00				PetroGrid 4582
Sta 119+60				
Sta 121+00				

Figure 2.11. Plan layout of Pharr District test sections (2005).

Evaluation of the test sections was conducted by documenting the cracks on the pavement surface before and periodically after overlay construction. Various types of cracks were quantified according to instruction provided in the Distress Identification Manual for the Long-Term Pavement Performance Studies. The frequency of visits was once per year in the initial stages and twice a year at the later stages.

Evaluation of the performance of the test sections in Pharr District in 2009 indicated minimal reflection cracking (Chowdhury et al. 2009). Also, considering the difference in the original pavement layer (i.e., rigid pavement in Waco District and flexible pavement in Amarillo District), Chowdhury et al. 2009 concluded that the field data for these two locations cannot be

38

directly compared. Comparison between the performances of various test sections in each project site was not reported.

In spite of the extensive scale of the study and the large number of field test sections and interlayer products, evaluation of the field data in this project did not result conclusive findings. That may partly be attributed to the lack in-situ measurement devices or insufficient field testing. According to Chowdhury et al. (2009), "The findings of this project and the literature review of other recent field evaluations of geosynthetic products show that their effectiveness in reducing the number of reflective cracks is marginal." However, the evaluation of the literature by the researchers suggested that "certain geosynthetic products can, however, reduce the severity of reflective cracks." Specifically, for future field evaluations, the researchers suggested that "test sections should be constructed using more popular and relatively good performing geosynthetic products."

Lastly, cost-effectiveness analysis of various geosynthetic materials used in this project indicated that "[b]ased on first cost alone, installation of an inexpensive fabric must increase the service life of an overlay by more than 15 percent to be cost effective." (Button and Chowdhury 2006). The Button and Chowdhury (2006) evaluation also suggested that "more expensive grid or composite material may need to double the service life of an overlay to be cost effective."

2.2.5. TxDOT Experience in Austin District: US77, Lee County, 2017-present

As part of this project, asphalt strain gauges were used to evaluate performance of geosynthetic-reinforced asphalt overlay in a pavement rehabilitation project along US77, located in Lee County, near Lincoln, TX. The existing pavement structure was afflicted by a network of transverse and longitudinal cracks, and it was decided to install an overlay (1.5 inch) to provide a smoother ride surface. The existence of cracks in the old pavement provided a good opportunity to understand the benefits of asphalt reinforcement in mitigating the reflection of these cracks through the new proposed overlay.

To understand the role of asphalt reinforcement, eight test sections (four reinforced and four control) were constructed, three of which were instrumented (two reinforced and one control). Two different interlayer reinforcement products were used. The three instrumented test sections comprised of sections with Polyester (PET) reinforcement, Polyvinyl Alcohol (PVA) reinforcement and control section. Each instrumented test section housed six asphalt strain gauges within the old pavement 2 inches below the surface of the existing pavement structure. The asphalt strain gauges were installed at different locations, in different orientations and either within or between the wheel paths (Figure 2.11). The asphalt reinforcement and the 1.5-inch overlay were constructed on top of the existing pavement. The instrumented test sections were

trafficked using a heavy vehicle of known load. The strains at the location of six asphalt strain gauges at each instrumented test section were recorded. Figure 2.12 shows an example of the asphalt strain data recorded by an asphalt strain gauge oriented in the longitudinal direction located within the wheel path. The three peaks in the strain data reflect the three axles of the heavy vehicle used for trafficking.
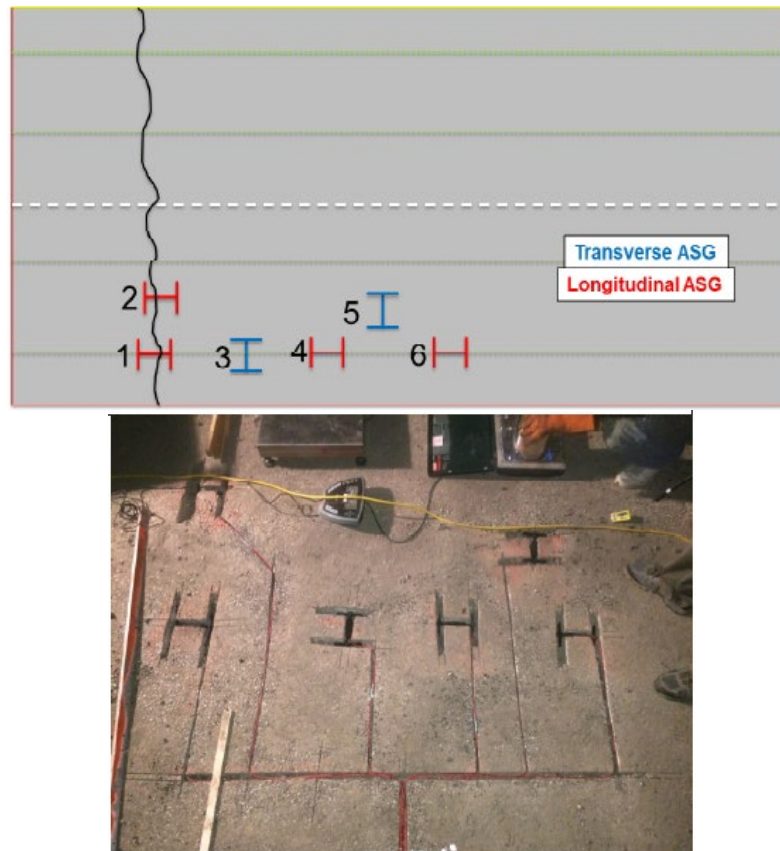
Figure 2.12. Location and orientation of asphalt strain gauges in instrumented sections (Phillips 2017).
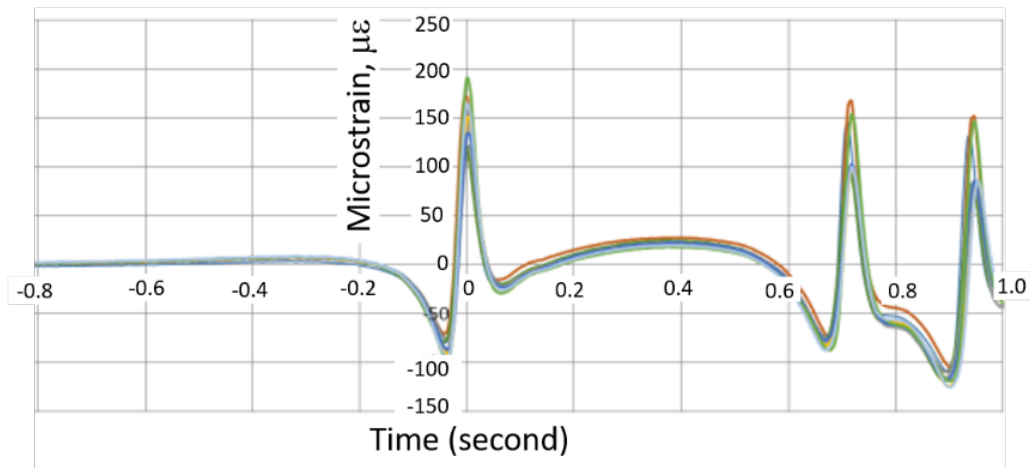
Figure 2.13. Example of strain data recorded under a heavy vehicle with three axles (Phillips 2017).

As part of the evaluation of benefits from asphalt reinforcement in the US77 rehabilitation project, a comprehensive controlled loading campaign was undertaken by Austin District to determine the response of the various strain gauges under controlled loading. The loading campaign involved the measurement of strains induced in both asphalt-reinforced and control sections under a heavy vehicle load, light vehicle load and Falling Weight Deflectometer (FWD) load (Figure 2.13). The heavy and light vehicle loads were applied at static conditions and two different speeds. To locate the sensors installed for configuring the loading campaign, a hand-held ground penetrating radar was used. Once the sensors were located, the chosen vehicles were driven over the sensors along the wheel path. The variation in magnitude (heavy vs. light) and type of load (rolling vs. cyclic vs. static) helped capture the non-linearity in the response of the asphalt layers to the load applied. This helped Austin District characterize the behavior of reinforced asphalt overlays.

Figure 2.14. Controlled loading of instrumented geosynthetic-reinforced overlay sections along US77, Austin District: (a) heavy vehicle; (b) light vehicle; and (c) FWD.
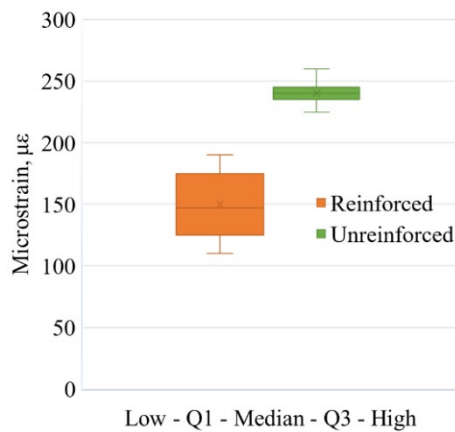
Figure 2.15. Comparison of strain under heavy vehicle.

Although no visible surface distress was observed in any test sections (control or reinforced) six months after the end of construction, the strain data recorded under the heavy vehicle showed stark differences (Figure 2.14). The strain in the longitudinal direction within the wheel path and beneath the asphalt reinforcement was found to be lower than the strain induced at the similar location but in the section without reinforcement. This clearly predicted a better performance of

the asphalt reinforced section when compared to the control section, early in the life of the pavement structure. Performance of the test sections in this project is still being evaluated.

2.2.6. TxDOT Specifications and Design Procedures Relevant to Reinforced Asphalt

A Departmental Material Specification (DMS) for "Geogrid-fabric Composite for Pavements" (DMS-6250) was adopted by TxDOT for a short period from March 2000 to May 2003. The scope of DMS-6250 was geogrid-fabric composite materials to "control surface moisture infiltration and retard reflective cracking." Accordingly, material requirements by this DMS included a specified range for asphalt retention and a minimum value for tensile modulus @ 2% strain (Table 2.6).

Table 2.6. Material requirements for geogrid-fabric composite from TxDOT DMS-6250.

Physical Property	Test Method	Requirements	
		Minimum	Maximum
Asphalt Retention, L/m² (gal/yd²)	Test Method "Tex-616-J"	0.68 (0.15)	2.72 (0.60)
Tensile Modulus @ 2% Elongation* N/m (lb./ft) (*secant modulus without offset allowances)	ASTM D 4595, modified	905,000 (62,000)	

In the absence of a relevant DMS for the specific objective of reinforcement, TxDOT Districts have typically adopted Special Specifications (SS) for their construction projects. In this case, several SS have adopted only the use of glass grid products (e.g., SS3231, SS3244, SS3285). These documents have typically specified two types of glass grids as follows:

Type I: intended for placement and reinforcement of the entire surface of the overlay. With mesh openings of 1" (center to center)

Type II: intended for reinforcement in transverse and longitudinal joints and to retard reflective cracking, and is placed directly over the joints as recommended by the manufacturer. With mesh opening of 1" x ¾" (center to center)

As specified in Table 2.7, material requirements in these SS included only physical characteristics of the geogrid and did not address the grid mechanical properties such as its tensile strength or stiffness.

Table 2.7. Grid material requirements in TxDOT SS3231, SS3244 and SS3285 adopted in 2011-2014.

Property	Type I	Type II
Area Weight (ASTM D5261-92)	300 g/m2 (11 oz/sy)	500 g/m2 (16 oz/sy)
% Open Area (Tex-621-J)	50 % min	50 % min
Softening Point (ASTM C338)	537 C (1000 F min)	537 C (1000 F min)
Loss on Ignition (ASTM D4963-89)	15 % min	15 % min

However, most recent SS (e.g., SS3057, SS3062) have focused on material requirements to specifically fulfill the reinforcement function. In particular, the SS adopted for construction of the geosynthetic-reinforced asphalt overlay along SH21 in the Austin District (SS3062) has required a composite material "composed of a polymeric grid structure (geogrid) that is covered by a polymeric textile fabric (geotextile) on one or both sides" to "provide mitigation against reflective crack propagation." As presented in Table 2.8, the material requirements by SS3062 includes mechanical properties of the geogrid (e.g., tensile strength and tensile stiffness) in both machine (MD) and cross-machine directions (CMD). It appears that findings from the US77 overlay construction project in Austin District have contributed to the development of the more comprehensive SS for geosynthetic-reinforced asphalt overlay construction along SH21. However, further field data still required to enhance this specification into more comprehensive departmental material specifications.

Table 2.8. Polymeric paving material requirements in SS3062 for construction of overlay along SH21.

Property	Test Method	Min	Max
Mass/Unit Area, (oz/yd^2)	ASTM D 5261	8	
Aperture Size, (in.)			1.5 x 1.5
Tensile Strength, lb/ft			
Machine Direction (MD)	ASTM D 6637	3,425	
Cross-Machine Direction (CMD)		3,425	
Tensile Strength at 3% Strain, lb/ft			
Machine Direction (MD)	ASTM 6637	835	
Cross-Machine Direction (CMD)		835	
Identification of Fibers, ºF (ºC)	ASTM D 276	490 (255)	
Asphalt Retention, gal/sy	ASTM D 6140	0.10	

In spite of several successful experiences with geosynthetic-reinforced asphalt layers, TxDOT has yet to adopt a design procedure for these roads. Flexible Pavement Design System 21 (FPS 21) is the most recent version of the design procedure adopted by TxDOT for flexible pavements. The mechanistic-empirical approach followed in FPS 21 enables the design of conventional flexible pavements with bound and unbound pavement layers. However, the design of flexible pavements with geosynthetic-stabilization of the base course has not been included in

this software. Only recently, TxDOT has begun approaching the problem of design of geosynthetic-stabilized base flexible pavements in the TxDOT Project 0-6834, which produced promising results. The conclusion of that project called for additional tests on full-scale test sections to determine conclusive results. So far, there are not well-established methods for design of asphalt overlays with asphalt reinforcement. It is generally designed as having no reinforcement and the reinforcement is simply added to mitigate reflective cracking and an empirical adjustment to the design life of the overlay is made. This is also largely due to the lack of understanding of the mechanisms associated with geosynthetic-reinforced asphalt overlays as well as lack of conclusive data on their performance.

2.2.7. Summary

TxDOT has had long experience with using various types of synthetic materials to enhance the performance of HMA overlays. Earlier research has typically focused on the interlayer systems that could primarily provide functions other than reinforcement. This included Stress-Absorbing Membrane Interlayers (SAMI) and paving fabric interlayer systems that have been used to fulfill primarily waterproofing functions or stress-relieving functions (e.g., Petromat Systems) (Huffman 1978; Amini 2005). However, early research was not conclusive regarding benefits obtained by these proposed interlayer systems, cost effectiveness of these techniques, and difficulties with their proper construction (Cooper et al. 1983; Button 1989; Rahman et al. 1989). Additional field studies were conducted in the Amarillo, Waco and Pharr Districts to evaluate field performance of geosynthetic-reinforced asphalt layer in different climates and geological characteristics (TxDOT Project 0-1777, Chowdhury et al. 2009). However, the results obtained in this research were also inconclusive regarding the effectiveness of geosynthetic products and relevant characteristics for asphalt reinforcement. A primary reason that the results of these projects were obscure was the absence of sufficient field data to allow comparative evaluation of performance between control (non-reinforced) test sections and geosynthetic-reinforced sections as well as among field sections that were reinforced using various geosynthetic products. Evaluation of a more recent asphalt overlay construction project in Austin District has resulted particularly promising findings (Phillips, 2017).

2.3. Previous Experience by Other DOT and Agencies in the US and overseas

A number of recent previous field trials and research studies completed by various DOTs and transportation agencies across the US and overseas have been reviewed and a few of the relevant research experiences have been outlined in the following sections.

2.3.1. Colorado DOT: Crack Reduction Strategies on a Pavement Warrant Project (IH25 at Fountain Head)

2.3.1.1. Background

The Colorado State Senate Bill 97-128, passed during the year 1997, suggested the Colorado DOT to start a pilot program to evaluate the pavement performance for a period of three years under the title "warranty projects." Three projects were chosen by the Colorado DOT under the warranty specification and as a requisite, the contractors had to guarantee the pavement quality and maintenance for a period of three years from their construction date. Out of the three warranty projects, the construction details of one of the projects (C-DOT-DTD-R-2003-5) has been reported. The selected project was a rehabilitation program of a four-mile stretch on I-25, south of Fountain, Colorado. Out of the several reflection crack retarding techniques available, the contractor chose to adopt eight experimental techniques and a control section. The experimental techniques included routing the cracks and sealing with two types of crack sealants, non-routing the cracks and sealing with two types of crack sealants, two geotextiles with different weights, and two types of heavily reinforced tape systems.

2.3.1.2. Construction

Two sets of experimental sections were constructed along the north and southbound lanes of the four-mile stretch on I-25 south of Fountain, Colorado, as shown in Figure 2.15, making a total of 18 experimental test sections. The contractor identified the distress type and mapped their exact locations before milling the existing asphalt surface. Between the two sets of experimental sections considered, the entire width of Section 1 (Figure 2.15a) was milled to a depth of 1 inch and an additional depth of a $^{1/2}$ inch was milled in the driving lane along with an entire width of 1-inch-deep milling in Section 2 (Figure 2.15b). A 5-inch Hot Bituminous Pavement (HBP) layer was laid in Section 1 and a 5 $^{1/2}$-inch-thick HBP was laid in the driving lane of Section 2 as shown in Figure 2.15.
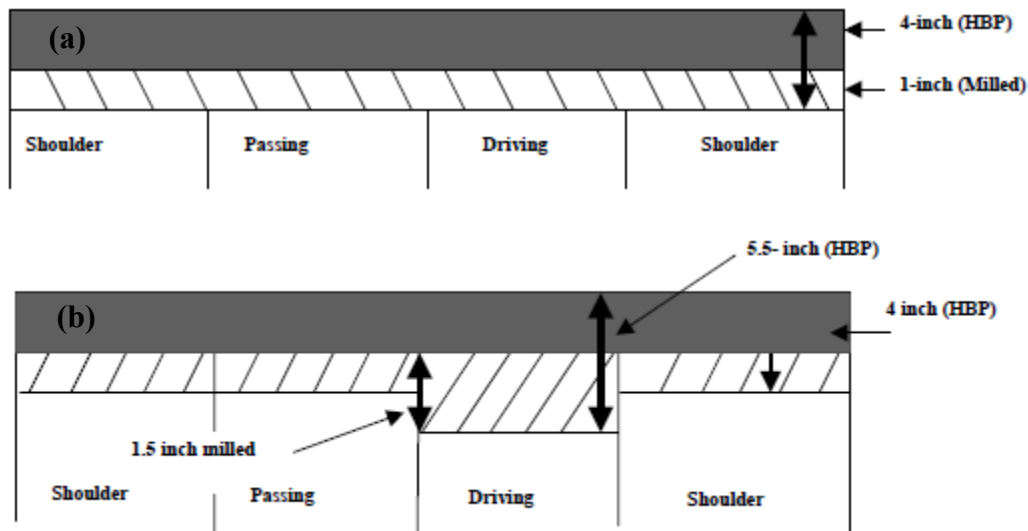
Figure 2.16. Schematic of experimental test sections (C-DOT-DTD-R-2003-5).

A schematic of the typical layout of Sections 1 and 2 is shown in Figure 2.16 and it can be observed that the first test section is a control section followed by two sections with Petromat 4599 and Petromat 4597 installed in the driving lanes. Petromat 4599 and 4597 had a tensile strength of 90psi and 120psi, respectively, and were available in 12-foot-wide rolls. In this study, both the products were installed on the milled surface with the help of an AC10 tack coat (Figure 2.17a). A 12-inch-wide self-adhering tape, Petrotac, was installed over the transverse cracks in the next test section as shown in Figure 2.17b. Similarly, another tape, Progaurd, was installed on the transverse cracks in the next section. Unlike Petrotac, Progaurd required a tack coat to be applied before its installation, hence an AC10 tack coat was applied prior to the installation of Progaurd (Figure 2.17c). The Type-A crack filler satisfying the requirements described in ASTM D3405 and Type -B crack filler named "Super Stretch" were placed in the routed and non-routed joints of the next four sections as presented in Figure 2.16. Figure 2.17d and Figure 2.17e present photographs of the equipment used to clean the crack and rout the crack, prior to filling it with sealant, respectively.
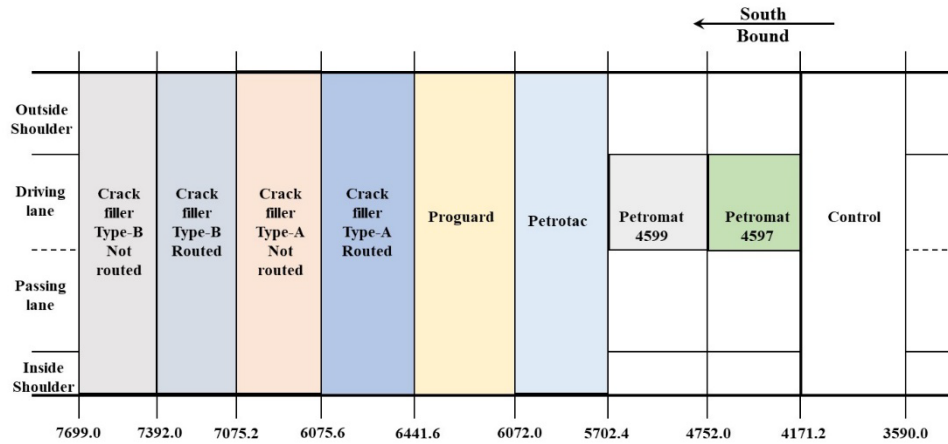
Figure 2.17. Schematic of typical test section layout.

| Outside Shoulder | | | | | | | | | | |

The table in Figure 2.17 contains the following labeled sections from left to right:

Crack filler Type-B Not routed | Crack filler Type-B Routed | Crack filler Type-A Not routed | Crack filler Type-A Routed | Proguard | Petrotac | Petromat 4599 | Petromat 4597 | Control

Position markers: 7699.0, 7392.0, 7075.2, 6075.6, 6441.6, 6072.0, 5702.4, 4752.0, 4171.2, 3590.0

South Bound (arrow pointing left)

Left side labels: Outside Shoulder, Driving lane, Passing lane, Inside Shoulder

Figure 2.18. (a) Placement of Petromat; (b) placement of Petrotac; (c) placement of Progaurd; (d) equipment used to clean cracks; and (e) equipment used to rout cracks. (C-DOT-DTD-R-2003-5).

2.3.1.3. Post-construction evaluation

The evaluations primarily consisted of mapping the recurrence of previously identified cracks in the test sections. The contractor had previously identified specific cracks and their locations in each test section, prior to pavement surface milling, and an average of six cracks were identified as representative cracks in each test section. The first post-construction evaluation was performed during the spring of 1999, which was almost a year after construction and minimal transverse cracking was observed, specifically in the shoulder and acceleration and deceleration lanes with a small percentage in the driving lanes. The evaluation was emphasized on the

49

recurrence of transverse cracks because the treatment techniques were typically applied to the transverse cracks.

In summary, less than a quarter of the cracks were observed to recur within a year of construction and were predominantly in Section 1 with 1-inch milling. About 21% of the transverse cracks in Section 1 recurred during the three-year warranty period and an additional 10% transverse cracking was observed after the three-year evaluation period. However, there was an excessive amount of longitudinal construction joint failure witnessed throughout the length of the project, after the three-year warranty period. Although it is apparent from the cracking that the additional milling reduced the amount of reflective cracking after three years, the majority of this research was based on visual observations, and consequently making sound engineering judgments based on this outcome would not be appropriate.

2.3.2. Maine DOT: Experimental Installation of Geosynthetic Pavement Reinforcement to Reduce Reflective Cracking

2.3.2.1. Background

The performance benefits of installing the geosynthetic pavement reinforcement fabric to minimize the reflective cracking on Auburn-Lewiston Municipal Airport runway was investigated in this project. This project was part of the runway overlay program administered by Maine DOT during the year 2000 and consisted of installing a geosynthetic fabric prior to the placement of a 40-mm-thick Superpave HMA overlay.

2.3.2.2. Construction

The installation of geosynthetic fabrics across the entire width of the runway was not feasible due to cost constraints and the fabrics were therefore installed in a "Band-Aid" style on the transverse cracks as shown in Figure 2.18.

Figure 2.19. Photographs showing the installation of fabrics on transverse cracks (ME 01-3)

The rolls were divided into half-width and full-width portions. The half-width portion of the fabrics were installed on the south end of the runway for an approximate length of 815 feet and the full-width portions were installed in the remaining portion of the test section. The geosynthetic fabric adopted in the study was a Glasgrid 8502 (see Figure 2.19), a fiberglass reinforcement with an elastomeric polymer and pressure sensitive adhesive backing, with a grid size of 12.5mm and weight of 560g/m^2. To evaluate the performance of these geosynthetic reinforcements against reflective cracking, a control section was selected on the north end of the runway.

Figure 2.20. Photograph showing close-up of glass grid installed on a transverse crack (ME 01-3).

The fabric adopted in the study was a self-adhesive and required rolling with a rubber tire roller to glue it to the existing surface before overlaying the HMA. However, the contractor failed to activate the glue as they were unable to achieve a sufficient number of passes with the rubber-tired rollers before overlaying. In addition, the sealant used in the transverse cracks reacted with the 40-mm-thick Superpave HMA and encountered a number of issues such as shoving and

51

creeping during compaction of the HMA layer. To overcome this issue, a 15-mm shim lift was placed in the rest of runway portion, the previously completed portions were milled up to a depth of 15mm and a 30-mm wearing course was placed. This problem was reported to be occasionally encountered on highway overlays by Maine DOT.

2.3.2.3. Evaluation and Summary

The evaluation was done by visual examination and with the help of the Automatic Road Analyzer (ARAN) shown in Figure 2.20. The location of the fabric and the transverse cracks were videotaped and documented with the help of ARAN prior to installation. The ARAN videotapes recorded during future evaluation processes would be compared to those recorded prior to the overlay installation to determine the rate of reflective cracking. In addition, the test results may not be accurate due to the construction issues. However, the reinforced sections would be monitored along with the control sections to evaluate any improvements in minimizing the reflective cracks.

Figure 2.21. Photograph of Automatic Road Analyzer (ARAN) surveying test section (ME 01-3).

2.3.3. Oregon DOT: Geosynthetic Materials in Reflective Crack Prevention

2.3.3.1. Objective

The main objective of this research was to test, evaluate and identify the most effective geosynthetic reinforcement to minimize the reflective cracking on a test section along US-97. The test sections, consisting of 98 transverse cracks, were treated with five different geosynthetic materials; 22 cracks were treated with a crack filler and a control section of 20 cracks without

any treatment were evaluated for a period of nine years from 1998 to 2007. The specifications of different geosynthetics adopted in the study have been summarized in Table 2.9 and the details of seven test sections are as follows:

Control section: overlay only

Crack filler: crack cleaning, fill with D-mix (max. size aggregate of 12.5mm), overlay

Glasgrid 8502: crack cleaning, fill with D-mix, place geosynthetic over cracks, overlay

GeoTac: crack cleaning, fill with D-mix, place geosynthetic over cracks, overlay

PavePep SA: crack cleaning, fill with D-mix, place geosynthetic over cracks, overlay

Polyguard Cold Flex 2000 SA: crack cleaning, fill with D-mix, place geosynthetic over cracks, overlay

Polyguard 665: crack cleaning, fill with D-mix, place geosynthetic over cracks, overlay

Table 2.9. Specifications of geosynthetic materials adopted in the study (Sposito and Brooks, 1999; OR-RD-08-01).

Material	Tensile Strength	Tensile Strength Test	Thickness (mm)	Width (mm)
Glasgrid 8502®	200 x 100 kN/m	G.R.I. GG 1-87	1.73	1.52
Pavement reinforcing mesh consisting of fiberglass reinforcement coated with an elastomeric polymer and a pressure sensitive adhesive backing (Bayex, 1997).				
GeoTac®	8.9 kN/m	ASTM D882 (modified)	2.03	0.61
Peel-and-stick, thick waterproofing membrane manufactured from a rubberized asphalt, with a top layer of durable, tightly bonded polyester geotextile (Contech, 1994).				
PavePrep SA®	167 kg/cm*cm	ASTM D412-87	3.43	0.61
Heavy-duty crack reduction/stress relief interlayer consisting of a flexible high density asphaltic membrane laminated between a nonwoven and woven polyester geotextile, with an adhesive backing (Contech, Guide, 1996).				
Polyguard Cold Flex 2000 SA™	53 kN/m	ASTM D412	3.43	0.61
Peel-and-stick pavement repair membrane consisting of two layers of high strength polypropylene fabric with a layer of flexible mastic to provide stress relief (Polyguard, May-June 1998).				
Polyguard 665™	16 kN/m	ASTM D882 (Method B)	1.65	0.61
Pavement waterproofing membrane consisting of a rubberized asphalt waterproofing adhesive, laminated to a strong woven polypropylene backing, with a silicone treated release sheet (Polyguard, January 1998).				

2.3.3.2. Construction

The test section area was located in the forested mountainous region of northern Klamath County, near Crater Lake and the test sections spanned a length of approximately four miles from 0.58 miles south of Diamond Lake Junction along US-97.

The entire width of the pavement was cleaned thoroughly before the installation of geosynthetic materials to achieve a good adhesion between them. The contractor installed geosynthetics from September 21-24, 1998 as shown in Figure 2.21 and the installation of some geosynthetics was highly labor intensive and costly due to the equipment and labor costs incurred. The installation costs for each of the seven test sections are summarized in Table 2.10 and it can be witnessed that the cost of installation of all the geosynthetics were consistently higher. No money was spent on the control sections because nothing was done to them and only crack fill was applied to the crack-fill only sections, which amounted to less than $100. Among the geosynthetic materials used on this project, the cheapest geosynthetic material to install was Polyguard 665, while the most expensive was Glasgrid 8502, followed by PavePrep SA.

After all test areas were treated as needed and geosynthetic materials were installed, an overlay was constructed. The overlay material was 50 mm of Class "F" (25 mm max. aggregate size) asphalt concrete mix wearing course placed full-width. In August 2000, the roads crew placed a fog seal over the test area.

Figure 2.22. Geosynthetic installed on test section (OR-RD-08-01).

Table 2.10. Summary of installation costs for each test section (OR-RD-08-01).

Material Used	MATERIAL (S/M)	LENGTH (M)	CRACK FILL (S/M)	LABOR & EQUIP (S/M)	COST	Cost Per Crack	Cost Per Meter
GLASGRID 8502® + CRACK FILL	$7.41	218.9	$7.28	$8.08	$4,984	$249.22	$22.77
GEOTAC® + CRACK FILL	$7.28	221.4	$7.28	$2.74	$3,830	$212.79	$17.30
PAVEPREP SA® + CRACK FILL	$11.77	246.0	$7.28	$2.47	$5,294	$264.70	$21.52
POLYGUARD COLD FLEX 2000 SA™ + CRACK FILL	$6.42	246.0	$7.28	$2.47	$3,978	$198.89	$16.17
POLYGUARD 665™ + CRACK FILL	$3.90	246.0	$7.28	$2.47	$3,358	$167.90	$13.65
CRACK FILL ONLY	none	297.7	$7.28	none	$2,167	$98.51	$7.28
CONTROL (none)	none	246.0	none	none	$ -	$ -	$0.00

2.3.3.3. Summary

The first evaluation (visual) was made one year after the 1999 installation and the subsequent yearly evaluations continued for eight years until May 2007. By the end of project, 132 of 140 transverse cracks had reflected through the pavement overlay (Figure 2.22).

Figure 2.23. Photographic comparison of crack 140 before overlay construction (left) and reflection of crack through overlay after construction (right) (OR-RD-08-01).

The severity and total number of cracks observed in 2007 were compared to those recorded prior to overlay construction in 1998 (Table 2.11). There is no conclusive data reported to suggest that geosynthetic materials helped minimize the reflective cracking. However, it was reported that the test sections with only crack filler outperformed all geosynthetic-reinforced test sections.

Table 2.11. Comparison of transverse crack severity, total number and length in 1998 and 2007 (OR-RD-08-01).

Treatment	1998 Low	2007 Low	1998 Med.	2007 Med	1998 High	2007 High	1998 sum	2007 sum	1998 length	2007 length
CONTROL(NONE)		6	8	8	12	3	20	17	146	94.8
CRACK FILL ONLY		8	9	9	13		22	17	160.6	116.8
GLASGRID 8502®		19	9	1	11		20	20	131.2	131.2
GEOTAC®		6	11	11	7	1	18	18	131.4	112.8
PAVEPREP SA®		9	10	6	10	5	20	20	146	131.4
POLYGUARD COLD FLEX 2000 SA™		6	5	13	15	1	20	20	146	146
POLYGUARD 665™		2	14	15	6	3	20	20	146	146
TOTAL	0	56	66	63	74	13	140	132	1007.2	879

Overall, the geosynthetics installed in the study performed poorly in the coldest years such as 1998, 1999, 2005 and 2006. No geosynthetic material tested was capable of restricting the reflective cracking completely. Among the geosynthetic materials tested, Glasgrid 8502 performed the best as it helped retard the severity of cracks.

2.3.4. NCAT Test Track: Glasgrid Performance at NCAT

2.3.4.1. Background

The test tracks at National Center for Asphalt Technology (NCAT), Auburn University, were the result of an industry and government collaboration with an agenda to improve the quality of flexible pavements. The primary aim was to provide an accelerated loading test facility to test a large number of test sections simultaneously. The track consisted of 26 sections in the tangents and another 20 sections in the curves as shown in Figure 2.23.
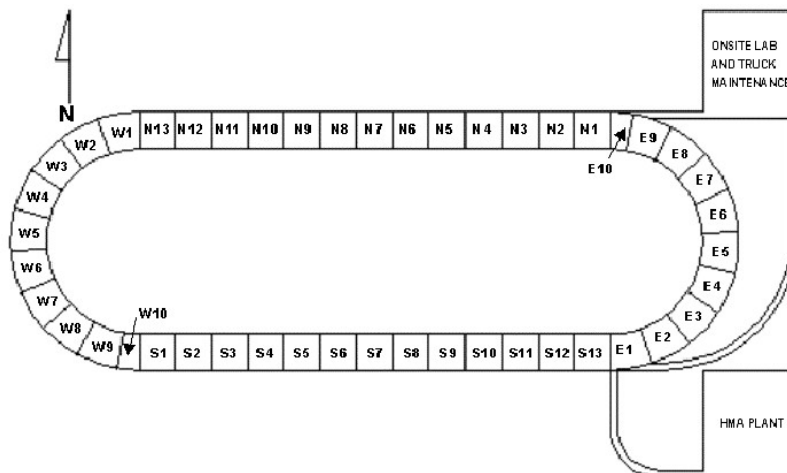
Figure 2.24. Schematic of NCAT test track layout (NCAT Report, 2002).

The sponsors of the first cycle at the track during the year 2000 included Alabama DOT, Florida DOT, Georgia DOT, Indiana DOT, Mississippi DOT, North Carolina DOT, Oklahoma DOT, South Carolina DOT, Tennessee DOT and the Federal Highway Administration (FHWA). Each sponsor was free to choose and establish the testing program for their test sections.

2.3.4.2. Construction

The study reported here was primarily focused on the evaluation of geogrid-reinforced asphalt pavements under real field traffic conditions. To accomplish this, a 200-foot-long test section W1 (Figure 2.23) was selected. The construction of W1 test section was scheduled during June 2000 and the 200-foot-long test section was divided into two portions 100 feet in length. No geogrid was installed in the first 100 feet of the test section to serve as a control section and Glasgrid 8501 was installed in the next 100-foot-length of the test section. The asphalt mix consisted of a maximum aggregate size of 12.5 mm and a binder PG 76-22 SBR with an optimum bitumen content of 6.1%. Glasgrid 8501 is a fiberglass geogrid with a tensile strength of 100kN/m in both machine and cross-machine directions.

The entire two-lane-wide track was supported by a 20-inch-thick HMA base and 4-inch-thick asphalt layers were paved above them in two 2-inch lifts in the test section. Glasgrid 8501 was placed between the two lifts of asphalt concrete with the help of an emulsion tack coat CQS-1H applied at a residual rate of 0.03gal/SY.

Four trucks hauled triple trailer (tractor with 3 loaded trailers as shown in Figure 2.24) assemblies around the track at 45mph for 17 hours a day (six days a week) to apply 10,000,000 axles of traffic load to the track within two years.

Figure 2.25. Photograph of traffic application using triple trailer assemblies (NCAT Report, 2002).

2.3.4.3. Summary

The geogrid-reinforced and unreinforced test sections were continuously monitored for a duration of 19 years to evaluate their performances. It was reported that there were no differences in the performances witnessed after 10 million-axle load applications by the end of

2004. Furthermore, by the end of 2006 after 20 million-axle load applications, cracking was observed in the control section along the length of the centerline pavement joint. However, for the same duration, no signs of crack development were reported in the geogrid-reinforced test section. By the end of 2018, after 60 million-axle load applications, the cracking in the control section was reported to extend into both lanes while a few hairline cracks were reported to have developed in the reinforced section.

2.3.5. IFSTTAR: French Fatigue Carrousel

2.3.5.1. Background

The primary objective was to evaluate the resistance of flexible pavement sections reinforced with fiberglass grids under a full-scale accelerated pavement test using the large pavement fatigue carrousel of IFSTTAR in Nantes, France. The performance of fiberglass grid-reinforced flexible pavement test sections were evaluated relative to the performance of unreinforced flexible pavement test (control) sections. Both the control and reinforced pavement structures followed a typical French low traffic pavement design with a 70-mm-thick bituminous wearing course placed over a granular base. The fiberglass grid used was a Glasgrid 8511, which is custom-knitted in a stable construction and coated with an elastomeric polymer and self-adhesive back. The grid apertures were 25-mm squares and had a tensile strength of 100kN/m in both machine and cross-machine directions.

The IFSTTAR accelerated pavement testing facility in Nantes is an outdoor circular carrousel with a diameter of 40m and comprises a central 750kW motor unit and four arms carrying wheel loads up to a maximum speed of 100km/h (Figure 2.25). The pavement test sections would be approximately 6 m wide with a diameter of 35 m, resulting in a total length of about 110 m. The position, intensity and location of load application could be varied with the movement of the arms and various load configurations such as single or dual wheels, and single, tandem or tridem axles could be applied simultaneously.

Figure 2.26. Photograph showing IFSTTAR fatigue test carrousel (IFSTTAR, 2012).

59

2.3.5.2. Construction and Testing

The test sections were 10-m-long typical French low traffic pavement structures and consisted of a sandy subgrade soil, 300-mm-thick granular subbase layer and a 70-mm-thick bituminous wearing course. To accommodate the fiberglass grid reinforcement within the bituminous layer, a 20-mm-thick bituminous course was laid and compacted on the subbase layer. The fiberglass grid was then installed and a tack coat was applied at a residual rate of $300g/m^2$ before the 50-mm-thick final bituminous layer was paved (Figure 2.26).

Figure 2.27. Photographs showing: (a) construction of 20-mm-thick bituminous layer; (b) fiberglass grid installation; (c) compaction of grid; and (d) paving of 50-mm-thick bituminous layer (IFSTTAR, 2012).

To evaluate the performance of reinforced and unreinforced test sections, two types of traffic were applied using the pavement fatigue carrousel. The traffic conditions are as follows:

1 million half-axle dual wheel loads of 65kN (corresponding to half of the French equivalent standard axle, loaded at 130kN) were applied between April and September 2011

To accelerate the fatigue, 200,000 additional dual wheel loads equal to 70kN were applied between January and March 2012

2.3.5.3. Summary

The performance evaluation of the fiberglass grids reinforced in a relatively thin bituminous wearing course (70 mm) was done relative to the unreinforced (control) section at the IFSTTAR accelerated pavement testing facility. The test sections were evaluated under traffic of 1 million dual wheel loads of 65kN representing the French standard axle load. In addition, about 200,000 cycles were applied at an increased load of 70kN. Based on the evaluation and monitoring program, it was reported that the deflections and rutting depths did not differ much between the fiberglass grid-reinforced and unreinforced (control) sections. Moreover, the control sections experienced some crack development after 800,000 cycles and 70% of the control section was cracked by the end of the test as shown in Figure 2.27. However, the fiberglass grid-reinforced sections did not develop any cracks until the end of the testing program (Figure 2.27).

Figure 2.28. Photograph showing control section (left) and fiberglass grid-reinforced section (right) at the end of testing (IFSTTAR, 2012).

2.3.6. Ancona, Italy: Instrumented Test Section for Evaluation of Geogrids in Asphalt Pavements

2.3.6.1. Background

The primary objective was to evaluate the geogrid reinforcements for asphalt pavement rehabilitation. To achieve this goal, an instrumented flexible pavement test section was constructed in Ancona, Italy along an in-service road. The research project, titled "Advanced Interface Testing of Geogrids in Asphalt Pavements," involved the construction of two full-scale pavement test sections, with the first section used to extract field specimens for laboratory evaluation. The second test section would be instrumented with earth pressure sensors and strain

gauges to evaluate the performance of geogrid-reinforced and unreinforced (control) sections under real field-traffic conditions.

2.3.6.2. Construction

The location for construction of the instrumented test sections was chosen along an existing secondary road near the Ancona Industrial Area in Italy. The test section location was chosen so that most of the traffic consisted of heavy trucks, which could be counted and weighed precisely. Two different geogrid types (Figure 2.28)—a Glass Fiber Reinforced Polymer (FP) geogrid and Carbon Fiber (CF) geogrid—were adopted in the study. In addition, an instrumented control section with a conventional tack coat applied at the interface of asphalt layers was constructed. The test sections were 15 m long and 5 m wide in a two-lane 9.5-m-wide roadway with low concrete walls on both sides as shown in Figure 2.29.
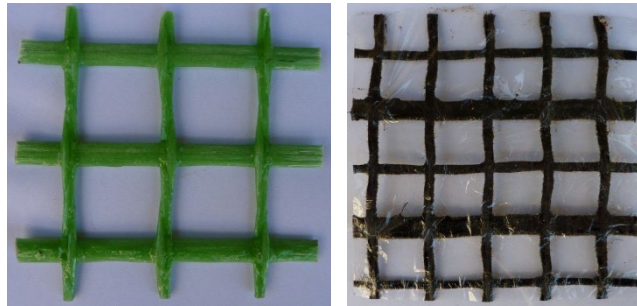
Figure 2.29. Photographs showing glass fiber polymer geogrid (left) and carbon fiber geogrid (right) (Graziani et al. 2011).
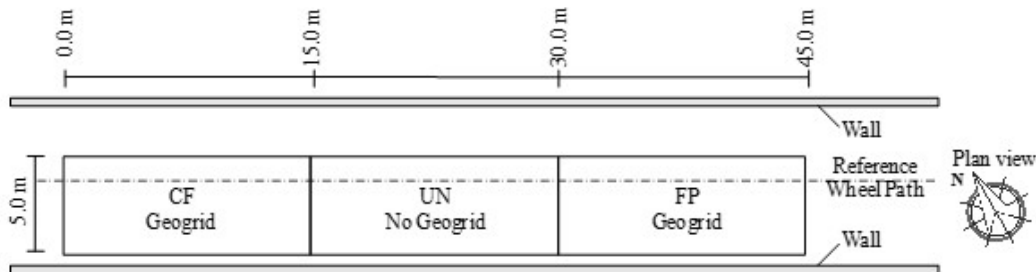
Figure 2.30. Schematic of instrumented test section layout (Graziani et al. 2011).

The existing asphalt layer was milled and reconstructed with a lower asphalt layer (40 mm thick), tack coat application and geosynthetic installation, and a final 50-mm-thick asphalt layer. The asphalt concrete used for the new lower and upper asphalt layers was a typical Italian dense graded mix formulation with a 12-mm maximum dimension (AC 12) and 70/100 penetration bitumen. All three test sections were instrumented with Earth Pressure Cells (EPC), Asphalt Strain Gauges (ASG) and temperature sensors as presented in Figure 2.30.
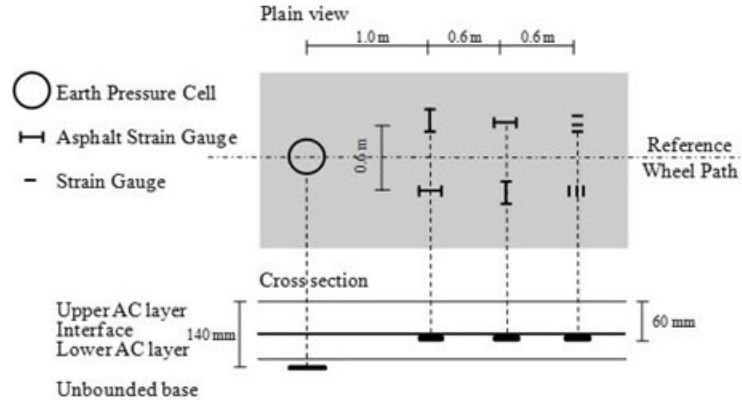
Figure 2.31. Schematic of plan and cross-section views of instrumented test section (Graziani et al. 2011).

2.3.6.3. Summary

A full-scale instrumented pavement test section was constructed along an in-service road to study the effectiveness of geogrid reinforcement in asphalt layers. The entire construction process was completed in six working days and over 90% of the major sensors (EPC and ASG) were reported to have survived the construction phase. The FWD tests and full-scale (truck) trafficking were performed on the test sections and the sensors were able to record the data effectively. However, the information obtained from the installed sensors have not been reported.

2.4. Summary and Remarks

This report focused on reviewing and assessing detailed information from all relevant previous TxDOT experiences on the use of geosynthetic interlayers in the HMA layer. In addition, all relevant previous experiences from other DOTs and transportation agencies in the US and overseas on the use of geosynthetic interlayers in the HMA layer have been reviewed. A summary of the main aspects of various past experiences by other state transportation agencies and around the globe is presented in Table 2.12.

Based on the past research experiences of various DOTs and transportation agencies, it can be summarized that there has been extensive research on a wide variety of treatment techniques available to minimize reflective cracking in HMA layers. Among the treatment techniques, many types of geosynthetic interlayers in the form of paving fabrics, paving mats and geogrids (polymeric and fiberglass) have been adopted as an anti-reflective cracking system. The research studies reported that few forms of geosynthetics (geogrids) were effective in minimizing reflective cracks, while the others were ineffective. In addition, the various functions provided by different geosynthetic interlayers and their corresponding mechanisms are completely

understood. Overall, it seems geogrids have been effective in minimizing cracks by providing a reinforcing function. However, any additional benefits of the geogrid reinforcing function have yet to be explored.

Table 2.12. Summary of past research experiences on use of geosynthetic interlayers in HMA layers.

Research	Location	Materials	Construction	Distress	Evaluation	Findings
Crack reduction strategies on a Pavement warrant project	I-25 at Fountain Head, Colorado. CDOT	Tack coat:AC-10 Treatment: Petromat 4597, Petromat 4599, Petrotac, Progaurd, Crack Fillers	Section-1: 1" milling & 5" HMA. Section-2: driving lane 1.5" milling & 5.5" HMA, rest 1" milling & 5" HMA.	Transverse cracks	Visual examination	21% of transverse cracks recurred during three years of evaluation.
Experimental installation of geosynthetic pavement reinforcement to reduce reflective cracking	Auburn-Lewiston Municipal Airport runway. Maine DOT	Treatment: Glasgrid 8502. AC: 40mm thick Superpave HMA	Crack cleaning and installing Glasgrid 8502 on cracks in Band-Aid style and 40mm HMA.	Reflective cracks	Visual examination and videotaping using Automatic Road analyzer	
Geosynthetic materials in reflective crack prevention	US-97. Oregon DOT	Treatment: Crack filler, Glasgrid 8502, GeoTac, PavePep SA, Polyguard Cold Flex SA, Polyguard 665. AC: 50mm of Class-F HMA	Crack cleaning, filling with D-mix, place geosynthetic over cracks, 50mm overlay.	Transverse cracks	Visual examination	No geosynthetic material tested could resist reflective cracking completely. Glasgrid 8502 reduced the severity of cracks. Crack filler performed better than geosynthetics

Research	Location	Materials	Construction	Distress	Evaluation	Findings
Glasgrid performance at NCAT test track	NCAT Test Track, Auburn University	Tack coat: CQS-1H, 0.03gal/sy Treatment: Glasgrid 8501 (100kN/m) AC: 4" thick HMA	20" thick HMA base layer, CQS-1H tack, 2" thick HMA, Glasgrid 8501, 2" thick HMA.	New Construction	Visual examination	After 10 msa (2years): No difference After 20 msa (4years): Cracking in control section After 60 msa (16years): extensive cracking in control, hairline cracks in Glasgrid 8501 section.
Performance of Glasgrid reinforced asphalt layer under French Fatigue Carrousel	IFSTTAR, Nantes. France	Tack coat: 300g/sq.m Treatment: Glasgrid (100kN/m) AC: 70mm thick HMA	20mm thick HMA on sub-base, tack coat, Glasgrid, 50mm thick HMA.	New Construction	Visual examination, Benkelman beam deflection (BBD) test, Profilometer.	After 0.8 msa: Deflection & rut- No change in control & Glasgrid section. Cracks: 70% in control, no cracks in Glasgrid section.

Research	Location	Materials	Construction	Distress	Evaluation	Findings
Instrumented test section for the evaluation of geogrids in asphalt pavements	Ancona, Italy. Polytechnic University of Ancona, Italy	Treatment: Glass Fiber Polymer geogrid, Carbon Fiber geogrid AC: 90mm thick HMA (AC12-Italian Dense Grade)	Milling the existing asphalt, 40mm thick HMA, tack coat, Geosynthetics, 50mm thick HMA	Rehabilitation project with milled asphalt layer and fresh HMA Overlay	Instrumented with Pressure sensors & Asphalt strain gauges. Visual examination, Plate load test, FWD, and controlled traffic loading	90% of the sensors sustained the construction phase and no data has been reported thereafter.

Chapter 3. Design of SH21 Field Monitoring Program

3.1. Introduction

This chapter reports the activities completed in Task 2 of TxDOT Project 0-7002. The main objective of this task was to design and develop a field monitoring program for the test sections. Specifically, the activities that conducted under the field monitoring program can be divided into two sub-tasks as follows:

Design of the experimental test sections

Design of the instrumentation plan for the test sections

The design of the experimental test sections is explained in Section 2 of this chapter and the instrumentation plan is discussed in Section 3.

3.2. Design of Test Sections

The primary objective of this sub-task was to determine locations for instrumented and non-instrumented test sections along State Highway (SH) 21 and to design a comprehensive layout for the test sections that incorporates a wide range of geogrid reinforcements for hot-mix asphalt overlay. As part of the activities completed under this task, several candidate locations were identified and various aspects that may influence the performance of the test sections at each location were evaluated. Subsequently, at the finalized test section locations, a wide range of layouts for experimental test sections was drafted and the suitability of each layout was carefully assessed. The activities conducted under this task to determine the final test section locations and the final design of the test section layout are explained next.

3.2.1. Project Details

The asphalt reinforcement project along SH21 spanned a total length of 20.92 miles, from the Bastrop/Lee County line in the west to the Burleson County line in the east. The project limit typically had a four-lane undivided carriageway, with a lane width of 11 ft. and shoulder width varying between 2 ft. and 4 ft. on the east and west bounds. Figure 3.1 presents the overall extensions of the geosynthetic-reinforced asphalt overlay project along SH21. It can be observed that the construction project was divided into two phases based on the contractor/construction company and details presented in Table 3.1. The treatment techniques, irrespective of the project phase, comprised full- or half-depth repairs with a 3/4 inch level-up, tack coat application, installation of polymeric grids and hot mix asphalt overlay construction. The overlay

construction consisted of a 2-inch-thick Type-D mix asphalt layer and a 1-inch-thick Thin Overlay Mix (TOM) asphalt layer.

Table 3.1. Details of SH21 asphalt reinforcement project.

Project Phase		Phase-1	Phase-2
Length		18.086 mi. (95494 ft.)	2.835 mi. (14969 ft.)
Limits	West	0.14 mi. W of CR2440 (STA: 0+00)	Bastrop/Lee County line (STA: 10+00)
	East	Burleson County line (STA: 954+54)	0.14 mi. W of CR2440 (STA: 149+69)
Contractor		Big Creek Constructions	Texas Materials
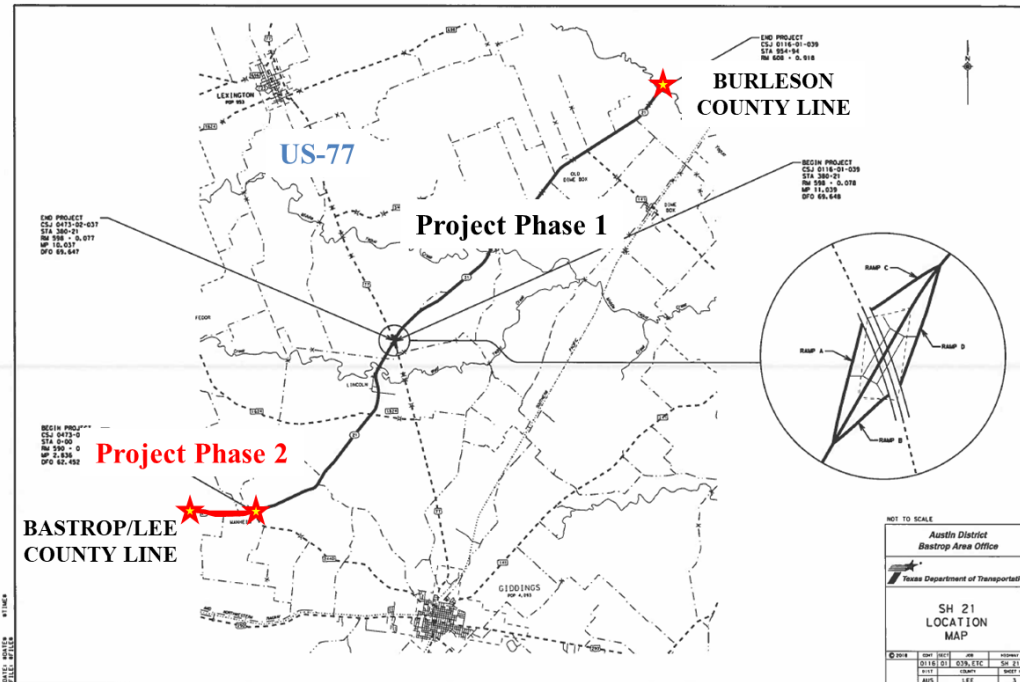
Figure 3.1. Overall extent of asphalt reinforcement project along SH-21.

3.2.2. Location and Layout of Test Sections

For a fair comparison between the performances of different test sections, they should have common conditions, in terms of subgrade soil, traffic condition, weather condition, existing surface condition, etc. The identification of a suitable location for the test sections and design of typical test section layouts was a two-step process in which the initial focus was on identifying a tentative location suitable for the instrumented and non-instrumented test sections. Once the tentative location was finalized, the initial test section layouts were drafted. The details for test section location identification and layout design are discussed next.

3.2.2.1. Location of Test Sections

Several visits to the project construction site were made with an intention to understand the existing surface condition and various factors affecting their performance. Based on several visits to the construction site for condition surveys and meetings with contractors and TxDOT officials, it was learned that a number of parameters affected the identification of an ideal location for the test sections. That is, for a location to be suitable for the test sections, the following factors needed to be satisfied:

Construction schedule and phasing adopted by the contractor

Existing surface condition

71

Subgrade soil type and characteristics

Installation recommendations by geosynthetic manufacturers

Geometric design of the roadway

3.2.2.1.1. Construction Schedule and Phasing

As listed in Table 3.1 and presented in Figure 3.1, the extent of the asphalt reinforcement project along SH21 was divided into two phases and construction was handled by two different contractors/construction companies. Phase-1 construction was anticipated to be completed earlier than Phase-2 construction. Hence, the locations for the test sections were initially identified between Stations 107+00 and 125+00 in the Phase-2 portion of the project. However, Phase-1 construction did not commence as scheduled and the possibility of test sections in Phase-1 was also explored in addition to the identified locations in Phase-2. Finally, based on discussions with the contractors and TxDOT officials, it was decided that the test sections in the Phase-1 portion of the project and condition surveys would be carried out accordingly. The tentative locations identified for the Phase-1 test sections were as follows:

Location 1: from STA 396+00 to STA 442+00

Location 2: from STA 24+00 to STA 29+00 and STA 46+00 to STA 51+00

Location 3: from STA 884+14 to STA 902+14

3.2.2.1.2. Existing Surface Condition

Condition surveys were done by visual examination and video recording using GoPro devices. A video of the entire length of the project was recorded to identify the locations with and without repairs, and these were updated into a Google Map showing information on repaired and unrepaired portions. The locations with repairs were carefully examined and the type of repairs were documented. The typical treatments done by the contractor were full-depth reclamation or half-depth reclamation of the pavement structure, across both lanes or shoulders or one lane. However, after the half-depth or full-depth repairs, the surface was levelled up using a 3/4-inch-thick hot mix asphalt layer.

3.2.2.1.3. Subgrade Soil

The subgrade soil plays an important role in the overall performance of a pavement system. To evaluate the performances of various test sections, the subgrade soil should have similar properties, along with other properties and factors influencing the performance of overlays and the pavement system. Hence, it was planned to drill through the existing asphalt layer into the

subgrade at locations identified in Phase-2 of the project to obtain borehole logs and collect undisturbed soil samples as shown in Figure 3.2 (Location 2). However, as discussed in Section 3.2.2.1.1, the test sections were now considered part of Phase-1 of the project. As shown in Figure 3.3, the boring locations (Location 1) were now identified as Phase-1 and unfortunately could not be executed due to the fast-approaching construction schedule and other unavoidable circumstances. As a fair alternative, United States Department of Agriculture (USDA) soil maps were adopted to obtain the subgrade soil information for the tentative locations identified in Phase-1 of the project. After extensive evaluation of the soil information from USDA soil maps, it was determined that the subgrade soil was consistent in Locations 1 and 2. Figure 3.4 presents the USDA soil map with different soil types in the vicinity of Location 1 and it can be observed that the region between Stations 396 and 440 have a consistent soil type termed as KgC. The composition and properties of the soil type in this region are presented in Figure 3.5. Figure 3.6 presents the USDA soil map for Location 2 and it can be observed that the subgrade soil types LuB and DwB remain unchanged from Stations 24 to 29 and from Stations 46 to 51, respectively.
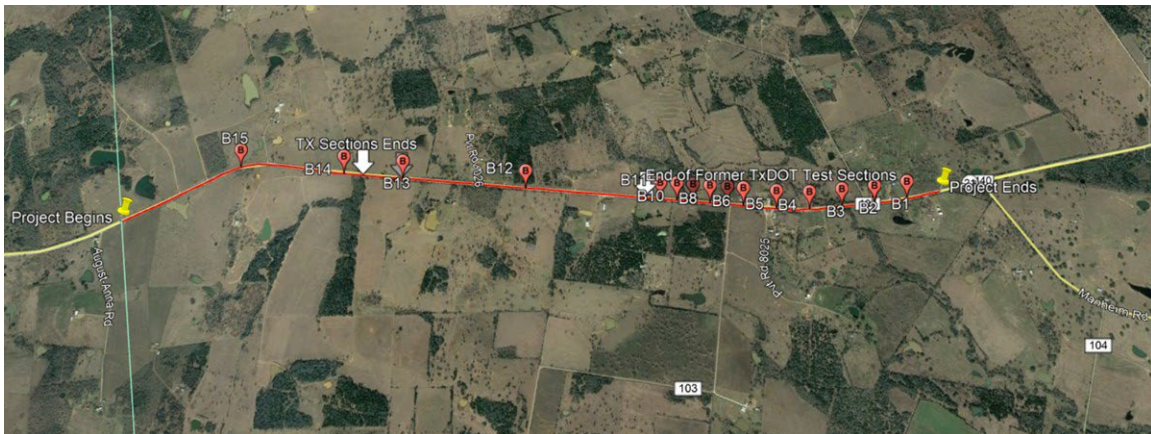
Figure 3.2. Google map showing boring locations identified in Phase-2 of the project.

Figure 3.3. Google Map showing boring locations identified in Phase-1 of the project.
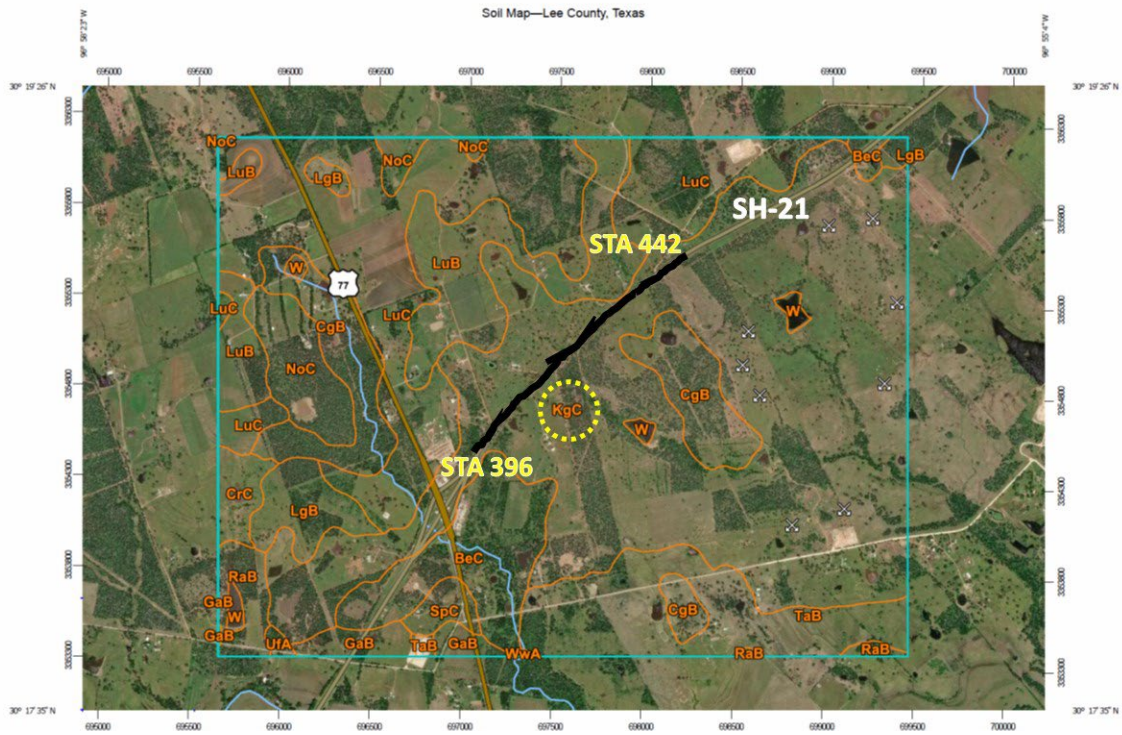
Figure 3.4. USDA soil map of Location 1.

74

Lee County, Texas

KgC—Kurten very gravelly fine sandy loam, 1 to 5 percent slopes

Map Unit Setting

National map unit symbol: rbfd
Elevation: 200 to 500 feet
Mean annual precipitation: 32 to 40 inches
Mean annual air temperature: 64 to 70 degrees F
Frost-free period: 240 to 270 days
Farmland classification: Not prime farmland

Map Unit Composition

Kurten and similar soils: 85 percent
Minor components: 15 percent

Estimates are based on observations, descriptions, and transects of the mapunit.

Description of Kurten

Setting

Landform: Ridges
Landform position (two-dimensional): Shoulder, backslope
Landform position (three-dimensional): Crest, side slope
Down-slope shape: Linear
Across-slope shape: Convex
Parent material: Residuum weathered from shale in cook mountain formation of eocene age

Typical profile

H1 - 0 to 7 inches: very gravelly fine sandy loam
H2 - 7 to 45 inches: clay
H3 - 45 to 53 inches: clay
H4 - 53 to 80 inches: clay

Figure 3.5. Composition and properties of Kurten (KgC) Soil.
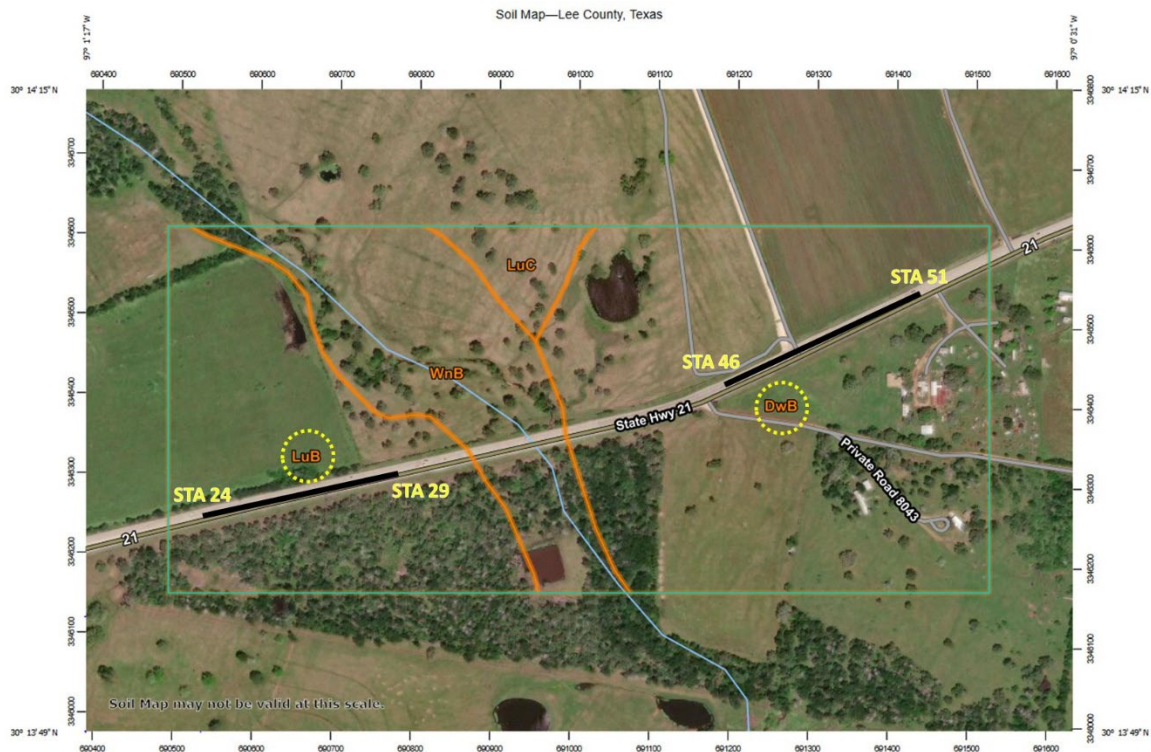
Figure 3.6. USDA soil map of Location 2.

75

Figure 3.7. Composition and properties of Luling clay (LuB) and Davilla-Wilson complex (DwB).

3.2.2.1.4. Installation Recommendation

The main objective of the asphalt reinforcement project along SH21 was to evaluate the performance of various geosynthetic products used as asphalt reinforcement in overlays. Hence, a number of geosynthetic products from different manufacturers were considered and the manufacturers subsequently provided the installation recommendations for their products. Based on an evaluation of the installation recommendations received, it was determined that the surface of the asphalt reinforcement installation (existing surface) was crucial for their performance. Specifically, it was important to understand if the existing surface was oxidized or levelled up after a full-depth or half-depth treatment (Figure 3.8). Hence, the locations for the test sections had to be chosen to comply with the installation recommendations without compromising the other factors discussed under Section 3.2.2.1. Consequently, the locations with asphalt surface level-up were considered for all geogrid-reinforced test sections.

Figure 3.8. Asphalt surface condition: (a) level-up; and (b) oxidized.

3.2.2.1.5. Geometric Design

The test section locations were preferably considered along a straight road with less variation in the grade and curvatures. The design speed and super elevation along the horizontal curves would change relative to the rest of the locations. Hence, the locations with minimum grade changes and curvatures were considered for test sections.

3.2.2.1.6. Summary

Based on the above discussions related to the influence of various factors on the location of test sections, it can be summarized that an ideal location for the test sections should satisfy all the above factors/conditions. Considering this objective, two different locations were finalized for the instrumented and non-instrumented test sections as shown in Figure 3.9, Figure 3.10 and Figure 3.11. Among them, a total of 17 test sections with 15 geosynthetic-reinforced and two unreinforced (control) sections were considered in Location 1. Out of the 17 test sections, seven were instrumented (six geosynthetic-reinforced and one control) and 10 were non-instrumented (nine geosynthetic-reinforced and one control) test sections. Figure 3.10 presents the Google Maps view of Location 1. The region between Stations 398+00 and 422+75 and Stations 430+00 and 442+00 had treated and leveled-up asphalt surface. The region between Stations 442+75 and 430+00 had an old and oxidized asphalt surface. Furthermore, to understand the influence of different subgrade soil types and surface conditions on the performance of project-specific geosynthetic reinforcement, two test sections were designed at Location 2 as shown in Figure

77

3.11. It can be observed that the region between Stations 24+00 and 29+00 had treated and leveled-up asphalt surface, while the asphalt surface between Stations 46+00 and 51+00 was old and oxidized, with different subgrade soil from that of Location 1. Eventually, the test section layout was designed for the finalized locations, the details of which are presented in subsequent sections.
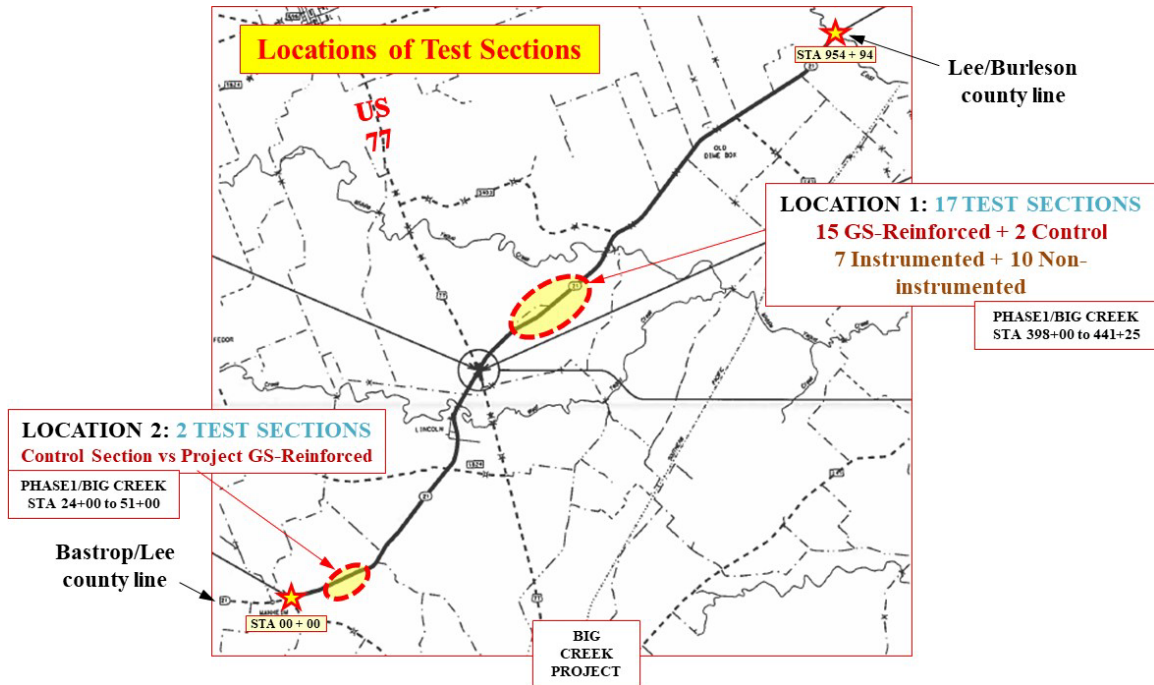
Figure 3.9. Two locations finalized for test section construction in Phase-1 of the project.
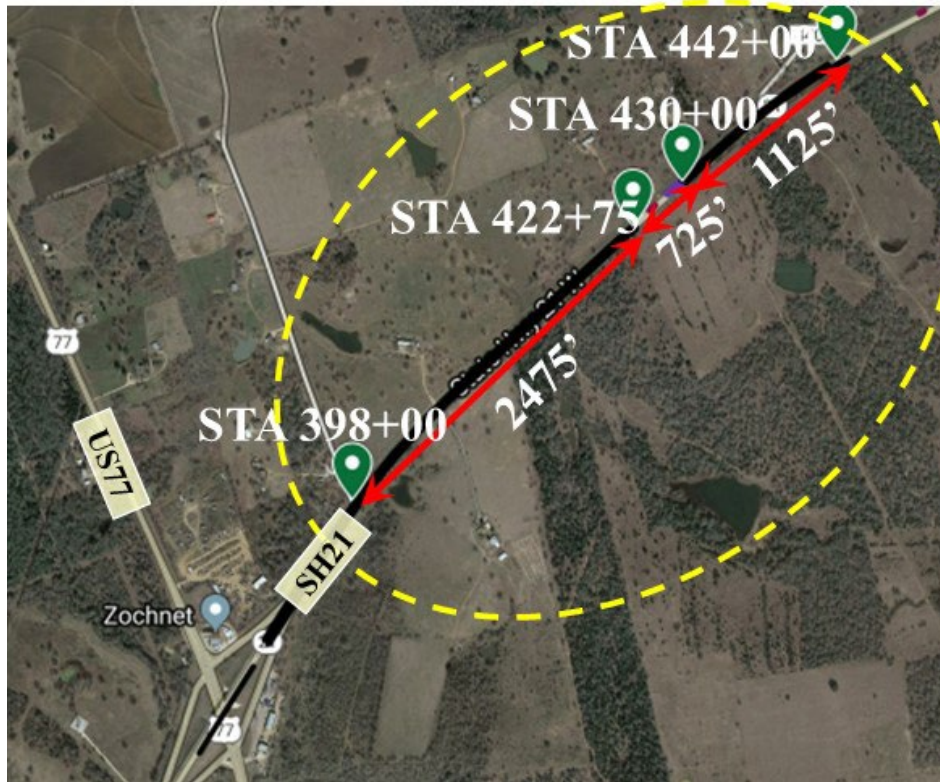
Figure 3.10. Google Maps view of Location 1 test sections.

Figure 3.11. Google Maps view of Location 2 test sections.

3.2.2.2. Layout of Test Sections

The layout of test sections was designed considering a number of factors that would influence the performance evaluation of various geosynthetic products considered against the control sections. The influencing factors are as follows:

Traffic conditions

Moisture variations in subgrade/shoulder soil

79

Ease of construction

3.2.2.2.1. Traffic Conditions

The finalized location along SH21 for test section construction had a four-lane undivided carriageway with 11-foot-wide lanes and 4-foot-wide paved shoulders. The traffic conditions along the outer and inner lanes were expected to be different because the outer lane is considered the driving lane and the inner lane the passing lane. In addition to the volume of traffic, the load induced by heavy truck traffic is also high on the outer lanes as they generally prefer driving lanes due to their low-speed levels. With this information, it was considered ideal to have test sections along both the driving and passing lanes to evaluate their performances under different traffic conditions.

3.2.2.2.2. Moisture Variations

The moisture variations in the subgrade soil and soil in the exposed shoulder areas often result in the development of longitudinal and transverse cracks in the outer lane and paved shoulder along the east and west bounds. The intensity of cracks depends on the level of moisture variations in the soil. To account for the effect of moisture conditions on the performance of the test sections, it was considered ideal to have test sections along the outer and inner lanes of the west and east bounds.

3.2.2.2.3. Ease of Construction

The test section length was mainly governed by the length of the geosynthetic rolls to be installed in the test sections and total length of the ideal roadway available for test sections. Table 3.2 presents the details of available roll lengths and widths of various geosynthetic reinforcements incorporated in this project. Based on the details listed in Table 3.2, the length of the instrumented and non-instrumented test sections at Location 1 were limited to 225 ft. for ease of construction and other factors discussed under Sections 3.2.1 and 3.2.2. The length of the non-instrumented test sections at Location 2 was 500 ft.

Table 3.2. Details of geosynthetic rolls used in test sections.

Geosynthetic Type	Roll Length (ft.)	Roll Width (ft.)	No. of Rolls reqd.
Instrumented Test Sections			
Hock (PET)	246	12.6	2
HaTelit C40/17 (PET)	492	13.2	1
HaTelit XP50 (PVA)	487	12.5	1
HaTelit G100 (Glass)	295	12.8	2
Tensar GG8511TF (Glass)	330	05.0	5
Tencate MPG100 (Glass)	150	12.5	4
Non-Instrumented Test Sections			
Hock (PET)	246	12.6	2
HaTelit C40/17 (PET)	492	13.2	1
HaTelit XP50 (PVA)	487	12.5	1
HaTelit G100 (Glass)	295	12.8	2
Tensar GG8511TF (Glass)	330	05.0	5
Tencate MPG100 (Glass)	150	12.5	4
Tensar GlasPave 50 (Glass)	910	12.6	1
HaTelit G50 (Glass)	492	13.1	1
Shandong (PET)	495	13.2	1

3.2.2.2.4. Summary

Based on the above discussions, it can be summarized the test sections were divided into two locations. Location 1 was divided into instrumented and non-instrumented test sections, which focused on the performance evaluation of different geosynthetic reinforcements. Hence, test section length was designed accordingly. Location 2 had two non-instrumented test sections focused on the performance evaluation of project-specific geosynthetic reinforcement (Hock) under different subgrade soil and asphalt surface conditions, and the layouts were designed accordingly. Overall, nine different types of geosynthetics were used in six different test configurations as follows:

Test Configuration 1 (TC1) (Control): without geogrid reinforcement

Test Configuration 2 (TC2) (Project Phase-1): with the project-specific geogrid reinforcement used in Phase-1 construction

Test Configuration 3 (TC3) (Project Phase-2): with the project-specific geogrid reinforcement initially selected for Phase-2 construction

Test Configuration 4 (TC4) (PET): with a Polyester (PET) geogrid reinforcement

Test Configuration 5 (TC5) (PVA): with a Polyvinyl Alcohol (PVA) geogrid reinforcement

Test Configuration 6 (TC6) (Glass Fibers): with several classes of glass grid reinforcements

Figure 3.12 and Figure 3.13 present the final layouts of the instrumented and non-instrumented test sections at Locations 1 and 2, respectively. As discussed, the test section length at Location 1 was limited to 225 ft. while the test section length at Location 2 was 500 ft. The instrumentation plan and layouts were designed for the test sections considered for sensor installation (from Station 398+00 to 413+75 as shown in Figure 3.12). The details of the instrumentation plan and layout are discussed next.
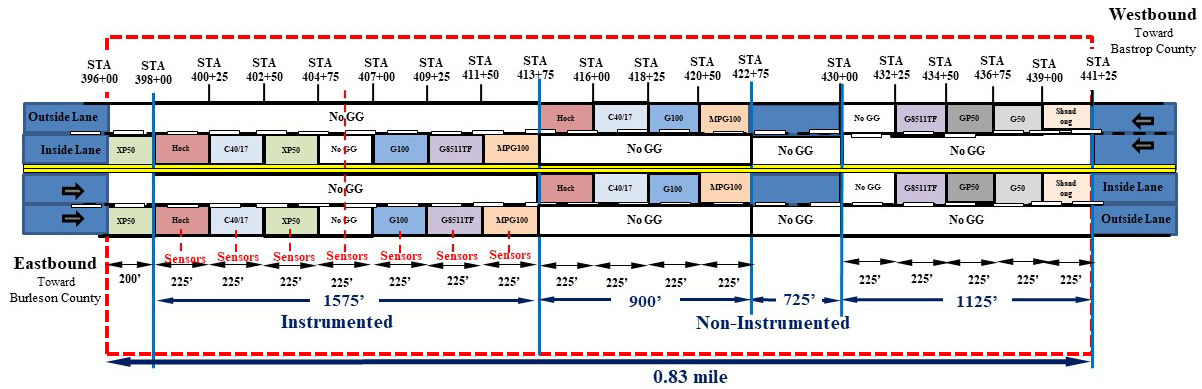
Figure 3.12. Schematic layout of instrumented and non-instrumented test sections at Location 1 along SH21.
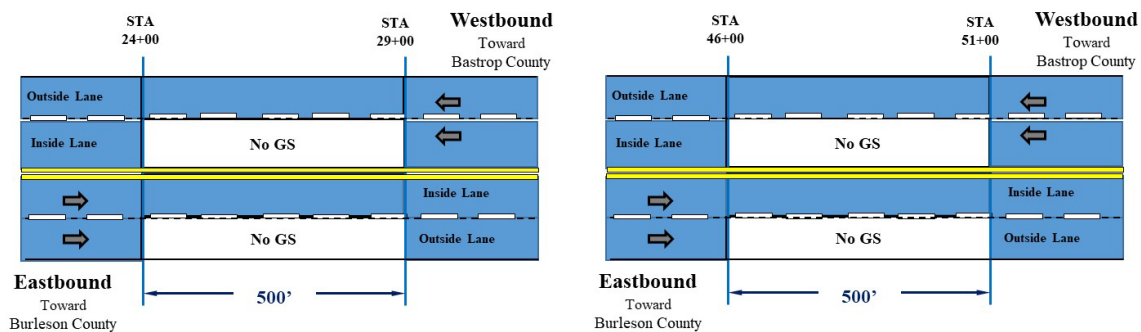
Figure 3.13. Schematic layout of non-instrumented test sections at Location 2 along SH21.

3.3. Design of Instrumentation

Seven sets of instrumentation were used in seven different test sections that were constructed using different test configurations. Out of the seven test sections, six were geosynthetic-reinforced and one was unreinforced (control) (Figure 3.14). The instrumentation plan for geophones and asphalt strain gauges was the same for all test sections. However, the instrumentation plan for moisture sensors in the control section was different from that in the other sections (Figure 3.14). It can be observed that the moisture sensors were planned for installation at various locations along the width of the control section in four lanes, while the moisture sensors in the geosynthetic-reinforced test sections were planned for installation only along the outer wheel path adjacent to the location of geophone installation. Figure 3.15 presents a schematic cross-section of a typical instrumented test section. It can be observed that triplicates of moisture sensors were planned for installation in the subgrade soil at an approximate depth of 5 ft. from the preexisting (old) asphalt surface. Similarly, other sensors were planned for installation in different pavement layers at different depths as shown in Figure 3.15, the details of which are discussed in the following sections.

83
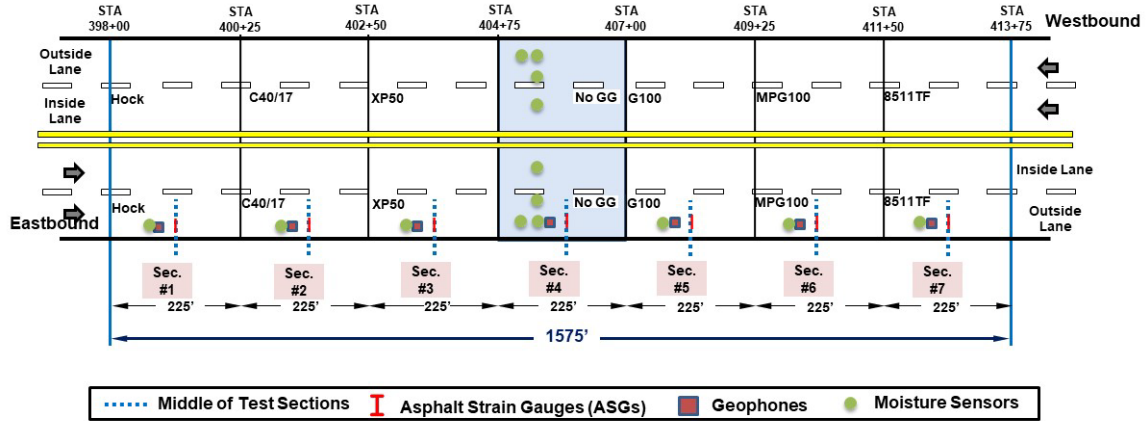
Figure 3.14. Schematic of sensor locations in instrumented test sections along SH21.
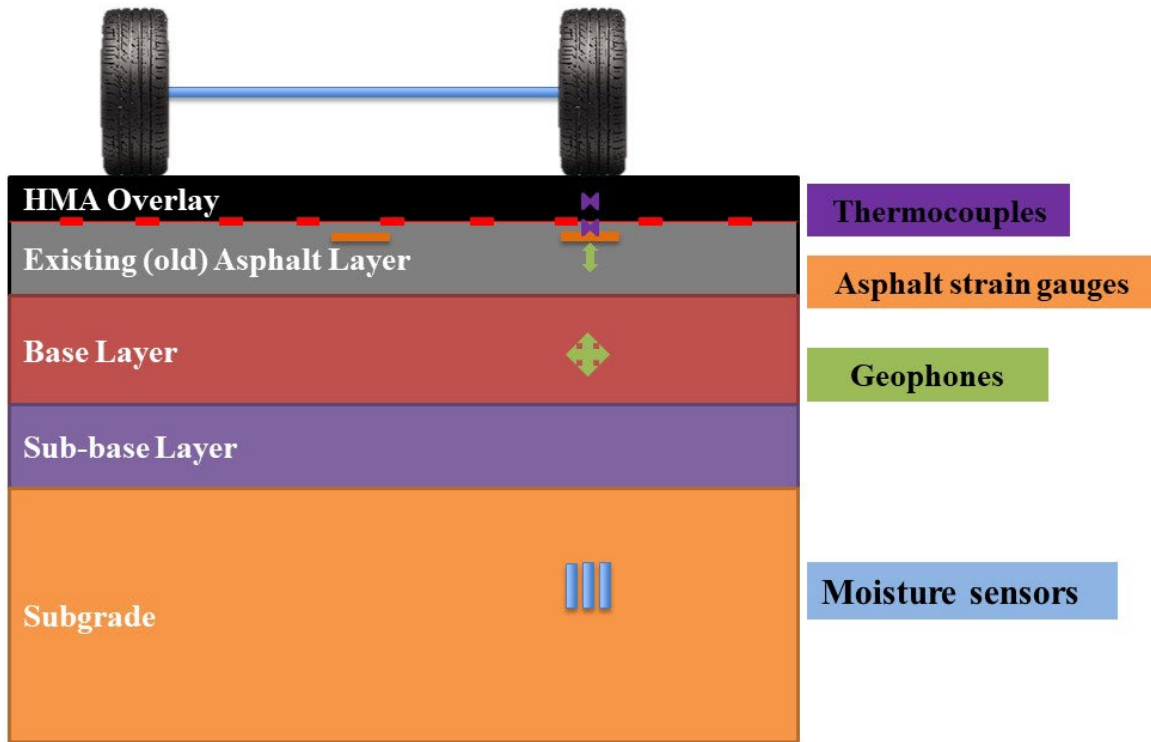
Figure 3.15. Schematic of cross-section of a typical instrumented test section at SH21.

3.3.1. Moisture Sensors

Moisture sensor arrays were installed 5 to 8 feet beneath the outer lane edge in all seven instrumented test sections. Each sensor group was located 10 ft. away from the midpoint of the test section beneath the white edge stripe. An additional transverse array consisting of eight sensor groups was installed across the entire width of the roadway in the control section (Section 4) as presented in Figure 3.16. In one selected location, an additional sensor was placed within the road base to provide additional information about the relative wetting and drying of the upper

portions of the pavement structure. From Figure 3.16, it can be observed that each sensor group included three moisture sensors and at one location (eastbound shoulder of Section 1), a sensor group consisting of three moisture sensors was installed to evaluate the moisture variations in the shoulder soil. Subsequently, these moisture variations would be compared with those obtained from the subgrade soil beneath the pavement and the moisture profile along the width of the roadway could eventually be estimated.
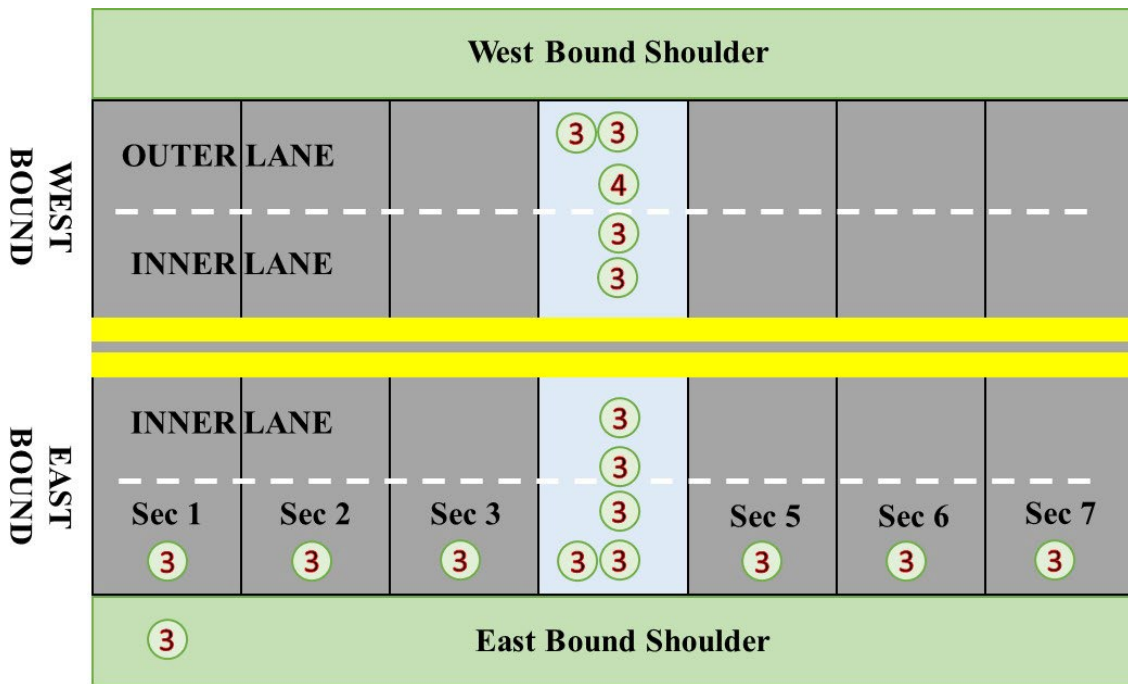
Figure 3.16. Schematic plan view of overall moisture sensor layout in instrumented test sections along SH21.

3.3.2. Geophones

Geophones were installed in several pavement layers including the subbase, base and existing asphalt layers to measure deflections in the vertical and horizontal directions within the pavement structure. The geophone array consisted of a complex three-dimensional layout identical for all instrumented test sections as shown in Figure 3.17, Figure 3.18, Figure 3.19 and Figure 3.20. Figure 3.17 shows a schematic of the plan view of the geophones installed in a typical test section. Specifically, in the asphaltic layer, geophones were installed along three locations spaced 1 ft. from each another. First, a 1-C geophone was installed along the wheel path in the preexisting asphalt layer. Then, 3-C and 1-C geophones were installed in the preexisting asphalt layer between the wheel paths at a radial distance of 2 ft. and 5 ft., respectively, from the first geophone (Figure 3.17). Finally, a 1-C geophone was installed along the wheel path in the preexisting asphalt layer at a distance of 2 ft. from the first geophone.

Two additional geophones, including a 3-C geophone and 1-C geophone, were installed within the base and subbase layers under the first geophone in the asphaltic layer. Figure 3.18, Figure 3.19 and Figure 3.20 present the locations of geophones in the cross-section view of test sections at the three locations specified in Figure 3.17.
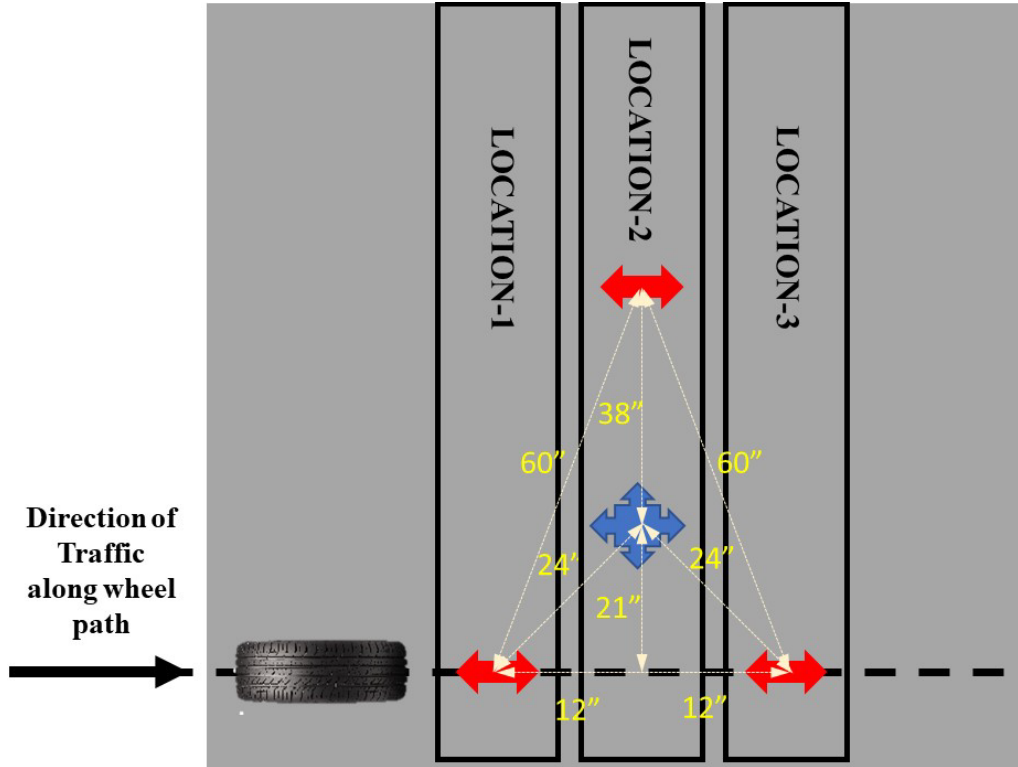
Figure 3.17. Schematic of plan view of geophones in instrumented test sections at SH21.

Figure 3.18. Schematic of cross-section layout of geophones in instrumented test sections at Location 1.
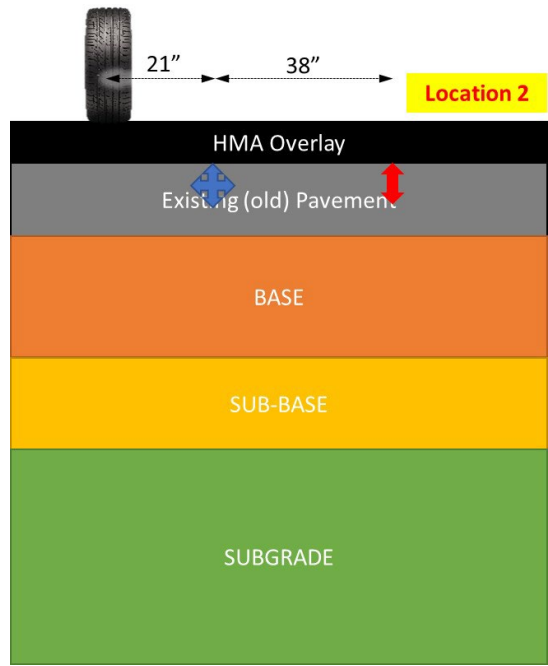
Figure 3.19. Schematic of cross-section layout of geophones in instrumented test sections at Location 2.

Figure 3.20. Schematic of cross-section layout of geophones in instrumented test sections at Location 3.

3.3.3. Asphalt Strain Gauges

Asphalt strain gauges were used to measure tensile strains in the asphalt layer at different locations along the instrumented test sections. They contain H-shaped sensors that could be installed in the direction of or perpendicular to the direction of traffic. Figure 3.21 presents a schematic plan layout of the location and orientation of the asphalt strain gauges as compared to the traffic wheel path in a typical instrumented SH21 test section. Specifically, along the outer wheel path of each instrumented test section, two asphalt strain gauges were installed transverse to the traffic direction and one asphalt strain gauge was installed along the traffic direction. In addition, two asphalt strain gauges were installed in each instrumented test section along the centerline of the wheel paths, including one sensor transverse to and one sensor in line with the traffic direction.
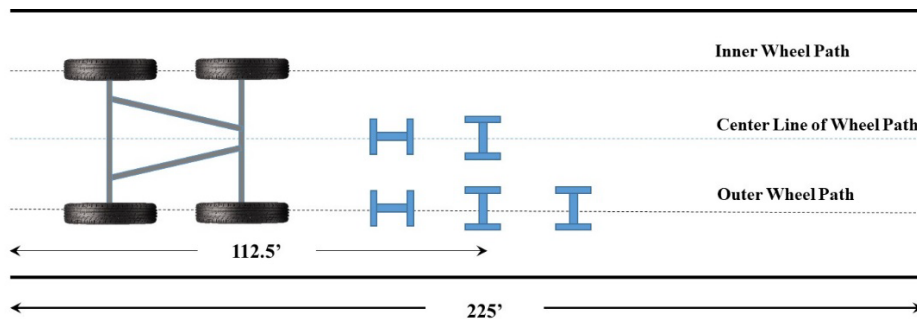
Figure 3.21. Schematic of plan view of asphalt strain gauge layout in instrumented test section at SH21.

88

3.3.4. Thermocouples

Three Thermocouples (TC) were installed at three depths in each instrumented test section. The deepest TC was installed with the asphalt strain gauge located in the wheel path and oriented along the traffic direction. This TC was approximately 3 inches deep in the preexisting asphalt layer (Figure 3.22). Directly above this TC, two additional TC were installed, including one on top of the preexisting asphalt layer (at an approximate depth of 3 inches from the pavement surface) and one on top of the first lift of overlay (Type-D) (at an approximate depth of 1 inch from the pavement surface) (Figure 3.22).
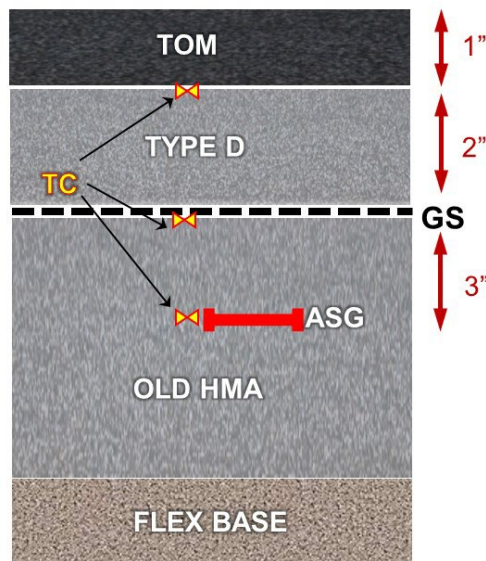
Figure 3.22. Schematic of cross-section of thermocouple locations in instrumented test sections at SH21.

3.4. Summary and Final Remarks

This report focuses on various activities completed under Task 2, including identifying test section locations, test section layout design and the design of the test section instrumentation plan. The various parameters governing the locations and layouts of test sections were discussed in detail. The final locations and layout for the experimental test sections were documented. In addition, the overall instrumentation plan for test sections that were considered for sensor installation along with the layout for individual sensors were presented. Procurement and installation procedures for various components of the instrumentation plan along with initial readings from each sensor were completed under Task 4 of this project and are documented in a separate chapter.

Chapter 4. Characterization of Materials in SH21 Test Sections

4.1. Introduction

This chapter reports on the activities that were completed in Task 3 of TxDOT Project 0-7002. The primary objective of this task was to characterize various materials including the existing pavement materials and new materials used in the construction of the unreinforced and reinforced asphalt overlays in the field test sections at SH21. The existing pavement materials include cores from the old asphalt layer, existing granular base/subbase and subgrade soil collected through boring, while the materials used for the overlay construction include different types of reinforcement interlayers, tack coat and hot mix asphalt overlay. Specifically, the material characterization activities are presented in two sections as follows:

Characterization of the existing pavement materials including:

Subgrade soil

Base and subbase course material

Old asphalt layer

Characterization of the materials used for overlay construction including:

Asphalt overlay

Tack coat

Reinforcement interlayers (geosynthetic and glass materials)

The characterization of various materials from the existing pavement layers and asphalt overlays are discussed in detail in Sections 4.2 and 4.3, respectively, of this chapter.

4.2. Characterization of Existing Pavement Materials

The materials from the existing pavement layers were not readily available for characterization since they were below the existing asphalt surface. However, during the installation of moisture sensors, holes were drilled through all existing pavement layers up to an approximate depth of 6 ft. in all test sections. Then, the materials from different layers such as the surface (asphalt), base/subbase (granular) and subgrade were carefully collected, recorded and stored for a detailed characterization in the laboratory. The characterization of different materials from the existing pavement layers includes:

Subgrade soil

Granular base/subbase

Cores from the old asphalt layer

These are discussed in the following sections.

4.2.1. Subgrade Soil

Subgrade soil samples were taken during installation of the sensors in the instrumented test sections. Sensor installation coincided with the midpoint of each test section. These test sections are located on the side-slopes and crest of a gentle hill. The subsurface soil has been mapped as the Kurten Very Gravelly Sandy Loam (KgC). A gravelly loam surface and high plasticity clays at depth (USDA Soil Maps, 2021) characterize the soil series. Figure 4.1 shows a map view of the site while Figure 4.2 shows the longitudinal profile of the site surveyed at the time of installation.

Figure 4.1. USDA soil map and USGS elevation data from site of instrumented test sections at SH-21.
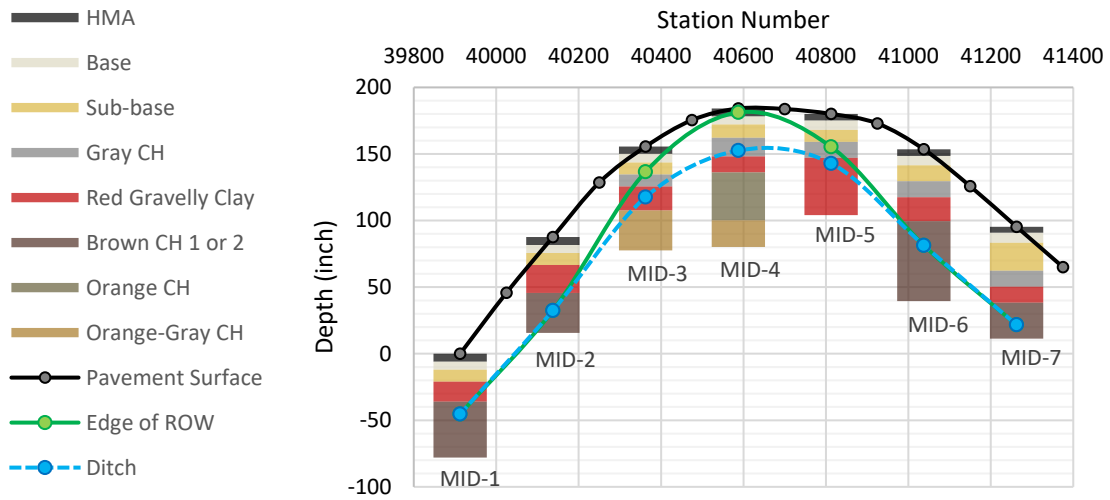
Figure 4.2: Longitudinal soil profile at instrumented test sections.

Subgrade soils were visually classified into five different types, in addition to the base and subbase materials, and representative intervals were selected for testing. The primary characterization of subgrade soils included Atterberg limits and centrifuge swelling for Potential Vertical Rise (PVR) determination (TEX 6048(B)). The recovered soil samples were insufficient for any additional testing. However, possible number of tests and characterization was completed and discussed in the following sections.

Figure 4.3 shows a summary of the PVR predictions for each section. Additional information on swell tests and PVR calculations is included subsequently. Table 4.1 shows the index properties of the representative subgrade soils and subbase material collected.
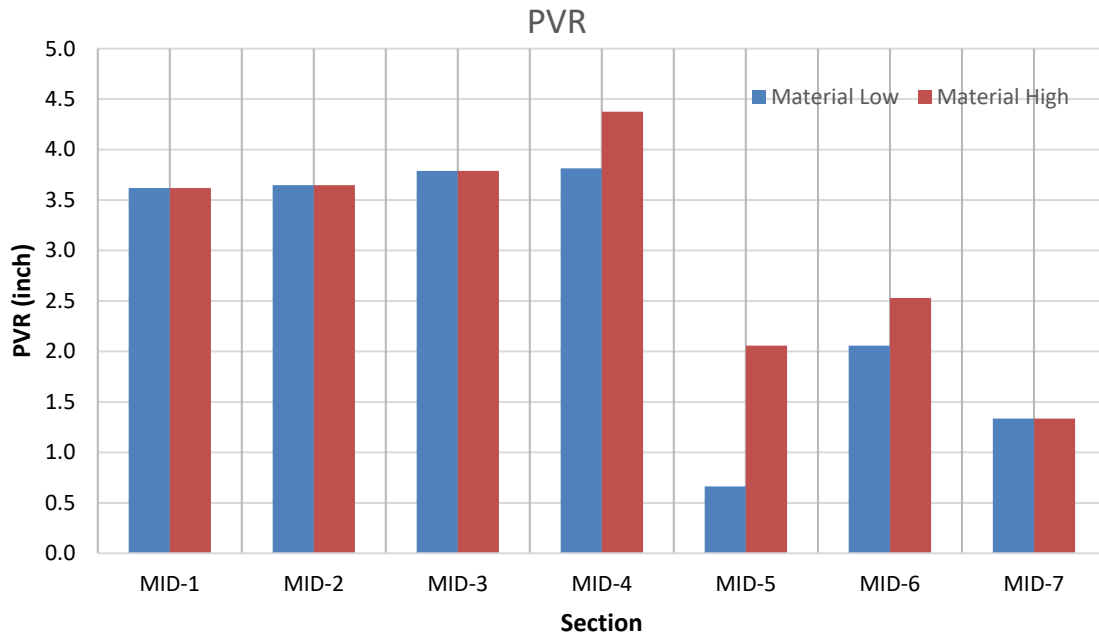
Figure 4.3: Summary of PVR predictions at SH-21 instrumented test sections.

Table 4.1: Index properties of representative subgrade materials.

Soil		USCS	Section	Liquid Limit, LL	Plastic Limit, PL	Plasticity Index, PI	A: log Slope of Swell-Stress Curve	B: Swelling at 1 psf	Sulfate Content
Subbase		SW-SC	All	27	18	9			
Subgrade	Gray Clay	CH	3-7	64	22	42	-0.0352	0.296	
	Red Clay	GC or CL*	1-7	36	17	19	-0.0013	0.000	1,710
	Brown Clay 1	CH	1-2	73	27	46	-0.0306	0.252	15,120
	Orange Clay	CH	3-4	80	25	55	-0.0294	0.248	
	Brown Clay 2	CH	6-7	55	19	37	-0.0161	0.129	

*depending on location sampled, material appeared gradational.

4.2.1.1. Atterberg Limits

Figure 4.4 - Figure 4.6 show the soil profiles and accompanying representative intervals from which Atterberg limits were determined. Figure 4.7 shows the Atterberg limits together for all subgrade soils tested.
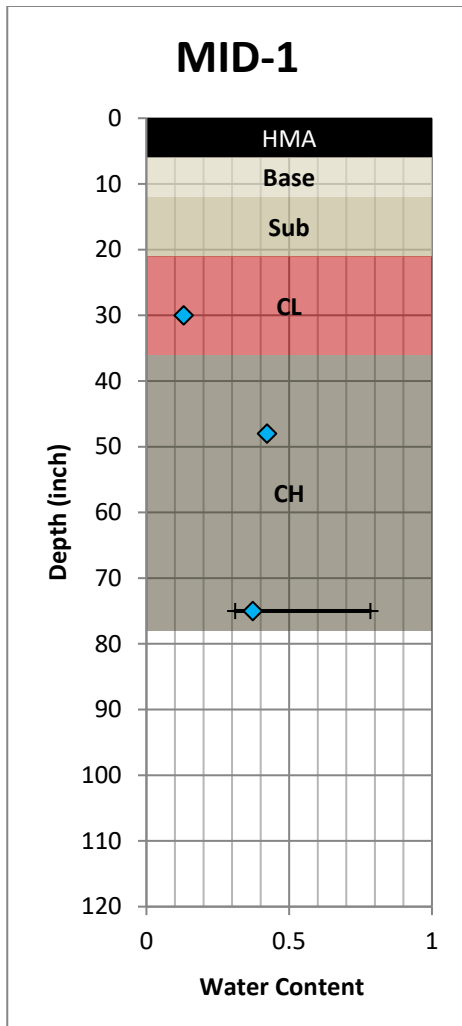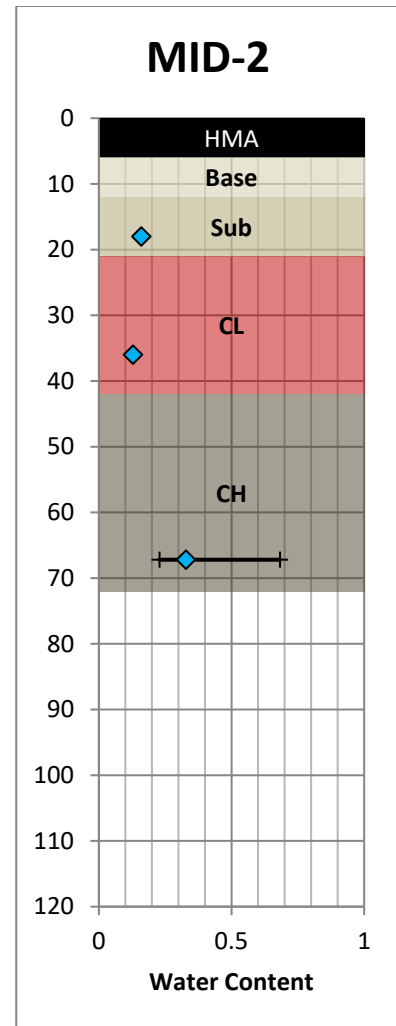
Figure 4.4: Soil profiles: (a) Section 1; and (b) Section 2.
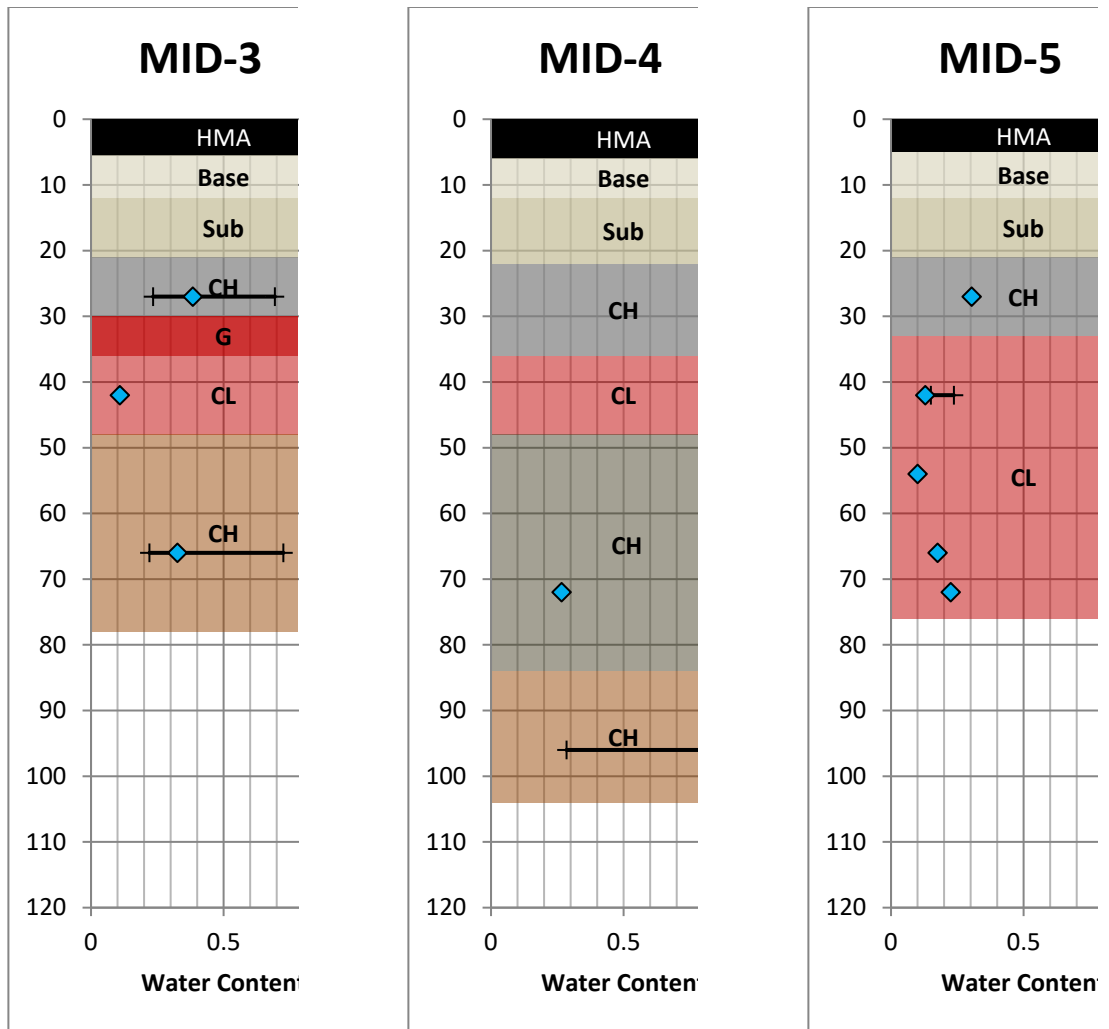
Figure 4.5: Soil profiles: (a) Section 3; (b) Section 4; and (c) Section 5.
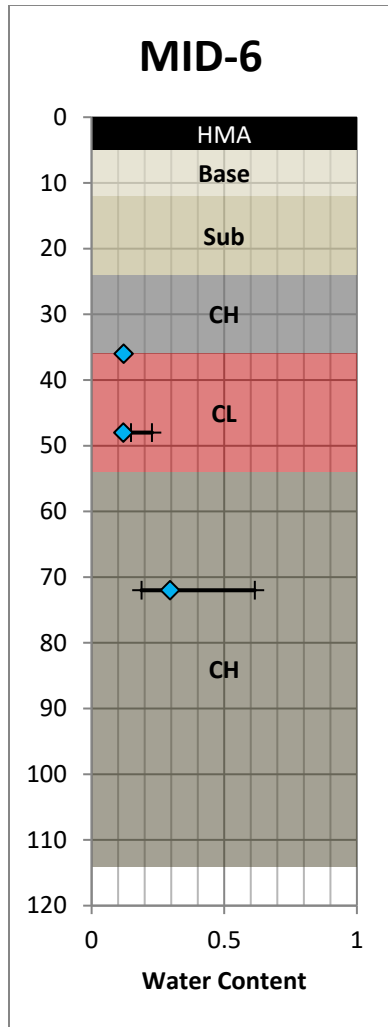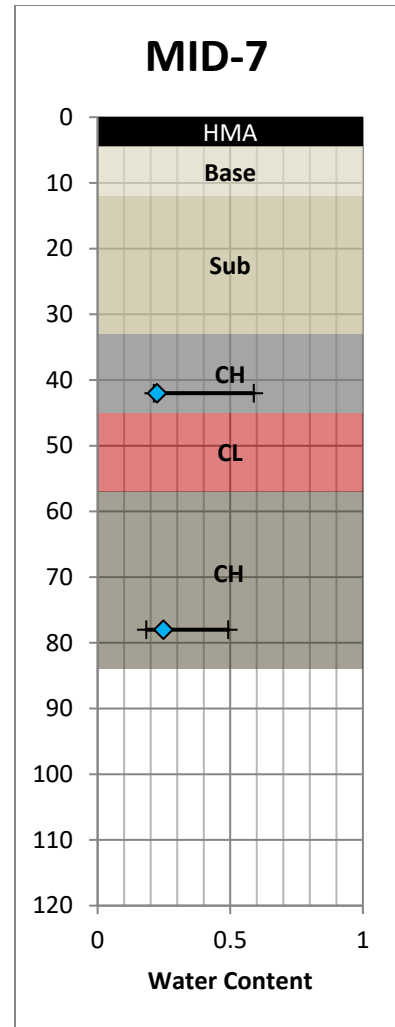
Figure 4.6: Soil profiles: (a) Section 6; and (b) Section 7.
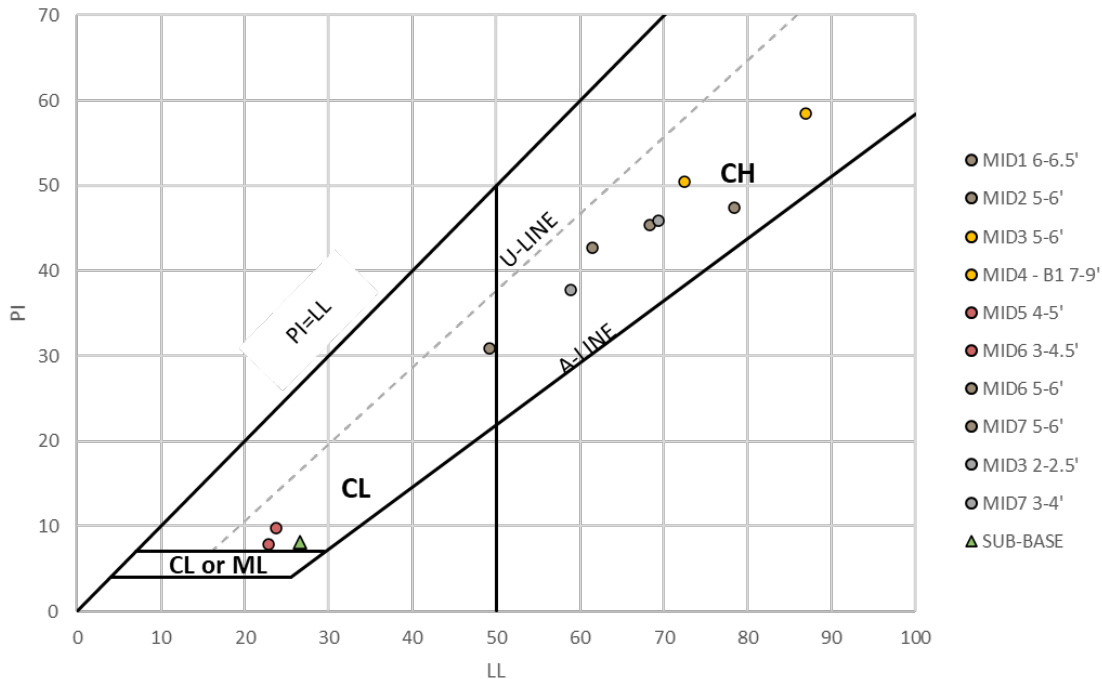
Figure 4.7: Atterberg limits of subgrade soils and subbase material.

4.2.1.2. Soil Classification

The majority of the subgrade materials classify as high plasticity clays (CH) under the USCS system. Only the red gravelly clay classifies as inert material from the standpoint of PVR calculations, having a variable amount of sand or gravel and fines classified as low plasticity clay (CL).

4.2.1.3. Sulphate Content

Sulfate contents were determined by a colorimetric method after filtering the solution from a slurry prepared from a 5:1 ratio of water to soil solids. Successive dilutions were performed when over-range readings were measured. Tested materials included high plasticity subgrade clay material in Section 1, which contained abundant visible gypsum crystals, and the low plasticity subgrade clay in Section 5. The sulfate content in Section 1 was 15,120 ppm, while the sulfate content in Section 5 was around 1,710 ppm.

4.2.1.4. Swell-stress Curves from Centrifuge Tests

Swell-stress data was collected on remolded specimens taken from select intervals in each boring. The data are grouped according to the soil type previously determined and used to predict PVR, which is the expected amount of surface heave if the soil profile were to experience full wetting to saturation from the initial condition. Initial conditions were selected as the TxDOT

97

"dry" condition (w = 0.2*LL+9%), and dry densities were chosen to correspond to a degree of saturation of 85%, corresponding to the conditions recommended in TxDOT/FHWA 5-6048-05. The initial conditions of testing are shown in Figure 4.8. The swell-stress data are shown in Figure 4.9. In the low-plasticity materials (MID 5, 4-5 FT, and MID 6 "middle"), test specimens actually collapsed from the target initial condition. In these cases, the soil materials are assumed not to swell for purposes of the PVR calculation.
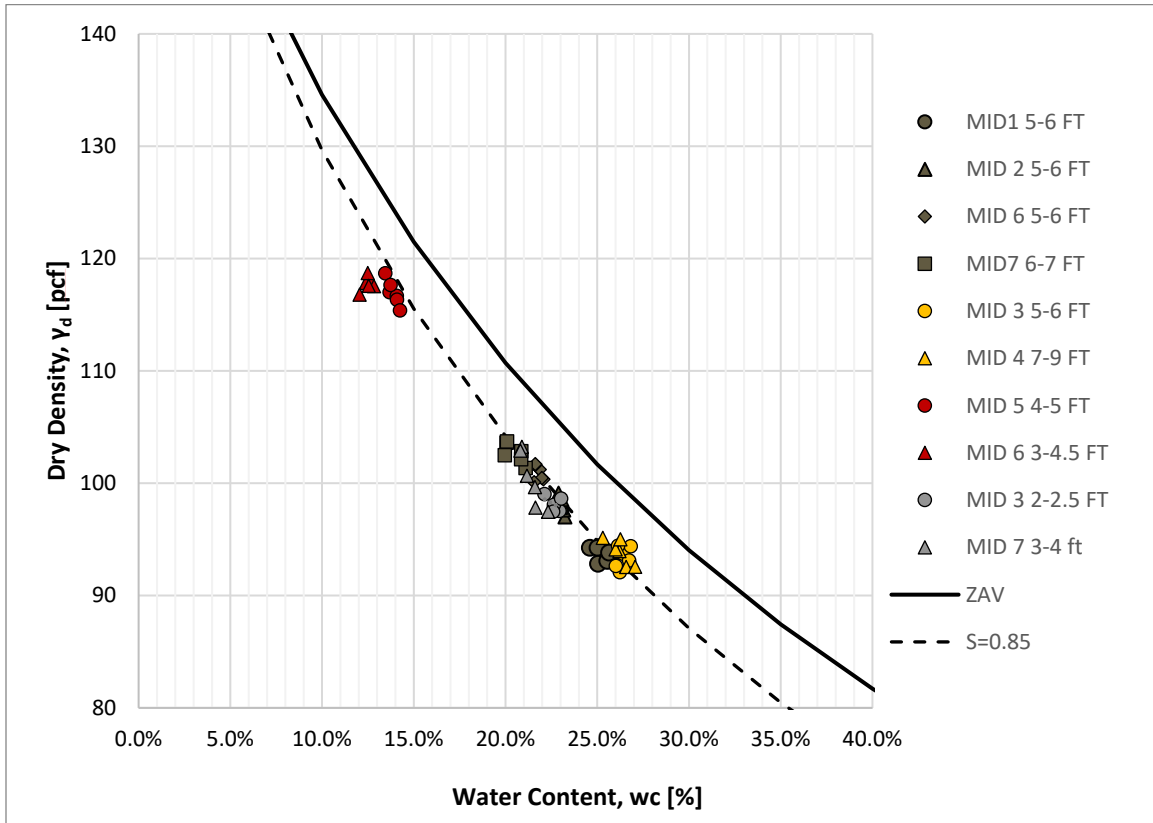
Figure 4.8: Initial conditions of swell testing.
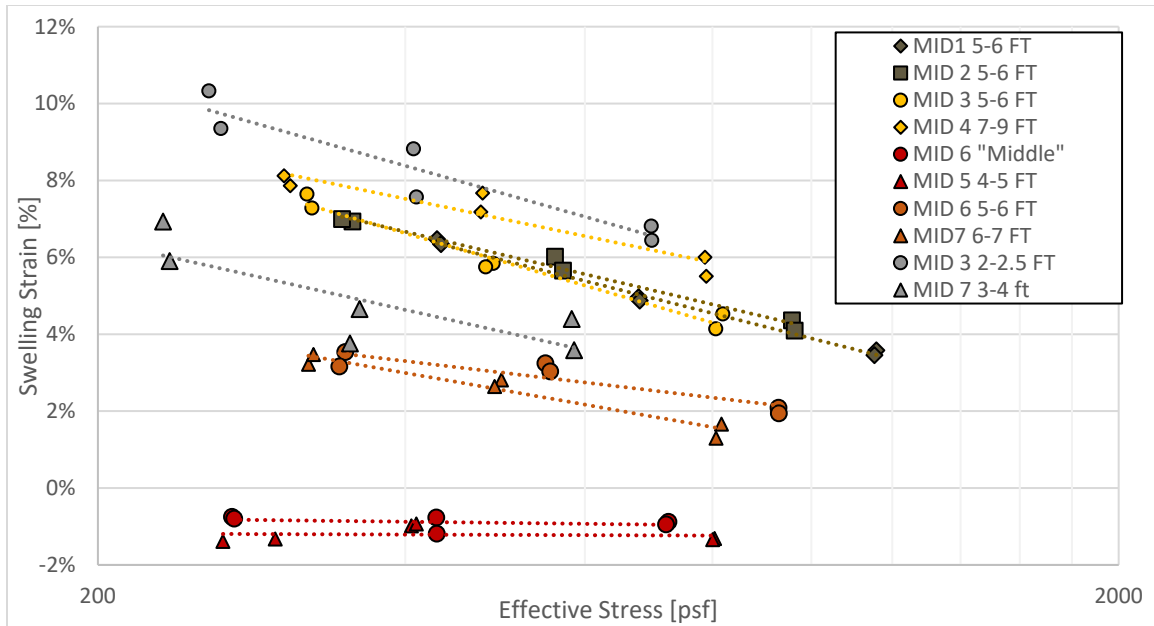
Figure 4.9. Swell-stress data from SH-21 instrumented test sections.

4.2.1.5. PVR Prediction Using TEX 6048(B)

Figure 4.10 - Figure 4.16 show the strain versus depth profiles used and the resultant cumulative PVR with depth. The gray clay material identified near the top of each boring in Sections 3-7 was found to have moderately variable swell-stress behaviors, so both lower and upper bound PVR curves were calculated for soil profiles with these materials. Since these soils were recovered from the borings in which sensors were installed, the depths in general do not extend to 10 feet. For the purpose of PVR calculation, the swelling behavior of the deepest soil layer sampled is extended to 10 feet below the pavement surface.

In addition, the low plasticity red clay material identified at the base of the boring in Section 5 did not swell significantly, but since the general soil profile in the area indicated that a high plasticity clay may lie beneath that, a second PVR calculation was performed using material properties from the base of Boring 6. The values ranged between 0.6 and 4.4 inches of PVR, and results are summarized in Figure 4.3.
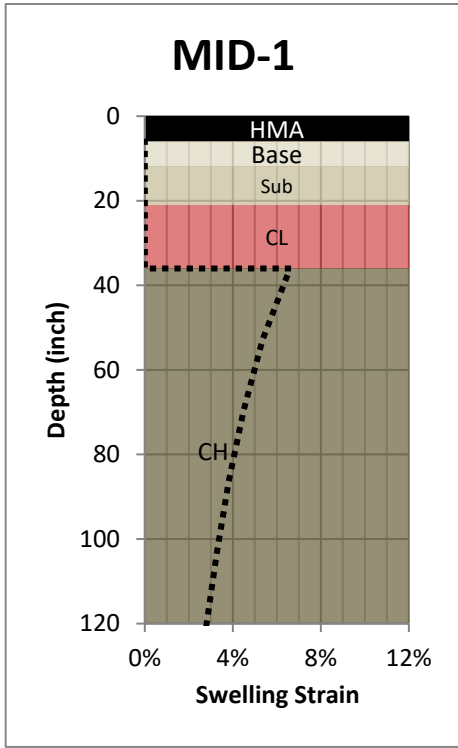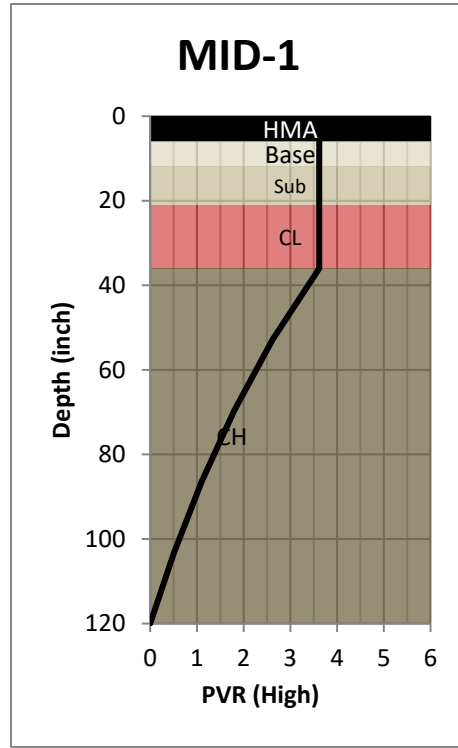
Figure 4.10: PVR for Section 1: (a) strain vs depth; and (b) cumulative PVR vs depth.
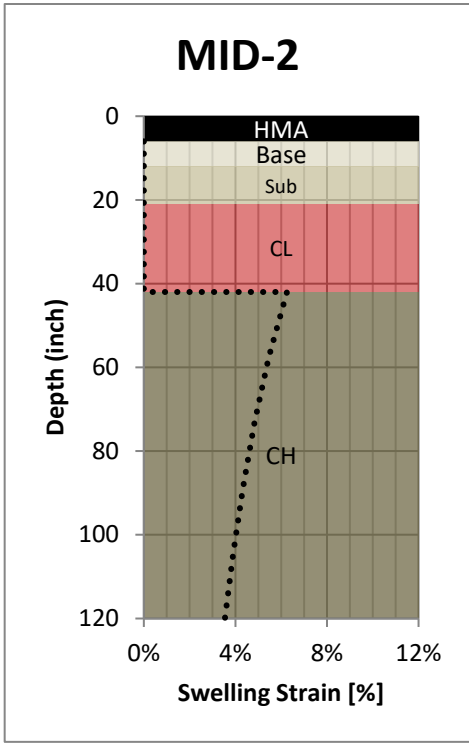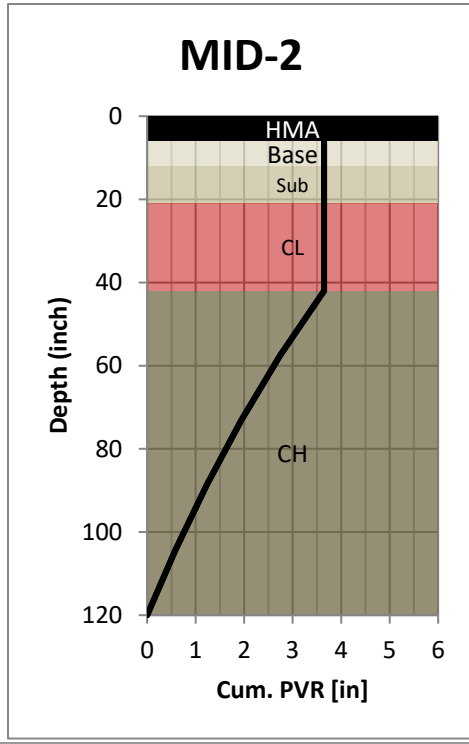
Figure 4.11. PVR for Section 2: (a) strain vs depth; and (b) cumulative PVR vs depth.
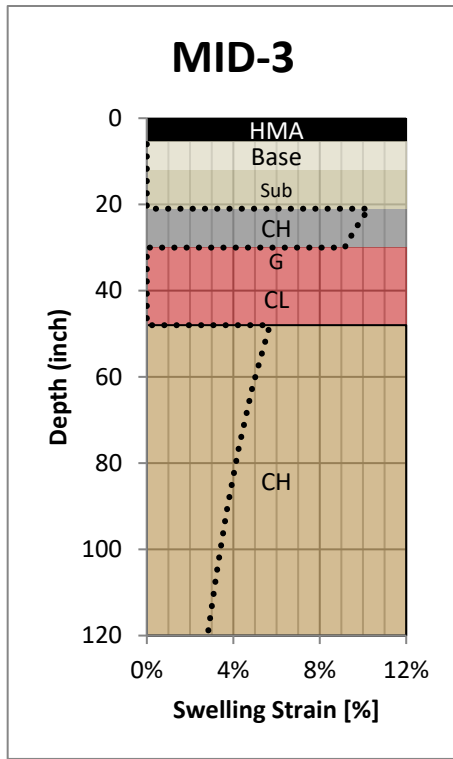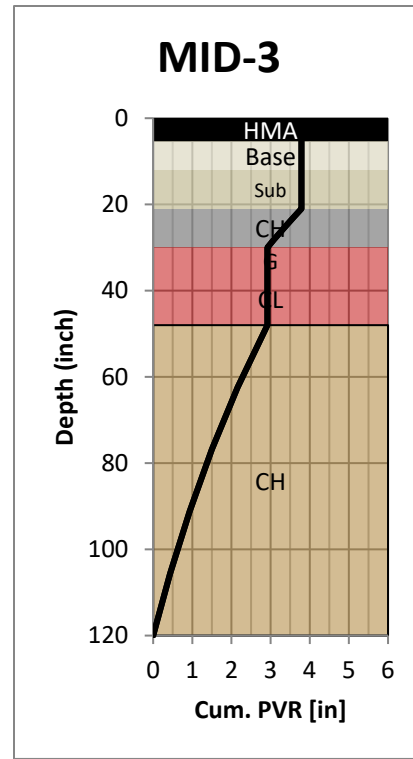
Figure 4.12. PVR for Section 3: (a) strain vs depth; and (b) cumulative PVR vs depth.
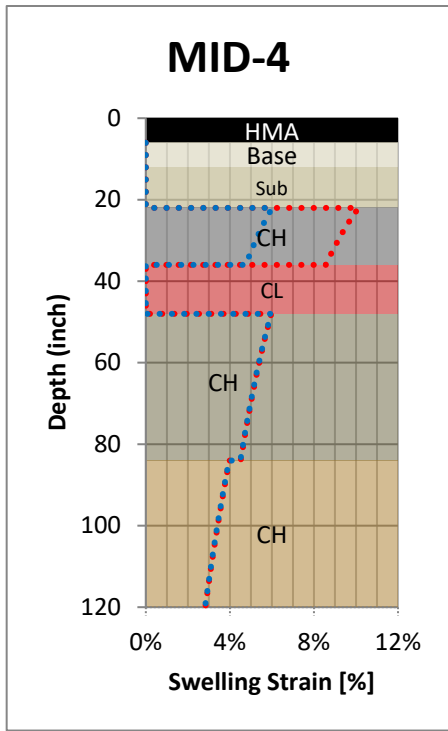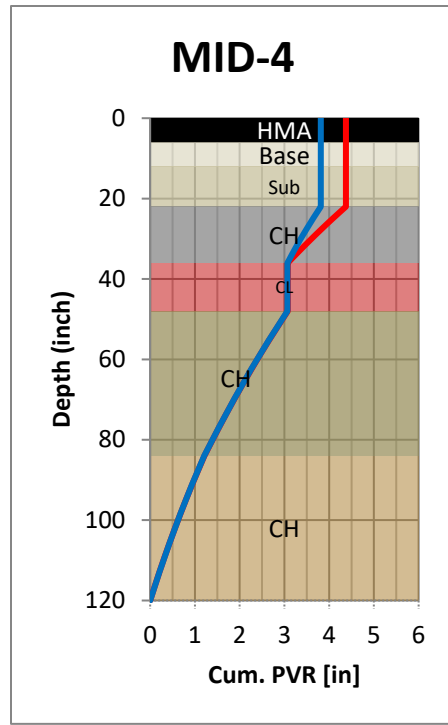
Figure 4.13. PVR for Section 4 shoulder array: (a) strain vs depth; and (b) cumulative PVR vs depth.
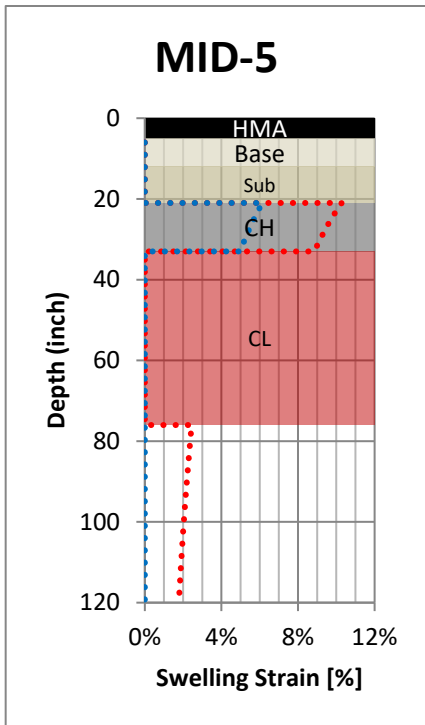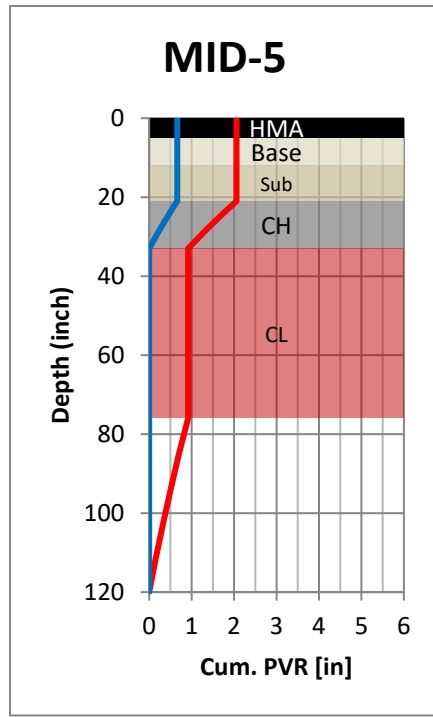
Figure 4.14: PVR for Section 5: (a) strain vs depth; and (b) cumulative PVR vs depth.
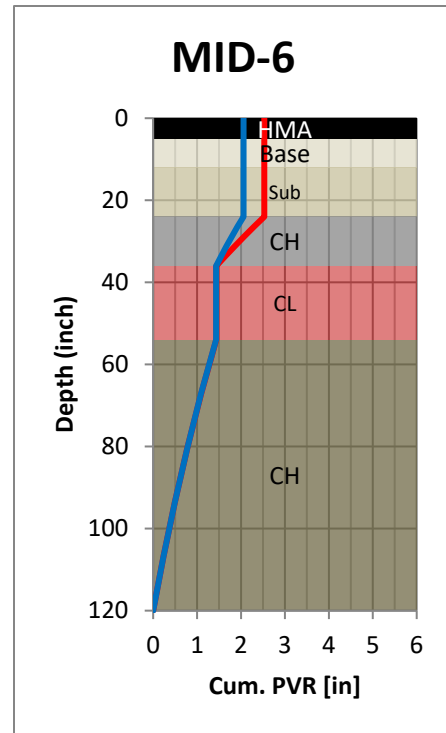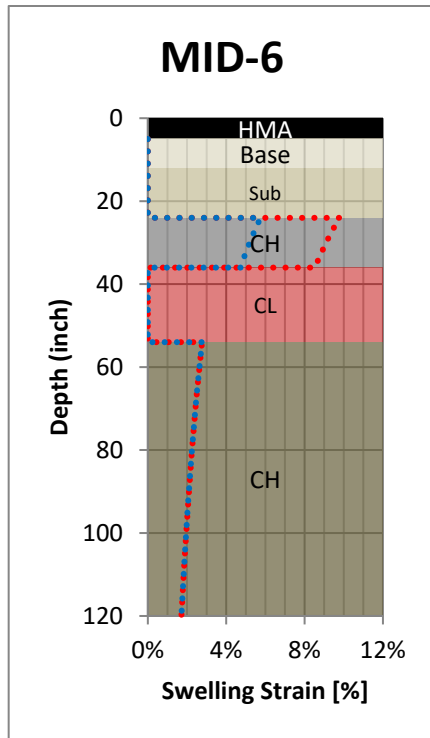
Figure 4.15: PVR for Section 6: (a) strain vs depth; and (b) cumulative PVR vs depth.
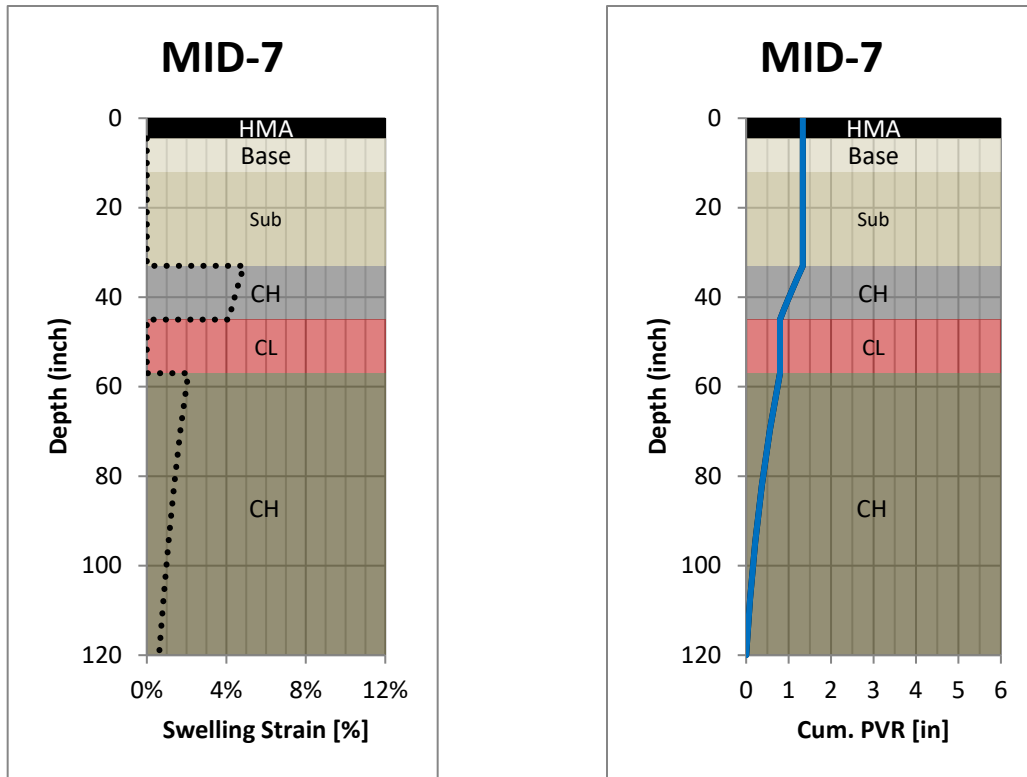
Figure 4.16: PVR for Section 7: (a) strain vs depth; and (b) cumulative PVR vs depth.

4.2.2. Base/Subbase Course Material

4.2.2.1. Grain Size Distribution

Grain size distributions were determined for material collected from borings created for the purpose of sensor installation. The curves are plotted in Figure 4.17. The subbase material is a well-graded sand (SW-SC) while the base course is a well-graded gravel (GW).
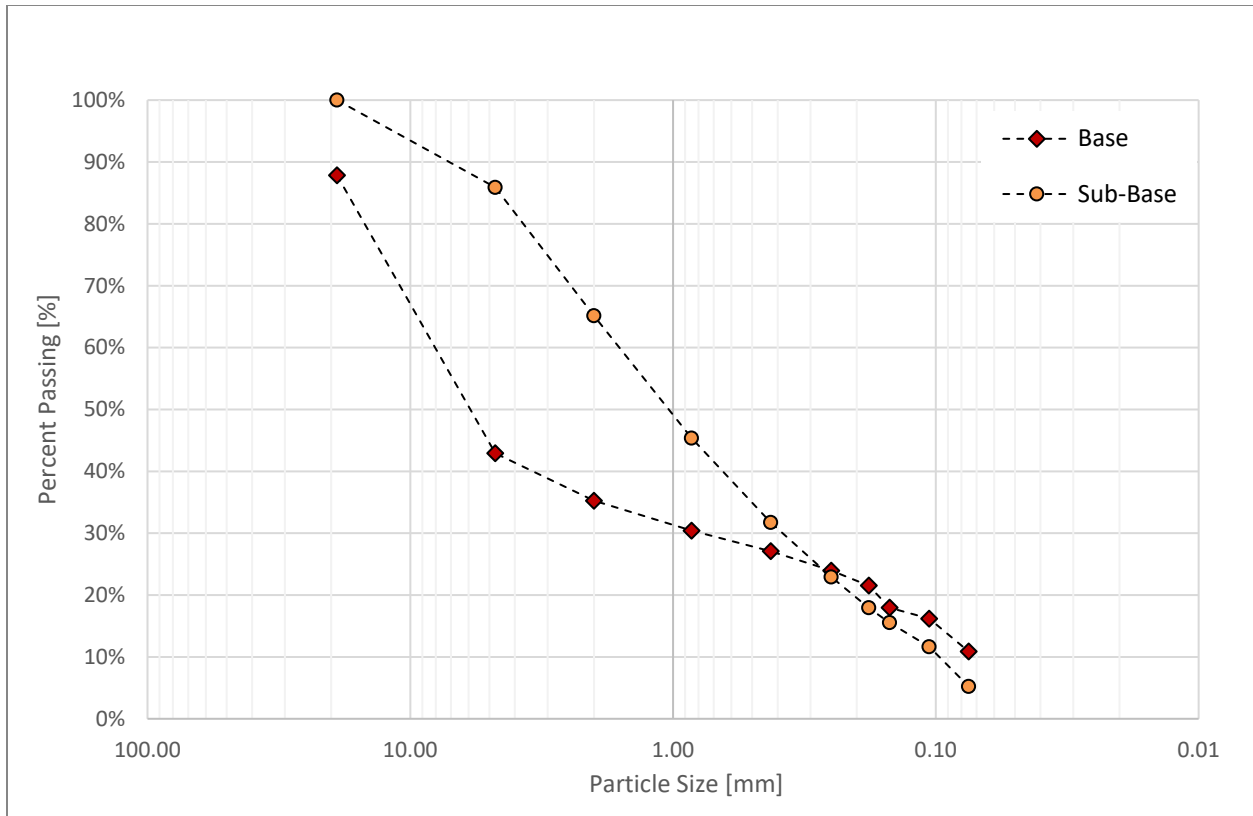
Figure 4.17. Grain size distributions for base and subbase materials.

4.2.2.2. Atterberg Limits

Atterberg limits were determined for the fines fraction of the subbase material. The material ranks as a low plasticity clay, with a liquid limit of 27 and a plasticity index of 8 as shown in Figure 4.18.
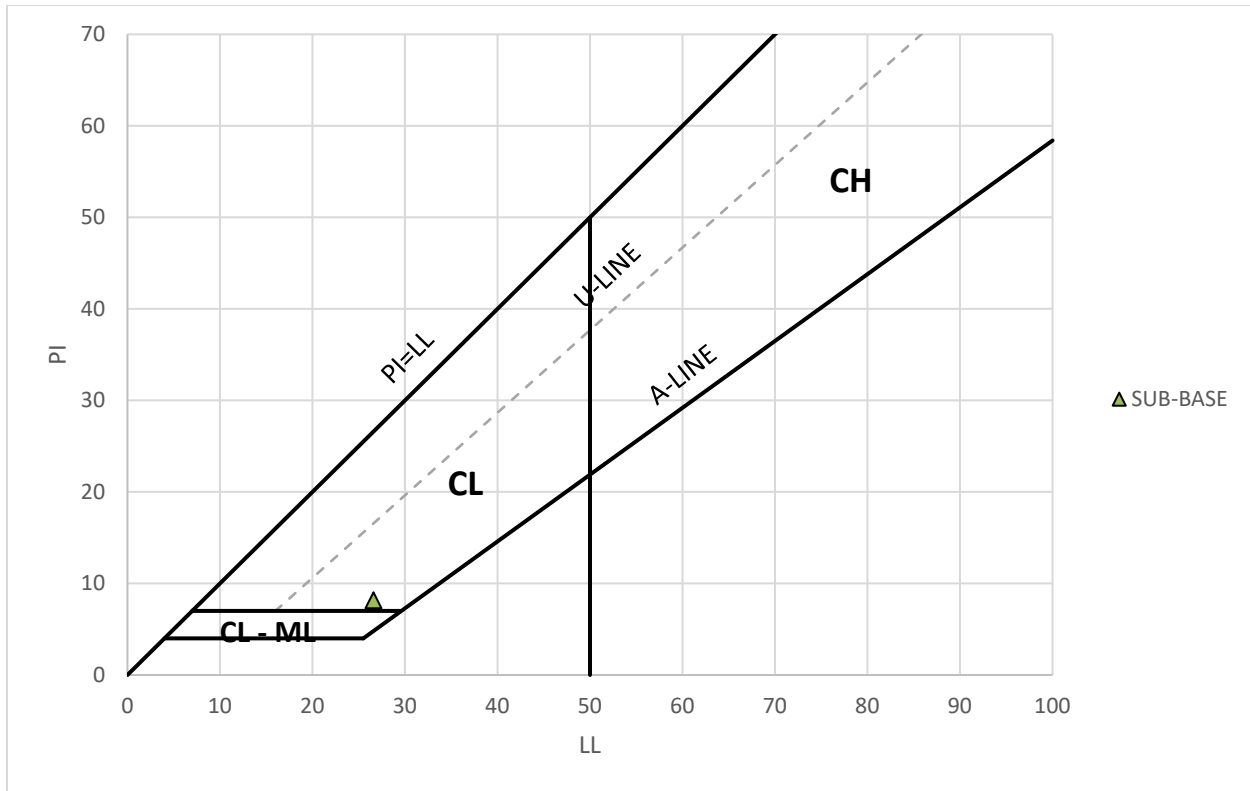
Figure 4.18. Atterberg limits of subbase material.

4.2.2.3. Soil Classification

Based on the grain size distribution and Atterberg limits, the USCS designation of the subbase is a SW-SC.

4.2.3. Old Asphalt Layer

The core samples from the existing (old) asphalt layer were carefully collected during sensor installation. These asphalt cores were tested in the laboratory to evaluate various properties of old asphalt layer including the bulk density and indirect tensile strength characteristics, which are discussed in the following sections.

4.2.3.1. Bulk Density/Bulk Specific Gravity

The bulk specific gravity may be defined as the ratio of the weight of the compacted bituminous mixture specimen to the bulk volume of the specimen. The bulk specific gravity of the old asphalt layer was determined in the laboratory by testing three different samples of cores collected from old asphalt layer per Tex-207-F: Test procedure for determining density of compacted bituminous mixtures. The core samples were collected and prepared for the tests per

Tex-251-F: Test procedure for obtaining and trimming cores of bituminous mixtures. The average bulk specific gravity of the old asphalt layer was determined to be 2.455.

4.2.3.2. Indirect Tensile Strength

The indirect tensile strength test is typically used to assess the tensile properties of the asphalt mixtures. The indirect tensile strength tests were performed on the cores collected from the old asphalt layer, as per Tex-226-F: Test procedure for indirect tensile strength test. The core specimens were trimmed to provide a level and smooth surface for testing (Figure 4.19) and the dimensions of the test specimens were carefully noted before the tests.

Figure 4.19. Photographs showing preparation of asphalt cores for characterization.

Figure 4.20 shows the Indirect Tensile strength (IDT) test device used in this research study and it can be observed that the IDT test rig consisting of top and bottom loading strips was placed on the loading platform so that the load can be applied through the top loading strip connected to a load cell. A data logger unit was connected to the device to control the movement of the loading platform, rate of loading, and to record the load and deformation data. The specimen was carefully placed between the top and bottom loading strips so that they were parallel to each other and the loading platform (Figure 4.20b). The IDT tests were performed in a deformation/strain-controlled mode and a constant deformation rate of 2 inches/minute was adopted per Tex-226-F and ASTM D6931 standard specifications.

The load and deformation were continuously recorded during the tests, and a typical load-deformation plot is presented in Figure 4.21. It can be observed that the loads increased with an increase in deformation to a peak value and reduced thereafter with a further increase in the deformation values. The peak load was carefully noted from the load-deformation plot and substituted in Eq. 1 to determine the indirect tensile strength of the asphalt core tested.

$$S_t = \frac{2P}{\pi t D} \qquad\qquad (1)$$

109

where, St is indirect tensile strength in psi; P is the ultimate load applied in pounds; and t and D are the thickness and diameter of the specimen before testing, respectively.
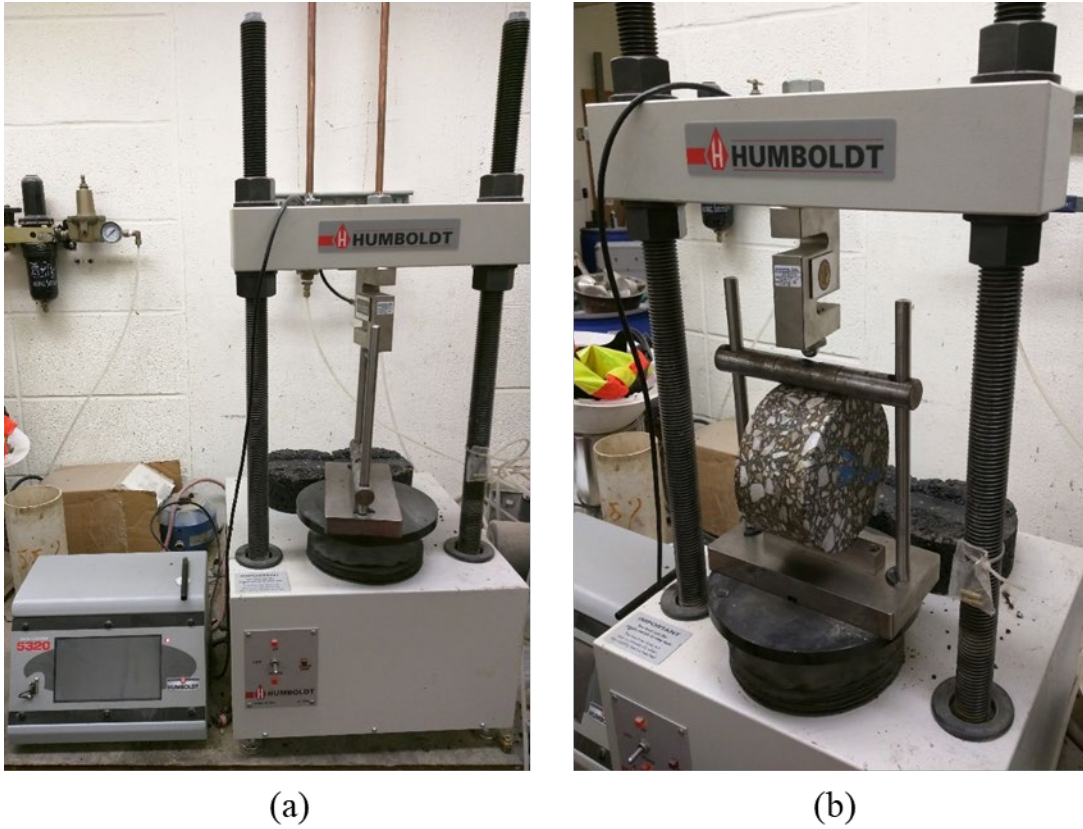
Figure 4.20. Indirect tensile strength test setup and asphalt core specimen.
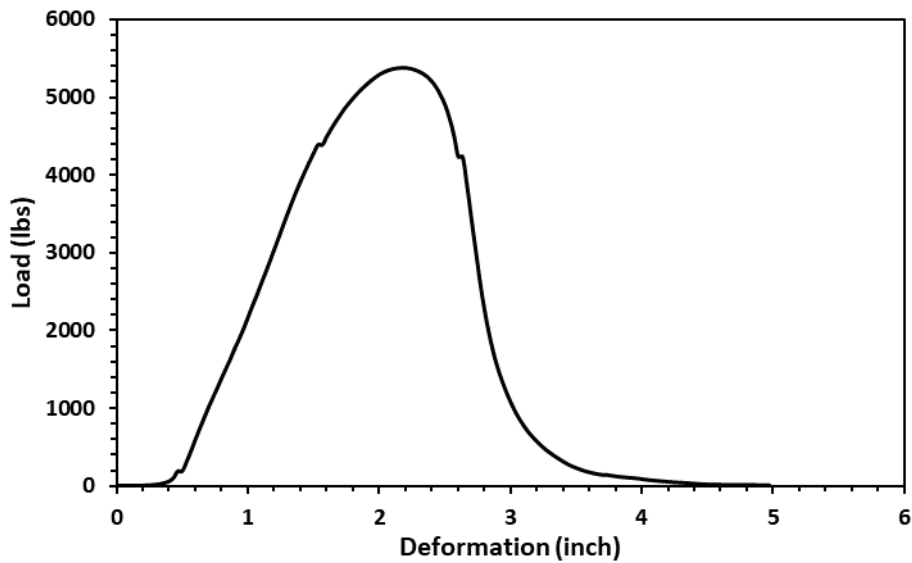
Figure 4.21. Typical load-deformation curve for asphalt cores tested from old asphalt layer.

The average indirect tensile strength of the asphalt core specimens collected from the old asphalt layer and tested in this study was determined to be 182.7 psi.

The old asphalt layer properties across all seven test section locations were similar in terms of density and strength characteristics. However, the old asphalt layer thickness and roadway profiles across the test sections was observed to slightly differ from each other.

4.3. Characterization of Materials Used for Overlay Construction

The materials used for overlay construction of the test sections and the rest of the project include asphalt mixtures, binder tack coats and different types of geosynthetic interlayers adopted in the test sections.

4.3.1. Asphalt Overlay

The asphalt overlay design adopted in the SH21 rehabilitation program, including the test sections, primarily consisted of a 2-inch-thick dense graded binder course overlain by a 1-inch-thick wearing course, referred to as Type-D asphalt and Thin Overlay Mixture (TOM), respectively. Samples and cores were collected from test sections during the construction of the asphalt overlay and were characterized in the laboratory to evaluate their index and engineering properties. The Type-D asphalt mix had a Valero PG 64-22 binder at an optimum binder content of 5.2% and 0.4% warm-mix additive (Evotherm) as a compaction aid. The TOM had a Valero PG 76-22 binder at an optimum binder content of 6% and 0.4% warm-mix additive (Evotherm) as a compaction aid. Figure 4.22 and Figure 4.23 present the gradation curves for the Type-D and TOM asphalt mixtures adopted in this study, respectively. The characterization of Type-D and TOM samples are discussed in detail in the following sections.
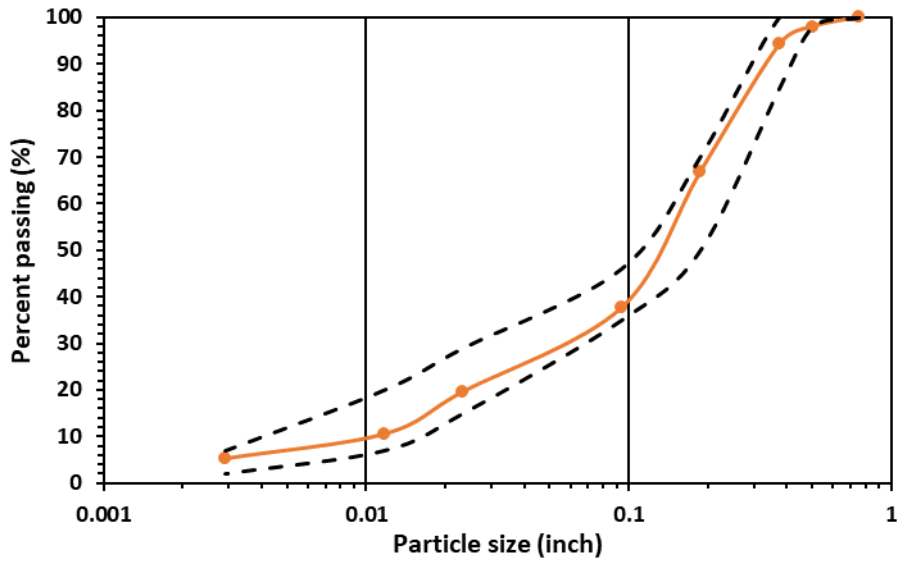
Figure 4.22. Gradation curve for Type-D asphalt mix adopted in this study.
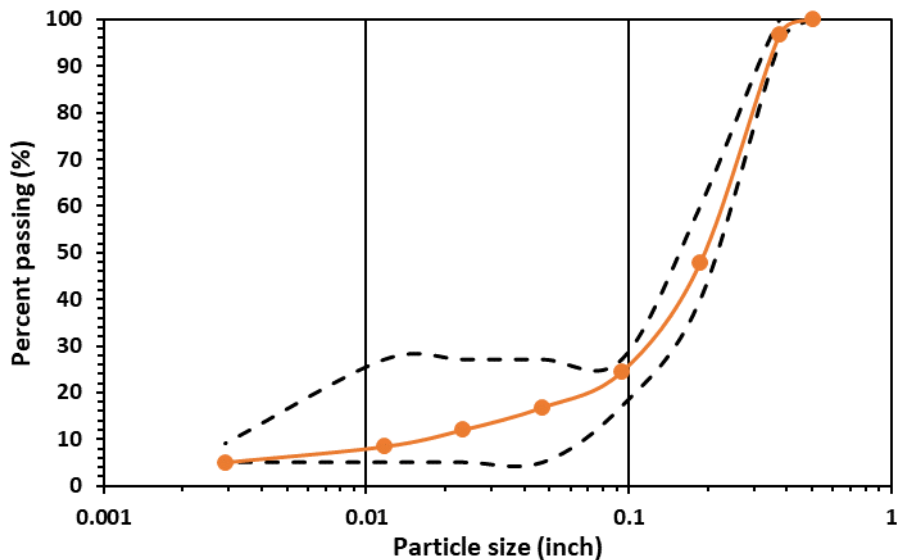
Figure 4.23. Gradation curve for thin overlay mixture adopted in this study.

4.3.1.1. Bulk Density/Bulk Specific Gravity

The bulk specific gravity may be defined as the ratio of the weight of the compacted bituminous mixture specimen to the bulk volume of the specimen. The bulk specific gravity of the Type-D and TOM asphalt layers was determined in the laboratory by testing three different samples of cores collected from the Type-D and TOM asphalt overlays per Tex-207-F: Test procedure for determining density of compacted bituminous mixtures. The average bulk specific gravity of the Type-D and TOM asphalt overlays was determined to be 2.427 and 2.386, respectively.

112

4.3.1.2. Percentage Air Voids

Air voids refers to the small pockets of air between the asphalt-coated aggregate particles in the final compacted asphalt mix. A certain percentage of air voids is required in all asphalt mixtures to allow for additional compaction of the asphalt layer under traffic. It is well known that the durability of an asphalt pavement is a function of their air-void content because a lower percentage of air voids results in flushing of asphalt under traffic and a higher air-void percentage results in moisture ingression and eventually damage to the pavement system. The percentage air voids in the compacted asphalt mix can be determined using the following expression:

$$P_a = \frac{(G_{mm} - G_{mb})}{G_{mm}} \times 100 \qquad\qquad (2)$$

where, Pa is percentage air voids; and Gmm and Gmb are the theoretical maximum specific gravity and bulk specific gravity of asphalt specimens, respectively.

The theoretical maximum specific gravity of the Type-D and TOM asphalt mixtures were determined to be 2.532 and 2.438 respectively per Tex-227-F: Test procedure for theoretical maximum specific gravity of bituminous mixtures. Then, the percentage air voids were calculated for the Type-D and TOM asphalt mixtures based on the bulk specific gravity and theoretical maximum specific gravity values determined. The percentage air voids for Type-D and TOM asphalt mixtures adopted in this study were found to be 4.15% and 2.13%, respectively.

4.3.1.3. Indirect Tensile Strength

The indirect tensile strength test is typically used to assess the tensile properties of the asphalt mixtures. The indirect tensile strength tests were performed on the Type-D and TOM asphalt overlay mixtures per Tex-226-F: Test procedure for indirect tensile strength test. The sample preparation and test procedure followed were similar to those performed on the old asphalt layers as described in Section 4.2.3. The average indirect tensile strength of Type-D and TOM asphalt overlay samples tested in the study was determined to be 152.6 psi and 196.1 psi, respectively.

4.3.1.4. Rut Depth: Wheel Tracking Test

The permanent deformation also referred as rut depth was determined for asphalt mixtures adopted as asphalt overlay in this study, using a Hamburg Wheel-Tracking Test (HWTT). The HWTT was performed per Tex-242-F: Test procedure for Hamburg wheel-tracking test and determines the premature failure susceptibility of bituminous mixtures due to weak aggregate structure, inadequate binder stiffness, moisture damage and other factors including insufficient

bonding between the aggregate and asphalt binder. The HWTT was performed on the TOM samples only and not on Type-D asphalt samples due to insufficient samples of the latter.

Figure 4.24 presents the HWTT device adopted in this study and it can be observed that a pair of steel wheels with a diameter of 8 inches and a width of 1.85 inches was used to apply a load of 158 lb. at a rate of 52 passes/minutes, resulting in a frequency of 0.87 Hz. The asphalt specimens were trimmed to match the requirements of the test, i.e., a dimeter of 5.9 inches and thickness of 2.4 inches. Furthermore, approximately 0.5 inches of the core specimens were cut from the 5.9-inch diameter to fit the HWTT device as shown in Figure 4.24.

Once the specimens were prepared and ready for testing, the specimen assembly was immersed in a water bath at a temperature of 122 °F and the load was applied repeatedly through the steel wheels. The rut depth below the wheel load was measured along the wheel path at an interval of 5,000 wheel passes before terminating at 20,000 wheel passes.

Figure 4.24. Hamburg wheel-tracking test device and asphalt specimen after test.

114

Table 4.2 presents the HWTT results for the TOM samples tested in this study and it can be observed that the rut depth increased with an increase in the number of wheel passes. Generally, asphalt samples are expected to have a rut depth less than 12.5 mm at the end of 20,000 wheel passes at a temperature of 122 °F to resist premature failure due to temperature, moisture and other parameters. The TOM samples tested were reported to have a rut depth of 5 mm at the end of 20,000 wheel passes, suggesting the ability of adopted mixtures to resist permanent deformations effectively under the influence of temperature and moisture parameters.

Table 4.2. Hamburg wheel-tracking test results for TOM.

No. of wheel passes	Rut depth (mm)
5,000	3.1
10,000	3.7
15,000	4.2
20,000	5.0

4.3.1.5. Fatigue Life: Overlay Test

The overlay test assesses the susceptibility of asphalt mixtures against fatigue and reflective cracking. Specifically, crack resistance index and critical fracture energy of the mixtures are the performance factors determined to characterize the asphalt mixtures' resistance to cracking. Critical fracture energy may be defined as the energy required for initiating a crack on the bottom of the specimen at the first loading cycle of the overlay test. The crack resistance index may be defined as the reduction in load required to propagate cracking under the cyclic loading conditions of the overlay test. These parameters characterize the fracture and fatigue properties of the asphalt mixture during crack initiation and propagation stages, respectively.

The HWTT was performed on the TOM samples only and not on Type-D asphalt samples due to insufficient samples of the latter. The specimens for overlay test were prepared per Tex-248-F and had a length of 6 inches, width of 3 inches and thickness of 1.5 inches. An epoxy resin was

used to carefully glue the prepared specimens to the base plates separated by a 4.2-mm spacer bar as shown in Figure 4.25. A weight was placed on the glued specimens to ensure complete bonding with the base plates and excess epoxy accumulated on the specimen sides was carefully scraped out. The weight was removed after the epoxy was completely set and the specimen assembly was conditioned at a temperature of 77 °F for a duration of one hour before testing.

Figure 4.25. Asphalt specimens glued to base plates with spacer.

The overlay test was performed on the TOM samples at a temperature of 77 °F per Tex-248-F: Test procedure for overlay test. A repeated tension load was applied under displacement-controlled mode with a loading rate of 0.025 inches displacement and a frequency of 0.1 Hz, which accounts for a duration of 5 seconds of loading and 5 seconds of unloading. The peak load corresponding to the displacement was recorded for every load cycle until a 93% reduction in the maximum load was experienced before application of 1,000 cycles. Figure 4.26 presents a typical load-displacement plot used to calculate the critical fracture energy at the peak load for the asphalt sample tested. The area under the load-displacement curve was used to calculate the critical fracture energy as shown in Figure 4.26 and using Eq. 3.
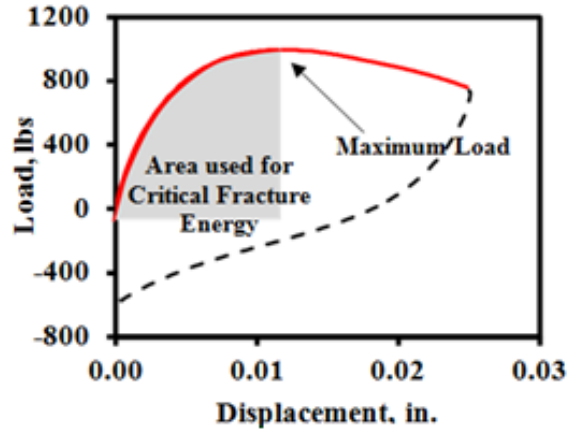
Figure 4.26. Typical load-displacement curve used to determine critical fracture energy.

$$G_c = \frac{W_c}{bh} \tag{3}$$

where, Gc is the critical fracture energy in lb.-in./in.2; Wc is the fracture area in lb.-in.; and b and h are specimen width and height, respectively.

The peak load corresponding to each cycle was plotted as a function of number of cycles and eventually a power function was fitted to determine the crack resistance index of the asphalt sample tested.

Table 4.3 presents the overlay test results for the TOM samples tested in this study. It can be observed that all specimens resisted 1,000 cycles without reaching a 93% decline in the peak load, suggesting a better resistance against fatigue and reflective cracking.

Table 4.3. Overlay test results for TOM samples tested in the study.

Specimen No.	Max. Load (lb.)	Critical Fracture Energy (lb.-in/in^2)	Crack Progression Rate (CPR)	Cycles to failure
1	526.3	1.79	0.27	1000
2	569.8	1.85	0.31	1000
3	644.7	1.90	0.32	1000
Average	580.3	1.84	0.30	1000

4.3.2. Tack Coat

Tack coat is a sprayed application of asphalt binder, emulsion or cutbacks between the hot mix asphalt layers to enhance their bonding. Two different types of tack coats were adopted in this study including AC-15P and CSS-1H for geosynthetic-reinforced and unreinforced (control) sections, respectively. However, tack coat samples could not be collected during the overlay construction to characterize them.

4.3.3. Reinforcement Interlayers (Geosynthetic and Glass Products)

4.3.3.1. General Characteristics

A total of nine reinforcement products were used in the test sections including a wide variation of polymeric and glass-made products in grid, mat and composite format. Table 4.4 lists the main characteristics of the reinforcement products used in the project. This section elaborates on activities conducted to characterize the products. Characteristics reported by manufacturers are presented first and sampling from specific rolls used in test section construction along with the experimental characterization of samples are presented thereafter.

Table 4.4. General characteristics of reinforcement materials used in test sections.

Product Acronym	Form	Material	Roll Length (ft.)	Roll Width (ft.)
GS1	Composite	Polyester (PET)	246	12.6
GS2	Grid	Polyester (PET)	495	13.2
GS3	Grid	Polyester (PET)	492	13.2
GS4	Grid	Polyvinyl Alcohol (PVA)	487	12.5
GS5	Grid	Glass	295	12.8
GS6	Grid	Glass	492	13.1
GS7	Grid	Glass	330	05.0
GS8	Mat	Glass	910	12.6
GS9	Composite	Glass	150	12.5

GS1: Hock; GS2: Shandong; GS3: C40/17; GS4: XP50; GS5: G50; GS6: G100; GS7: 8511TF; GS8: GlasPave50; GS9: MPG100.

4.3.3.2. Characteristics by Manufacturers

Technical data sheets for reinforcement products were requested from manufacturers and were evaluated to establish initial understanding of each product. The material composition, physical and geometrical properties, and mechanical characteristics reported in the data sheet of each reinforcement were assessed and compared to the requirements listed in the specific specifications of the project. Based on the material composition, the reinforcement products

classified in three main groups: (1) polymeric-based products (GS1 to GS4); (2) glass-based products (GS5 to GS8); and (3) combined polymeric- and glass-based products (GS9). Based on the ultimate tensile strength, the reinforcement products classified in two groups of 50 kN/m (GS1 to GS5 and GS8) and 100 kN/m (GS6, GS7 and GS9). Based on the shape and formation, the reinforcements classified in three groups: (1) grid shape (GS2 to GS7); (2) mat shape (GS8); and (3) composite shape (GS1 and GS9) products.

Table 4.5 to Table 4.11 summarizes characteristics of various reinforcement products reported by manufacturers.

Table 4.5. Characteristics of GS3.

PROPERTY	TEST	ENGLISH units[1]	SI units[1]
Mass/ Unit Area	ASTM D-5261	8.0 oz./yd^2	270 g/m^2
Aperture Size	Measured	1.5 in. x 1.5 in.	40 mm x 40 mm
Open Area of Grid	CWO 22125	> 80%	> 80%
Tensile Strength-Single Rib			
Machine Direction (MD)	ASTM D-6637	3,425 lb/ft.	50 kN/m
Cross-Machine Direction (CMD)	ASTM D-6637	3,425 lb/ft.	50 kN/m
Tensile Strength @ 3% Strain	ASTM D-6637	835 lb/ft.	12 kN/m
Elongation at 50kN +/-	ASTM D-6637	10%	10%
Shrinkage @ 375° F for 15 min		<1%	<1%
Identification of Fibers	ASTM D-276	490° F	255° C
Asphalt Retention	ASTM D 6140	0.10 gal/yd2	0.47 l/m^2

[1]Minimum average roll values are based on a 95% confidence level

Standard Roll Size: 13.2 ft (4.0 m) wide x 492.1 ft (150 m) long = 717 yd^2 (500 m^2)
Weight (includes core) = 485 lbs. (220 kg)

Table 4.6. Characteristics of GS4.

PROPERTY	TEST METHOD	ENGLISH units[1]	SI units[1]
Mass/Unit Area	ASTM D-5261	6.25 oz/yd^2	210 g/m^2
Aperture Size	Measured	1.5 x 1.5 inch	40 x 40 mm
Open Area of Grid	CWO 22125	>80 %	>80 %
Wide Width Tensile Strength			
Machine Direction (MD)	ASTM D-6637	3,425 lb/ft	50 kN/m
Cross-Machine Direction (CMD)	ASTM D-6637	3,425 lb/ft	50 kN/m
Tensile Strength @ 3% Strain	ASTM D-6637	1,712 lb/ft	25 kN/m
Elongation at Break	ASTM D-6637	5 %	5 %
Shrinkage @ 375° F for 15 min		<1%	<1%
Melting Point	ASTM D-276	445° F	230° C

[1] MARV - Minimum average roll values are based on a 95% confidence level.

Standard Roll Size: 13.12 ft (4 m) wide x 492.1 ft (150 m) long = 717 yd^2 (600 m^2)
Weight: 485 lb/roll (220 kg)

Table 4.7. Characteristics of GS5.

PROPERTY	TEST	ENGLISH units[1]	SI units[1]
Mass/ Unit Area	ASTM D-5261	9.5 oz./yd^2	320 g/m^2
Aperture Size	Measured	1.2 in. x 1.2 in.	30 mm x 30 mm
Open Area of Grid	CWO 22125	> 80%	> 80%
Tensile Strength-Single Rib			
Machine Direction (MD)	ASTM D-6637	3,425 lb/ft.	50 kN/m
Cross-Machine Direction (CMD)	ASTM D-6637	3,425 lb/ft.	50 kN/m
Elongation at Brake	ASTM D-6637	< 3%	<3%
Identification of Fibers	ASTM D-276	490° F	255° C
Asphalt Retention	ASTM D-6140	0.10 gal/yd2	0.47 l/m^2

[1]Minimum average roll values are based on a 95% confidence level

Standard Roll Size: 1: 12.80 ft. (3.90 m) wide x 492.13 ft (150 m) long = 700 yd2 (585 m2)
Weight (includes core) = 465 lbs (211 kg)

Table 4.8. Characteristics of GS6.

PROPERTY	TEST	ENGLISH units[1]	SI units[1]
Mass/ Unit Area	ASTM D-5261	17.7 oz/yd^2	596 g/m^2
Aperture Size	Measured	1.2 in. x 1.2 in.	30 mm x 30 mm
Open Area of Grid	CWO 22125	> 80%	> 80%
Tensile Strength-Single Rib			
Machine Direction (MD)	ASTM D-6637	6,850 lb/ft.	100 kN/m
Cross-Machine Direction (CMD)	ASTM D-5261	6,850 lb/ft.	100 kN/m
Elongation at Brake	ASTM D-5261	< 3%	<3%
Identification of Fibers	ASTM D-276	572° F	300° C
Asphalt Retention	ASTM D-6140	0.10 gal/yd2	0.47 l/m^2

[1]Minimum average roll values are based on a 95% confidence level

Standard Roll Size: ′ 12.80 ft. (3.90 m) wide x 328.1 ft (100 m) long = 467 yd2 (390 m2)
Weight (includes core) = 567 lb (257 kg)

Table 4.9. Characteristics of GS7.

Specifications for Use in Asphalt Overlays					
Property	Test Method	8501		8511	
		Metric	Imperial	Metric	Imperial
Tensile Strength (Ultimate) (MD x XD)	ASTM D6637 EN-ISO 10319	100 x 100 kN/m	571 x 571 lbs/in	100 x 100 kN/m	571 x 571 lbs/in
Tensile Elongation (Ultimate)	ASTM D6637 EN-ISO 10319	< 3%	< 3%	< 3%	< 3%
Tensile Resistance @ 2% Strain (MD x XD)	ASTM D6637 EN-ISO 10319	80 x 80 kN/m	456 x 456 lbs/in	80 x 80 kN/m	456 x 456 lbs/in
Young's Modulus E		73,000 MPa	10.6 x 10^6 psi	73,000 MPa	10.6 x 10^6 psi
Mass/Unit Area	ASTM D5261 ISO 9864	405 g/m^2	12.0 oz/yd^2	405 g/m^2	12.0 oz/yd^2
Melting Point Coating **Melting Point Glass**	ASTM D276/EN-ISO 3146 ASTM C338	>232° C >820° C	>450° F >1508° F	>232° C >820° C	>450° F >1508° F
Roll Length		100 m	328 ft	100 m	328 ft
Roll Width		1.5 m	5 ft	1.5 m	5 ft
Roll Area		150 m^2	179 yd^2	150 m^2	179 yd^2
Adhesive Backing		Pressure Sensitive		Pressure Sensitive	
Grid Size (Center to Center of Strand)		12.5 x 12.5 mm	0.5 x 0.5 in	25 x 25 mm	1.0 x 1.0 in
Material		Fiberglass reinforcement with modified polymer coating and pressure-sensitive adhesive backing			

123

Table 4.10. Characteristics of GS8.

Specifications for Use in Asphalt Overlays			
Property	**Test Method**	**GlasPave50**	
		Metric*	Imperial**
Tensile Strength	ASTM D 5035	50 kN/m	280 lb/in.
Elongation at Break	ASTM D 5035	≤5%	≤5%
Melting Point	ASTM D 276	> 232°C	> 450°F
Mass/Unit Area	ASTM D 5261	237 g/m^2	7.0 oz/yd^2
Asphalt Retention	ASTM D 6140	0.47 l/m^2	0.10 gal/yd^2
Roll Sizes[†]		1.91 x 109.7 m 3.81 x 65.8 m	75 in x 120 yds 150 in x 72 yds
Roll Areas[†]		209.5 m^2 250.8 m^2	250 yd^2 300 yd^2

We believe all statements herein to be accurate and reliable, but are presented without guarantee or responsibility on our part. Statements concerning possible use of our product are not intended as recommendations for their use in the infringement of any patent. No patent warranty of any kind, expressed or implied, is made or intended. Values presented above are nominal and only to be used as guidelines.

[†] Product is sold by the roll.   *All metric values are nominal.   **All imperial values are approximate.

Table 4.11. Characteristics of GS9.

Mechanical Properties	Test Method	Units	MPG 100
			Average Roll Value
Tensile Strength @ 0°	ASTM D6637	lbs/in	655 (115)
Tensile Strength @ 90°	Method A	(kN/m)	655 (115)
Tensile Elongation	modified	%	< 3
Melting Point	ASTM D276	F° (C°)	Glass filaments are incombustible and temperature resistant up to 1472° (800°)
Mass/Unit Area	ASTM D5261	oz/yd^2 (g/m^2)	20.0 (678)
Glass by Weight		%	77.4
			Minimum Test Value
Asphalt Retention	ASTM D6140	gal/yd^2 (l/m^2)	0.27 (1.2)

Tensile Strength values refer to strength of the glass filaments.

Physical Properties	Unit	MPG 100
Grid Aperture Size	in (mm)	1.5 (38.1)
Roll Dimensions (width x length)	ft (m)	6.25 x 300 (1.9 x 91)
	ft (m)	12.5 x 150 (3.8 x 45.7)
Roll Area	yd^2 (m^2)	208 (174)
Estimated Roll Weight	lbs (kg)	260 (169)

4.3.3.3. Sampling

Several samples were collected from specific rolls used in the construction of the test sections. Samples were collected in accordance with the recommendations provided by the ASTM Standard Practice for Sampling of Geosynthetics and Rolled Erosion Control Products for Testing (ASTM D4354). Initial portions of the rolls that may have been damaged during transportation and handling were skipped and samples were taken from the intact portions of the rolls to be representative of the product. Some of the samples were sent to an independent laboratory for testing and results were sent to TxDOT for quality control purposes. In addition, remnants of several rolls that were used in the instrumented test sections were also collected and transported to the Austin District lab and stored in a protected storage room (Figure 4.27). For experimental characterization of the rolls, specimens were cut from the collected rolls and transported to the UT Austin laboratory for testing.

Figure 4.27. Remnants of rolls used in test sections in Austin District storage room.

4.3.3.4. Experimental Characterization

Asphalt-Reinforcement Interface Shear Test: Leutner Shear Test
One of the most common devices to test bond strength in asphalt interfaces is the Leutner shear tester. This device consists of a guillotine apparatus that can be attached to common laboratory equipment. A monotonic load is applied at a rate of 2 inches per minute on one layer of a 6-inch-diameter asphalt specimen through a U-shaped arm while the other layer remains stationary.

Experimental Setup

Several pavement cores were collected by TxDOT from the entire asphalt layer during the field visit conducted in December 2019 (Figure 4.28). The diameter of the cores was approximately 6

inches and the height of the cores varied depending on their location and thickness of the asphalt layer at that location.

Figure 4.28. Pavement cores collected from field test sections.

The cores obtained from each reinforced test section were carefully explored to find the most suitable specimen for the bond strength test. Specifically, careful attention was paid to ensure that in the specimen selected for bond testing, the interface between the overlay and old pavement (where the reinforcement layer is located) remained intact during drilling and specimen transportation to the laboratory. The heights of the specimens were then trimmed to be consistent with the dimensions of the Leutner shear tester device. The specimens were then placed in the Leutner shear tester device so that the interface was placed between the stationary side and moving side of the device (Figure 4.29).
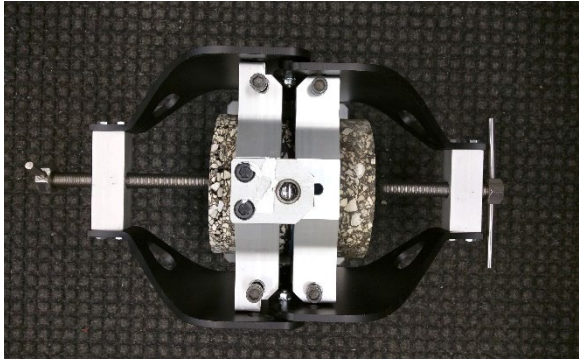
Figure 4.29. Pavement cores installed in Leutner shear tester device.

The Leutner shear tester device was used in an Instron 8872 loading machine and a monotonic load was applied at a displacement rate of 2 inches per minute until full shear developed at the interface (Figure 4.30). Maximum possible displacement in the shear device was approximately ½ inch (12 mm).

Figure 4.30. Asphalt-reinforcement interface shear test.

Test Results

Shear load versus relative shear displacement data was plotted and compared among pavement cores collected from reinforced field test sections. In addition, specimens were explored after testing to evaluate the failure mode and conditions of the reinforcement layer after shear. As shown in the example picture from the pavement core from test Section 7 in Figure 4.31, complete shear was observed in all tests at the interface while the top and bottom asphalts remained intact. The shear plane was found to be formed below the reinforcement layer where the tack coat had been applied to the old asphalt layer.

Figure 4.31. Pavement core from Section 7 after interface shear testing.

Figure 4.32 summarizes the shear force versus relative shear displacement data for all reinforcement products used in the instrumented test sections. Among all specimens, the maximum shear load was found to be approximately 3,250 lbs. in GS3 and GS4. The maximum shear load in GS7 and GS9 was below 2,000 lbs. This value for the project-specific product (GS1) was also less than 2,000 lbs. The relative shear displacement at the peak shear was also found to range from 2 mm (in GS7) to 5 mm (in GS4 and GS8).

Geosynthetic Tensile Strength Tests: Wide Width Tensile Test Procedure and Setup

Wide width tensile tests were conducted in accordance with the procedure recommended by the Standard Test Method for Determining Tensile Properties of Geogrids by the Single or Multi-Rib Tensile Method (ASTM D6637). The width of the specimens was approximately 7.9 in (200 mm) and the length of the specimens in the direction of the tensile load was approximately 10 in (250 mm). All tests were conducted using a SATEC Systems, Inc. loading machine with a maximum capacity of 60 kips. Roller grips were used to attach the reinforcement specimens to the load frame and tension was applied by pulling the top grip (Figure 4.33). The edge ribs were cut as per recommendations by the standard test procedure and the effective number of ribs in tension was three in most tests. Blue square markers with black crosses in their centers were glued to the effective ribs in tension of each specimen in three rows (Figure 4.34). Images were captured during the test using a high-resolution camera installed in front of the specimen (Figure 4.33). Tensile strains in each specimen were measured using image analysis of the pictures taken in the test. The tensile strains were then plotted against the tensile load recorded by the load cell attached to the top grip.
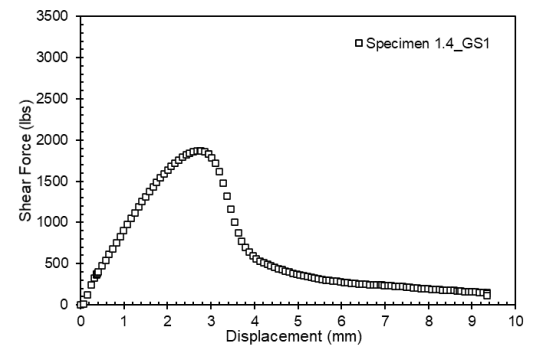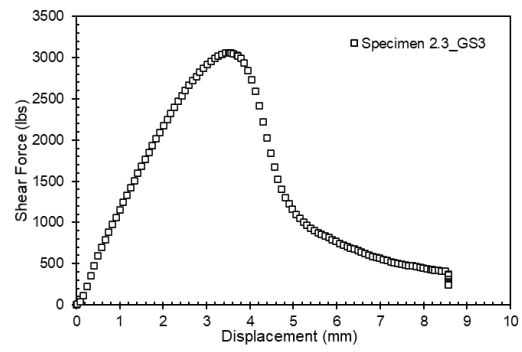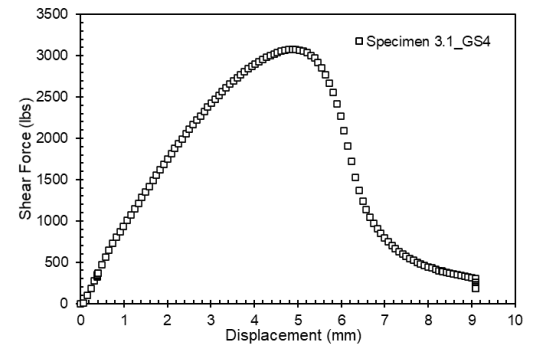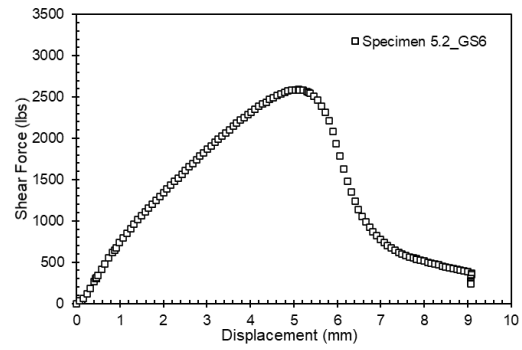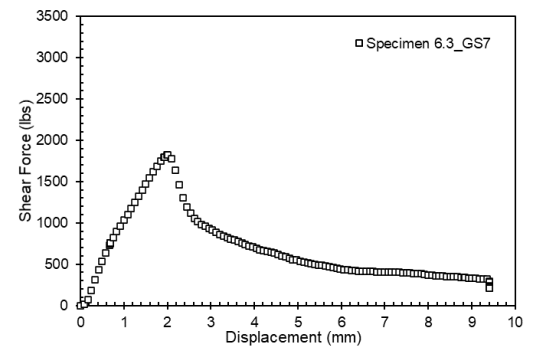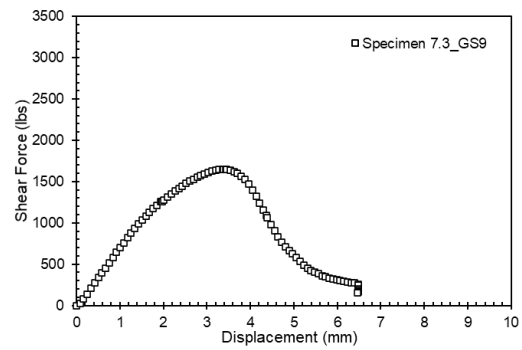
Figure 4.32. Results of asphalt-reinforcement interface shear tests: a) GS1; b) GS3; c) GS4; d) GS6; e) GS7; and f) GS9.

Figure 4.33. Wide width tensile test setup showing roller grips, reinforcement specimen and high-resolution camera for image capturing.
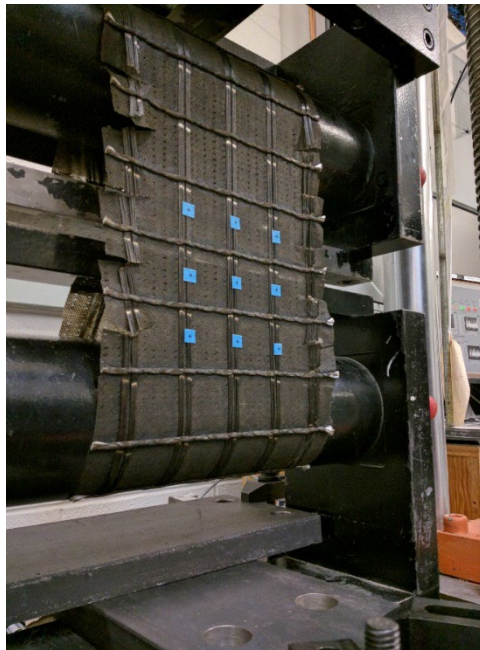
Figure 4.34. Reinforcement specimen used in wide width tensile tests with blue markers glued on for image analysis.

Test Results

Wide width tensile test results were analyzed to determine tensile properties of the reinforcements. Specifically, tensile load versus tensile strains data were compared among various reinforcement products along with the tensile loads at 2% strain were obtained. In addition, ultimate tensile load obtained in each test was found and the failure mode for each specimen was explored and documented. Tensile tests were conducted in the Cross-machine Direction (CD) and Machine Direction (MD) of the reinforcement rolls. Example results for several reinforcement products are presented in this section.

Figure 4.35 presents the tensile load versus tensile data for GS4 in the CD (Figure 4.35a) and MD (Figure 4.35b). This data is presented for initial strains from 0 to 2.5%. The maximum load recorded in the CD and MD was approximately 970 and 990 lbs., respectively, and the tensile load at 2% strain in the CD and MD was approximately 510 and 550 lbs., respectively. Figure 4.36 also shows the specimens in both directions after the test. The specimens were failed by breaking in a few ribs close to the top grip.

(a)   (b)
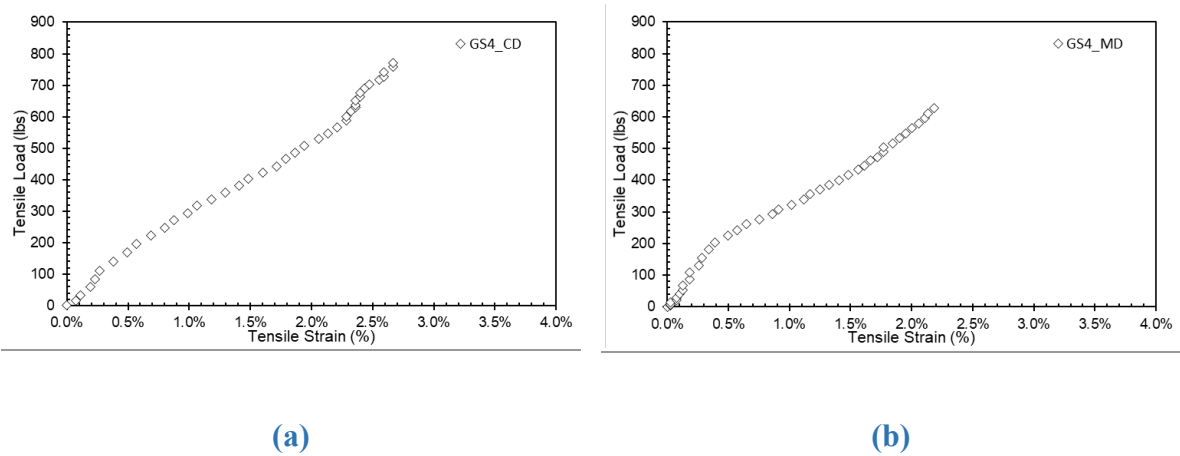
Figure 4.35. Wide width tensile test results for GS4: a) Cross-machine Direction (CD); and b) Machine Direction (MD).

Figure 4.39. GS4 specimens in MD and CD after tensile test.

Figure 4.37 presents the tensile load versus tensile data for GS1 in the CD (Figure 4.37a) and MD (Figure 4.37b). This data is presented for the initial strains from 0 to 4%. The maximum load recorded in the CD and MD was approximately 1,350 and 1,100 lbs., respectively, and the tensile load at 2% strain in the CD and MD was approximately 225 and 260 lbs., respectively.

(a)

(b)
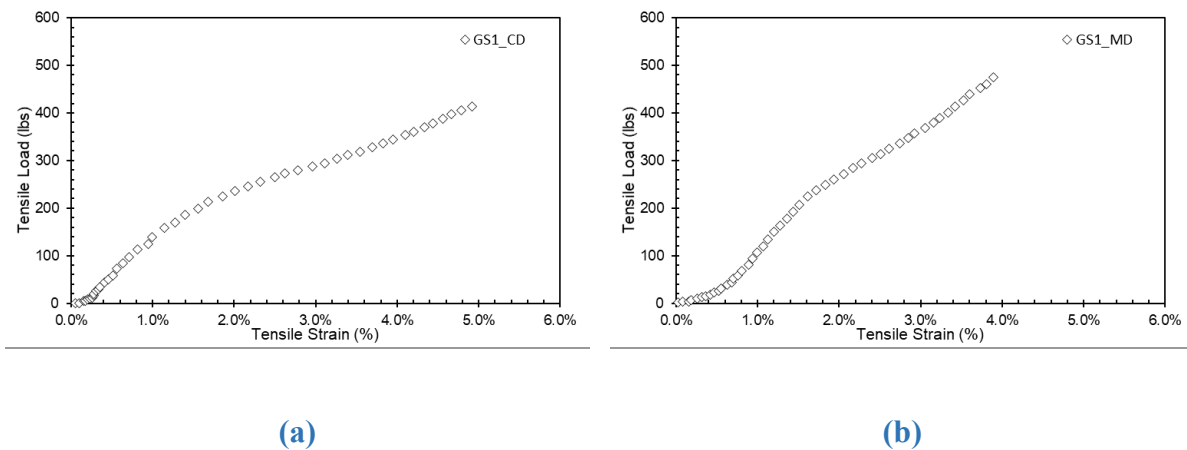
Figure 4.37. Wide width tensile test results for GS1: a) CD; and b) MD.

132

Figure 4.38 presents the tensile load versus tensile data for GS2 in the CD (Figure 4.38a) and MD (Figure 4.38b). This data is presented for the initial strains from 0 to 2%. The maximum load recorded in the CD and MD was approximately 665 and 850 lbs., respectively, and the tensile load at 2% strain in the CD and MD was approximately 390 and 355 lbs., respectively.

(a)

(b)
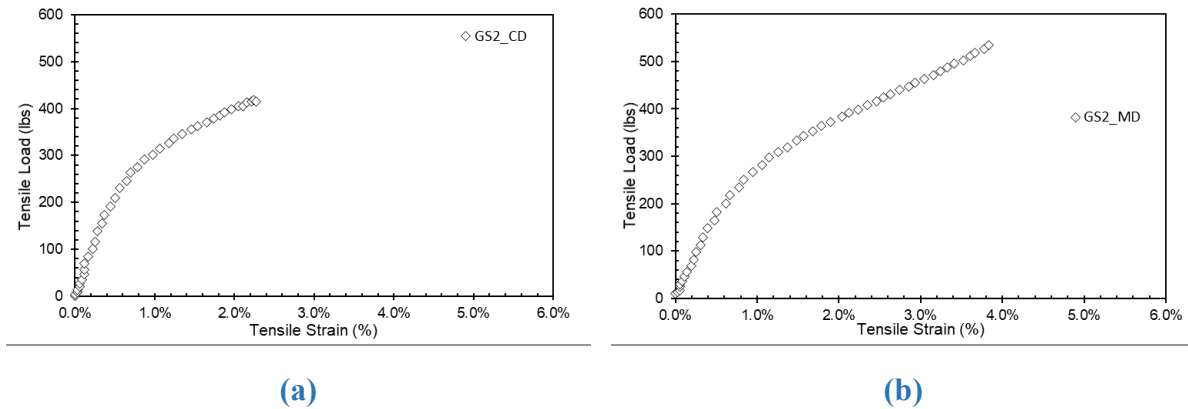
Figure 4.38. Wide width tensile test results for GS2: a) CD; and b) MD.

4.4. Final Remarks

A detailed characterization of materials from the existing pavement layers and materials used in the construction of asphalt overlay was reported. A few properties including, compaction characteristics of the subgrade soil, base and subbase materials could not be determined due to insufficient quantity of samples collected from the boreholes during the sensor installation process. In addition, the pavement core samples to perform the overlay fatigue and shear fatigue tests on the asphalt-geosynthetic composite could not be collected since the area office suggested not coring through the overlay sections. However, a Hamburg wheel-tracking test and overlay fatigue tests were performed on the TOM samples collected during construction as an additional characterization of the asphalt overlay.

Chapter 5. Procurement and Installation of Sensors

5.1. Introduction

This chapter reports the activities completed in Task 4 of TxDOT Project 0-7002. The main objective of this task was to procure, test and install the various instrumentation components, listed in Task 2, in the test sections and eventually record the initial readings after installation in test sections. Specific activities that were conducted and completed under this task were as follows:

Evaluated characteristics required for various components of the instrumentation

Identified vendors for each instrumentation component and evaluated the suitability of the vendor's products for the specific objectives of this project

Procured the selected instrumentation

Tested and calibrated each instrument and confirmed proper signaling

Developed specific protocols for proper installation of each sensor

Conducted a trial installation for each sensor at the job site and identified modification in the developed installation protocols

Identified refinements in the construction procedure to ensure proper installation of sensors

Coordinated necessary precautions with the contractor and TxDOT regarding sensitive sensor installation steps to minimize potential damage to the sensors

Installed sensors in various pavement layers including subgrade, base, old Hot Mix Asphalt (HMA) and the new overlay

Installed on-site data acquisition systems along with on-site power supply

Developed a protection mechanism against flooding to minimize potential damage to on-site data acquisition system

Confirmed signal from the installed sensors, and acquired and evaluated initial readings from various sensors

In this chapter, the procurement and installation of sensors in the SH21 test sections is explained in two sections. In Section 5.2, the main characteristics of the selected sensors, data loggers and power supply components are provided and in Section 5.5, specific protocols followed during the

installation of sensors, data loggers and power supply components are discussed. Examples from initial readings collected from various sensors installed in the test sections are presented in Section 5.6.

5.2. Sensor Specifications

5.2.1. Moisture Sensors

The moisture sensors (TDR-310S) used in this research study were manufactured by the manufacturer Acclima. Figure 5.1 presents a typical sensor with its dimensions. The length of the sensing portion of the sensor is about 4 in. (100 mm). The size of the sensors was chosen so that three could be installed vertically inside a 6-inch borehole to provide better reliability in the data from each installed location. A TDR-310S is a true waveform digitizing Time Domain Reflectometer (TDR) that derives soil permittivity and water content from the propagation time of an electromagnetic impulse conveyed along its waveguide. Time Domain Reflectometer technology was required to allow additional sensor de-bugging abilities in the field and when sensors are installed under marginal sensing conditions. The specifications of TDR-310S sensors employed have been summarized in Table 5.1.
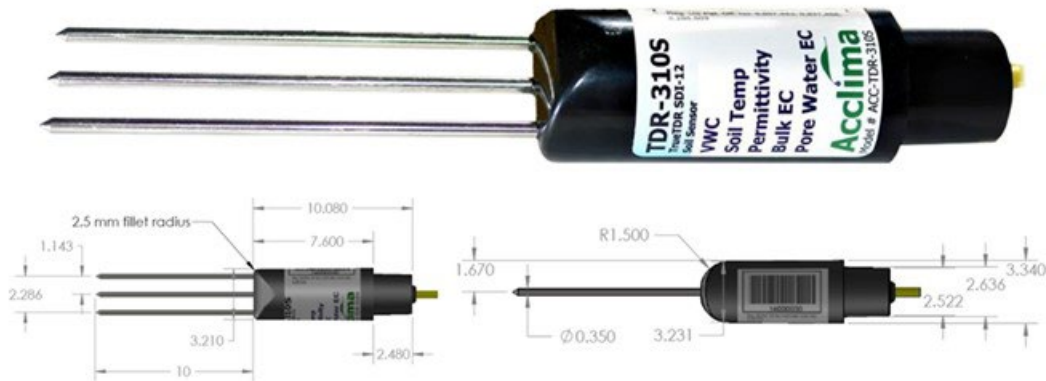
Figure 5.1. TDR-310S moisture sensor from Acclima.

Table 5.1. Characteristics of Acclima TDR-310S moisture sensor.

Maximum length of sensing portion	**4 in. (100 mm)**
Volumetric Water Content (WVC) Resolution	**0.1% VWC**
Volumetric Water Content (WVC) Accuracy	**± 2% typical**
VWC temp stability	**± 1% of full scale (34°F-122°F) (1°C-50°C)**
Temp reporting accuracy	**± 0.2 °C to 50 °C**
Technology	**TDR***

*TDR = Time-Domain Reflectometry

5.2.2. Geophones

The geophone layout designed in this research study consist of both 1 vertical Component (1-C) and 1 vertical and 2 horizontal component (3-C) geophone configurations manufactured by HGS India. The geophone element used for the vertical component in both cases is the HG-6 UB 4.5Hz 375Ω element (Figure 5.2a). The geophone element used for the horizontal component is the HG-6 HB 4.5Hz 375Ω element similar to HG-6 UB 4.5Hz 375Ω element, except for the change in orientation. Both 1-C and 3-C geophone elements were encased in a strong waterproof land case designed specifically for the adopted geophone elements. An HL-5 land case (Figure 5.2b) was used for 1-C geophone elements and HL-6B land case (Figure 5.2c) was used for 3-C geophone elements. It can be observed from Figure 5.2c that the orientation of HG-6 HB horizontal geophone components within the HL-6b land case have been clearly marked with arrows. The characteristics and specifications of the geophone elements are as listed in Table 5.2. Sensitivity and phase-lag curves for these geophones are also presented in Figure 5.3 and Figure

5.4, respectively.
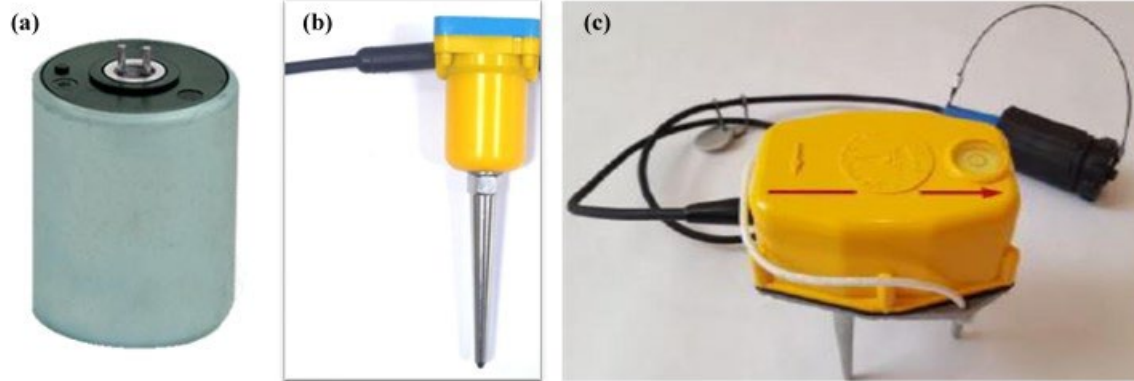
Figure 5.2. Geophone sensors from HGS India: (a) HG-6 geophone element; (b) HL-5 land case; and (c) HL-6B land case.

Table 5.2. Specifications of HG-6 geophone element.

Frequency	
Natural Frequency	4.5 Hz
Tolerance	±0.5 Hz
Maximum tilt angle for specified F_n	0°
Typical spurious frequency	140 Hz
Distortion	
Distortion with 17.78 mm/s p.p. coil-to-case velocity	<0.3%
Distortion measurement frequency	12 Hz
Maximum tilt angle for distortion specification	0°
Damping	
Open Circuit (typical)	0.560
Tolerance (open circuit)	±5%
Shunt for 0.60 damping	32960 Ω
Shunt for damping	9090 Ω
Damping for above mentioned shunt	0.70
Resistance	
Standard coil resistance	375 Ω
Tolerance	±5%
Sensitivity	
Open-circuit sensitivity	28.8 V/m/s
Tolerance	±5%
$R_t B_c f_n$	6000 ΩHz
Moving Mass	11.1 g
Maximum coil excursion p.p.	4 mm
Physical characteristics	
Diameter	1 in. (25.4 mm)
Height	1.4 in. (36 mm)
Weight	2.85 oz (81 g)
Operating Temperature Range	-40°F to 212°F (-40 °C to 100 °C)
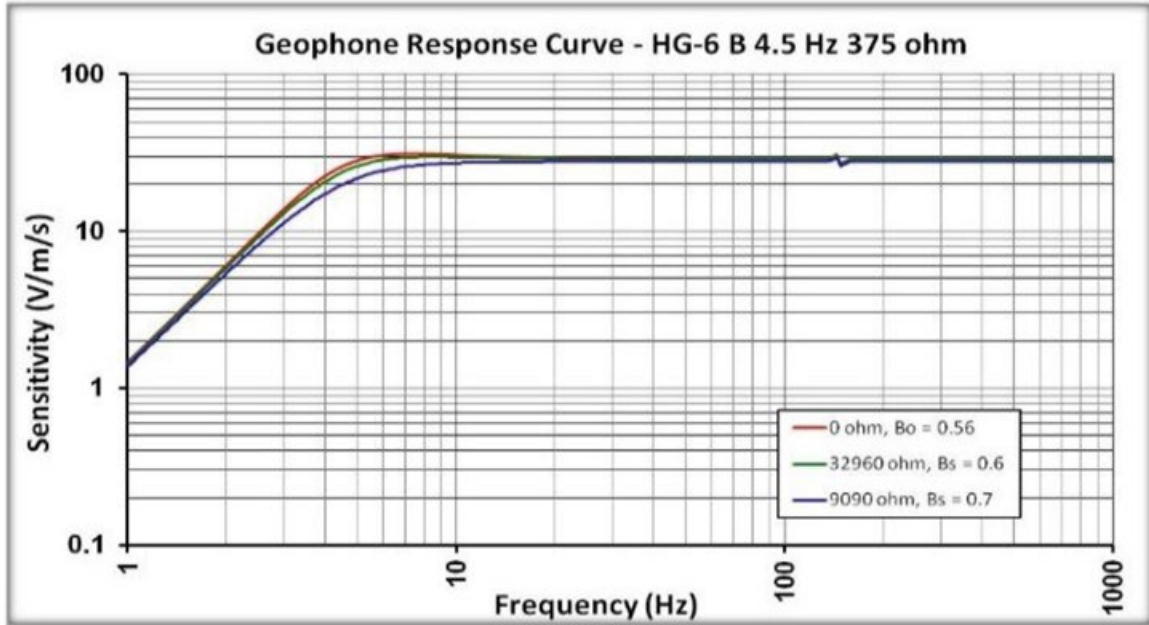
Figure 5.3. Sensitivity curve of HG-6 B 4.5 Hz 375 Ω.
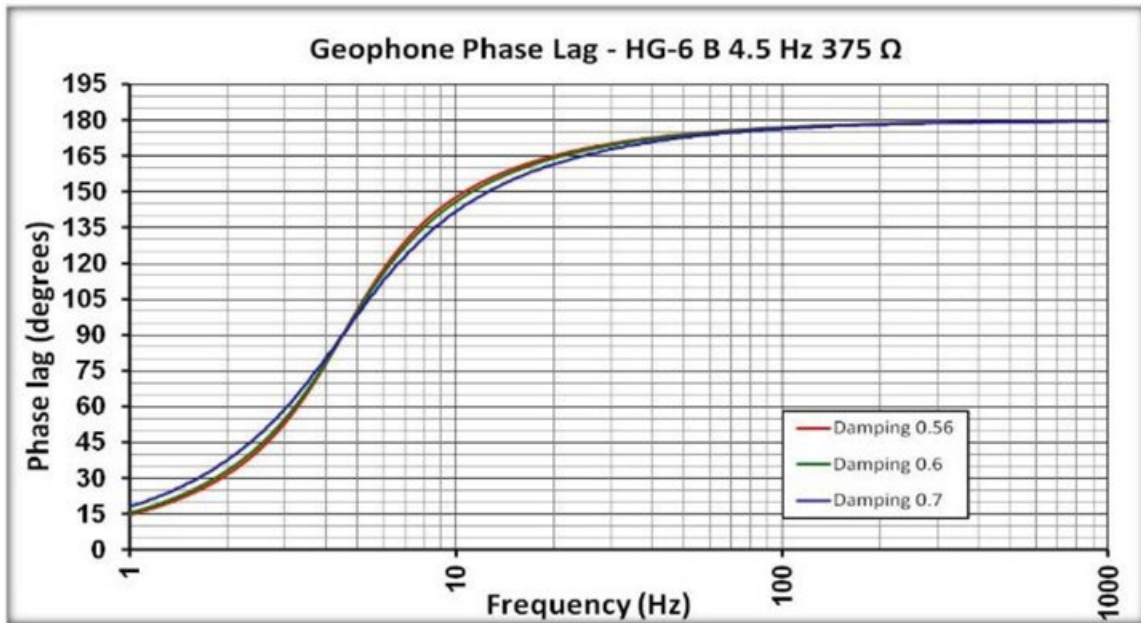
Figure 5.4. Phase-lag curve of HG-6 B 4.5 Hz 375 Ω.

5.2.3. Asphalt Strain Gauge

The Asphalt Strain Gauges (ASG) used in this study were manufactured by CTL Group. They were designed to withstand high temperatures and compaction loads associated with asphalt pavement construction. Figure 5.5 presents an example picture of the ASG sensor (model ASG-

152) adopted in this project specifically to measure the horizontal strains in the asphalt layer. The detailed specifications of ASG-152 are listed in Table 5.3.
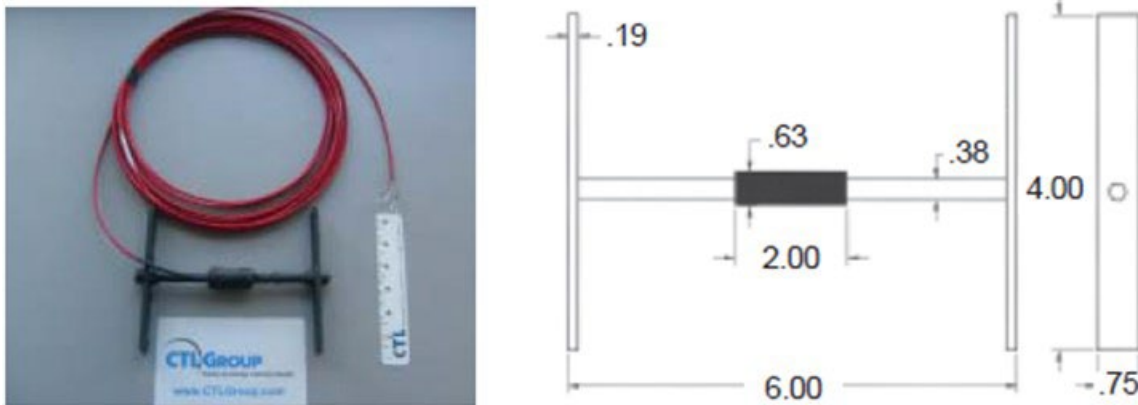
Figure 5.5. ASG – 152 from CTL Group.

Table 5.3. Specifications of ASG-152 from CTL Group.

Bridge Configuration	Full Bridge
Gauge Resistance	350 Ω
Excitation	Up to 10 V
Output	≈ 2 mV/V @ 1500 με
Grid Area	0.133 cm²
Gauge Area	1.22 cm² overall
Fatigue Life	$< 10^5$ repetitions @ ± 1500 με
Modulus	≈2,340,000 psi
Cell Material	Black 6/6 nylon
Coating	Two-part polysulfide liquid polymer, encapsulate in silicone with butyl rubber outer core
Temperature	-30 °F to 400 °F (-34 °C to 204 °C)
Lead Wire	22 AWG, braided shielded, four conductor

5.2.4. Thermocouples

The thermocouples used in this research study were T-type ready-made insulated thermocouples from Omega Engineering (Figure 5.6). They have a higher accuracy than other types of thermocouples but come with a limited range. However, the temperature range of T-type thermocouples was sufficient for the purposes of this project. The characteristics and specifications of the thermocouples are listed in Table 5.4.

Figure 5.6. T-type thermocouple from Omega Engineering.

Table 5.4. Specifications of T-type thermocouples from Omega Engineering.

Model No. @ Omega	**5TC-GG-T-20-240**
Thermocouple Type	**T**
Process Temperature Range	**32 $^\circ$F to 500 $^\circ$F (0 $^\circ$C to 260 $^\circ$C)**
Junction Type	**Exposed**
Accuracy	**1.0 $^\circ$C or 0.75% above 0 $^\circ$C**
Number of Wires	**2**
Cable Insulation	**Fiber Glass Braid**
Termination Connection Type	**Stripped Leads**
Cable Length	**240" (6 m)**
Wire Gauge	**20 AWG**
+ Lead	**Copper**
- Lead	**Copper-Nickel (Constantan)**

5.3. Data Acquisition Systems

A wide variety of data acquisition systems were used to log data from different sensors used in this study. The data acquisition systems differ in the type, accuracy and frequency of the data measured. The details of the data loggers used and the corresponding sensors from which they record data are presented in Table 5.5.

141

Table 5.5. Characteristics of data acquisition systems.

Data Acquisition System	Sensor logged	Frequency	Accuracy	Stand-alone
Acclima DataSnap	Moisture Sensors	Low (1S/30 min)	Low	Yes
DATAQ Instruments DI-710-ELS	Asphalt Strain Gauge	Low (1S/10 min)	Low	Yes
National Instruments USB-6289	Asphalt Strain Gauge Geophones	High (1kS/s)	High	No
Omega Engineering OM-20A-T	Thermocouple	Medium (1S/2s)	High	Yes

5.3.1. Acclima: DataSnap

The Acclima DataSnap (Figure 5.7) used in this research study offers a low resolution, accuracy and sampling rate for measurement of moisture variations in the subgrade soil. Each DataSnap can accommodate a maximum of 10 SDI-12 sensors capable of acquiring data under regular (PC-connected) and standalone modes. The specifications of the adopted data loggers are listed in Table 5.6.

Figure 5.7. Datasnap SDI-12 data logger.

Table 5.6. Technical specifications of DataSnap SDI-12 data logger.

Parameter	ACC-AGR-D01
Physical Characteristics	
Length	4" (10.3 cm)
Width	1.9" (5 cm)
Height	1.2" (2.75 cm)
Environmental	
Operating Temperature	-20 °C to 60 °C (-4 °F to 140 °F)
Humidity	0 to 90% RH, non-condensing
Electrical	
Input Voltage (USB)	5V DC, ±0.5V
Input Current (USB)	700mA Max.
Input Voltage (External Supply)	6-12V DC, 15V Abs. Max.
Input Voltage (External Supply)	700mA Max.
Connector Type (External Supply)	2.1mm barrel, center positive
Signal Voltage (SDI-12 Output)	Typically 0-5V DC
Power Output Voltage (SDI-12 Output)	Input Voltage – 0.5V
Short Circuit Current (SDI-12 Output)	700mA ±20%

5.3.2. DATAQ Instruments

The DATAQ DI-710-ELS data logger used in this research study offers PC-connected and standalone data acquisition options, with an Ethernet interface and removable storage (SD card) option (Figure 5.8). This data logger is capable of acquiring continuous data from ASG, linear potentiometer and thermocouples. However, as listed in Table 5.5, DI-710-ELS was adopted to measure the permanent strains in the asphalt layer with the aid of a standalone data acquisition option. The specifications of the adopted data logger are presented in Table 5.7.

Figure 5.8. DATAQ DI-710 ELS data logger.

Table 5.7. Specifications of DATAQ DI-710-ELS data logger.

Parameter	DI-710-ELS
Number of Channels	16 SE or 8 DIF
Range	±10V, ±1V, ±100mV, ±10mV
Accuracy	±.05%FSR ±50µV
Resolution	14 bits
Max. Sample Rate	1.2 kS/s
Min. Sample Rate	1S/hr
Memory	2 GB
Interface	Ethernet
Operating Temperature	0 ˚C to 70 ˚C

5.3.3. National Instruments

The National Instruments data acquisition system NI 6289 (Figure 5.9) used offers high resolution, accuracy and a sampling rate for measurement of the elastic response of the ASG and geophones under traffic loading and FWD loading. The characteristics of these data loggers are listed in Table 5.8.

Figure 5.9. NI 6289 data logger.

144

Table 5.8. Characteristics of NI 6289 data logger.

Parameter	NI 6289
Number of Channels	16 DIF or 32 SE
Resolution	18 bits
Max. Sample Rate	31.25kS/s
Range	±0.1 V, ±0.2 V, ±0.5 V, ±1 V, ±2 V, ±5 V, ±10 V
Max. Voltage	±11 V of AI GND
Filter	40 kHz, 750 kHz

5.3.4. Omega Engineering

The Omega Engineering OM-20A-T single-channel thermocouple data logger with LCD display (Figure 5.10) offers PC connection through USB and standalone data acquisition options. They are capable of measuring and storing over 85,000 temperature readings from either Type K, Type J, Type S, Type R or Type T thermocouples. They offer higher resolution, accuracy and a sampling rate as high as 1S/2s for measurement of temperature variations within the asphalt layer at different depths from the surface. The characteristics and specifications of this data logger are as listed in Table 5.9.

Figure 5.10. Omega OM-20A-T thermocouple data logger.

Table 5.9. Characteristics of Omega OM-20A-T data logger.

Parameter	OM-20A-T
Input Type	Thermocouple Types K, J, S, T & R
No. of Channels	Single
Accuracy	±0.5%
Resolution	0.1 °C
Temperature Units	°C or °F
Logging Interval	2 Secs- 24 Hrs.
Memory Capacity	85,000 Points
Thermocouple Connection	Female sub-miniature thermocouple connector
Battery Type	Lithium
Battery Life	Up to 2 years
Operating Temperature	-35 °C to 80 °C

5.4. Power Supply

5.4.1. Solar Panel

Solar panels manufactured by Renogy were installed in the test sections to power the data loggers acquiring data in the SH21 test sections. Figure 5.11 presents a typical 100W 12V monocrystalline solar panel employed in this research study and these solar panels are regarded

as a reliable, durable and versatile source for off-grid applications. The characteristics and specifications of this solar panel are listed in Table 5.10.

Figure 5.11. Renogy 100W 12V monocrystalline solar panel.

Table 5.10. Characteristics of Renogy 100W 12V monocrystalline solar panel.

Parameter	RNG-100D
Electrical Data	
Max Power at STC (P_{max})	100 W
Open-Circuit Voltage (V_{OC})	22.5 V
Optimum Operating Voltage (V_{mp})	18.9 V
Optimum Operating Current (I_{mp})	5.29 A
Short-Circuit Current (I_{sc})	5.75 A
Module Efficiency	15.47%
Max System Voltage	600 VDC (UL)
Max Series Fuse Rating	15 A
Mechanical Data	
Solar Cell Type	Monocrystalline
No. of Cells	36 (4 × 9)
Dimensions	42.2 ×19.6 ×1.38 in.
Weight	7.5 kg/16.5 lbs.
Front Glass	Tempered Glass 0.13 in (32 mm)
Frame	Anodized Aluminum Alloy
Connectors	MC4 Connectors
Thermal Characteristics	
Temp Coefficient of P_{max}	-0.23%/ °C
Temp Coefficient of V_{OC}	-0.33%/ °C
Temp Coefficient of I_{sc}	0.05%/ °C
Operating Module Temperature	-40 °C to 80 °C
Nominal Operating Cell Temperature (NOCT)	47±2 °C
Junction Box	
IP Rating	IP65
Diode Type	HY 10SQ050
No. of Diodes	2
Output Cables	12 AWG (2.10 ft. long)
MC4 Connectors	
Rated Current	30A
Maximum Voltage	1000VDC
Maximum AWG Size Range	10AWG
Temperature Range	-40 °F to 194 °F
IP Rating	IP67

5.4.2. Charge Controller

The charge controller (Figure 5.12) used in this research study is manufactured by Renogy. The main purpose of its inclusion is to control/stabilize the charge rate transferred from the solar

panels to the batteries powering the data acquisition systems and sensors. The characteristics and specifications of the charge controllers are listed in Table 5.11.

Figure 5.12. Renogy 12V 20A charge controller for solar panel.

Table 5.11. Characteristics of Renogy 20A charge controller.

Parameter	RCC20VOYP-G1
Nominal Voltage	12V
Rated Charge Current	20A
Max. PV Input Voltage	55VDC
Self-consumption	0.24W (12V)
Max. PV Power	260W (12V)
Operating Temperature	-24°F to 235°F (-31 °C to 113 °C)
Storage Temperature	-24°F to 333°F (-31 °C to 167 °C)
Enclosure	IP67
Dimensions	6.08×3.83×1.40 in.
Terminals	20-6 AWG, 2 pin connectors
Weight	0.55 lbs.

5.4.3. Battery

The battery used in this research study to store the charge from the solar panels and power the data acquisitions systems and sensors was manufactured by Mighty Max Battery. The ML55-12GEL (Figure 5.13) battery is made with highly absorbent polyester or fiberglass mat separators, also termed Absorbed Glass Mat (AGM) batteries. The characteristics and specifications thereof are listed in Table 5.12.

Figure 5.13. ML55-12GEL replacement battery for Renogy solar panels.

Table 5.12. Characteristics of M replacement battery.

Parameter	ML 55-12GEL
Amp Hour	55Ah
Terminal	Internal Thread
Chemistry	Gel
Volts	12V
Weight	38.58 lbs.
Dimensions	9.02×5.43×9.13 in.

5.5. Installation Protocols

5.5.1. Moisture Sensors

Installation protocols were reviewed based on previous field installation projects. Moisture sensors were installed vertically within a 6-inch-diameter borehole at a depth of 1 to 2 feet in the subgrade layer as shown in Figure 5.14. It can be observed that triplicates of the sensors were installed at the bottom of the 6-inch-diameter borehole for better reliability in the moisture data obtained from each test section/borehole.
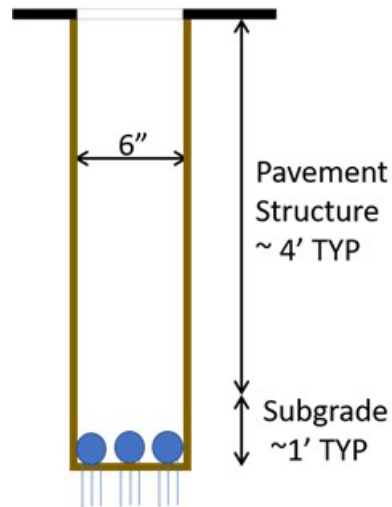
Figure 5.14. Schematic of moisture sensor installation.

The detailed step-by-step procedure followed during moisture sensor installation are as follows:

The locations for the installation of moisture sensors as discussed in Task 2 were marked on the existing road surface.

Asphalt cores were extracted from the existing asphalt surface using a 6-inch core bit at the marked locations. Then, the base, subbase and subgrade material were extruded with a 6-inch continuous flight auger.

The depth of each boring was extended approximately 1 to 2 feet once the subgrade clay material was identified in soil cuttings coming from the boring.

Moisture content samples were collected from the spoils generated from each boring/test section.

Augering was stopped once the required depth was reached and moisture sensors were then installed by inserting each probe vertically into the subgrade soil exposed in the bottom of the borehole.

Each borehole was then backfilled with an 8.5% bentonite-sand mixture to provide a stiff material with low hydraulic conductivity, up to the subbase and native subbase, and base material was backfilled and compacted before compacting the cold patch for the last 6 inches of the borehole.

Sensor cables were routed through saw cuts in the existing pavement and to the data logging enclosures via a trench cut into the shoulder material.

The saw cuts and top portions of each coring were backfilled with cold-patch asphalt once all cable routing was complete.

Figure 5.15 presents photographs summarizing the different stages of moisture sensor installation in the SH21 test sections.

Figure 5.15. Photographs summarizing sequence of moisture sensor installation.

5.5.2. Geophones

Geophones were installed in two different stages, the details of which are as follows:

Installation of 1-C and 3-C geophones in subbase and base layers, respectively

Installation of 1-C and 3-C geophones in preexisting asphalt layers

5.5.2.1. Installation in Subbase and Base Layers

The geophones were installed in the subbase and base layers during moisture sensor installation. Specifically, boreholes drilled for moisture sensor installation in the subgrade soil were used to install the 1-C geophones in the subbase layer (at an approximate depth of 18 inches from the surface) and 3-C geophone in the base layer (at an approximate depth of 10 inches from the surface).

The detailed step-by-step procedure followed during geophone installation in the subbase and base layers is as follows:

> The boreholes excavated for moisture sensor installation were backfilled with an 8.5% bentonite-sand mixture up to the bottom level of the subbase, i.e., 21 inches from the surface layer.

> The native subbase material collected during borehole drilling was filled and compacted up to a height of 3 inches from the bottom of the subbase.

> The 1-C geophone was then installed on the compacted subbase material at a depth of 18 inches from the surface and backfilled with the remaining subbase material up to the bottom of the base layer, namely at a depth of 12 inches from the surface.

> The native base layer material was filled and compacted up to a height of 2 inches from the top of the subbase layer.

> The 3-C geophone was then installed on the compacted base material at a depth of 10 inches from the surface and backfilled with the remaining base material up to a depth of 6 inches from the surface.

> The remaining 6-inch depth was filled by cold patch and compacted up to the level of the existing surface.

> Sensor cables were routed through saw cuts in the existing pavement and to the data logging enclosures via a trench cut into the shoulder material.

> The saw cuts and top portions of each coring were backfilled with cold patch asphalt once all cable routing was complete.

Figure 5.16 presents photographs summarizing the different stages of geophone installation in the base and subbase layers of the SH21 test sections.

Figure 5.16. Photographs summarizing sequence of geophone installation in base and subbase layers.

5.5.2.2. Installation in Existing Asphalt Layer

Additional geophones were installed in the preexisting asphalt layers per the instrumentation layout discussed under Task 2. Specifically, three 1-C geophones and one 3-C geophone were installed at a depth of 4 inches in the preexisting asphalt layer at specific locations.

The detailed step-by-step procedure followed during geophone installation in the existing asphalt layer is as follows:

The locations for the installation of 1-C and 3-C geophones (discussed in Task 2) were marked on the existing asphalt surface.

The locations marked for installation of 1-C and 3-C geophones were cored up to a depth of 4 inches using 3- and 6-inch core bits, respectively.

The bottom of the core was trimmed carefully using a chisel and an asphalt mastic prepared in a 2:1 ratio of sand to CSS-1H binder was applied at the base.

1-C and 3-C geophones were then leveled and installed on the applied asphalt mastic before compacting the rest of the cores with the cold patch.

Sensor cables were routed through saw cuts in the existing pavement and to the data-logging enclosures via a trench cut into the shoulder material.

The saw cuts and top portions of each coring were backfilled with cold patch asphalt once all cable routing was complete.

Figure 5.17 presents photographs summarizing the different stages of geophone installation in the existing asphalt layer in SH21 test sections.

Figure 5.17. Photographs summarizing sequence of geophone installation in asphalt layer.

5.5.3. ASG

The ASG in transverse and longitudinal directions of traffic, along the outer wheel path and middle of the lane, were installed at a depth of 3 inches within the preexisting asphalt layer. The detailed step-by-step procedure followed during ASG installation in the existing asphalt layer is as follows:

The locations for ASG installation (discussed in Task 2) were marked on the existing asphalt surface.

A combination of two 5-inch cores 1 inch apart and a 2-inch-wide slit connecting them was created at the marked locations to install the ASG. The depth of the cores was consistently 3±0.5 inches.

The bottom of the core was trimmed carefully using a chisel and all dust particles were vacuumed out.

An asphalt mastic prepared in a 2:1 ratio of sand to CSS-1H binder was applied at the bottom of the cores and slits.

ASG were then placed on the prepared base so that the two flanges were resting in the cores and the web connecting them was in the slit.

ASG were leveled carefully before filling the rest of the cores with the HMA (Type D mix) used by the contractor for overlay construction.

Sensor cables were routed through saw cuts in the existing pavement and to the data logging enclosures via a trench cut into the shoulder material.

The saw cuts and top portions of each coring were backfilled with the HMA once all cable routing was complete.

Figure 5.18 presents photographs summarizing the different stages of ASG installation in the existing asphalt layer in SH21 test sections.

Figure 5.18. Photographs summarizing sequence of ASG installation in preexisting asphalt layer.

5.5.4. Thermocouples

The thermocouples were installed at three different depths within the existing and new asphalt layers. The adopted installation protocol is as follows.

For the thermocouple at the level of ASG in the preexisting asphalt layer:

1. The exposed end of the thermocouple was tied to the ASG and installed with them.

2. Sensor cable was routed through saw cuts in the existing pavement and to the data logging enclosures via a trench cut into the shoulder material.

For the thermocouple on top of the preexisting asphalt layer:

1. The exposed end of the thermocouple was glued to the existing asphalt layer and HMA was placed on top of it and compacted.

2. Sensor cable was routed through saw cuts in the existing pavement and to the data logging enclosures via a trench cut into the shoulder material.

For the thermocouple on top of the HMA (Type-D) layer:

1. The exposed end of the thermocouple was glued to the top of the Type-D HMA layer and a Thin Overlay Mix (TOM) asphalt layer was then placed on top and compacted.

2. Sensor cable was routed on top of the Type-D HMA layer and to the data logging enclosures via a trench cut into the shoulder material.

5.5.5. Power Supply

The power supply to run the data loggers and sensors to acquire the data continuously under different traffic and weather conditions was provided with the help of solar panels and a 12V 55Ah gel replacement battery. The step-by-step installation protocol adopted is as follows:

1. Poles with a 2-inch inner diameter to mount the solar panels were first installed at about 30 to 40 feet from the edge of the pavement shoulder.

2. The top and bottom mounts to hold the solar panels were pre-assembled in the laboratory and transported to the field, and mounted on the previously installed poles using U-bolts.

3. Solar panels were then placed and firmly fixed between the mounts installed on the poles.

4. Water and dust-proof electrical enclosures were mounted on the same poles at a lower level using U-bolts to house the battery and charge controller.

5. Cables from the solar panel were connected to the battery through a charge controller to control the rate of the power supply from the solar panel to the battery.

6. Power cables from the battery to the data logging enclosures were run through a trench cut into the shoulder material.

Figure 5.19 presents photographs summarizing the different stages of installation of the power supply components in SH21 test sections.

Figure 5.19. Photographs summarizing sequence of installation of power supply components.

5.5.6. Data Logger Enclosures

The data loggers were installed within a three-level enclosure/storage system consisting of an underground concrete enclosure as the outer shell within which a water- and dust-proof polycarbonate enclosure was installed. Separate enclosures were nested inside the polycarbonate enclosure to house the ASG and moisture sensor data loggers. The data loggers were configured into a standalone mode to continuously acquire data from the ASG, thermocouples and moisture sensors installed in the test sections. The data loggers were powered with the help of the battery and solar panel combination discussed under Section 3.5. The step-by-step installation procedure for the data logger enclosures is discussed below:

1. An appropriate location to install the outer underground concrete enclosure was located considering the length of sensor cables.

2. The chosen location was excavated using a mini excavator to fit the underground enclosure. Geonet material was placed inside the excavated pit as a drainage layer before installing the underground enclosure.

3. Holes were drilled in the underground enclosure to accommodate the entry of sensor cables and power cables into the enclosure and data logger boxes.

4. A drain pipe was also installed from the bottom of the underground enclosure to a nearby ditch. The bottom of the underground enclosure was then filled with gravel up to a couple of inches to improve drainage inside the enclosure.

5. Wooden planks were placed on the gravel and polycarbonate enclosures and cable glands to pass sensor cables were installed.

6. Sensor and power cables were then passed through the cable glands of the polycarbonate enclosure into the nested boxes and connected to the data loggers.

7. A plastic container was placed in an inverted position inside the polycarbonate box, covering the nested boxes to protect them in case of flooding.

8. The polycarbonate box was then closed and the underground concrete enclosure was finally closed.

Figure 5.20 presents photographs summarizing the different stages of data logger enclosure installation in SH21 test sections.
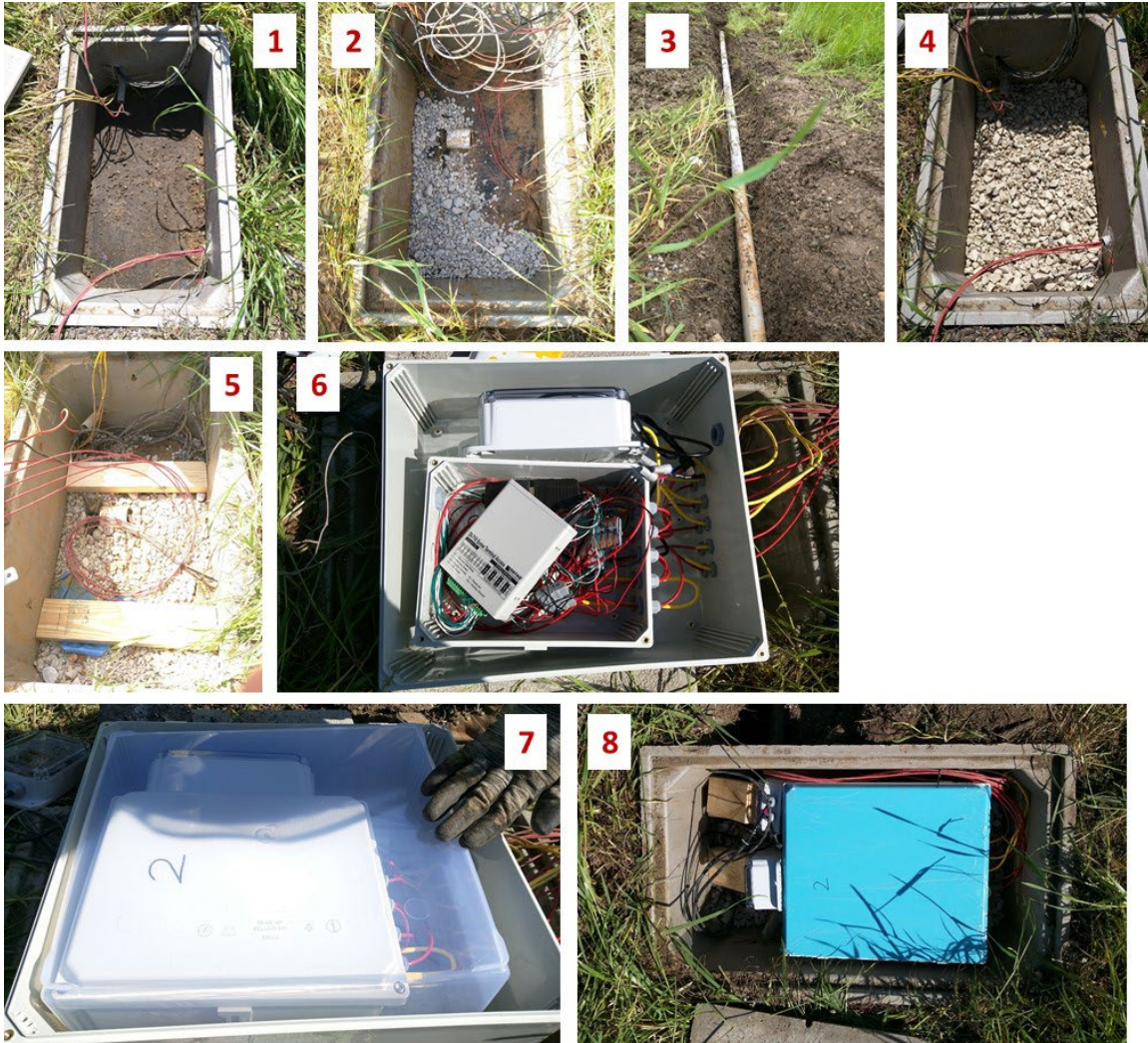
Figure 5.20. Photographs summarizing sequence of installation of data logger enclosures.

5.6. Example Data from Sensors

Constructions of the overlay was closely monitored by UT Austin team members to ensure the installed sensors were not damaged during construction. All sensors were tested after construction was completed, and signals were received and confirmed from various sensors. Data was collected from various sensors under controlled traffic loads in several field loading campaigns conducted after overlay construction. In addition, continuous data recording from moisture sensors was initiated in November 2019. Continuous data recording from ASG and thermocouples was also initiated in March and April 2020.

Figure 5.21 presents example data collected from thermocouples in test Sections 2 and 6. The horizontal axis in this plot corresponds to the time from March 24 to April 17, 2020. The vertical axis shows temperature at various depths of the HMA layer. During the period presented in this

figure, the temperature in the TOM layer ranged from a minimum of 50°F (10°C) to a maximum of 122°F (50°C). For the same period, the temperature in the deeper asphalt layers, including Type D and the old asphalt, ranged from 54°F to 108°F and from 57°F to 104°F, respectively.
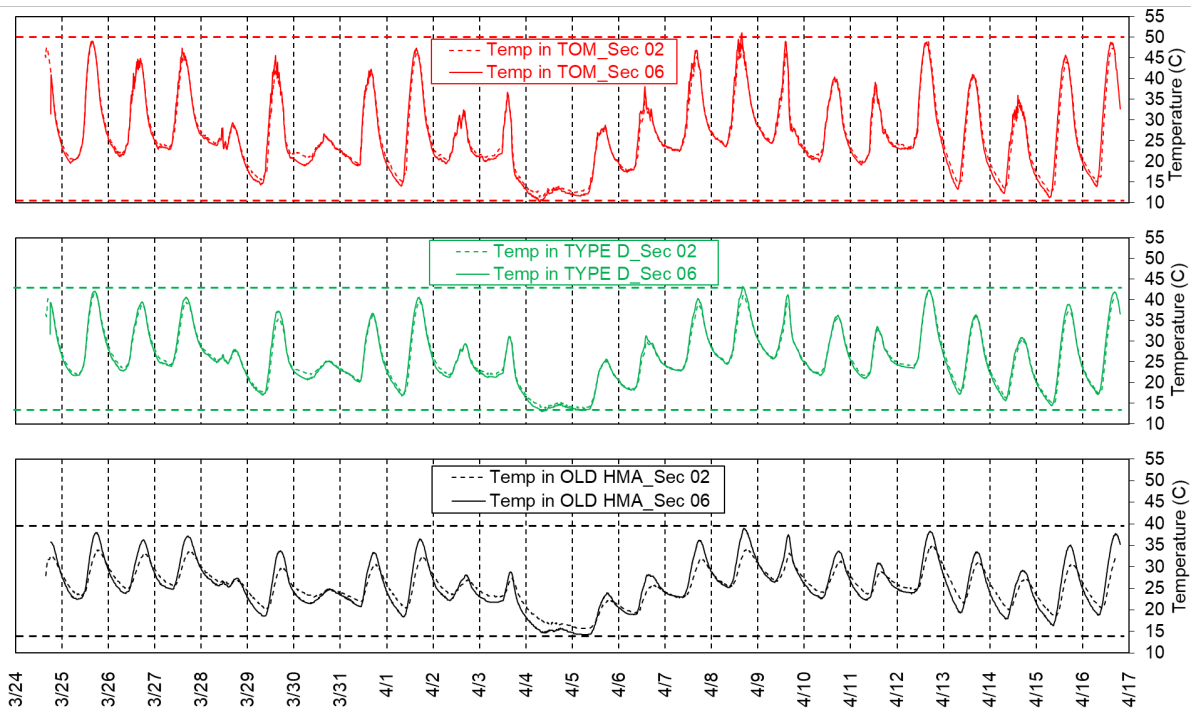
Figure 5.21. Example data from thermocouples in test Sections 2 and 6.

Figure 5.22 shows example data collected from ASG during the same period as the temperature data reported in Figure 5.21. The data in Figure 5.22 corresponds to the sensors installed in test Section 1. The vertical axis in this figure corresponds to the strain in the preexisting asphalt layer. The asphalt strains ranged from approximately -600 micro strain to approximately +600 micro strain. Changes in asphalt strains show a consistent trend with changes in the temperature in the asphalt layers. Thermal strains should be decoupled from this data to obtain the strain developed by the passing traffic.

163
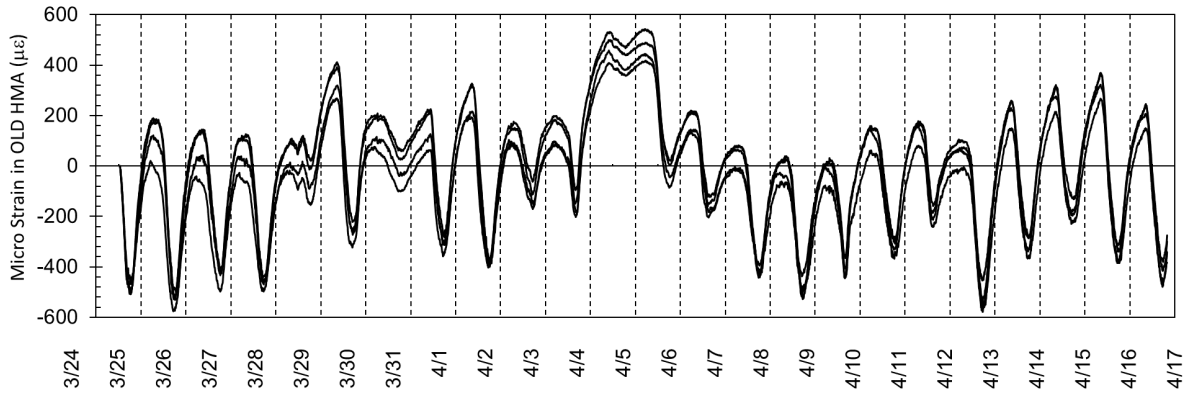
Figure 5.22. Example data from ASG in Section 1.

Lastly, example data from one of the geophones installed in the preexisting asphalt layer in test Section 2 is presented in Figure 5.23. This data corresponds to the controlled traffic loading campaign conducted in December 2019. The horizonal axis in this plot corresponds to the time in seconds and expands from the time before the truck passed over the sensor to after the pass was completed (a total of seven seconds). The vertical axis shows the data recorded by the sensor in volts. The peak data point in this plot corresponds to the moment the truck passed the exact location of the sensor so that the response from the sensor was maximum. The data presented in Figure 5.23 should be analyzed using Fourier transform to obtain the deflection of the pavement layer at the location of this sensor.
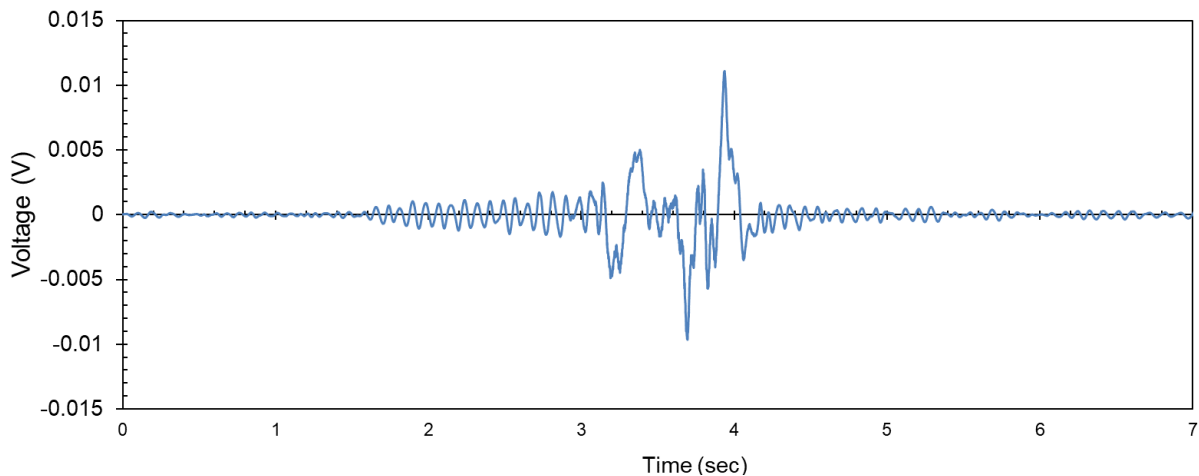
Figure 5.23. Example data from a geophone sensor installed in preexisting asphalt in Section 2.

5.7. Summary & Final Remarks

This chapter focused on various activities completed under Task 4 such as the procurement and installation of various types of sensors, data loggers and power supply components to evaluate the performance of test sections under varying traffic and weather conditions. The specifications

of various sensor types, data loggers and power supply components employed in this research study along with their installation protocols has been summarized in detail. Example initial readings from various sensors were also presented.

Chapter 6. Field Testing During and Immediately after Construction

6.1. Introduction

This chapter reports the activities completed in Task 5 of TxDOT Project 0-7002. The main objective of this task was to conduct field testing during and immediately after asphalt overlay construction in the sensor-instrumented experimental test sections.

A typical cross-section of the SH21 roadway is shown in Figure 6.1 and it can be seen that the preexisting roadway had a six-inch-thick asphalt layer, 15-inch-thick flexible base and subbase layers, and a semi-infinite soil subgrade depth. The rehabilitation program included the application of tack coat, geosynthetic installation and construction of the asphalt overlay. The asphalt overlay was constructed in two lifts that included a two-inch-thick dense graded asphalt mixture referred to as TYPE D overlain by a one-inch-thick wearing course referred to as Thin Overlay Mixture (TOM). Asphalt Strain Gauges (ASG) and other sensors were installed in the preexisting roadway prior to the tack coat application and geosynthetic installation in experimental test sections.

The field-testing campaigns were conducted at three different times: before, during and immediately after overlay construction. The first testing campaign was conducted before the installation of geosynthetics and overlay (i.e., on top of the preexisting asphalt layer) and the responses recorded from the sensor and non-sensor locations were considered to be baseline for future comparisons. Subsequent testing campaigns were conducted during the construction of the overlay, after the construction of the first lift (TYPE D layer) and final lifts of the asphalt overlay (TOM layer).
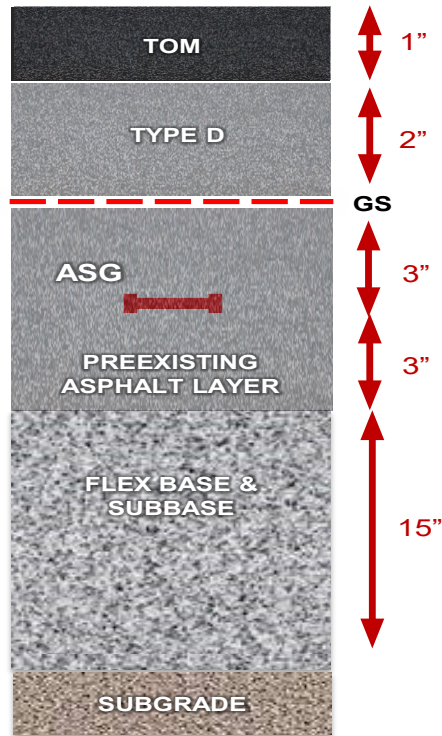
Figure 6.1. Schematic of typical cross-section of SH21 roadway.

This chapter provides specifics of the various field tests conducted before, during and immediately after construction of the asphalt overlay. The following field tests were conducted:

Controlled traffic loading with a heavy truck and light car

Falling Weight Deflectometer (FWD) tests:

At non-sensor locations

At sensor locations

Static Plate Load Tests (sPLT):

On the wheel path at non-sensor locations

On the Transverse Middle (TM) ASG at sensor locations

Light Weight Deflectometer (LWD) tests

Ground Penetrating Radar (GPR) survey of the wheel paths

Total Station Survey of the horizontal profile of the roadway

6.2. Controlled Traffic Loading

The primary objective of the field-testing campaign was to understand the elastic response of the installed sensors under traffic loading. Although the sensors were installed in the expected wheel path, general public traffic is not expected to pass over the exact sensor locations across multiple sections. Because of this spatial variability of the applied traffic load from the sensors, their response is affected depending on whether the applied load is closer to or further away from them. This makes direct comparison of sensor response across different sections difficult since any difference in response could be attributed to the difference in pavement structures across sections or simply difference in location of load application.

To overcome this uncertainty in spatial variability of applied traffic load, the sensor response was recorded under controlled traffic passes with vehicles of known weight. This was accomplished by closing the instrumented test sections for public traffic and using vehicles of known weights to perform traffic passes exactly over the sensors. Figure 6.2 shows the location of the sensors marked using white paint and the wheel path highlighted using blue tape.
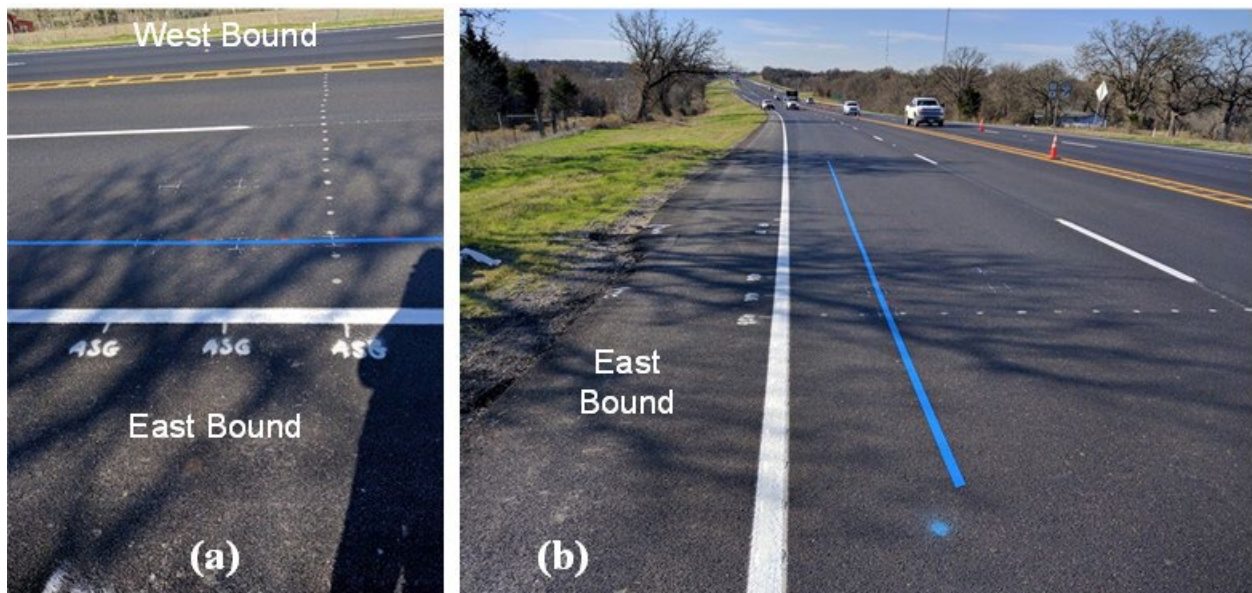
Figure 6.2. (a) Photo showing sensor locations marked in white; and (b) wheel path highlighted in blue to facilitate accurate trafficking of instrumented sections.

The controlled traffic loading was conducted on top of the preexisting asphalt surface (before geosynthetic installation and overlay construction) using a light car provided by UT Austin. The controlled traffic loading conducted on TYPE D and TOM layers (during and immediately after the overlay construction) included two different vehicle classes: a fully-loaded heavy truck provided by TxDOT and a light car provided by UT Austin. The wheel loads from both vehicles

were weighed on the spot using a custom scale designed at UT Austin as shown in Figure 6.3 in addition to the total gross weight measured on a commercial scale.

Figure 6.3. Custom scale used to weigh wheel load of: (a) heavy truck; and (b) light car.

As presented in Figure 6.4 and Figure 6.5, the location of the ASG were first determined on the day of the loading campaign using a handheld GPR. Long blue tape was then attached to the road surface marking the outside wheel path that passes the sensor locations (see Figure 6.5a). The truck and sedan drivers were then requested to drive exactly on the blue tape at a specified speed of approximately 25 mph. GoPro cameras were also installed on the truck to capture the specific path that the front and rear wheel passed as compared to the blue tape (see Figure 6.6); thus, the location of the wheel compared to the sensors' location will be determined. An additional GoPro camera was mounted on the front right side of the car to capture the specific path that the front wheel and possibly rear wheel might have passed compared to the location of the blue tape, hence the location of the wheel compared to the sensors' location will be determined, which will be considered during the analysis of elastic strains under controlled traffic loads.
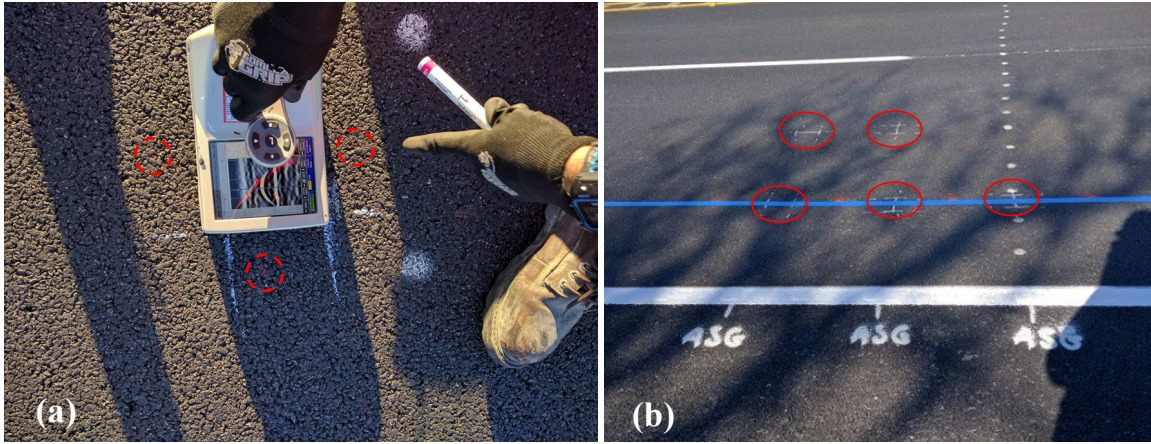
Figure 6.4. Marking ASG locations: (a) handheld GPR; and (b) marked ASG locations.
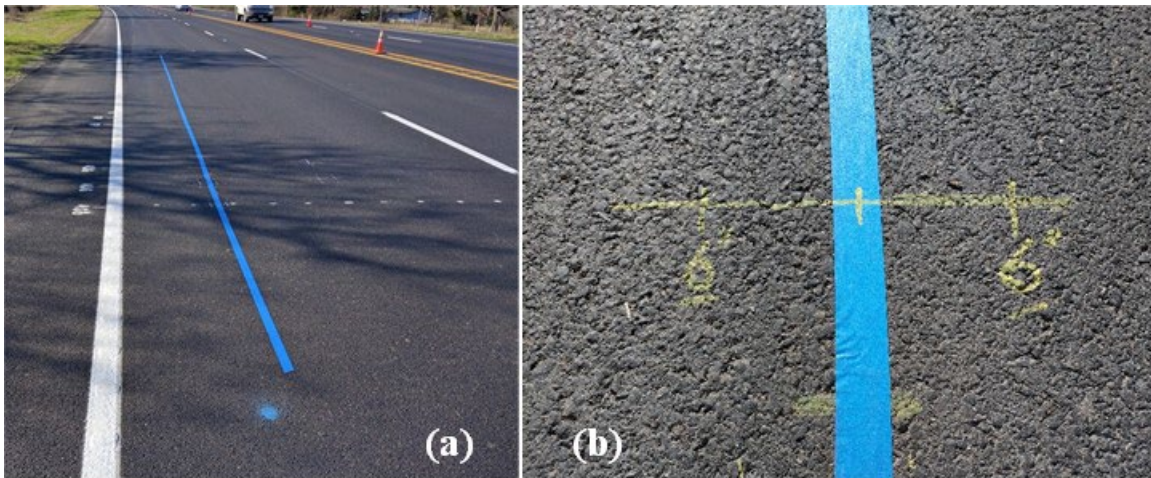
Figure 6.5. (a) Installation of blue tape; and (b) marking wheel path for controlled traffic loading.

Figure 6.6. GoPro cameras mounted to capture front and rear wheel paths.

170

The drivers were asked to drive at least 10 passes on top of the sensors while the data loggers collected the data from ASG and geophones. The data from each pass in each test section was then carefully analyzed. The first step of the analysis was to determine if the pass was accurately on top of the sensors or off. This evaluation was done using the videos captured from the front and rear wheels of the truck. As presented in Figure 6.7, snapshots from the videos at the exact moment when the wheel was passing the sensors' locations were taken for each pass. As an example, Figure 6.7a shows the location of the truck front wheel in Pass 1 in Section 1 compared to the location of the ASG installed in the wheel path along the transverse direction in the center of the test section (ASG-TWPC). Figure 6.7b shows the same but for the ASG installed as the duplicate of ASG-TWPC (i.e., ASG, Transverse Wheel Path Repeat or ASG-TWPR).
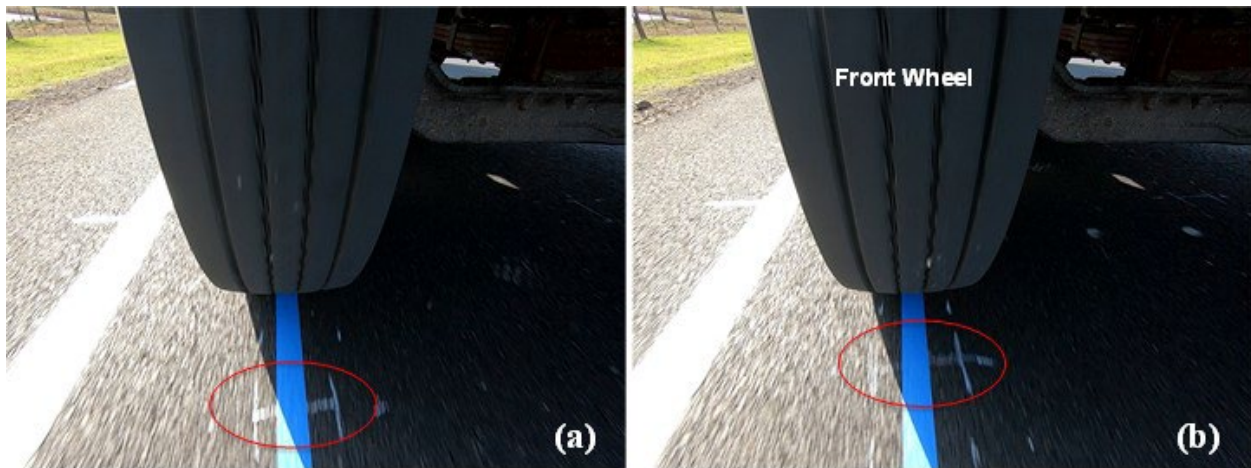
Figure 6.7. Location of truck front wheel relative to ASG in wheel path: a) ASG – transverse wheel path center; and b) ASG – transverse wheel path repeat.

After determining suitability of the traffic pass, the next step of the analysis involved filtering the noise from the data. As an example, for the same pass presented in Figure 6.7a (i.e., Pass 2 of the truck in Section 2), Figure 6.8a and Figure 6.8b show the original (with noise) and filtered (without noise) data, respectively. Fourier transform was used to transfer the original data from the time domain to the frequency domain; then, a low-pass filter was used to filter the frequencies corresponding to the noise, and lastly, the filtered data were transformed back from the frequency domain to the time domain. The peak values in the filtered data indicate the maximum strains induced in the asphalt strain gauge as the truck passed the location of the sensors. In the next step of the analysis, the peak values will be compared among different test sections to evaluate performance of the sections under the same controlled traffic load.
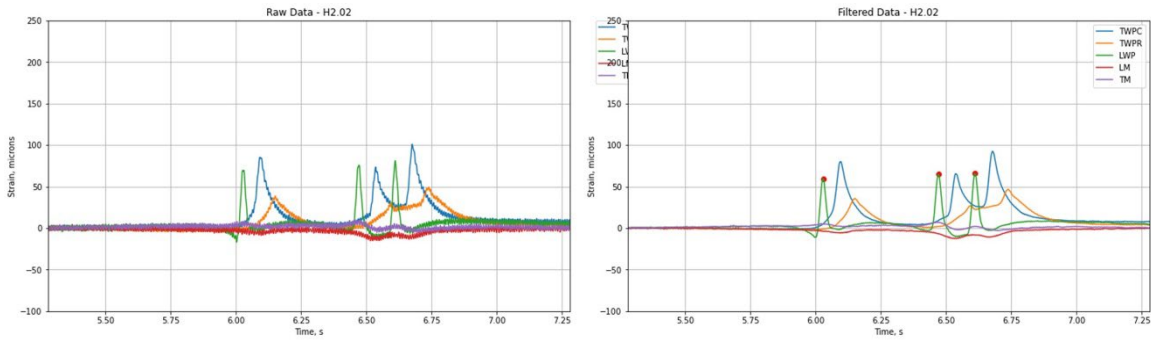
Figure 6.8. Data recorded under controlled heavy traffic by asphalt strain gauges in Pass 2 in test Section 2: a) original data (with noise); and b) filtered data (without noise).

(a)   **(b)**

The sequence of controlled traffic loading conducted before the overlay construction involved trafficking each of the seven instrumented test sections using a light car individually one after the other. While the sequence of controlled traffic loadings conducted during and immediately after the overlay construction involved trafficking the seven instrumented test sections in three different phases (see Figure 6.9), using heavy truck and light car. As shown in the figure, Phase-1 involved trafficking test sections 1-3, while Phase-2 and Phase-3 involved trafficking test sections 4-5 and 6-7, respectively. Trafficking the instrumented test sections in different phases led to a change in the asphalt surface temperature during the trafficking between different test sections. Consequently, a revised traffic loading sequence was developed that involved trafficking test sections 1-4 followed by trafficking test sections 4-7. Test section 4 (a control section) was trafficked during both phases so that the performance of geosynthetic-reinforced sections could be directly compared with that of the control section.
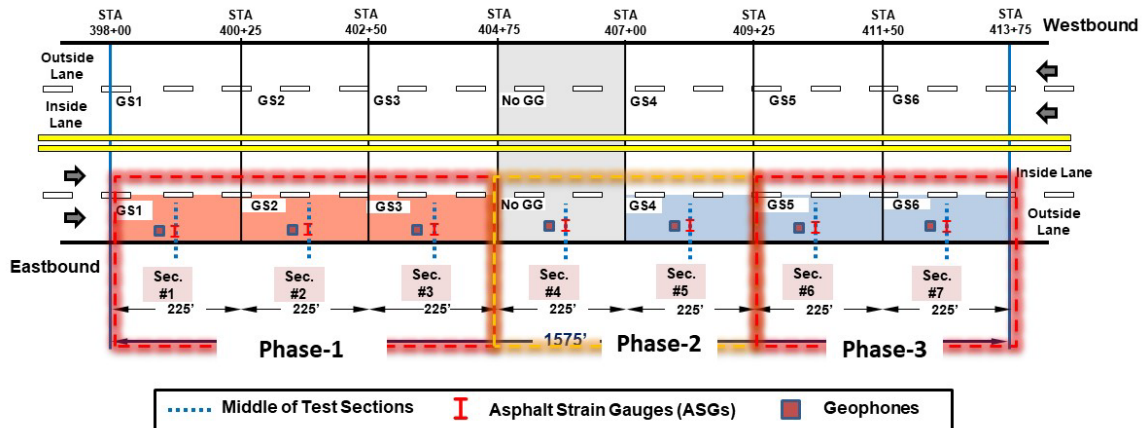
Figure 6.9. Sequence of controlled traffic loading conducted on TYPE D and TOM layers.

172

6.3. Falling Weight Deflectometer (FWD) Tests

The FWD tests were conducted on top of the preexisting asphalt surface (before overlay construction), TYPE D and TOM surfaces (during and after overlay construction) with help from TxDOT Austin District, which provided the FWD equipment. The FWD is a dynamic plate load test used to determine the modulus and thickness of multiple pavement layers. The test involves dropping standard weights from standardized heights (which determines the maximum impulse load) and measuring the applied load and deflection bowl surrounding the point of impact of the load itself (Figure 6.10). From this data, the modulus and thickness of the various bound and unbound layers are back-calculated using Multilayer Linear Elastic Analysis (MLEA). In an FWD test, the loads applied range from 6 kips to 12 kips that result in deflections up to 60 mils. In the instrumented test sections, in addition to collecting data from surface deflection sensors, data was also collected from geophones buried within the pavement section.

The data collected from the FWD tests consisted of: (1) the load from the load cell; (2) the deflection from the surface deflection sensors; and (3) the deflection from buried geophone sensors.
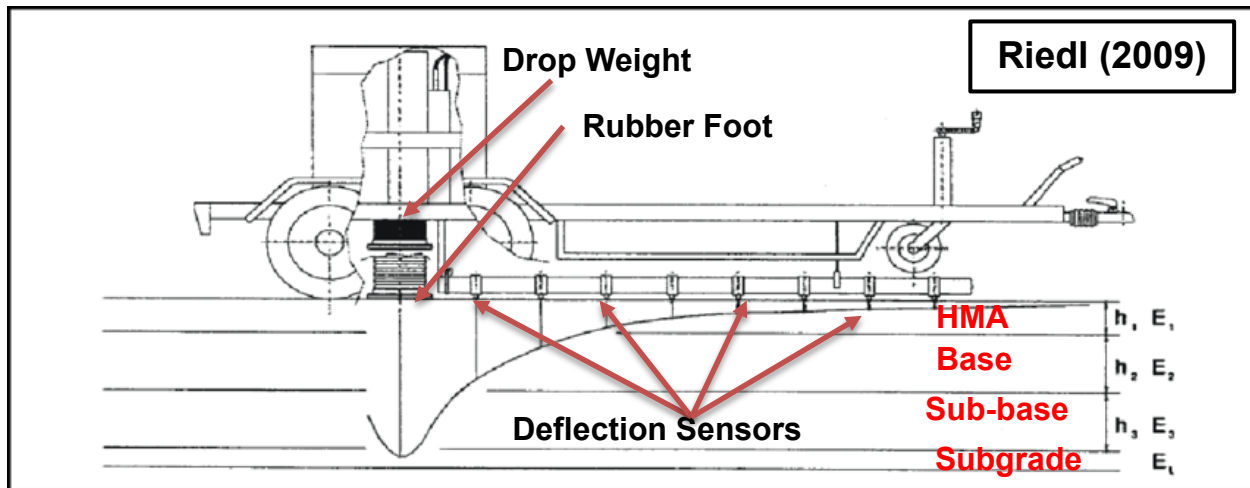
Figure 6.10. Schematic of FWD test.

The test locations for FWD tests are classified into two groups as follows:

Group A: General locations that conform to the philosophy of evenly distributed test locations along the length of test section (see Figure 6.11)

Group B: Sensor-specific locations chosen closer to the location of the ASG and geophones installed within the pavement layers (see Figure 6.12)

The FWD tests were conducted at various locations along the test sections as shown in Figure 6.11. It can be seen from the figure that test locations were distributed more or less evenly along

the length of the test sections to avoid the installed sensor instrumentation. Figure 6.12 shows the various test locations closer to the sensor locations in all seven instrumented test sections. It can be seen that test locations 10 and 12 were exactly on top of the geophone locations. One-component geophones were installed in the subbase and preexisting asphalt layers and three-component geophones in the base layer at location 10. Location 12 had a one-component geophone installed in the preexisting asphalt layer. In addition, multiple locations (11, 13, 15, etc.) between the geophones and ASG were chosen to conduct FWD tests and record the corresponding response from the installed sensors. The general locations provide data relevant to the overall variation of the moduli of pavement layers along the test sections, while the sensor-specific locations allow the measurement of the response of geophones and ASG installed within the pavement layers under FWD loading.

Figure 6.11. Non-sensor locations at which FWD tests were conducted in all seven instrumented test sections.

174
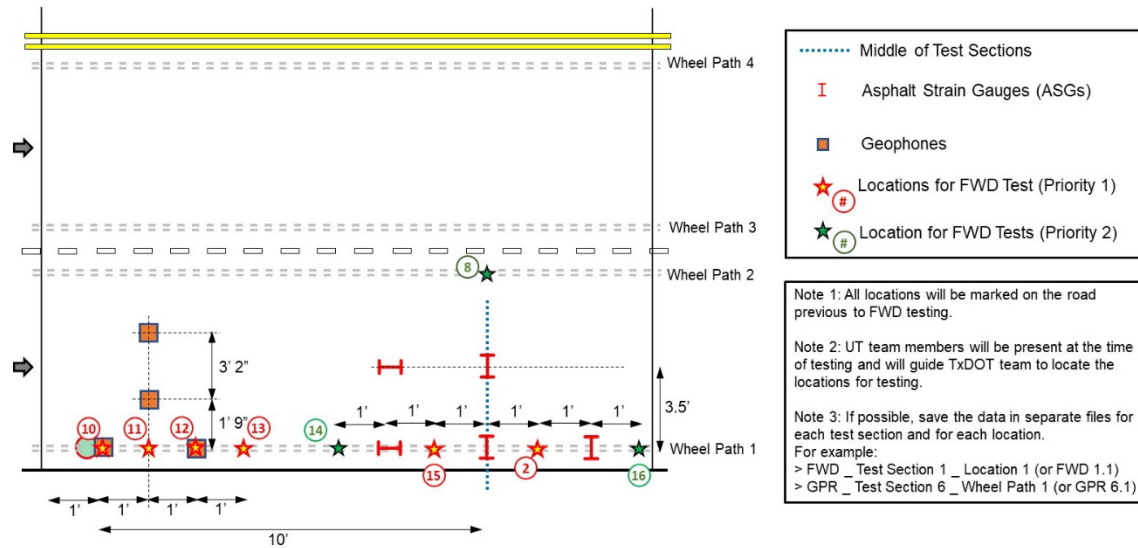
Figure 6.12. Sensor locations at which FWD tests were conducted in all seven instrumented test sections.

6.4. Static Plate Load Test (sPLT)

The Static Plate Load Test (sPLT) was used to assess the bearing capacity of the pavement system before, during and immediately after overlay construction (Figure 6.13). The tests were conducted in conformance with German Standard DIN 18134-2012 (equivalent to ASTM D 1196). The test involves application of loads to a rigid plate 12 inches (300 mm) in diameter. The loads are incremented from 80 kPa to 500 kPa, roughly doubling with each incremental step similar to a consolidation test. The deflection is measured to the nearest 0.2 mm.

Figure 6.13. UT's static plate load test apparatus with loaded truck as reaction.

175

The typical data collected from the test is shown in Figure 6.14. As can be seen, the test involves loading the plate from 80 kPa to the maximum load (blue), unloading back to 80 kPa (brown) and reloading back to 450 kPa (green). This enables the calculation of E_v for both the virgin loading curve (blue) and recompression curve (green) using the equation shown in Figure 6.14. The test subjects the surface to a maximum stress of 500 kPa and up to 5 mm in settlements.

$$E_v = \frac{1.5 r \sigma_{o,max}}{s} = \frac{1.5 r}{a_1 + a_2 \sigma_{o,max}}$$

$y = 8.3891x^2 + 7.5634x + 0.306$

$y = 4.5513x^2 + 2.5099x + 4.4001$
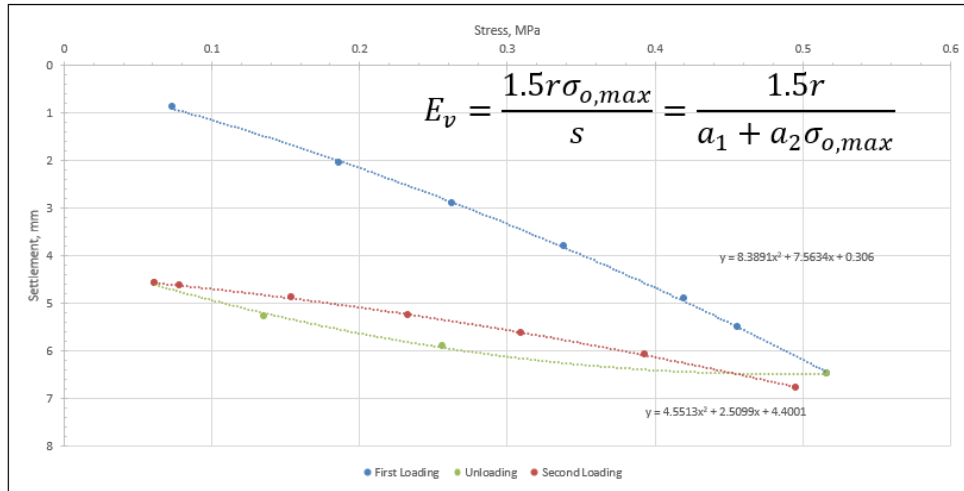
Figure 6.14. Typical test data from static plate load test.

The sPLT were performed at two non-sensor locations in all seven instrumented test sections (Figure 6.11). It can be seen that the FWD tests were conducted along both the inner and outer lanes, while the more intensive tests such as the sPLT were conducted only along the outer wheel path where most of the instrumentation was installed. Another aspect regarding the number of tests conducted is that the FWD tests were conducted at nine different locations in each test section, while sPLT were conducted two per section. This was done to accommodate completion of testing in two days along with the sensor installations as construction could not be held up longer and the sPLT takes about one hour per test to perform.

Additional sPLT were performed on sensor locations, specifically on top of the ASG-TM (Transverse Middle ASG) in all seven instrumented test sections during the field-testing campaigns conducted after the completion of overlay construction (Figure 6.15). The main objective of the sPLT conducted on top of the sensors was to record the asphalt strain response under different stages of sPLT.
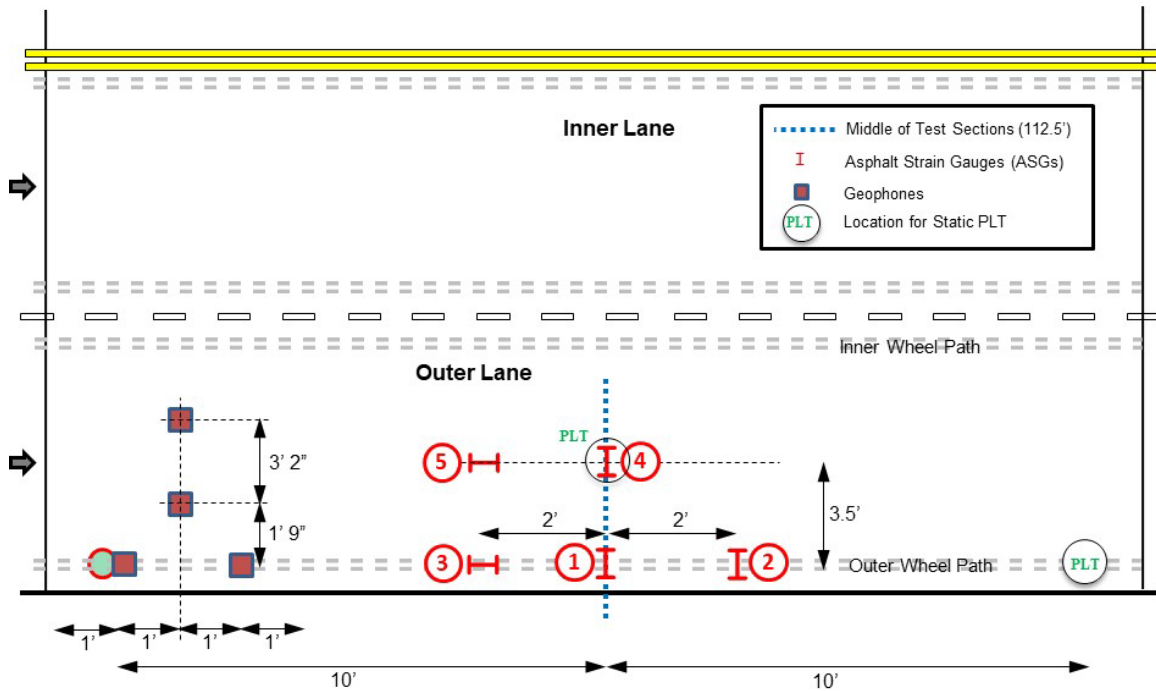
Figure 6.15. Sensor locations at which sPLT were conducted in all seven instrumented test sections.

6.5. Light Weight Deflectometer (LWD) Tests

A Light Weight Deflectometer (LWD) is a portable dynamic plate loading device that measures the in-situ stiffness of compacted earth as well as thin asphalt layers. It is predominantly used in quality control applications similar to a GeoGauge and other non-destructive testing techniques. The LWD uses an impact load (drop weight) similar to the FWD test, while the load intensity in the LWD test is relatively very small compared to that of the FWD test. The LWD applies a load of about 12 psi over a 12-inch-diameter solid plate, while the FWD applies a load of about 6 kips to 12 kips and consequently imparts greater deflections (about 60mils) than the LWD tests.

The apparatus consists of a circular plate at the bottom with a guide rod perpendicular to the plate (Figure 6.16). As shown in the figure, the guide rod guides the drop weight to ensure a vertical fall. Weights are dropped from standardized heights (which depend on the pavement layer being tested and stresses needed). A load cell measures the load pulse as the weight falls on the bottom plate. Geophones are used to measure the deflection of the plate and surrounding surface.

177

Figure 6.16. UT's light weight deflectometer during testing.

The modulus of the layer can be calculated by assuming a constant Poisson's ratio (υ) using the expression:

$$E = \frac{2F_p(1-\vartheta^2)}{w_p A r_o}$$

(1)

where F_p is the peak force applied

υ is the Poisson's ratio

w_p is the peak deflection observed

A is the stress distribution factor (depends on the type of soil and stiffness of plate)

r_o is the radius of the plate

Typical data collected from an LWD test drop include the load pulse and deflection pulse as measured from the load cell and geophones in the system (Figure 6.17).
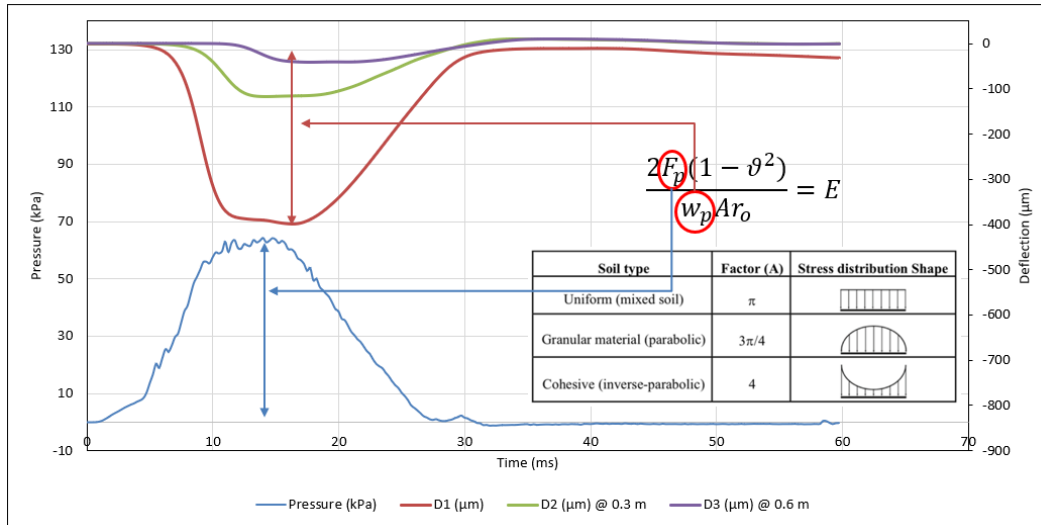
Figure 6.17. Typical data collected from an LWD drop: load pulse, deflection from geophones at center, 300 mm & 600 mm from center.

The LWD test locations were identical to those of non-sensor locations for FWD tests in all test sections (see Figure 6.11). It can be seen from the figure that there were about nine locations at which the FWD and LWD tests were performed, the main objective for such a testing plan being understanding the deflection profile under different intensities of impact loads applied on exactly the same locations. In addition, the test locations were chosen so they conform to the philosophy of evenly distributed test locations along the length of the test section.

6.6. Ground Penetrating Radar (GPR) Surveys

The vehicle-mounted Ground Penetrating Radar (GPR) available at TxDOT Austin was used to profile the left and right wheel paths along the instrumented and non-instrumented test sections (Figure 6.18). As shown in the figure, the right wheel path consisted of the sensor-instrumented locations, while the left wheel path did not include any sensors. The GPR surveys conducted on the sensor and non-sensor locations help verify the location of sensors and thickness of asphalt overlay in the sensor and non-sensor locations.

179
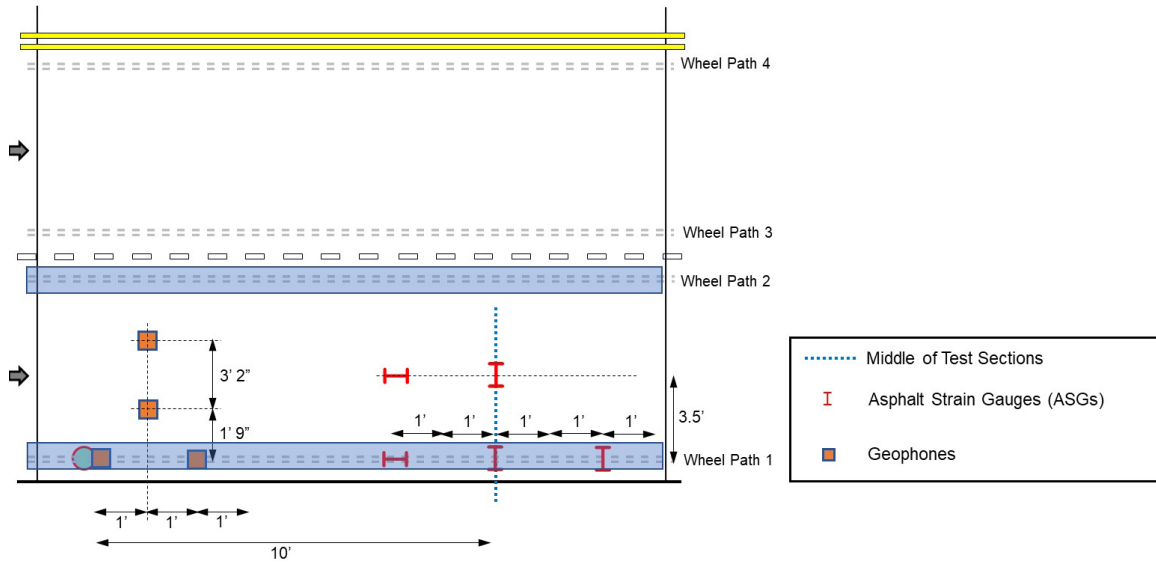
Figure 6.18. GPR surveys conducted on left and right wheel paths in all seven instrumented test sections.

The GPR system consisted of an air-coupled GPR antenna mounted on an extended boom from the front of the vehicle that could swing between the left and right wheel paths. The data from GPR surveys are obtained in the form of a radargram, which is a two-dimensional graphical representation of the length and depths of the test section at any particular wheel path along X and Y directions. The radargrams will be primarily used to access the thickness of the various pavement layers as built and also to qualitatively look at the stiffness of the various layers across test sections, considering both sensor and non-sensor locations.

Figure 6.19 and Figure 6.20 show an example of processed radargrams from Section 2 along the left (non-sensor) and right (sensor) wheel paths of the instrumented test section. It is evident from the figures that a strong sensor reflection can be seen in the processed radargram from the GPR survey conducted on the right wheel path (see Figure 6.20), while the GPR survey conducted on the left wheel path does not show any strong reflections (see Figure 6.19). In addition, there are five reflections in the radargram from the GPR survey conducted on the right wheel path confirming the two geophone locations and three ASG locations along the wheel path.
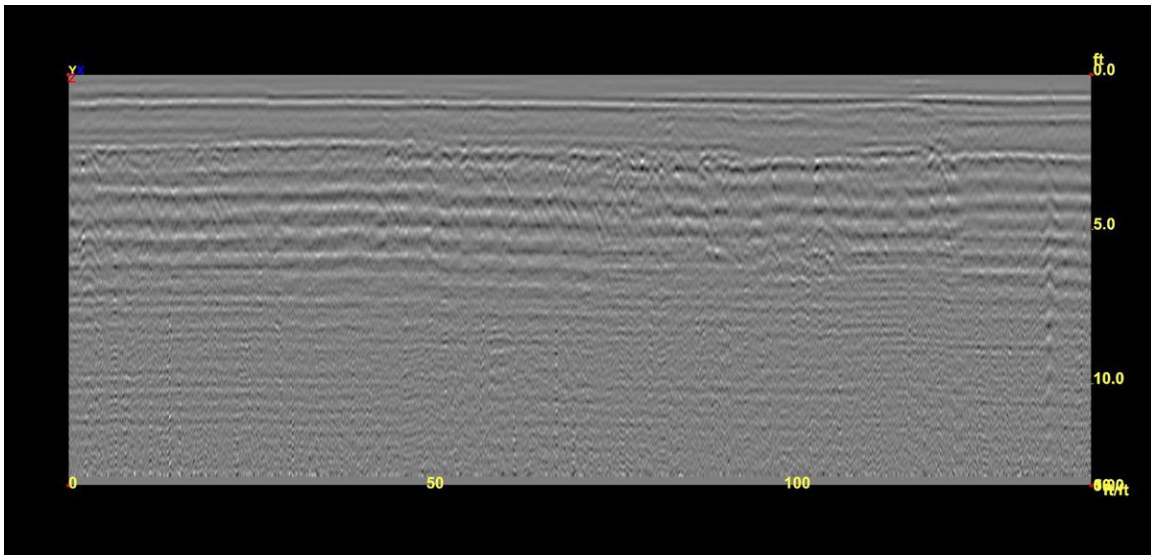
Figure 6.19. Processed radargram from GPR survey conducted on left wheel path of instrumented test Section 2.
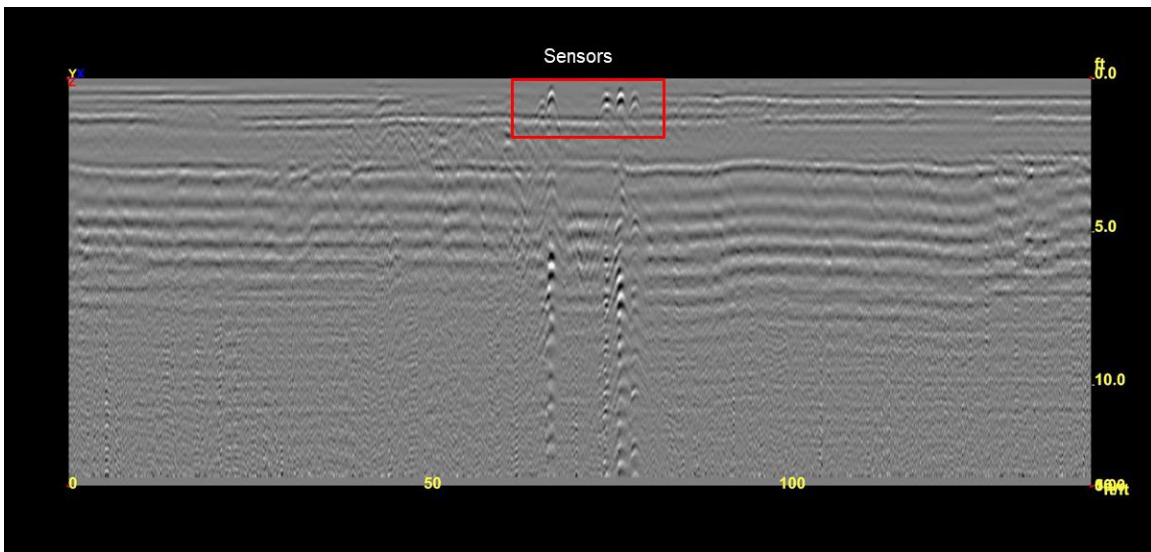
Figure 6.20. Processed radargram from GPR survey conducted on right wheel path of instrumented test Section 2.

6.7. Total Station Survey

The Sokkia Total Station available at UT Austin was used to profile the test sections (see Figure 6.21). A series of survey points, 1foot apart were marked across the cross-section of the test sections as shown in Figure 6.22. This was repeated for each instrumented test section before, during and after overlay construction. A comparison of measurements from the surveys conducted before, during and immediately after overlay construction provides the elevations of those locations and the thickness of each asphalt overlay lift could be estimated. In addition, the

181

measurement after overlay construction forms the baseline against which future measurements will be compared to determine any relative movement of the pavement surface with time.

Figure 6.21. Sokkia Total Station available at UT Austin.

Figure 6.22. (a) Process of marking survey points across the road; and (b) survey points marked on the road (white dots across the road).

6.8. Summary & Final Remarks

This chapter focuses on various activities completed under Task 5, specifically the various field tests conducted before, during and immediately after overlay construction at SH21. The specifications and objectives of various field tests conducted in this research study along with example data obtained and future analysis has been summarized in detail. The field-testing

activity was continued as part of Task 6 (post construction monitoring) with an objective of evaluating the long-term performance of geosynthetic-reinforced sections under controlled traffic and varying environmental loads in comparison with the unreinforced section.

Chapter 7. Post Construction Monitoring

7.1. Introduction

This chapter reports the activities completed in Task 6 of TxDOT Project 0-7002. The main objective of this task was to develop and conduct a post-construction monitoring program of the experimental field test sections at Texas State Highway (SH) 21. The research team conducted field testing activities since the completion of the final lift of the asphalt overlay (i.e., TOM layer). Additionally, the research team proactively developed, revised and refined the protocols relevant to the post-construction monitoring program.

This chapter provides specifics of the various field tests and evaluation activities conducted after construction of the asphalt overlay. Specifically, the following activities were conducted:

Controlled traffic loading with a heavy truck and light car

Falling Weight Deflectometer (FWD) tests:

At non-sensor locations

At sensor locations

Static Plate Load Tests (sPLT):

On wheel path at non-sensor locations

On the Transverse Middle (TM) Asphalt Strain Gauge (ASG) at sensor locations

Light Weight Deflectometer (LWD) tests

Ground Penetrating Radar (GPR) survey of wheel paths

Total Station survey of the horizontal profile of the roadway

Condition survey of the roadway

Long-term roadway performance data collection

Environmental data collection

7.2. Controlled Traffic Loading

The primary objective of the field-testing campaign was to understand the elastic response of the installed sensors under traffic loading. Although the sensors have been installed in the expected

wheel path, general public traffic is not expected to pass over the exact location of sensors across multiple sections. Because of this spatial variability of the applied traffic load from the sensors, their response is affected depending on whether the applied load is closer to or farther away from them. This makes direct comparison of sensor responses across different sections difficult since any difference in response could be attributed to the difference in pavement structures across sections or simply differences in location of load application.

To overcome this uncertainty in spatial variability of applied traffic load, the sensor response was recorded under controlled traffic passes with vehicles of known weight. This was accomplished by closing the instrumented test sections to public traffic and using vehicles of known weight to perform traffic passes exactly over the sensors. Figure 7.1 shows the location of the sensors marked using white paint and the wheel path highlighted using blue tape.
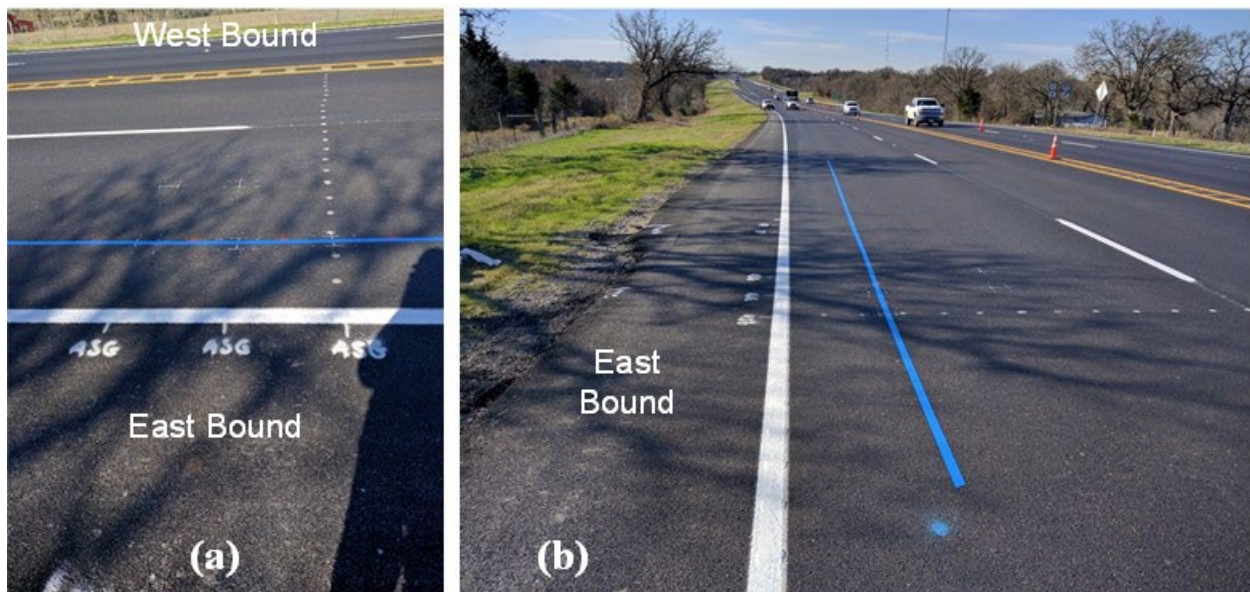
Figure 7.1. (a) Photo showing sensor locations marked in white; and (b) wheel path highlighted in blue to facilitate accurate trafficking of instrumented sections.

The controlled traffic loading was conducted on top of the preexisting asphalt surface (before geosynthetic installation and overlay constructions) using a light car provided by UT Austin. The controlled traffic loading conducted on TYPE D and TOM layers (during and immediately after overlay construction) included two different vehicle classes: a fully-loaded heavy truck provided by TxDOT and light car provided by UT Austin. The wheel load from both vehicles was weighed on the spot using a custom scale designed at UT Austin as shown in Figure 7.2 in addition to the total gross weight measured on a commercial scale.

Figure 7.2. Custom scale used to weigh wheel load of: (a) heavy truck; and (b) light car.

As presented in Figure 7.3 and Figure 7.4, the locations of the ASG were first determined on the day of the loading campaign using a handheld GPR. A long blue tape was then attached to the road surface marking the outside wheel path that passes the sensor locations (see Figure 7.4a). The truck and sedan drivers were then requested to drive exactly on the blue tape at a specified speed of approximately 25 mph. GoPro cameras were also installed on the truck to capture the specific path that the front and rear wheel passed compared to the blue tape (see Figure 7.5); thus, the location of the wheel compared to the sensors' location will be determined. An additional GoPro camera was mounted on the front right side of the car to capture the specific path that the front wheel and possibly rear wheel might have passed compared to the location of the blue tape, hence the location of wheel compared to the sensors' location will be determined, which will be considered during the analysis of elastic strains under controlled traffic loads.
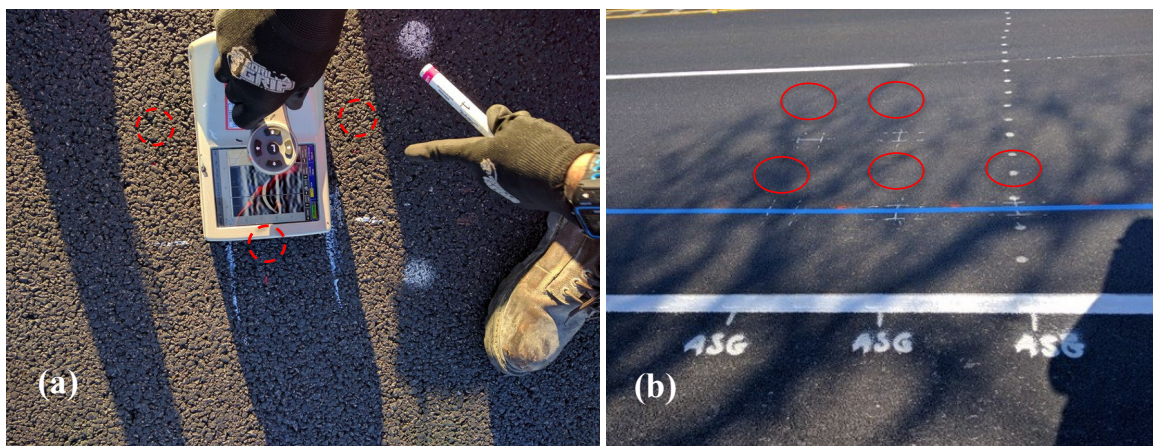
Figure 7.3. Marking ASG locations: (a) handheld GPR; and (b) marked ASG locations.
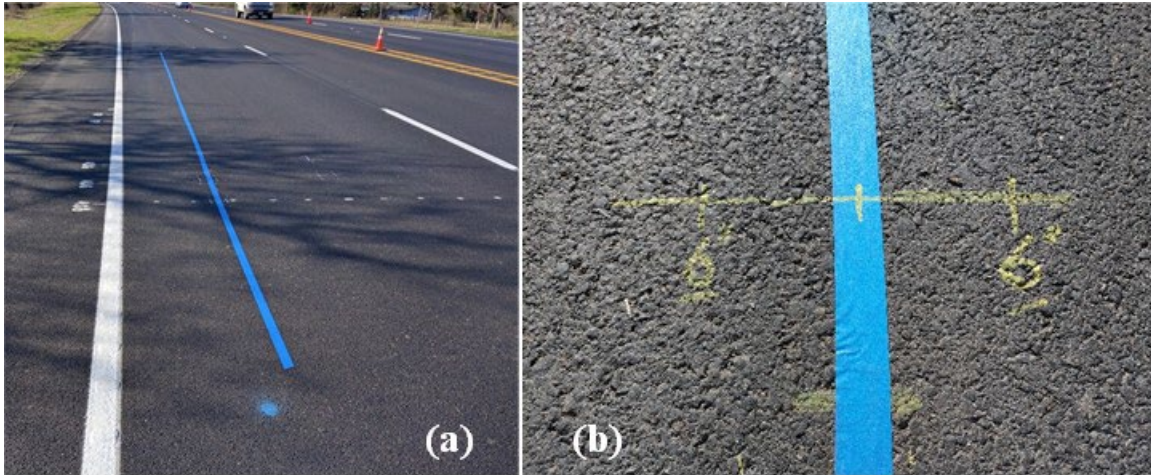
Figure 7.4. (a) Installation of blue tape; and (b) marking wheel path for controlled traffic loading.

Figure 7.5. GoPro cameras mounted to capture front and rear wheel paths.

The drivers were asked to drive at least 10 passes on top of the sensors while the data loggers collected the data from ASG and geophones. The data from each pass in each test section was then carefully analyzed. The first step of the analysis was to determine if the pass was accurately on top of the sensors or off. This evaluation was done using the videos captured from the front and rear wheels of the truck. As presented in Figure 7.6, snapshots from the videos at the exact moment when the wheel was passing the sensors' locations were taken for each pass. As an example, Figure 7.6a shows the location of the truck front wheel in Pass 2 in Section 2 compared to the location of the ASG installed in the wheel path along the transverse direction in the center of the test section (ASG-TWPC). Figure 7.6b shows the same but for the ASG installed as the duplicate of ASG-TWPC (i.e., ASG, Transverse Wheel Path Repeat or ASG-TWPR).
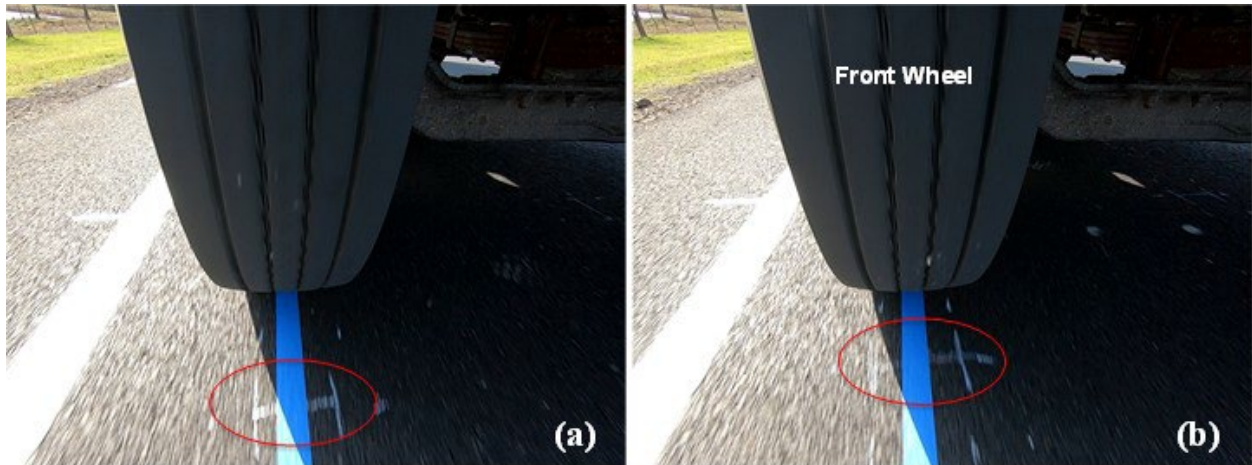
Figure 7.6. Location of truck front wheel relative to ASG in wheel path: a) ASG – Transverse Wheel Path Center; and b) ASG – Transverse Wheel Path Repeat.

After determining the suitability of the traffic pass, the next step of the analysis involved filtering the noise from the data. As an example, for the same pass presented in Figure 7.6a (i.e., Pass 2 of the truck in Section 2), Figure 7.7a and Figure 7.7b show the original (with noise) and filtered (without noise) data, respectively. Fourier transform was used to transfer the original data from the time domain to the frequency domain; then, a low-pass filter was used to filter the frequencies corresponded to the noise; and lastly, the filtered data were transformed back from the frequency domain to the time domain. The peak values in the filtered data indicate the maximum strains induced in the ASG as the truck passed the location of the sensors. In the next step of the analysis, the peak values will be compared among different test sections to evaluate the performance of the sections under the same controlled traffic load.
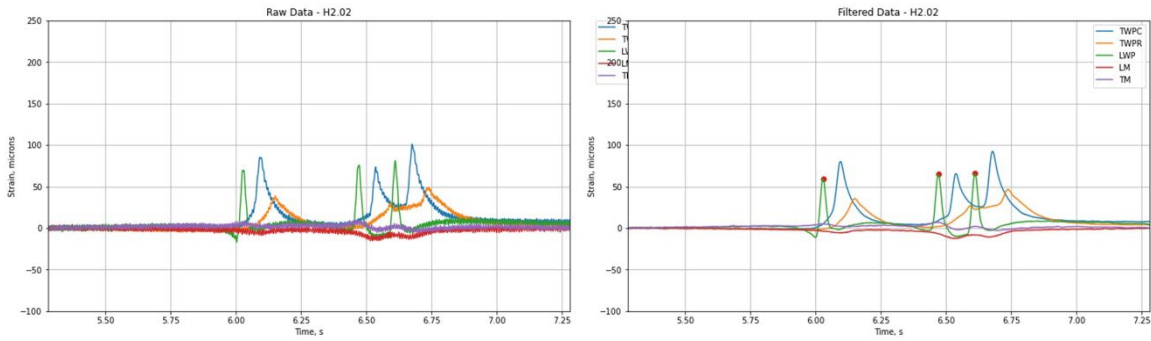
Figure 7.7. Data recorded under controlled heavy traffic by ASG in Pass 2 in test Section 2: a) original data (with noise); and b) filtered data (without noise).

(a) **(b)**

The sequence of controlled traffic loading conducted before overlay construction involved trafficking all seven instrumented test sections individually and sequentially using a light car. The sequence of controlled traffic loadings conducted during and immediately after overlay construction involved trafficking all seven instrumented test sections in three different phases (see Figure 7.8) using a heavy truck and light car. As shown in the figure, Phase-1 involved trafficking test sections 1-3, while Phase-2 and Phase-3 involved trafficking test sections 4-5 and 6-7, respectively. Trafficking the instrumented test sections in different phases led to a change in the asphalt surface temperature during the trafficking between different test sections. Consequently, a revised traffic loading sequence was developed that involved trafficking test sections 1-4 followed by trafficking test sections 4-7. Test section 4 (a control section) was trafficked during both phases so the performance of geosynthetic-reinforced sections could be directly compared with that of the control section.
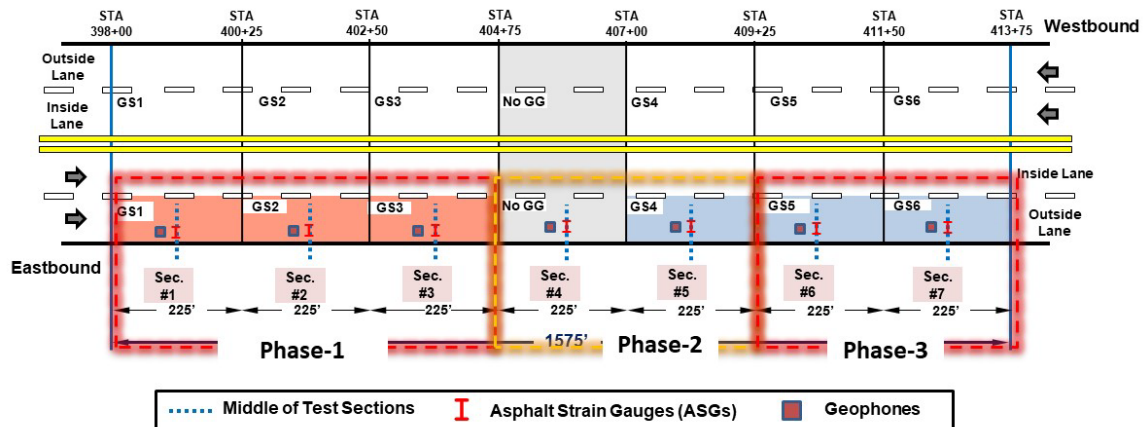
Figure 7.8. Sequence of controlled traffic loading conducted on TYPE D and TOM Layers.

189

7.3. Falling Weight Deflectometer (FWD) Tests

The FWD tests were conducted on top of the preexisting asphalt surface (before overlay construction), TYPE D and TOM surfaces (during and after overlay construction) with help from TxDOT Austin District, which provided the FWD equipment. The FWD is a dynamic plate load test used to determine the modulus and thickness of multiple pavement layers. The test involves dropping standard weights from standardized heights (which determines the maximum impulse load) and measuring the applied load and deflection bowl surrounding the point of impact of the load itself (Figure 7.9). From this data, the modulus and thickness of the various bound and unbound layers are back-calculated using Multi-layer Linear Elastic Analysis (MLEA). In an FWD test, the loads applied range from 6 kips to 12 kips and result in deflections up to 60 mils. In the instrumented test sections, in addition to collecting data from surface deflection sensors, data was also collected from geophones buried within the pavement section.

The data collected from the FWD tests consisted of: (1) the load from load cell; (2) the deflection from surface deflection sensors; and (3) the deflection from buried geophone sensors.
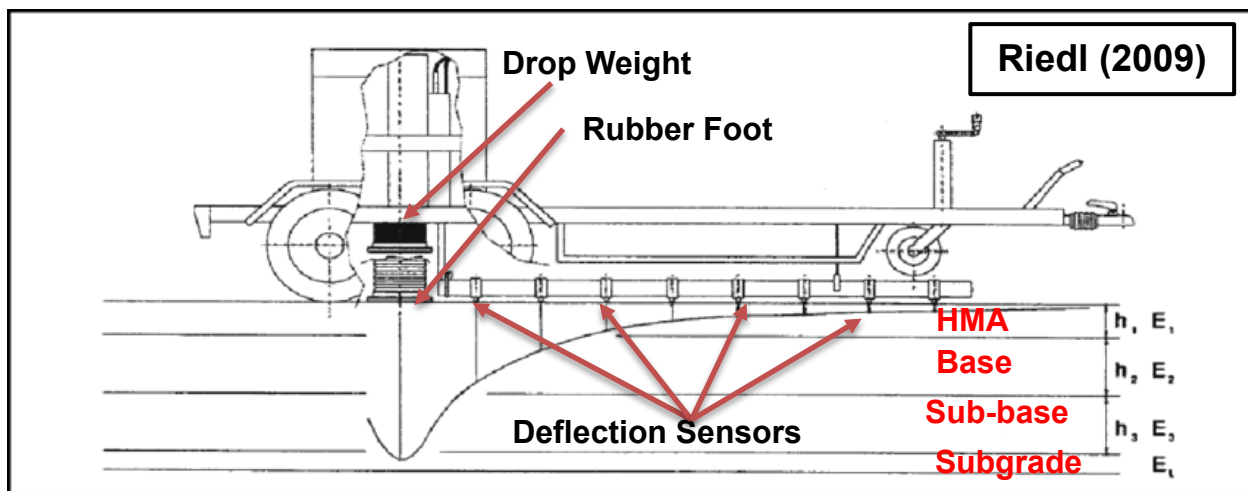
Figure 7.9. Schematic of FWD test.

The test locations for FWD tests are classified into two groups as follows:

Group A: General locations that conform to the philosophy of evenly distributed test locations along the length of the test section (see Figure 7.10)

Group B: Sensor-specific locations chosen closer to the location of the ASG and geophones installed within the pavement layers (see Figure 7.11)

The FWD tests were conducted at various locations along the test sections as shown in Figure 7.10. It can be seen from the figure that test locations were distributed more or less evenly along the length of the test sections to avoid the installed sensor instrumentation. Figure 7.11 shows the

various test locations closer to the sensor locations in all seven instrumented test sections. It can be seen that test locations 10 and 12 were exactly on top of the geophone locations. One-component geophones were installed in the subbase and preexisting asphalt layers and three-component geophones in the base layer at location 10. Location 12 had a one-component geophone installed in the preexisting asphalt layer. In addition, multiple locations (11, 13, 15, etc.) between the geophones and ASG were chosen to conduct FWD tests and record the corresponding response from the installed sensors. The general locations provide data relevant to the overall variation of the moduli of pavement layers along the test sections, while the sensor-specific locations allow the measurement of the response of geophones and ASG installed within the pavement layers under FWD loading.

Figure 7.10. Non-sensor locations at which FWD tests were conducted in all seven instrumented test sections.

191
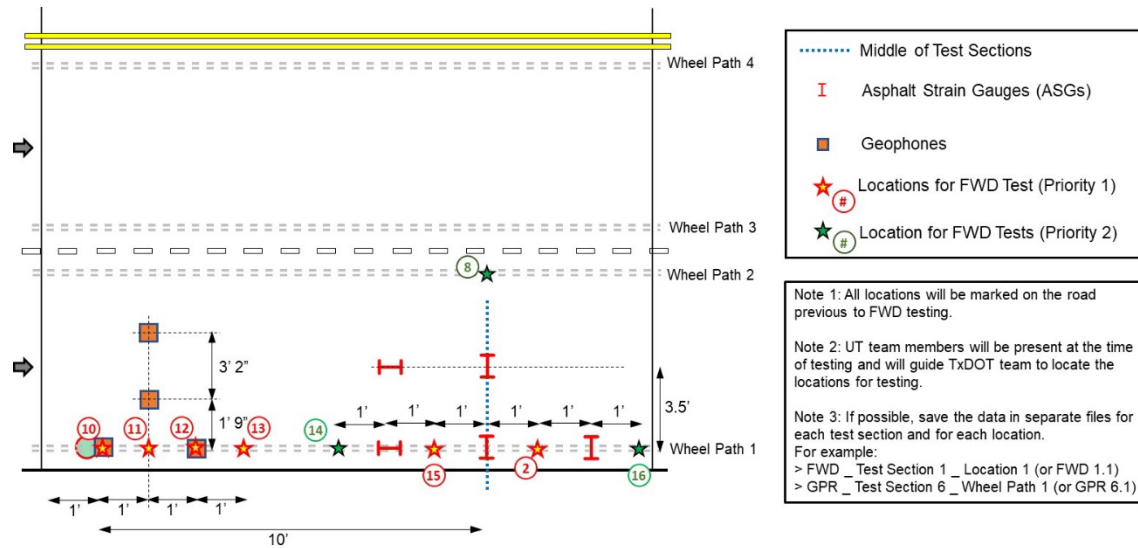
Figure 7.11. Sensor locations at which FWD tests were conducted in all seven instrumented test sections.

7.4. Static Plate Load Test (sPLT)

The Static Plate Load Test (sPLT) was used to assess the bearing capacity of the pavement system before, during and immediately after overlay construction (Figure 7.12). The tests were conducted in conformance with German Standard DIN 18134-2012 (equivalent to ASTM D 1196). The test involves the application of loads to a rigid plate 12 inches (300 mm) in diameter. The loads are incremented from 80 kPa to 500 kPa, roughly doubling with each incremental step similar to a consolidation test. The deflection is measured to the nearest 0.2 mm.

Figure 7.12. UT's static plate load test apparatus with loaded truck as reaction.

192

The typical data collected from the test is shown in Figure 7.13. As can be seen, the test involves loading the plate from 80 kPa to the maximum load (blue), unloading back to 80 kPa (brown) and reloading back to 450 kPa (green). This enables the calculation of E_v for both the virgin loading curve (blue) and recompression curve (green) using the equation shown in Figure 7.13. The test subjects the surface to a maximum stress of 500 kPa and up to 5 mm in settlements.
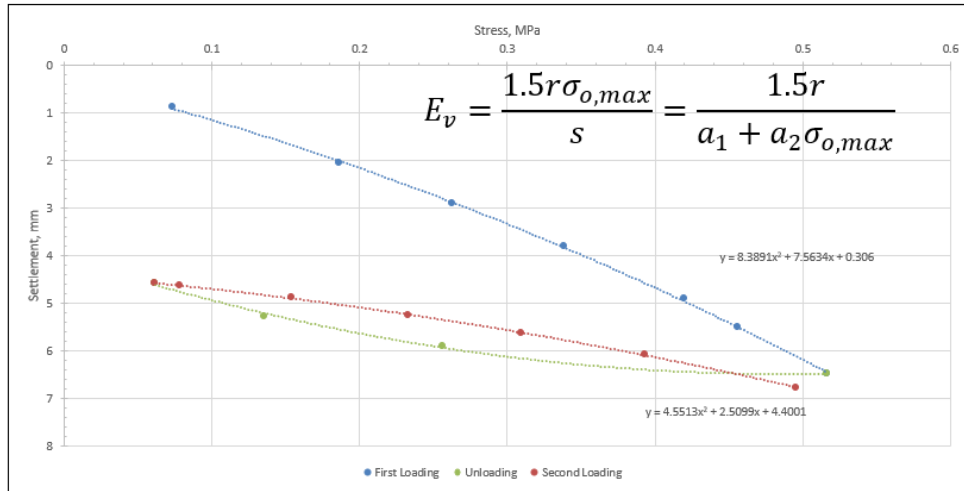
Figure 7.13. Typical test data from static plate load test.

The sPLT were performed at two non-sensor locations in all seven instrumented test sections (Figure 7.10). It can be seen that the FWD tests were conducted along both the inner and outer lanes, while the more intensive tests such as the sPLT were conducted only along the outer wheel path where most of the instrumentation was installed. Another aspect regarding the number of tests conducted is that the FWD tests were conducted at nine different locations in each test section while sPLT were conducted two per section. This was done to accommodate completion of testing in two days along with the sensor installations as construction could not be held up longer and the sPLT takes about one hour per test to perform.

Additional sPLT were performed on sensor locations, specifically on top of the ASG-TM (Transverse Middle ASG) in all seven instrumented test sections during the field-testing campaigns conducted after the completion of overlay construction (Figure 7.14). The main objective of the sPLT conducted on top of the sensors was to record the asphalt strain response under different stages of sPLT.
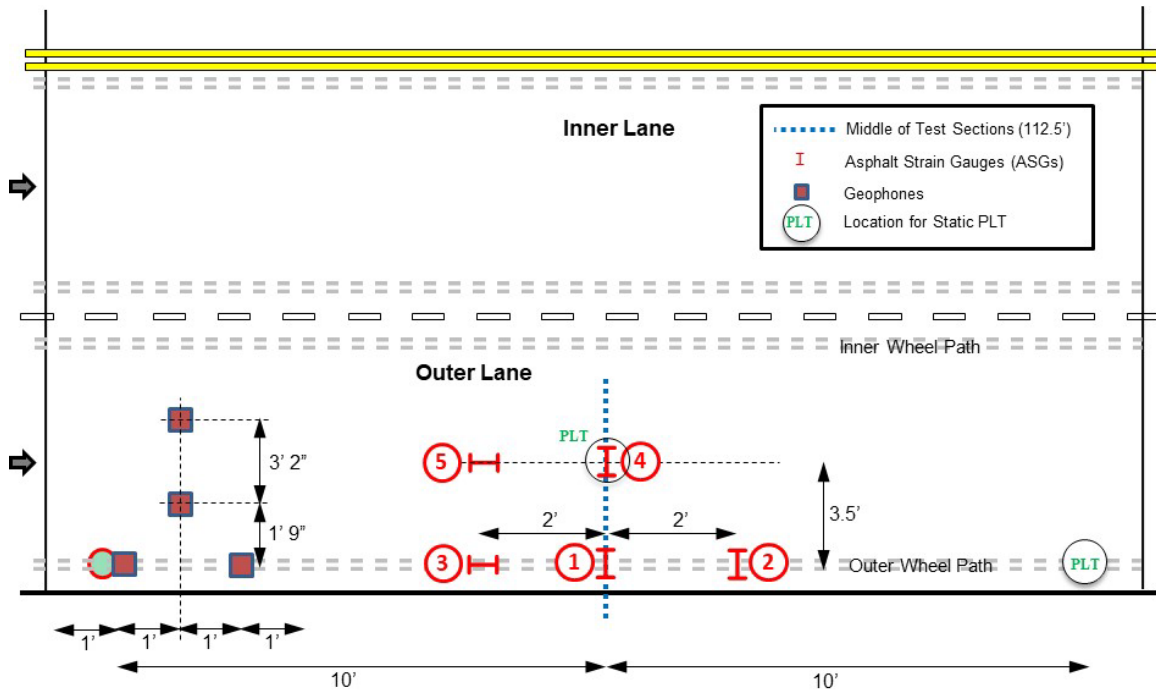
Figure 7.14. Sensor locations at which sPLT were conducted in all seven instrumented test sections.

7.5. Light Weight Deflectometer (LWD) Tests

A Light Weight Deflectometer (LWD) is a portable dynamic plate loading device that measures the in-situ stiffness of compacted earth as well as thin asphalt layers. It is predominantly used in quality control applications similar to a GeoGauge and other non-destructive testing techniques. The LWD uses an impact load (drop weight) similar to the FWD test, while the load intensity in the LWD test is relatively very small compared to that of the FWD test. The LWD applies a load of about 12 psi over a 12-inch-diameter solid plate, while the FWD applies a load of about 6kips to 12 kips and consequently imparts greater deflection (about 60mils) than the LWD tests.

The apparatus consists of a circular plate at the bottom with a guide rod perpendicular to the plate (Figure 7.15). As shown in the figure, the guide rod guides the drop weight to ensure a vertical fall. Weights are dropped from standardized heights (which depend on the pavement layer being tested and stresses needed). A load cell measures the load pulse as the weight falls on the bottom plate. Geophones are used to measure the deflection of the plate and the surrounding surface.

194

Figure 7.15. UT's light weight deflectometer during testing.

The modulus of the layer can be calculated by assuming a constant Poisson's ratio (υ) using the expression:

$$E = \frac{2F_p(1-\vartheta^2)}{w_p A r_o}$$

(1)

where F_p is the peak force applied

       υ is the Poisson's ratio

       w_p is the peak deflection observed

       A is the stress distribution factor (depends on the type of soil and stiffness of the plate)

       r_o is the radius of the plate

Typical data collected from an LWD test drop includes the load pulse and deflection pulse as measured from the load cell and geophones in the system (Figure 7.16).
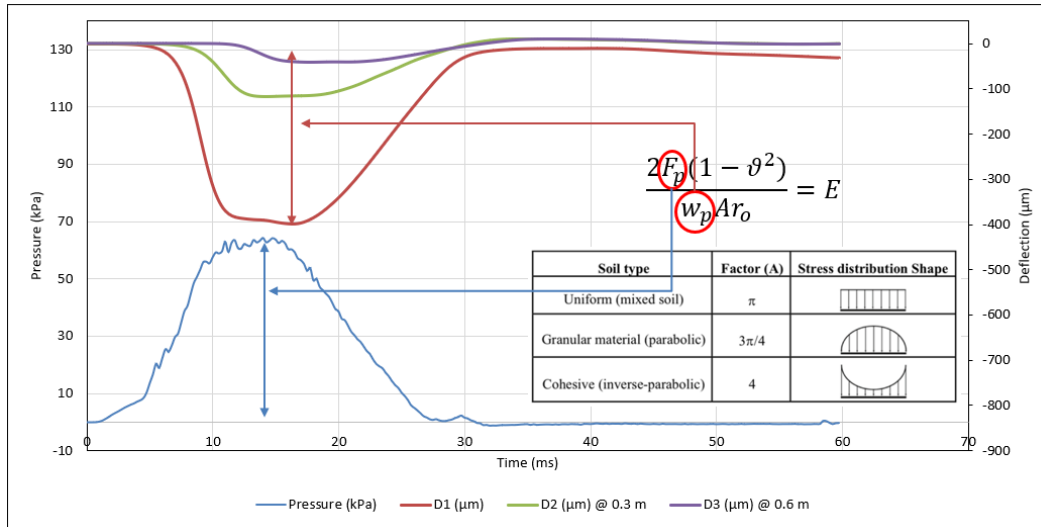
Figure 7.16. Typical data collected from an LWD Drop: load pulse, deflection from geophones at center, 300 mm & 600 mm from center.

The LWD test locations were identical to those of non-sensor locations for FWD tests in all test sections (see Figure 7.10). It can be seen from the figure that there were about nine locations at which the FWD and LWD tests were performed, the main objective for such a testing plan being understanding the deflection profile under different intensities of impact loads applied on exactly the same locations. In addition, the test locations were chosen to conform to the philosophy of evenly distributed test locations along the length of the test section.

7.6. Ground Penetrating Radar (GPR) Surveys

The vehicle mounted Ground Penetrating Radar (GPR) available at TxDOT Austin was used to profile the left and right wheel paths along the instrumented and non-instrumented test sections (Figure 7.17). As shown in the figure, the right wheel path consisted of the sensor-instrumented locations, while the left wheel path did not include any sensors. The GPR surveys conducted on the sensor and non-sensor locations help verify the location of sensors and thickness of the asphalt overlay in the sensor and non-sensor locations.
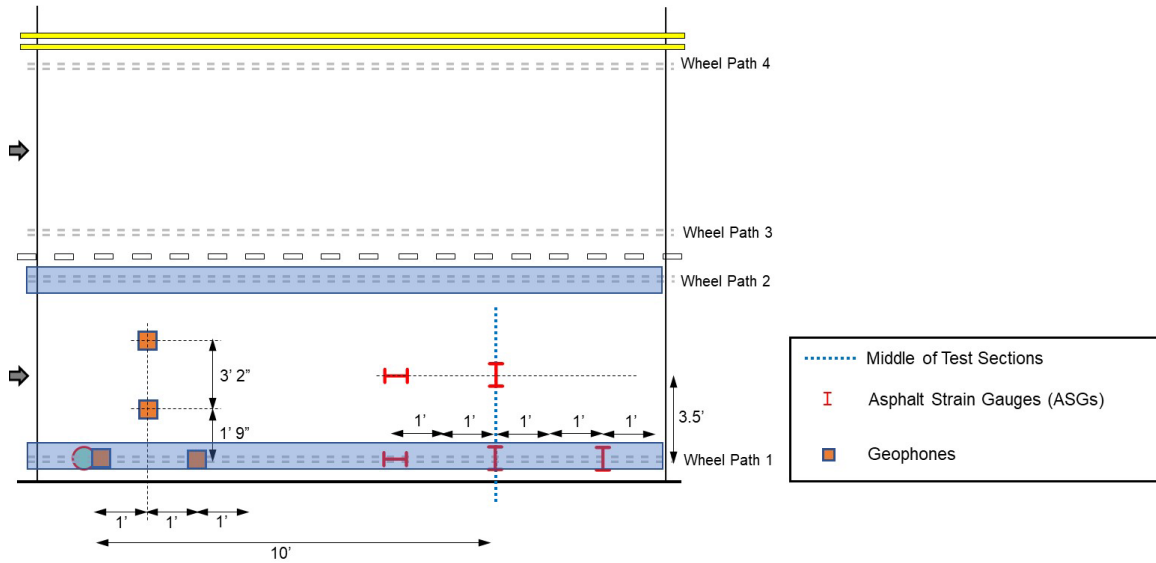
Figure 7.17. GPR surveys conducted on left and right wheel paths in all seven instrumented test sections.

The GPR system consisted of an air-coupled GPR antenna mounted on an extended boom from the front of the vehicle that could swing between the left and right wheel paths. The data from GPR surveys are obtained in the form of a radargram, which is a two-dimensional graphical representation of the length and depths of the test section at any particular wheel path along X and Y directions. The radargrams will be primarily used to access the thickness of the various pavement layers as built and also to qualitatively look at the stiffness of the various layers across the test sections, considering both sensor and non-sensor locations.

Figure 7.18 and Figure 7.19 show an example of processed radargrams from Section 2 along the left (non-sensor) and right (sensor) wheel paths of the instrumented test section. It is evident from the figures that a strong sensor reflection can be seen in the processed radargram from the GPR survey conducted on the right wheel path (see Figure 7.19) while the GPR survey conducted on the left wheel path does not show any strong reflections (see Figure 7.18). In addition, there are five reflections in the radargram from the GPR survey conducted on the right wheel path, confirming the two geophone locations and three ASG locations along the wheel path.

197
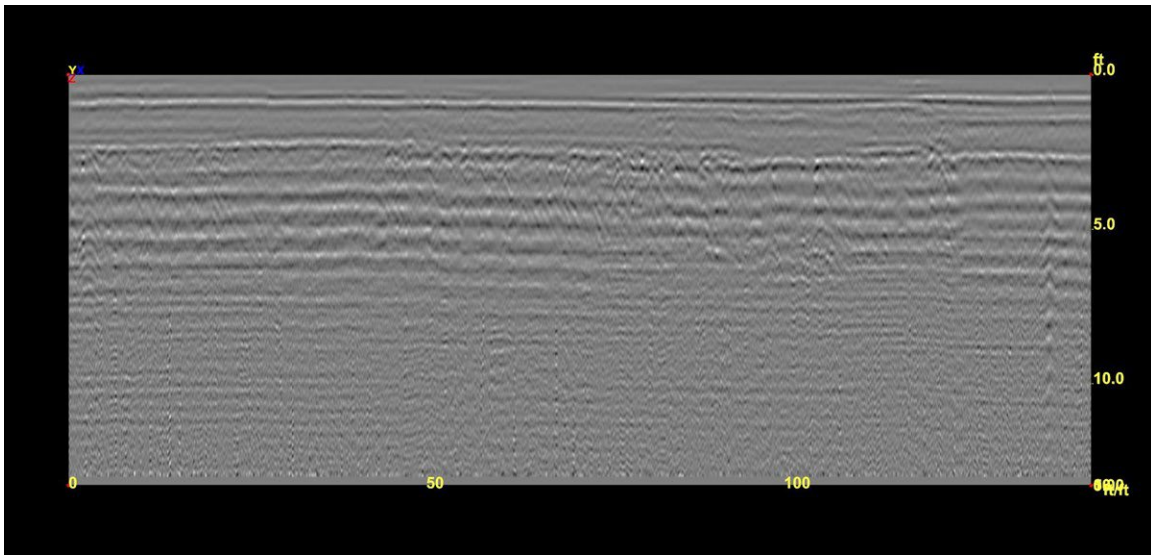
Figure 7.18. Processed radargram from GPR survey conducted on left wheel path of instrumented test Section 2.
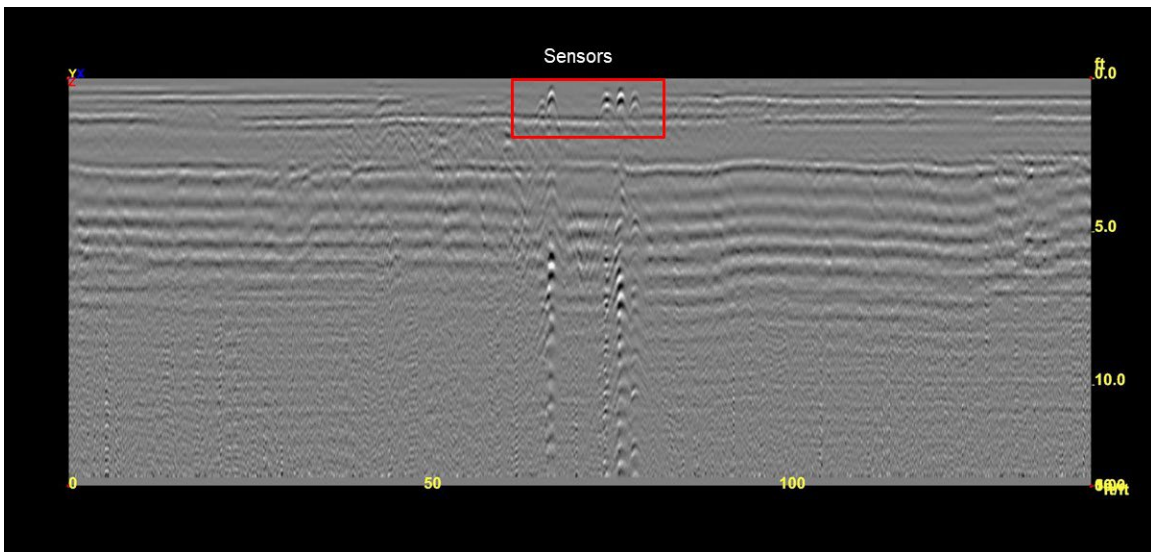
Figure 7.19. Processed radargram from GPR survey conducted on right wheel path of instrumented test Section 2.

7.7. Total Station Survey

The Sokkia Total Station available at UT Austin was used to profile the test sections (see Figure 7.20). A series of survey points 1 foot apart were marked across the cross-section of the test sections as shown in Figure 7.21. This was repeated for each instrumented test section before, during and after overlay construction. A comparison of measurements from the surveys conducted before, during and immediately after overlay construction provides the elevations of those locations and the thickness of each asphalt overlay lift could be estimated. In addition, the

198

measurement after overlay construction forms the baseline against which future measurements will be compared to determine any relative movement of the pavement surface with time.

Figure 7.20. Sokkia Total Station available at UT Austin.

Figure 7.21. (a) Process of marking survey points across road; and (b) survey points marked on road (white dots across road).

7.8. Condition Survey of the Roadway

- Protocols to conduct visual condition surveys and document surface distresses were developed, revised and refined as needed.

- A visual condition survey of the existing road before reconstruction was conducted to establish a basis for future comparison among the performance of the test sections.

- No substantial differences in surface conditions were observed between the unreinforced and geosynthetic-reinforced sections.

7.9. Long-term Roadway Performance Data Collection

- As previously mentioned, the data acquisition system for most of the installed sensors operate from an AC/DC power supply. UT Austin completed the installation of all data acquisition systems for all sensors by November 2019. While the initial signal was confirmed and example data were collected from all sensors, continuous collection of data was not possible from most of the sensors because of flooding issues in the data logger housing. This was rectified and resolved in March-April 2020, however the activities had to be stopped for a period because of COVID-19 travel restrictions. Thus, data from all sensors were collected since the beginning of summer 2020.

- The data logging system for moisture sensors installed in the subgrade were installed as early as July 2019 right after installation. Hence logging of data was started as soon the installation of the DAQs for these sensors was completed.

7.10. Environmental Data Collection

- Environmental data, including precipitation, temperature and relative humidity data was collected from a nearby weather station.

- Data collection began at the time of construction and was continued throughout the project construction time until the completion of the project.

7.11. Summary & Final Remarks

This chapter focused on various activities completed under Task 6, specifically the various field tests and evaluation activities conducted after asphalt overlay construction at SH21. The specifications and objectives of various field tests and evaluations conducted in this research study has been summarized in detail.

Chapter 8. Synthesis and Analysis of Data

8.1. Introduction

This chapter reports the activities completed in Task 7 of TxDOT Project 0-7002. The main objective of this task was to synthesize, analyze and interpret the data collected in Tasks 3 through 6 to understand the performance of various sections under public and controlled traffic loads as well as the performance under environmental loads. This chapter provides specifics of the various factors influencing the performance of geosynthetic-reinforced asphalt and eventually the development of design charts for geosynthetic-reinforced asphalt layers.

8.2. Controlled Traffic Loading

The controlled traffic loading was conducted on top of the preexisting asphalt surface (before geosynthetic installation and overlay constructions) using a light car provided by UT Austin. The controlled traffic loading conducted on TYPE D (TYD) and TOM layers (during and immediately after overlay construction) included two different vehicle classes: a fully-loaded heavy truck provided by TxDOT and light car provided by UT Austin. The wheel load from both vehicles was weighed on the spot using a custom scale designed at UT Austin as shown in Figure 8.1 in addition to the total gross weight measured on a commercial scale.

(a)   (b)

Figure 8.1. Custom scale used to weigh wheel load of: (a) heavy truck; and (b) light car.

As presented in Figure 8.2 and Figure 8.3, the locations of the Asphalt Strain Gauges (ASG) were first determined on the day of the loading campaign using a handheld Ground Penetrating Radar (GPR). A long blue tape was then attached to the road surface marking the outside wheel path that passes the sensor locations (see Figure 8.3a). The truck and sedan drivers were then requested to drive exactly on the blue tape at a specified speed of approximately 25 mph. GoPro

cameras were also installed on the truck to capture the specific path that the front and rear wheel passed compared to the blue tape (see Figure 8.4); thus, the location of the wheel compared to the sensors' location will be determined. An additional GoPro camera was mounted on the front right side of the car to capture the specific path that the front wheel and possibly rear wheel might have passed compared to the location of the blue tape, hence the location of wheel compared to the sensors' location will be determined, which will be considered during the analysis of elastic strains under controlled traffic loads.
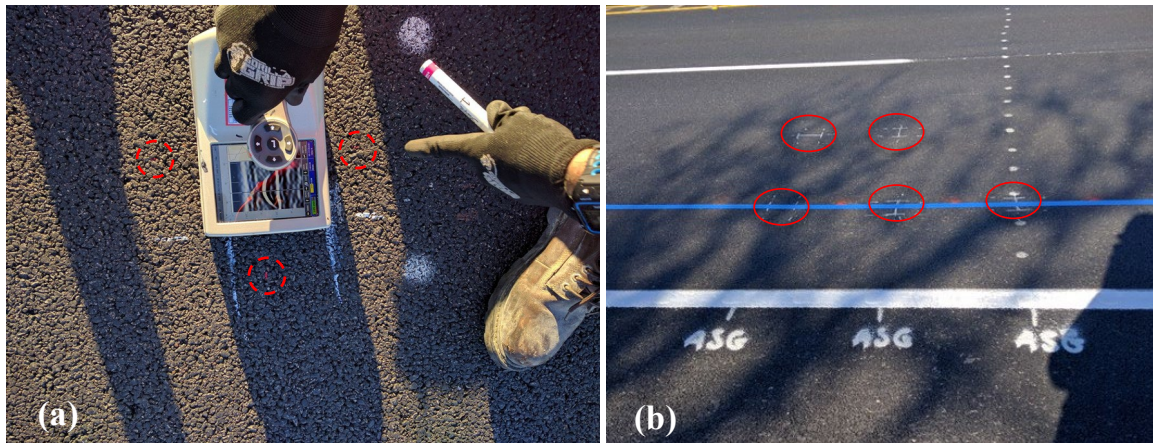
Figure 8.2. Marking ASG locations: (a) handheld GPR; and (b) marked ASG locations.
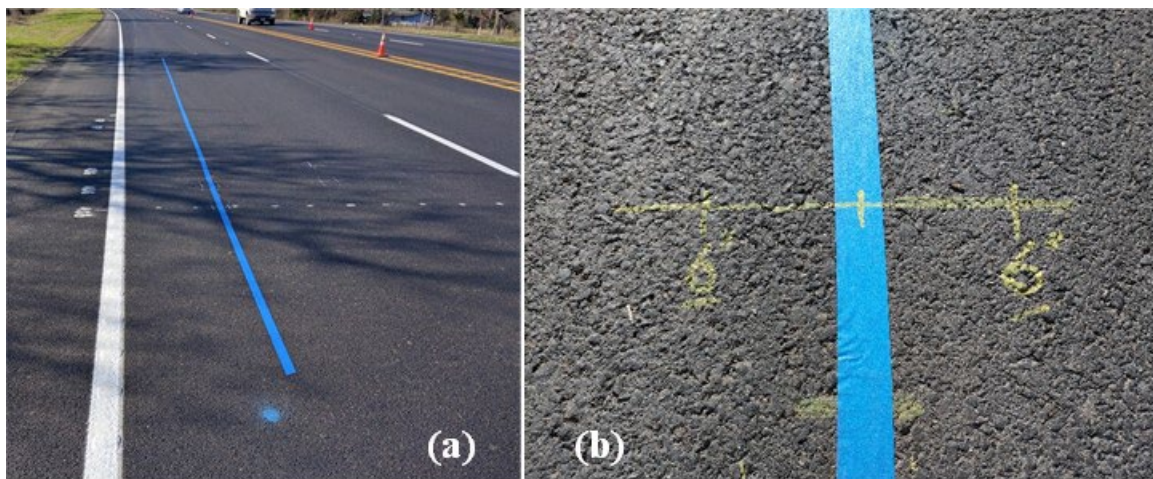
Figure 8.3. (a) Installation of blue tape; and (b) marking wheel path for controlled traffic loading.

Figure 8.4. GoPro cameras mounted to capture front and rear wheel paths.

The drivers were asked to drive at least 10 passes on top of the sensors while the data loggers collected the data from ASG and geophones. In the section below, the results of these 10 passes at speed under the heavy truck (with three axles) are presented. Figure 8.5 shows the response of the five sensors for all 10 passes. As can be seen from the figures, the entire loading and unloading of all three axles occurred within a time period of 2 seconds. The time histories of strain response for the 10 passes have been corrected so the peak from the first axle lines up at the same time (i.e., the first peaks from each pass are synchronized with each other). Firstly, this allows for the inspection of the quality of the passes relative to the magnitude of first peak. Secondly, this facilitates inspection of the peaks from the rear wheel passes and assessing if all passes were conducted at more or less the same speeds.

Figure 8.5a and Figure 8.5b show the response of the ASG in the wheel path measuring strains in the transverse direction (critical horizontal tensile strains). As can be seen from the figures, each pass produces a slightly different response from the others due to the spatial variability of the truck passes. Some passes were also found to produce significantly lower responses. In such cases, the GoPro videos corresponding to the passes were verified to confirm the location of the passes. The pass was discarded from further analysis if the deviation was beyond acceptable margins. Furthermore, because the sensors labeled Transverse Wheel Path Repeat (TWPR) and Transverse Wheel Path Center (TWPC) are repeats, the responses measured from them were also similar in magnitude and characteristics.
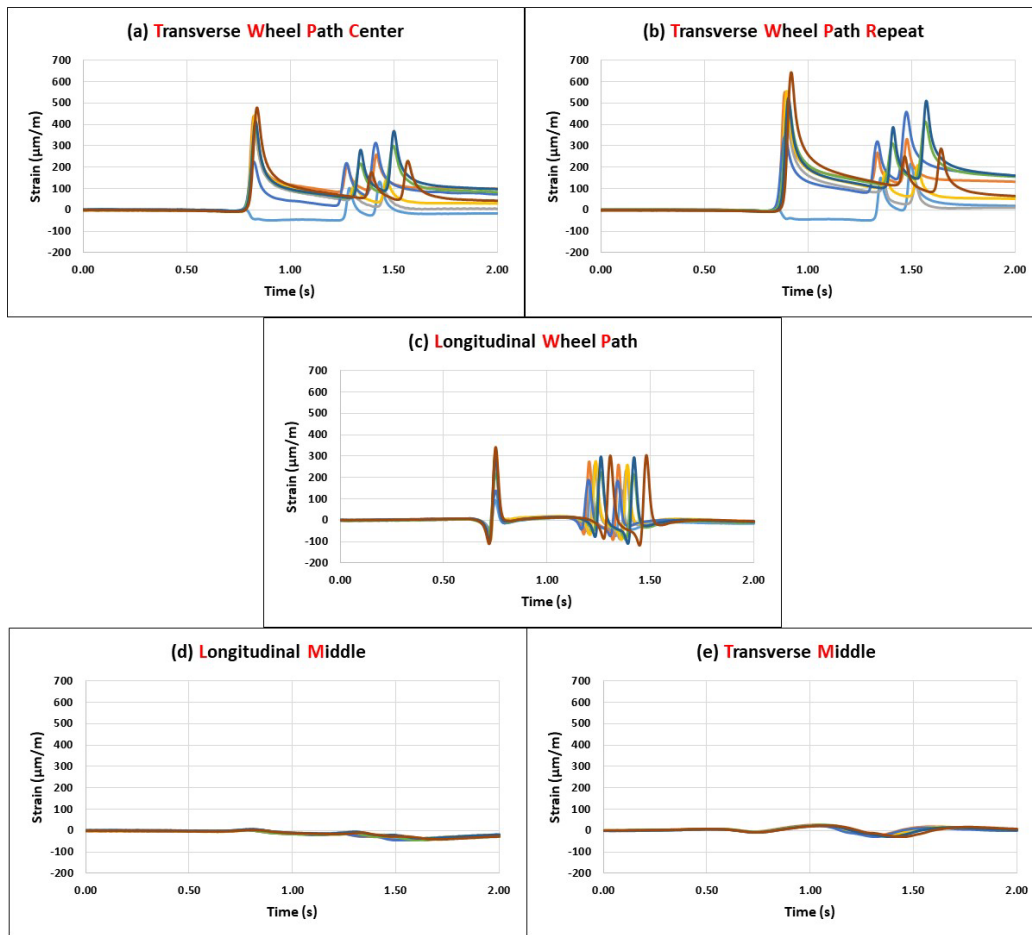
Figure 8.5. Responses of ASG under heavy truck trafficking.

Figure 8.5c shows the response of the sensor installed in the Longitudinal Wheel Path (LWP) measuring strain in the longitudinal direction. The response from this sensor was much sharper than the sensor measuring strain in the transverse direction. This is due to the transitive nature of the strains produced as the loaded axle approaches the sensor (compression), passes on top of the sensor (tension) and recedes from the sensor (compression again), which causes sharp responses and thus is more sensitive to minor variations in vehicle speed. The effect of vehicle speed is more clearly observed from the rear axle response of the LWP sensor. By contrast, the TWP sensors undergo only tension and therefore the response is much smoother and less sensitive to vehicle speed.

Figure 8.5d and Figure 8.5e show the response of the sensors installed between the two wheel paths measuring strains in the Longitudinal Middle (LM) and Transverse Middle (TM) directions. The TM is subjected to pure compression since both flanges are subjected to inward stresses from the two wheel loads on either side, whereas the LM response is similar to that

204

observed from the corresponding sensor in the wheel path but with a much lower magnitude due its distance from the two wheel paths.

The data from each pass in each test section was carefully analyzed. The first step of the analysis was to determine if the pass was accurately on top of the sensors or off. This evaluation was done using the videos captured from the front and rear wheels of the truck. As presented in Figure 8.6, snapshots from the videos at the exact moment when the wheel was passing the sensors' locations were taken for each pass. As an example, Figure 8.6a shows the location of the truck front wheel in Pass 2 in Section 2 compared to the location of the ASG installed in the wheel path along the transverse direction in the center of the test section (ASG-TWPC). Figure 8.6b shows the same but for the ASG installed as the duplicate of ASG-TWPC (i.e., ASG-TWPR).
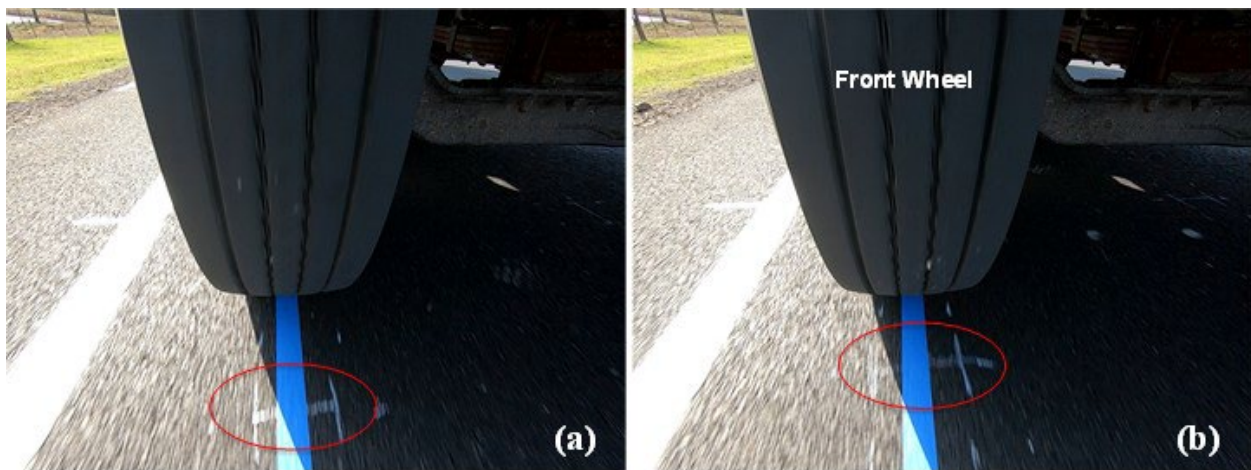
Figure 8.6. Location of truck front wheel relative to ASG in wheel path: a) ASG – Transverse Wheel Path Center; and b) ASG – Transverse Wheel Path Repeat.

After determining the suitability of the traffic pass, the next step of the analysis involved filtering the noise from the data. As an example, for the same pass presented in Figure 8.6a (i.e., Pass 2 of the truck in Section 2), Figure 8.7a and Figure 8.7b show the original (with noise) and filtered (without noise) data, respectively. Fourier transform was used to transfer the original data from the time domain to the frequency domain; then, a low-pass filter was used to filter the frequencies corresponded to the noise; and lastly, the filtered data were transformed back from the frequency domain to the time domain. The peak values in the filtered data indicate the maximum strains induced in the ASG as the truck passed the location of the sensors. In the next step of the analysis, the peak values will be compared among different test sections to evaluate the performance of the sections under the same controlled traffic load.

(a)   **(b)**
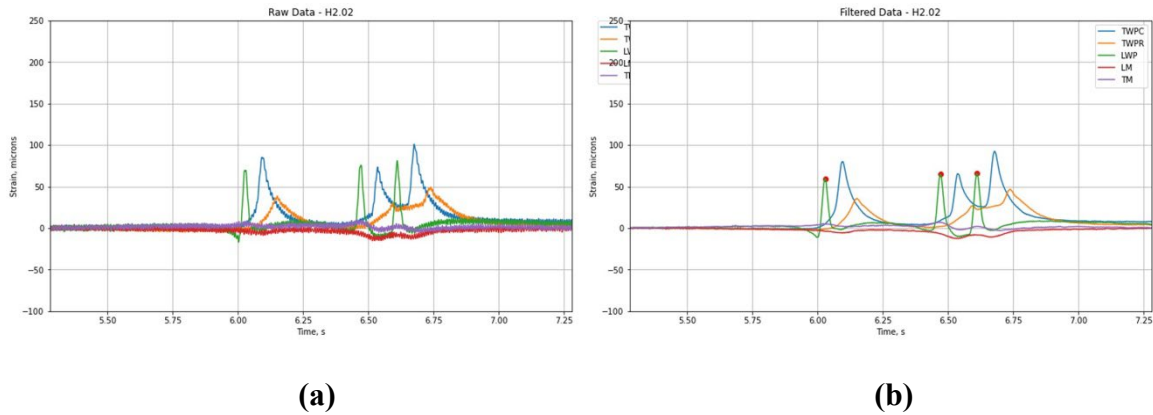
Figure 8.7. Data recorded under controlled heavy traffic by ASG in Pass 2 in test Section 2:
a) original data (with noise); and b) filtered data (without noise).

8.3. Effect of Asphalt Type and Thickness

The influence of asphalt overlay type, thickness and different geosynthetic interlayers on the performance of asphalt overlays were evaluated with data collected as part of controlled traffic loadings performed in the seven sensor-instrumented test sections considered in this study. The controlled traffic loadings were performed on all sensor-instrumented test sections prior to installation of the geosynthetic reinforcement, i.e., the preexisting pavement (see Figure 8.8a), after construction of the 50-mm-thick TYD layer (see Figure 8.8b) and finally after construction of the 25-mm-thick TOM layer (see Figure 8.8c) during the SH21 roadway rehabilitation program. Controlled traffic loadings involved driving multiple (about 10) passes in a passenger van with a known weight directly over the sensor locations at a controlled speed of about 40 kph. The tensile strain responses induced by the controlled traffic loading were recorded by the ASG embedded in the preexisting asphalt layer. The tensile strain results recorded from various sensor-instrumented test sections are discussed in the following sections.
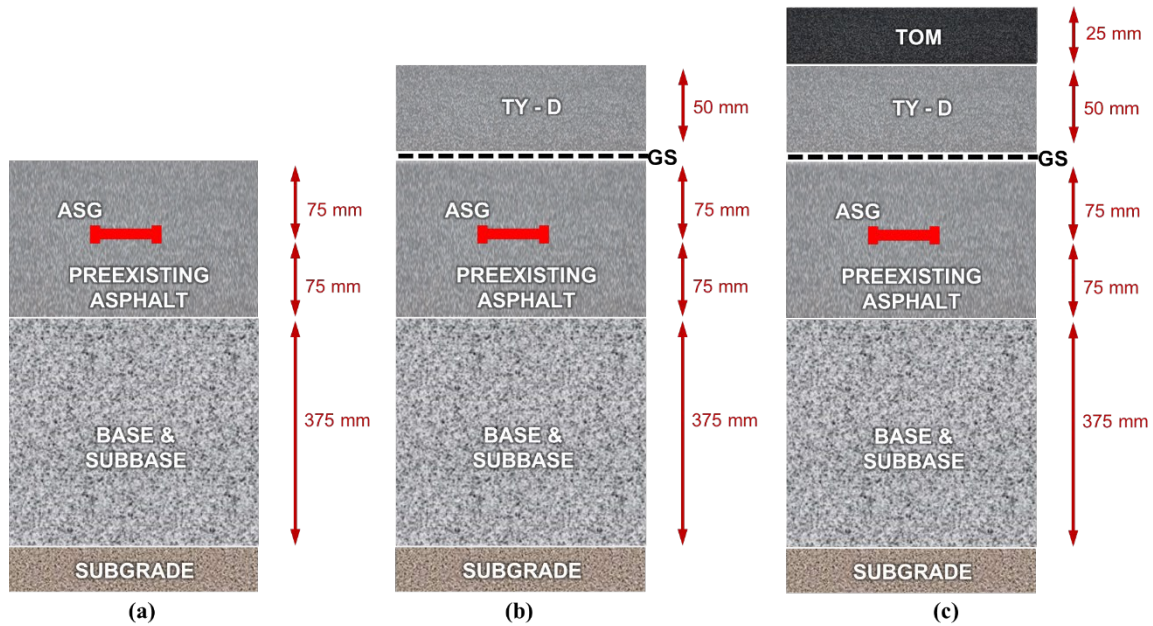
Figure 8.8. Schematic of road profile and sensor instrumentation: (a) preexisting pavement section; (b) pavement section with 50-mm-thick asphalt overlay; and (c) pavement section with 75-mm-thick asphalt overlay.

8.3.1. Peak Tensile Strains

A typical tensile strain response obtained from the ASG installed in the transverse direction along the wheel path in the control section under a controlled traffic load using a passenger van (i.e., light axle load) applied on the preexisting pavement (i.e., prior to geosynthetic installation and overlay construction) is presented in Figure 8.9. As shown in the figure, two distinct peaks representing two axles/wheels of the passenger van were obtained. It can also be observed that the tensile strains under the front and rear axle loads are comparatively similar, suggesting consistency in the tensile strains recorded in this study. The peak tensile strains recorded for different axle loads (i.e., front and rear axles) from different traffic loadings applied on the preexisting pavement (see Figure 8.10) and pavement sections with 50- (see Figure 8.11) and 75-mm-thick overlays (see Figure 8.12) in all sensor-instrumented test sections are plotted as 'box and whisker' plots.
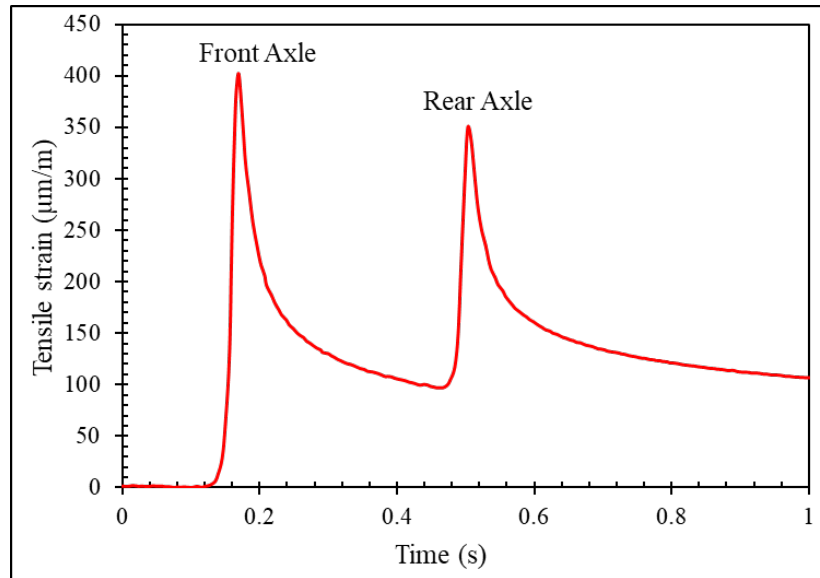
Figure 8.9. Typical tensile strain response under light axle load applied on preexisting pavement.

| (a) | (b) |
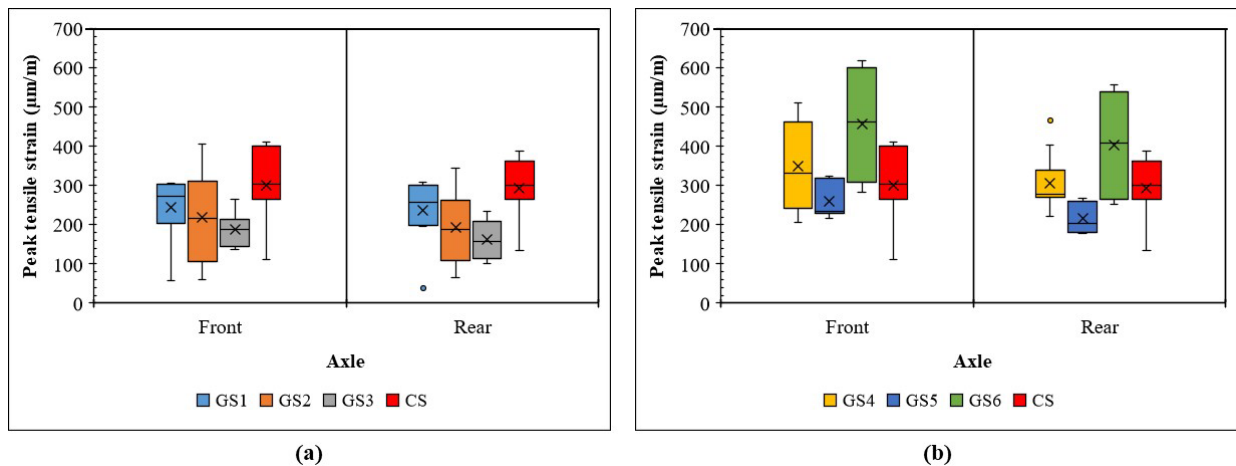
Figure 8.10. Box and whisker plots presenting peak tensile strains recorded in preexisting pavement section under: (a) front axle load; and (b) rear axle load.

As shown in Figure 8.10, box and whisker plots represent the variations in peak tensile strains for multiple passes of light axle loads, including the front and rear axles, applied on the preexisting pavement in all seven sensor-instrumented test sections. The top and bottom whiskers represent the maximum and minimum values, respectively, while the upper and lower portions of the box represent the upper and lower quartiles, respectively. Additionally, the line dividing the box represents the median value, and the cross-mark represents the mean value of the peak tensile strains recorded from traffic loadings. As can be observed from Figure 8.10a and Figure 8.10b, the magnitude of peak tensile strains in the test sections with fiberglass reinforcements (see Figure 8.10b) were slightly higher than those with polymeric reinforcements

208

(see Figure 8.10a). For instance, the peak tensile strains in sections with fiberglass reinforcements varied from 200 μm/m to 600 μm/m, while those with polymeric reinforcements varied from 50 μm/m to 400 μm/m. These results confirm the variations in tensile strains among various test sections prior to installation of the geosynthetic reinforcement and overlay construction. However, the peak tensile strains under the front and rear axle loads were almost similar for all seven test sections, suggesting that the recorded tensile strain data is consistent. Similar observations could be made from box and whisker plots of the peak tensile strains under the front and rear axle loads applied on pavement sections with 50- and 75-mm-thick asphalt overlays. To facilitate comparison of the peak tensile strains between the control and reinforced sections for different overlay configurations, the 90th percentile (90pth) values of peak tensile strains were determined for all test sections and pavement configurations and are discussed next.
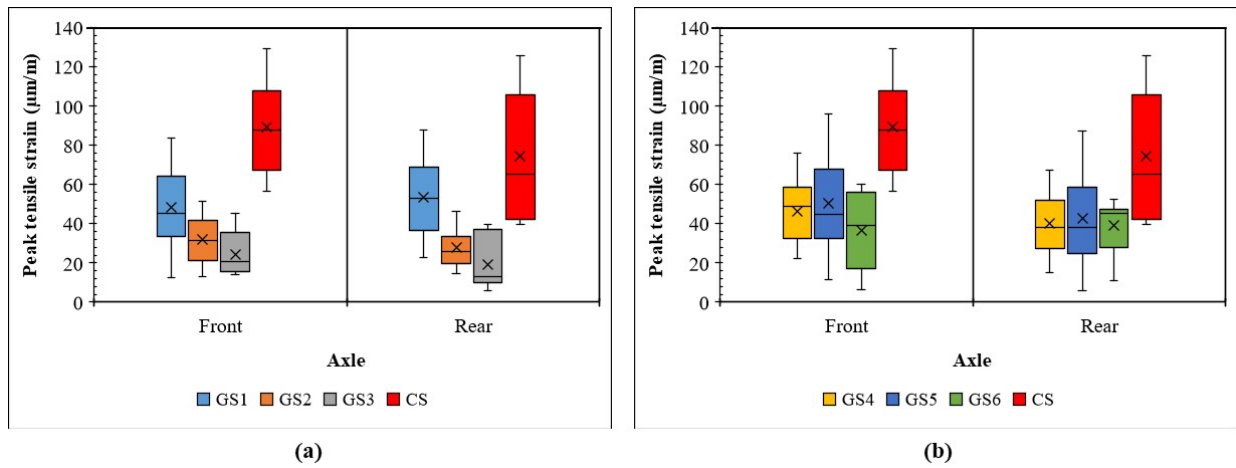
Figure 8.11. Box and whisker plots presenting peak tensile strains recorded in pavement section with 50-mm-thick asphalt overlay under: (a) front axle load; and (b) rear axle load.
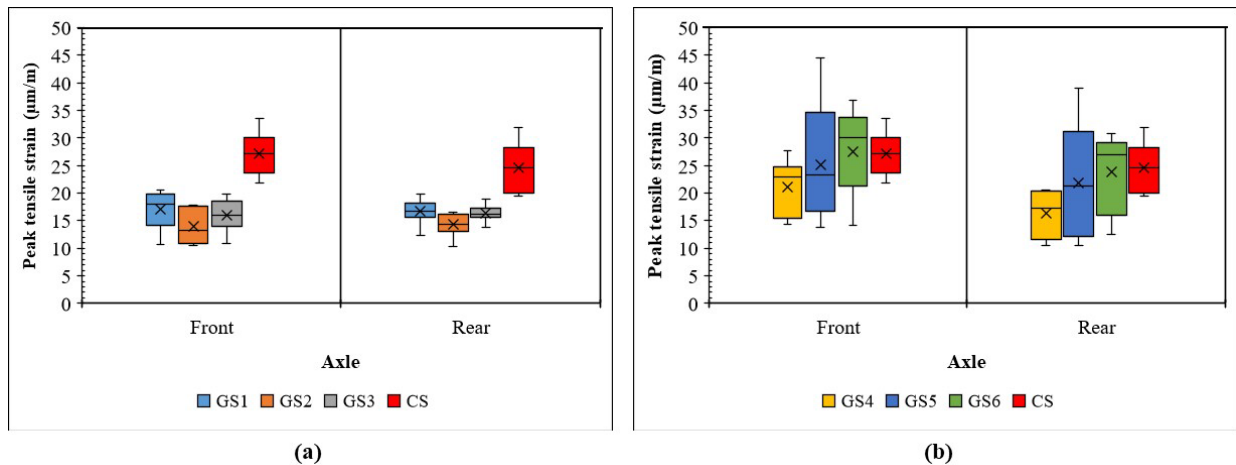
Figure 8.12. Box and whisker plots presenting peak tensile strains recorded in pavement section with 75-mm-thick asphalt overlay under: (a) front axle load; and (b) rear axle load.

209

8.3.2. 90th Percentile of Peak Tensile Strains

Figure 8.13 and Figure 8.14 present the 90th percentile of peak tensile strains for the front and rear axle loads applied on all pavement configurations in sections with polymeric and fiberglass reinforcements, respectively. As shown in Figure 8.13, it is apparent that the tensile strains decreased with increasing asphalt thickness, irrespective of the presence or absence of geosynthetic (polymeric) reinforcements. For instance, the results in Figure 8.13a indicate that tensile strains of 304 μm/m, 346 μm/m, 260 μm/m and 408 μm/m were recorded in sections GS1, GS2, GS3 and CS, respectively, under the front axle loads applied on the preexisting pavement. Subsequently, with the installation of polymeric reinforcements (excluding the control section) and construction of the 50-mm-thick TYD asphalt overlay, tensile strains reduced to about 75 μm/m (GS1), 47 μm/m (GS2), 42 μm/m (GS3) and 119 (CS). Eventually, the tensile strains reduced further to about 20 μm/m (GS1), 18 μm/m (GS2), 19 μm/m (GS3) and 31 μm/m (CS) after construction of the final lift (25-mm-thick TOM) of asphalt overlay. Tensile strains reduced by about 70-85% with the installation of the geosynthetic reinforcement and construction of the 50-mm-thick TYD asphalt overlay, which then reduced further by about 60-75% with the construction of the 25-mm-thick TOM asphalt overlay. Similar trends in tensile strain reductions could also be observed under the rear axle loads applied on different pavement configurations in sections reinforced with polymeric products and the control section.
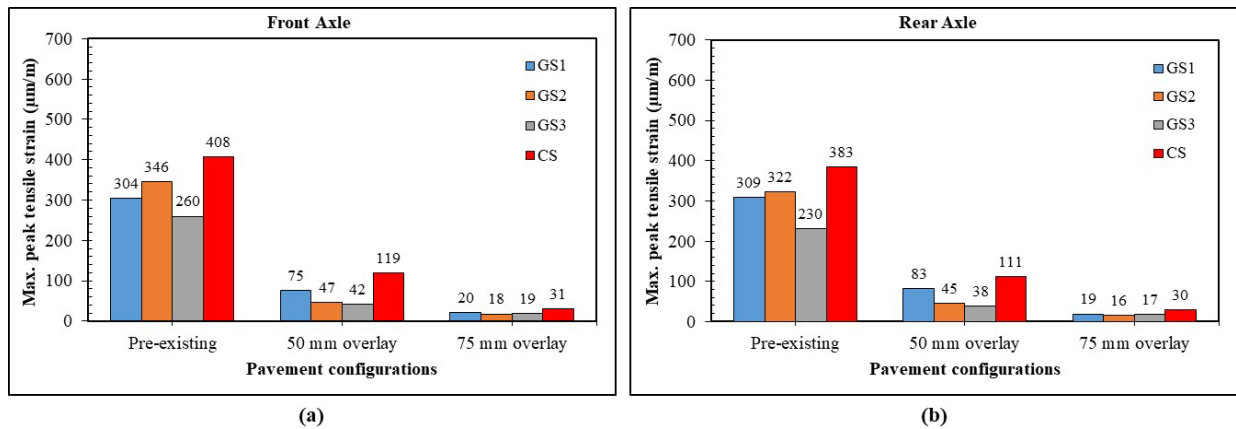
Figure 8.13. Maximum of peak tensile strains for various pavement configurations for polymeric products under: (a) front axle load; and (b) rear axle load.
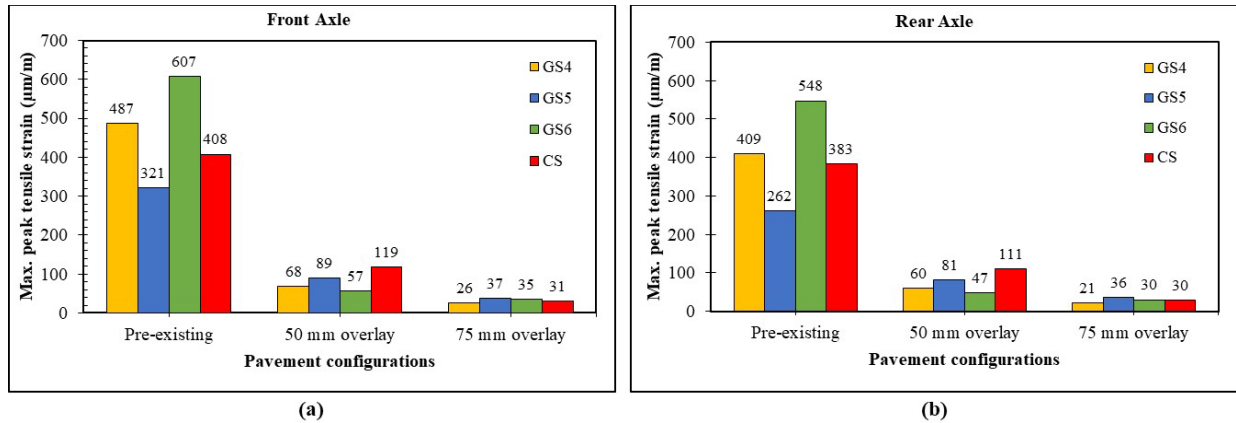
Figure 8.14. Maximum of peak tensile strains for various pavement configurations for fiberglass products under: (a) front axle load; and (b) rear axle load.

On the other hand, the results in Figure 8.14a indicate that tensile strains of 487 μm/m, 321 μm/m, 607 μm/m and 408 μm/m were recorded in sections GS4, GS5, GS6 and CS, respectively, under the front axle loads applied on the preexisting pavement. Subsequently, with the installation of fiberglass reinforcements (excluding the control section) and construction of the 50-mm-thick TYD asphalt overlay, tensile strains reduced to about 68 μm/m (GS4), 89 μm/m (GS5), 57 μm/m (GS6) and 119 (CS). Eventually, the tensile strains reduced further to about 26 μm/m (GS4), 37 μm/m (GS5), 35 μm/m (GS6) and 31 μm/m (CS) after the construction of the final lift (25-mm-thick TOM) of asphalt overlay. Tensile strains reduced by about 70-90% with the installation of the geosynthetic reinforcement and construction of the 50-mm-thick TYD asphalt overlay, which then reduced further by about 40-70% with the construction of the 25-mm-thick TOM asphalt overlay. Similar trends in tensile strain reductions could also be observed under the rear axle loads applied on different pavement configurations in sections reinforced with polymeric products and the control section. These observations from Figure 8.13 and Figure 8.14 suggest that tensile strains reduced with increasing asphalt overlay thickness. On average, tensile strains reduced by at least 70% and 40% with 50- and 75-mm-thick (50-mm-thick TYD and 25-mm thick TOM) asphalt overlays, respectively. However, the tensile strains recorded under the front and rear axle loads applied on the preexisting asphalt in all seven test sections differed from each other, confirming that the preexisting pavement conditions were not exactly identical across all seven test sections prior to installation of the geosynthetic reinforcement and subsequent asphalt overlay construction. Hence, tensile strains recorded after geosynthetic installation and overlay construction under both the front and rear axle loads were normalized relative to their preexisting conditions to facilitate comparison with each other.

8.3.3. Normalized Tensile Strain

Normalized Tensile Strain (NTS) maybe defined as the ratio between the 90th percentile of peak tensile strains in any given section (i.e., unreinforced or reinforced) after overlay construction

and prior to overlay construction (i.e., preexisting pavement), which is mathematically expressed in Eq. 1.

$$NTS = \frac{TS_{post}}{TS_{pre}} \qquad \text{Eq. (1)}$$

where NTS is the normalized tensile strain in any given section after geosynthetic installation and overlay construction; and TS_{post} and TS_{pre} are tensile strains in any given section after and before geosynthetic installation and overlay construction, respectively. Accordingly, a lower NTS value represents reduced tensile strains, irrespective of the presence or absence of geosynthetic reinforcements.

Figure 8.15 and Figure 8.16 show the variation in NTS with overlay thickness under the front and rear axle loads in polymeric- and fiberglass-reinforced sections, respectively. As expected, the NTS for all seven sensor-instrumented test sections prior to geosynthetic installation and overlay construction was 1, which subsequently decreased with increasing asphalt overlay thickness. However, the rate of decrease in the NTS for polymeric-reinforced (see Figure 8.15) and fiberglass-reinforced sections (except GS5, see Figure 8.16) were lower than that for the control section. The NTS values in polymeric-reinforced sections were determined to be on the order of 0.25 (GS1), 0.14 (GS2) and 0.16 (GS3) against 0.29 in the control section with 50-mm-thick TYD asphalt overlay under front axle loads (see Figure 8.15a). Subsequently, with the construction of an additional 25-mm-thick TOM asphalt overlay, the NTS values further reduced to about 0.07 (GS1), 0.05 (GS2), 0.07 (GS3) and 0.08 (CS). Similar trends were observed for the polymeric-reinforced and control sections under the rear axle loads (see Figure 8.15b). These observations confirm that all polymeric-reinforced sections had consistently lower NTS values (i.e., lower tensile strains) in comparison with those for the control section, irrespective of the asphalt overlay thickness. However, significantly higher differences between the NTS values in polymeric-reinforced sections and the control section could be observed for the thin overlay (i.e., 50-mm-thick TYD asphalt overlay) in contrast to the thick overlay (i.e., 50-mm-thick TYD and 25-mm-thick TOM asphalt overlay combined).
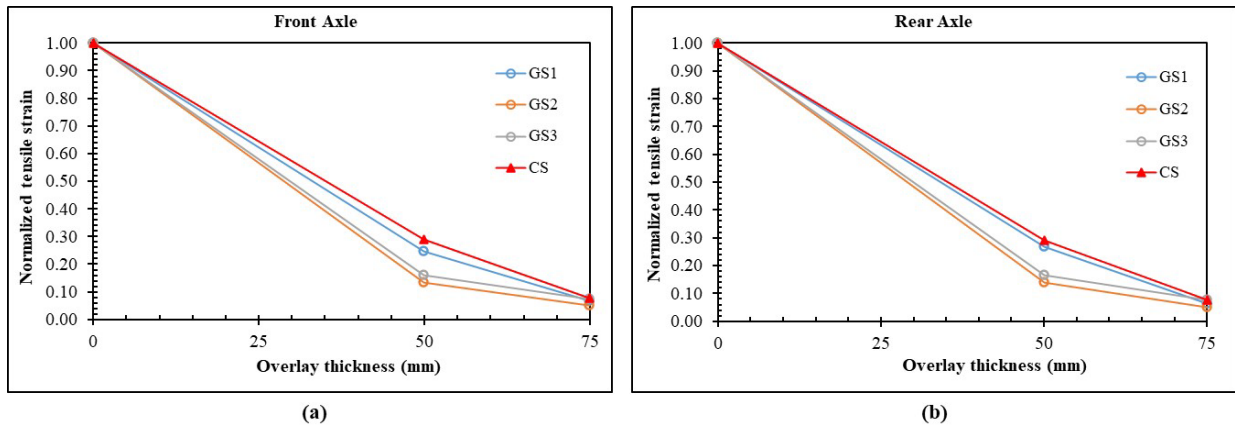
Figure 8.15. Variation of NTS with overlay thickness for polymeric products under: (a) front axle load; and (b) rear axle load.
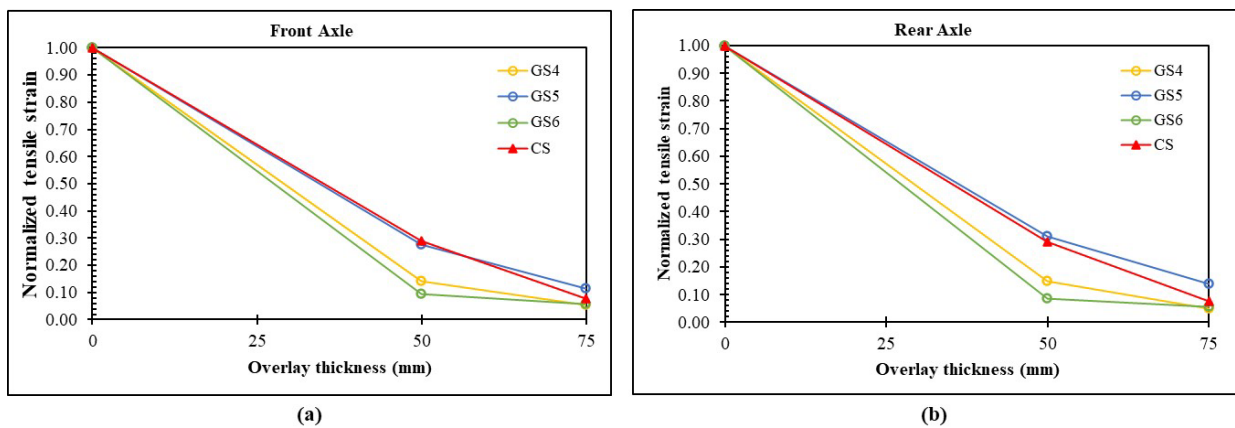
Figure 8.16. Variation of NTS with overlay thickness for fiberglass products under: (a) front axle load; and (b) rear axle load.

The NTS values in fiberglass-reinforced sections were determined to be on the order of 0.14 (GS4), 0.28 (GS5) and 0.09 (GS6) against 0.29 in the control section with the 50-mm-thick TYD asphalt overlay under front axle loads, which further reduced to about 0.05 (GS4), 0.11 (GS5), 0.06 (GS6) and 0.08 (CS) with the construction of an additional 25-mm-thick asphalt overlay (see Figure 8.16a). Similar trends could be observed for fiberglass-reinforced sections with 50- and 75-mm-thick asphalt overlays under rear axle loads from Figure 8.16b. It can also be observed from Figure 8.16a and Figure 8.16b that the NTS values for all fiberglass-reinforced sections, except GS5, were consistently lower than that for the control section, irrespective of the asphalt overlay thickness. These results also demonstrate that the inclusion of the geosynthetic reinforcements considered in this study, when placed at the interface between the preexisting and new asphalt layers, is effective in reducing tensile strains under traffic loads. However, such benefits depend on the actual thickness and quality of the asphalt overlay. Accordingly, a comparatively small benefit may be expected when using a comparatively thick, high-quality asphalt layer, at least immediately after placement of the asphalt overlay.

To further quantify the improvement in terms of tensile strain reductions in the geosynthetic-reinforced sections against the control section, the tensile strain reduction ratio is introduced as a performance indicator and discussed in the following section.

8.3.4. Tensile Strain Reduction Ratio

The tensile strain reduction ratio (α) maybe defined as the ratio between the NTS in a reinforced section to that in the control section, irrespective of the axle loads and overlay thicknesses. Accordingly, a tensile strain reduction ratio of comparatively small magnitude represents a significant reduction in tensile strain (i.e., enhanced performance corresponds to low 'α' values). The tensile strain reduction ratios for the front and rear axle loads in polymeric- and fiberglass-reinforced sections as a function of asphalt overlay thickness are presented in Figure 8.17 and Figure 8.18, respectively. The results shown in the figures indicate that the tensile strain reduction ratios for loads applied on 50-mm-thick overlay are consistently smaller than the ratios corresponding to loads applied on 75-mm-thick overlay, irrespective of the geosynthetic reinforcement type (i.e., polymeric or fiberglass). For instance, the tensile strain reduction ratios under front axle loads range from 0.46 to 0.85 for polymeric-reinforced sections with 50-mm-thick overlay, and from 0.67 to 0.95 for polymeric-reinforced sections with 75-mm-thick overlay (see Figure 8.17a). The tensile strain reduction ratios under front axle loads in fiberglass-reinforced sections with 50- and 75-mm-thick asphalt overlays ranged between 0.32 and 0.95, and 0.69 and 1.50, respectively. Similar trends in tensile strain reduction ratios were also obtained under rear axle loads applied in polymeric- and fiberglass-reinforced sections with 50- and 75-mm-thick asphalt overlays. Additionally, it is evident that the tensile strain reduction ratios were consistently lower for the 50-mm-thick asphalt overlay compared to the 75-mm-thick asphalt overlay (i.e., combined thickness of TYD and TOM asphalt layers), irrespective of the geosynthetic reinforcement products used. This observation suggests that the geosynthetic reinforcements (polymeric and fiberglass products) provide significantly higher benefits (i.e., tensile strain reductions) in pavement sections with 50-mm-thick asphalt overlay compared to those with 75-mm-thick asphalt overlay. Accordingly, a comparatively small benefit may be expected when using a comparatively thick, high-quality asphalt layer, at least immediately after placement of the asphalt overlay. The benefit of using geosynthetic reinforcements will become more significant once the modulus of a comparatively thick asphalt overlay degrades with time. Additionally, adopting a comparatively thin layer of reinforced asphalt would not only result in reduced construction costs but would also lead to a more efficient geosynthetic reinforcement. The incorporation of geosynthetic interlayers in projects involving a comparatively thick layer of reinforced asphalt will still capitalize on the geosynthetic benefits but only after degradation of the thick asphalt layer.
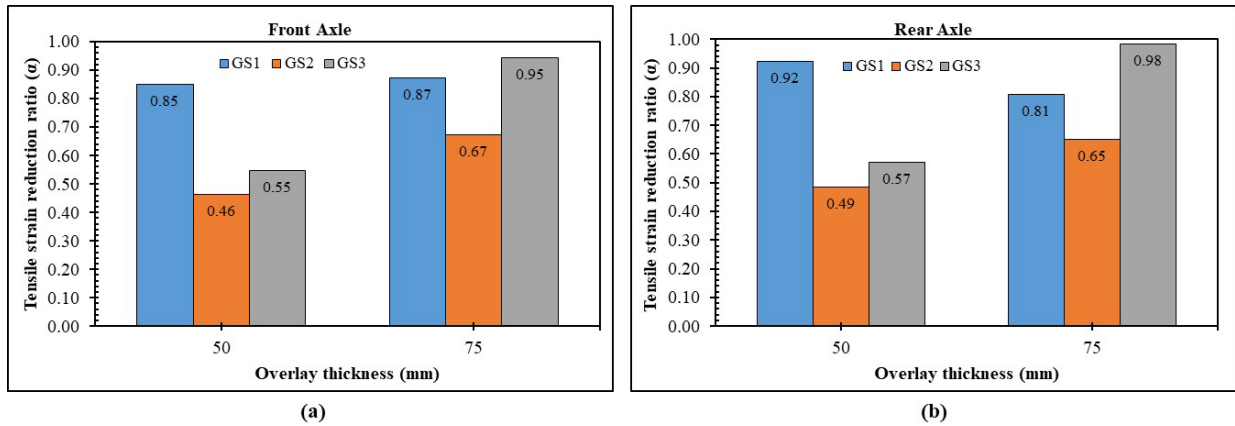
Figure 8.17. Variation of tensile strain reduction ratio with overlay thickness for polymeric products under: (a) front axle load; and (b) rear axle load.
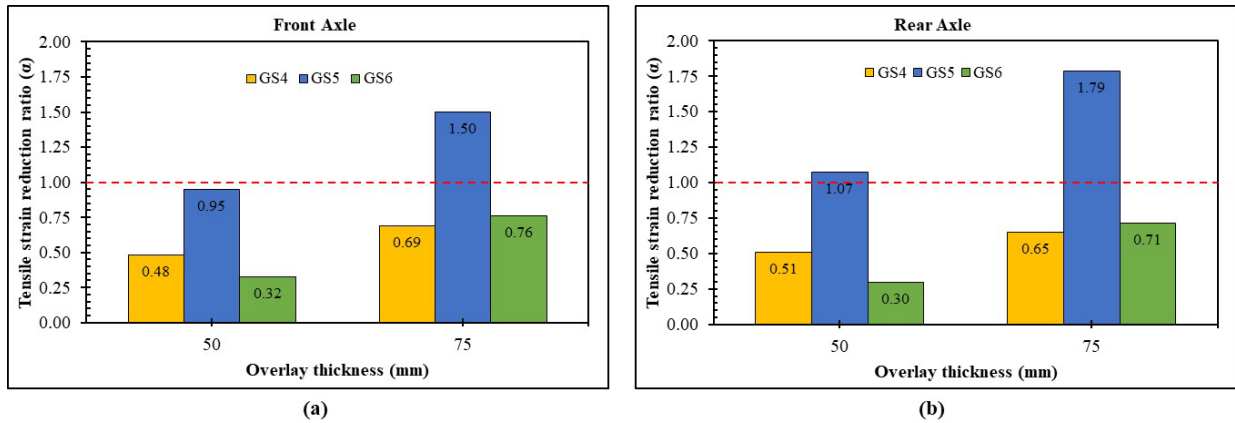
Figure 8.18. Variation of tensile strain reduction ratio with overlay thickness for fiberglass products under: (a) front axle load; and (b) rear axle load.

As previously discussed, all polymeric-reinforced sections performed significantly better than the control section (see Figure 8.17a). However, among the polymeric-reinforced sections, GS2 performed significantly better, followed by GS3 and GS1. These variations in performance among the three polymeric-reinforced sections maybe attributed to their tensile properties (see Table 8.1) and interface bond strength characteristics. Among the fiberglass-reinforced sections, GS4 and GS6 performed significantly better than the control section, while GS5 had similar or inferior performance compared to the control section. The comparatively better performance of the GS4 and GS6 sections could be attributed to their tensile properties and interface bonding characteristics, while the inferior performance of the GS5 section could be attributed to its poor interface bonding characteristics caused by the insufficient temperature of the TYD asphalt mixture that was required to activate the pressure-sensitive tack film coated on the GS5 product. Typically, hot asphalt mixtures are prepared and placed at around 165 °C and 145 °C, respectively, while the TYD and TOM asphalt mixtures adopted in this study involved a warm-mix additive (Evotherm) that reduced the mixing and laying temperatures by at least 20 °C to 30

215

°C compared with hot-mix asphalt temperatures. Kumar et al. (2023) reported the interface bond strength characteristics of the seven sensor-instrumented test sections evaluated in this research study. The reported values for polymeric-reinforced sections indicate that the interface bond strength of GS2 and GS3 were significantly better than the minimum bond strength requirement per FGSV 770 (2013) while the interface bond strength of GS1 was slightly below the required bond strength. Those reported for fiberglass-reinforced sections indicated a higher interface bond strength for GS4, followed by GS6 and finally GS5, with the lowest interface bond strength. Additionally, the interface bond strengths of GS5 and GS6 did not meet the minimum bond strength requirement per FGSV 770 (2013). However, these bond strength values for all sections would improve with time as the repeated vehicular movement increased with time.

The stiffness of the asphalt overlay may have also slightly influenced the magnitude of the tensile strain reduction ratios of the two reinforced sections evaluated in this study. The benefits that result from using reinforcements appear to be maximized when the stiffness of the asphalt layer is comparatively low. Overall, it can be inferred that all polymeric- and fiberglass-reinforced sections (except GS5) showed a clearly superior structural capacity to that of the control section, as evidenced by the reduced tensile strains under the front and rear axle loads applied on 50- and 75-mm-thick asphalt overlays. The tensile strain reduction ratios determined from geosynthetic-reinforced sections may be adopted as part of the pavement design to reduce the asphalt overlay thickness and/or extend the service life without compromising the overall performance of the pavement system. The performance of such a flexible pavement system with reduced thickness and an extended service life is expected to ultimately be verified under the framework of a Mechanistic-Empirical Pavement Design approach.

8.3.5. Summary

The influence of geosynthetic (e.g., material composition, tensile properties) and asphalt characteristics (e.g., type, thickness, preexisting conditions) on the quantification of structural capacity of full-scale sensor-instrumented experimental comprising an unreinforced and six geosynthetic-reinforced sections constructed along the Texas State Highway 21 in US were evaluated under controlled traffic loading conditions. Following conclusions can be summarized from this study:

- The tensile strains recorded by ASG installed at a depth of 75 mm in the preexisting asphalt layer in all seven sensor-instrumented sections were determined to be similar for both the front and rear axle loads of a passenger van, suggesting a consistency in the tensile strain data recorded in this study.

- The tensile strains recorded in all seven sensor-instrumented sections prior to the installation of geosynthetic reinforcements and overlay construction differed significantly

from each other. Hence, tensile strains recorded after the geosynthetic installation and overlay construction were normalized with respect to their preexisting conditions to be comparable among each other.

- As expected, the NTS in all seven sections decreased with an increase in the asphalt overlay characteristics (e.g., thickness, quality), irrespective of the presence or absence of geosynthetic reinforcements. However, the rate of decrease in the NTS with increasing overlay characteristics was significantly higher in all geosynthetic-reinforced sections (except GS-5) compared to the control section.

- A performance indicator, tensile strain reduction ratio, was determined for all six geosynthetic-reinforced sections from ratios of NTS in geosynthetic-reinforced and control sections for pavement sections with 50-mm- and 75-mm-thick asphalt overlays, respectively.

- The tensile strain reduction ratios for sections with polymeric products ranged from 0.46 to 0.85 and 0.67 to 0.95 for front axle loads applied on 50- and 75-mm-thick asphalt overlays, respectively. The ratios ranged from 0.49 to 0.92 and 0.65 to 0.98 for rear axle loads applied on 50- and 75-mm-thick asphalt overlays, respectively.

- The tensile strain reduction ratios for sections with fiberglass products ranged from 0.32 to 0.95 and 0.69 to 1.50 for front axle loads applied on 50- and 75-mm-thick asphalt overlays, respectively. The ratios ranged from 0.30 to 1.07 and 0.65 to 1.79 for rear axle loads applied on 50- and 75-mm-thick asphalt overlays, respectively.

- These trends indicate that all geosynthetic reinforcement products (except the fiberglass product GS-5) reduced tensile strains and enhanced the roadway structural capacity significantly. Additionally, the trends also indicate that the tensile strain reduction ratios are influenced by asphalt type, thickness, and geosynthetic characteristics including the material composition, tensile properties and interface bond strength characteristics.

Overall, all geosynthetic-reinforced sections (except GS-5) considered in this study were found to perform distinctly better than the control section in terms of minimizing the critical tensile strains and, consequently, enhancing the structural response of the asphalt overlay and pavement system. This is a particularly relevant finding considering that geosynthetic interlayers are often selected in asphalt overlays with the objective of minimizing reflective cracking rather than increasing the structural capacity of a flexible pavement. Ultimately, the use of geosynthetic reinforcements in asphalt overlays may result in a reduction in asphalt thickness and/or an extension in the service life of geosynthetic-reinforced overlay sections.

8.4. Effect of Temperature

The influence of temperature on the performance of asphalt overlays reinforced with different geosynthetic interlayers was evaluated with data collected as part of the controlled traffic loadings performed on the seven sensor-instrumented test sections considered in this study. Controlled traffic loadings were performed on all sensor-instrumented test sections after construction of the 25-mm-thick TOM layer (see Figure 8.8c), and during different seasons and weather conditions. Controlled traffic loading involved driving a loaded dump truck with a known weight in multiple (about 10) passes directly over the sensor locations at a controlled speed of about 40 kph. The tensile strain responses induced by the controlled traffic loading were recorded by the ASG embedded in the preexisting asphalt layer. A typical tensile strain response obtained from the ASG installed in transverse direction along the traffic wheel path in the control section under a controlled traffic load using a loaded dump truck (i.e., standard axle load) is presented in Figure 8.19. As shown in the figure, three distinct peaks representing three axles/wheels of the loaded dump truck (i.e., standard axle load) were obtained.
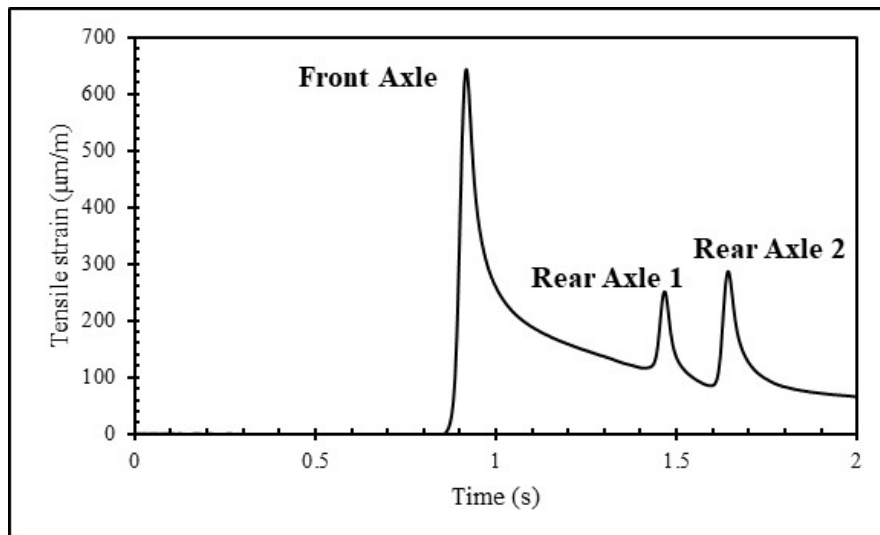
Figure 8.19. Typical tensile strain response under standard axle load applied in control section.

8.4.1. 90th Percentile of Peak Tensile Strains

Figure 8.20 presents a 3D plot summarizing the 90th percentile of peak tensile strains in the control sections at different temperatures and years (time) after the asphalt overlay construction. As shown in the figure, the peak tensile strain data corresponds to six different loading campaigns conducted right after completion of the asphalt overlay construction up to about three years after overlay construction, and at different temperatures between 45 °F and 85 °F. To better present the data from all seven sensor-instrumented test sections, the 90th percentile of peak tensile strain data were plotted separately for the front and rear axle loads, respectively.
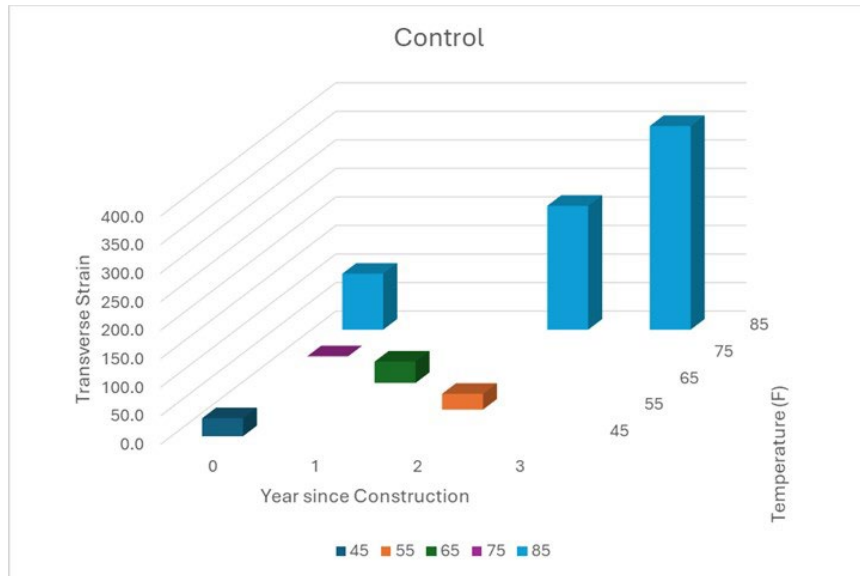
Figure 8.20. 3D plot of 90th percentile of tensile strains at different temperatures and years.

Figure 8.21 and Figure 8.22 show the 90th percentile of tensile strains under the front and rear axle loads of a loaded dump truck applied at a speed of about 40 kph. The three figures correspond to the variation of tensile strains with ambient air temperatures under front, rear-first and rear-second axles of the loaded dump truck in all seven sensor-instrumented test sections. The ambient air temperatures were recorded by the nearest weather station on the day of each loading campaign. It can be observed from the figures that with increasing temperatures, the transverse tensile strains increased under similar loaded dump truck loads. This behavior is expected since the asphalt modulus reduces with increasing ambient air temperatures. Additionally, it can be observed that the loading from the rear axles was more consistent than the front axle in the observed tensile strains.
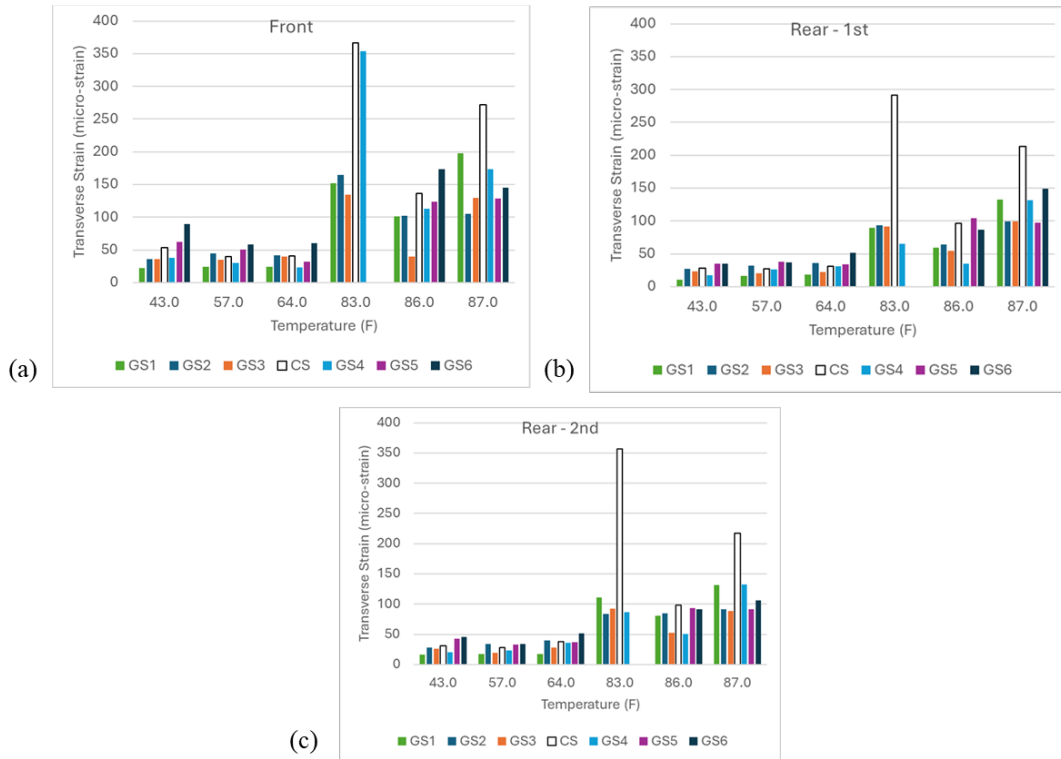
Figure 8.21. Variation of transverse (tensile) strains with temperature under: (a) front axle; (b) rear-first axle; and (c) rear-second axle loads.

It can also be observed from the figures that the tensile strains in control section and the geosynthetic-reinforced sections are almost similar at low temperatures, while the tensile strains in control sections increase to be higher than those in geosynthetic-reinforced sections at higher temperatures. To further quantify the improvement in terms of tensile strain reductions in the geosynthetic-reinforced sections against the control section, the tensile strain reduction ratio is introduced as a performance indicator, as discussed in the following section.

8.4.2. Tensile Strain Reduction Ratio

The tensile strain reduction ratio (α) maybe defined as the ratio between the tensile strains in a reinforced section to that in the control section, irrespective of the axle loads and ambient air temperatures. Accordingly, a tensile strain reduction ratio of comparatively small magnitude represents a significant reduction in tensile strain (i.e., enhanced performance corresponds to low 'α' values). The tensile strain reduction ratios for the front and rear axle loads as a function of ambient air temperature are presented in Figure 8.22a-Figure 8.22c, respectively. Please note that the figures are plotted with the y-axis at tensile strain reduction ratio equal to 1. Thus, any value that is pointed downward indicates a tensile strain reduction ration less than 1 or a section performs better than the control section, and vice-versa. It can be observed that most geosynthetic-reinforced sections performed better than that of the control section (i.e., values

220

pointing downward). The exception to this rule is GS5, where interface bond strength was poor, and GS6, due to their preexisting conditions. It can also be observed that the response under front axle load is more poorly behaved than those under rear axle loads. Such a behavior is likely due to the wider footprint of the rear axle compared to the front axle loads, resulting in more consistent traffic passes. In other words, the rear axle is more forgiving in terms of the alignment of the trafficking path and center of the sensor.

(a)

(b)

(c)
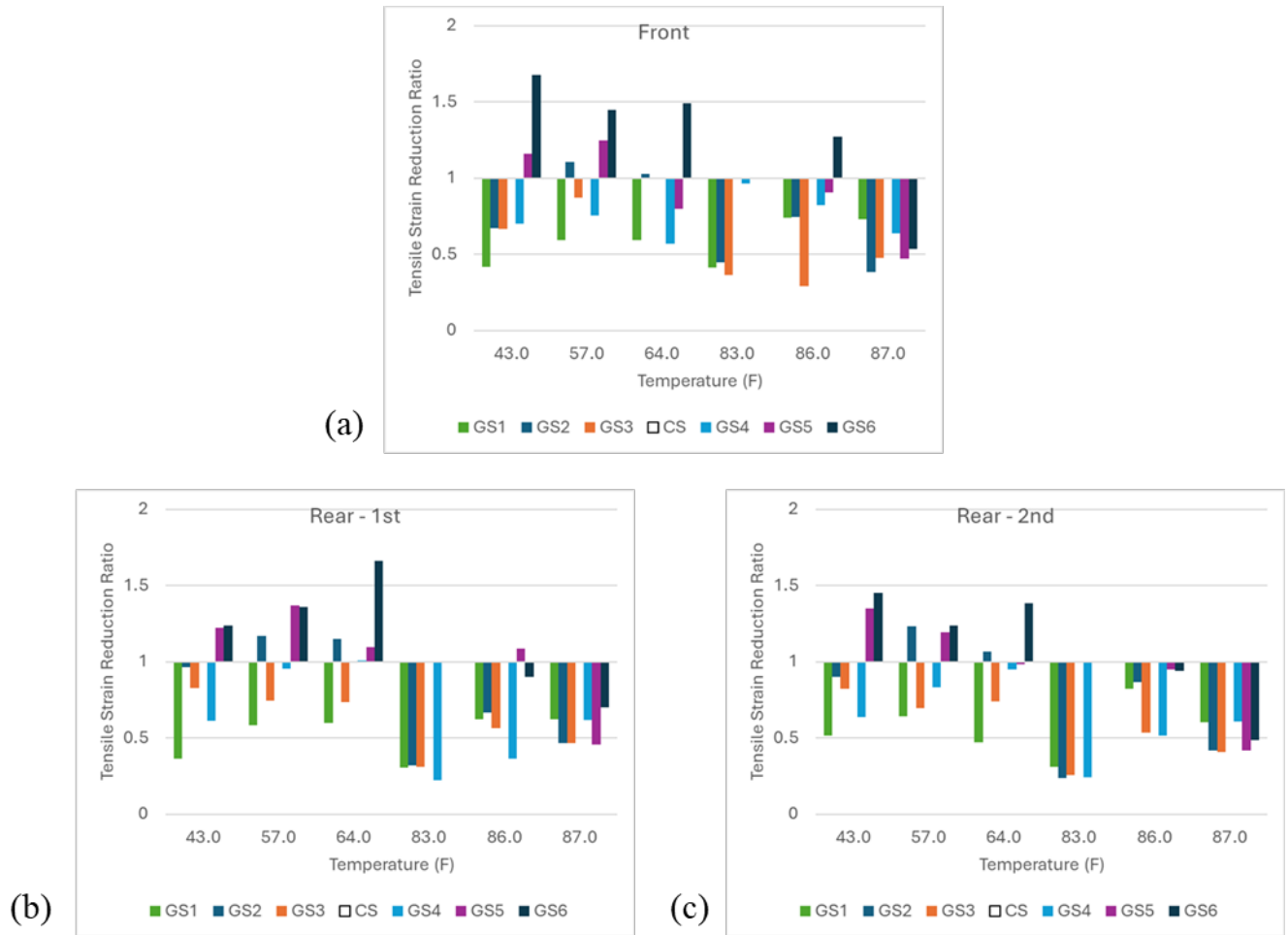
Figure 8.22. Variation of tensile strain reduction ratio with temperature under (a) Front axle; (b) Rear-first axle; and (c) Rear-second axle loads.

It can also be observed from the figures that, with increasing ambient air temperatures, all the geosynthetic-reinforced sections show better performance compared to that of the control section. Additionally, with increasing ambient air temperatures, the tensile strain reduction ratio decreases, although not necessarily monotonically. Such a behavior may be due to the fact that while the ambient air temperatures were different, other factors, such as aging of asphalt layer, consolidation, variation of subgrade, subbase, etc. were present, as the tests were conducted over a period of 3 years.

8.4.3. Summary

The influence of geosynthetic (e.g., material composition, tensile properties) and ambient air temperature on the quantification of structural capacity of full-scale sensor-instrumented experimental comprising an unreinforced and six geosynthetic-reinforced sections constructed along the Texas State Highway 21 in US were evaluated under controlled traffic loading conditions. Following conclusions can be summarized from this study:

- Tensile strains increased with increasing ambient air temperatures, irrespective of presence or absence of geosynthetic reinforcements.

- The rate of increase in tensile strains with increasing ambient air temperatures was found to be more significant in the control section compared to those in the geosynthetic-reinforced sections.

- The tensile strains recorded in control section was found to exhibit the earliest and highest sensitivity to temperature variations (i.e., for both, hold and cold temperature conditions).

- The tensile strains recorded in polymeric-reinforced sections were found to exhibit moderate sensitivity at cold temperatures, while they exhibited low sensitivity at hot temperatures.

- The tensile strains recorded in fiberglass-reinforced sections were found to exhibit low sensitivity at cold temperatures, while they exhibited moderate sensitivity at hot temperatures.

8.5. Effect of Asphalt Aging and Degradation

The influence of asphalt aging and degradation on the performance of asphalt overlays reinforced with different geosynthetic interlayers were evaluated with data collected as part of controlled traffic loadings performed in the seven sensor-instrumented test sections considered in this study. Specifically, the controlled traffic loadings were performed on all the sensor-instrumented test sections, after construction of the 25-mm-thick TOM layer, during different years since construction. Controlled traffic loading involved driving in multiple (about 10) passes a loaded dump truck with known weights, directly over the sensor locations at a controlled speed of about 40 kph. The tensile strain responses induced by the controlled traffic loading were recorded by the ASG embedded in the preexisting asphalt layer.

8.5.1. Normalization of Tensile Strains

The tensile strains recorded prior to the installation of geosynthetic reinforcements and construction of asphalt overlay were not same in all seven sensor-instrumented test sections. Hence, the tensile strains recorded under controlled traffic loads post overlay construction need to be normalized with the tensile strains prior to the overlay construction to normalize the influence of preexisting pavement conditions. Accordingly, the normalization factors for all seven sensor-instrumented test sections were determined for preexisting conditions. Specifically, the tensile strains recorded in all the sections prior to the overlay construction were compared to that in the control section. Figure 8.23 shows the normalization factor for preexisting conditions in all the sensor-instrumented test sections. As shown in the figure, control section has a normalization factor of 1, while the polymeric-reinforced sections have a normalization factor greater than 1, and the fiberglass-reinforced sections have a normalization factor lower than 1 (except GS5).
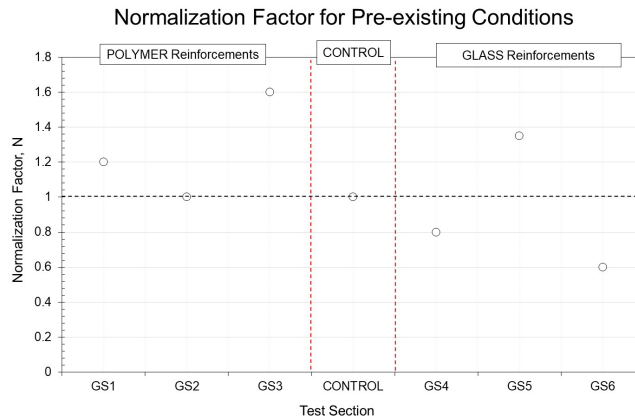
Figure 8.23. Normalization factor for preexisting conditions.
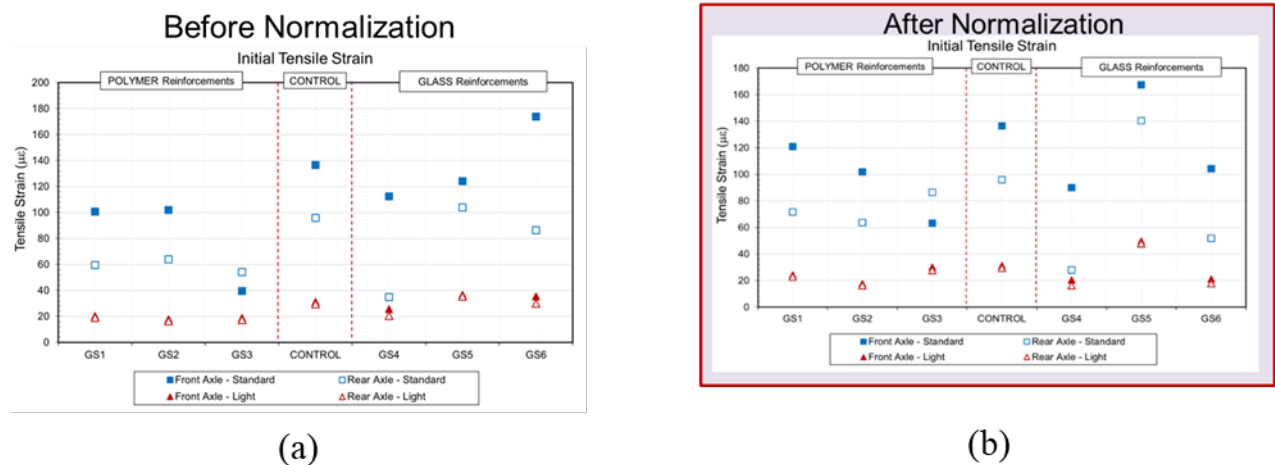
Figure 8.24. Tensile strains right after the asphalt overlay construction: (a) Before normalization; and (b) After normalization.

223

Figure 8.24 shows the tensile strains recorded right after the asphalt overlay construction before and after normalization. As shown in the figures, the tensile strains after the overlay construction under standard and light axle loads in all the geosynthetic-reinforced sections (except GS6) are smaller than the control section prior to normalization. However, after normalization of tensile strains to eliminate the influence of preexisting conditions, the amplitude of tensile strains changed slightly, with all the geosynthetic-reinforced sections presenting lower tensile strains than the control section, except GS5. This observation is consistent with that observed in Section 8.3. The NTS right after the overlay construction (i.e., 0 years) and 2 years after the overlay construction are plotted as shown in Figure 8.25. As expected, the figures show that the tensile strains have increased with increase in time since construction due to asphalt aging and degradation. The tensile strains increased with increasing aging and degradation in all seven sensor-instrumented test sections, irrespective of presence or absence of geosynthetic reinforcements. However, the rate of increase in tensile strains in the control section was significantly higher than those in the geosynthetic-reinforced sections. Such trends suggest that the presence of geosynthetic reinforcements help reduce the rate of accumulation of tensile strains over time. To further quantify the improvement in terms of tensile strain reductions in the geosynthetic-reinforced sections against the control section, the tensile strain reduction ratio is introduced as a performance indicator, as discussed in the following section.
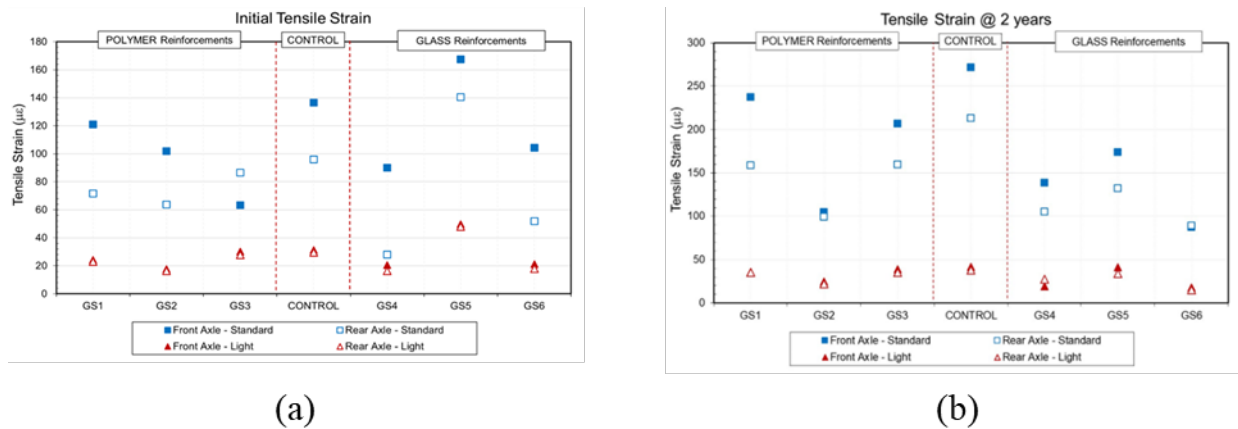
Figure 8.25. NTS values post overlay construction: (a) Initial; and (b) 2 years.

8.5.2. Tensile Strain Reduction Ratio

The tensile strain reduction ratio (α) maybe defined as the ratio between the NTS in a reinforced section to that in the control section, irrespective of the axle loads and time since construction. Accordingly, a tensile strain reduction ratio of comparatively small magnitude represents a significant reduction in tensile strain (i.e., enhanced performance corresponds to low 'α' values). The tensile strain reduction ratios for the front and rear axle of standard and light axle loads right after and 2 years after the asphalt overlay construction are presented in Figure 8.26a and Figure

224

8.26b, respectively. As can be seen from the figures that the tensile strain reduction ratios have decreased with increasing time since construction, indicating significant benefits from using geosynthetic reinforcements over time. Additionally, unlike the initial condition, after 2 years since the asphalt overlay construction, the tensile strain reduction ratios for all the geosynthetic-reinforced sections are below 1. Thus, a significantly better performance than that of the control section in terms of increased roadway structural capacity.

(a)   (b)
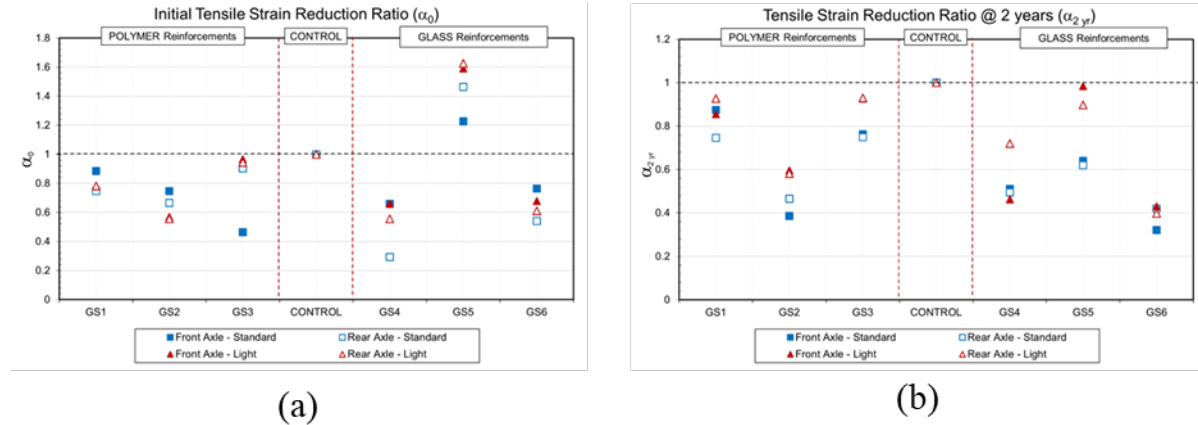
Figure 8.26. Tensile strain reduction ratio post overlay construction: (a) Initial; and (b) 2 years.

8.5.3. Summary

The influence of geosynthetic (e.g., material composition, tensile properties), asphalt aging and degradation on the quantification of structural capacity of full-scale sensor-instrumented experimental comprising an unreinforced and six geosynthetic-reinforced sections constructed along the Texas State Highway 21 in US were evaluated under controlled traffic loading conditions. Following conclusions can be summarized from this study:

- Tensile strains increased with increasing time since construction (i.e., asphalt aging and degradation), irrespective of presence or absence of geosynthetic reinforcements.

- The rate of increase in tensile strains with increasing time (i.e., asphalt aging and degradation) was found to be more significant in the control section compared to those in the geosynthetic-reinforced sections.

- The tensile strain reduction ratio trends indicate that all the geosynthetic-reinforced sections reduced the accumulation of tensile strains with time, as asphalt started aging and degrading, thereby increasing the roadway structural capacity.

8.6. Design of Geosynthetic-reinforced Asphalt (HMA-GS Composite)

The HMA-GS Composite Design Method is based on modifications to the AASHTO 1993 empirical pavement design procedure. The proposed design method relies on availability of a tensile strain reduction factor (α), which is defined as the ratio between the elastic tensile strain at the bottom of the HMA layer in a geosynthetic-reinforced asphalt road and that in an equivalent unreinforced road, measured under the 80-kN (18-kips) standard single axle load. That is:

$$\alpha = \frac{\varepsilon_{HGC}}{\varepsilon_{HMA}}$$ Eq. (1)

where, ε_{HGC} and ε_{HMA} are the elastic tensile strains at the bottom of the HMA layer in geosynthetic-reinforced and unreinforced roads, respectively.

Two approaches are presented in this paper to implement the proposed design method. The first approach involves determining an equivalent (increased) HMA-GS Composite modulus (E_{HGC}), which is subsequently used to obtain an equivalent (increased) layer coefficient for the HMA layer. The equivalent (increased) layer coefficient is then used to determine an equivalent (increased) SN, or alternatively used to reduce the asphalt thickness. The second approach of the proposed design method involves determining an equivalent HMA-GS Composite axle load factor (EALF$_{HGC}$), which is subsequently used to determine an equivalent (increased) ESAL, or alternatively used to reduce the design SN.

8.6.1. Equivalent HMA-GS Composite Modulus (E_{HGC})

The proposed design method can be implemented using an approach based on Multi-layer Linear Elastic Analysis (MLEA) to determine an equivalent (increased) modulus for HMA-GS composite using the tensile strain reduction factor α.

The elastic tensile strain in a geosynthetic-reinforced asphalt road is lower than that in an unreinforced road. Consequently, such reduced elastic tensile strain can be used to back-calculate an equivalent (increased) modulus for HMA-GS Composite (E_{HGC}). The procedure involves initially predicting the tensile strain at the bottom of the HMA in the unreinforced road (ε_{HMA}) using MLEA. The tensile strain at the bottom of the HMA in the geosynthetic-reinforced asphalt road can then be obtained using the tensile strain reduction factor (α), as follows:

$$\varepsilon_{HGC} = \alpha\, \varepsilon_{HMA}$$ Eq. (2)

Finally, MLEA is performed by varying the HMA modulus values to back-analyze the equivalent modulus of the HMA-GS Composite (i.e., E$_{HGC}$) that will result in 'ε_{HGC}' at the bottom of the HMA.

The AASHTO empirical pavement design procedure (AASHTO 1993) established an empirical relationship between $ESAL$ and the road SN, as follows:

$$\log(ESAL) = \frac{1}{0.40 + \frac{1094}{(SN+1)^{5.19}}} G_t + 9.36 \log(SN+1) - 0.2 + 2.32 \log(M_R) - 8.07 \quad \text{Eq. (3)}$$

$$G_t = \log\left(\frac{4.2 - P_t}{4.2 - 1.5}\right) \qquad\qquad \text{Eq. (4)}$$

where, G_t is the loss of serviceability factor, p_t is the serviceability at the end of time t and M_R is the resilient modulus of the subgrade in psi. For simplicity, Eq. (3) does not show the effect of the reliability level. The SN of an unreinforced road is defined by AASHTO (1993) as:

$$SN = a_1 D_{HMA} + a_2 D_2 m_2 + a_3 D_3 m_3 \qquad\qquad \text{Eq. (5)}$$

where, D_{HMA}, D_2 and D_3 are the thicknesses of the HMA, base and subbase layers, respectively; m_2 and m_3 are the base and subbase layer drainage coefficients, respectively; and a_1, a_2 and a_3 are the HMA, base and subbase layer coefficients, respectively. The layer coefficients have been correlated empirically with the moduli of the corresponding layers, as follows (Huang 2004):

$$a_1 = 0.384 \left(\log E_{HMA}\right) + 0.184 \qquad\qquad \text{Eq. (6A)}$$

$$a_2 = 0.249(\log E_2) - 0.977 \qquad\qquad \text{Eq. (6B)}$$

$$a_3 = 0.227(\log E_3) - 0.839 \qquad\qquad \text{Eq. (6C)}$$

where, E_{HMA}, E_2 and E_3 are the moduli of the HMA, base and subbase layers, respectively.

The increased modulus value as determined by MLEA back-analyses (i.e., E_{HGC}) for the HMA-GS Composite can be used in Eq. (6A) to predict the equivalent (increased) layer coefficient for the HMA-GS Composite layer (a'_1) as follows:

$$a'_1 = 0.384(\log E_{HGC}) + 0.184 \qquad\qquad \text{Eq. (7)}$$

The increased HMA modulus (E_{HGC}), as compared to E_{HMA}, results in a comparatively larger equivalent HMA layer coefficient (a'_1) for the geosynthetic-reinforced road. The coefficient a'_1 can then be used to optimize the design of the flexible pavement. Two most common design objectives for incorporating geosynthetic reinforcements in the design of a flexible pavement involve increasing the traffic volume (for a given HMA layer thickness) or reducing thickness of the HMA layer (for a given pavement design life).

8.6.1.1. Increased Traffic Volume

If the design objective is to achieve an increased traffic volume (for a given asphalt layer thickness), the increased layer coefficient (a'_1) can be used to define an equivalent structural number (SN') corresponding to the same pavement configuration, as follows:

$$SN' = a'_1 D_{HMA} + a_2 D_2 m_2 + a_3 D_3 m_3 \qquad \text{Eq. (8)}$$

The thickness of the geosynthetic-reinforced asphalt layer (D_{HMA}) and characteristics of the base and subbase layers (i.e., $a_2, a_3, D_2, D_3, m_2, m_3$) in the reinforced road (Eq. (8)) remain the same as those in the unreinforced road (Eq. (5)). However, the larger equivalent HMA layer coefficient (a'_1), obtained from using E_{HGC}, results an increased equivalent structural number (SN') for the geosynthetic-reinforced asphalt road. The increased structural number (i.e., SN') can be used in Eq. (3) to obtain an increased traffic volume, as follows:

$$\log(ESAL') = \frac{1}{0.40 + \frac{1094}{(SN'+1)^{5.19}}} G_t + 9.36 \log(SN'+1) - 0.2 + 2.32 \log(M_R) - 8.07 \qquad \text{Eq. (9)}$$

where $ESAL'$ is the equivalent $ESAL$ for the geosynthetic-reinforced asphalt road. Comparing Eqs. (3) and (9), the ratio between the traffic volume on the geosynthetic-reinforced asphalt road and that on the unreinforced road can be defined as the HMA-GS Composite Traffic Benefit Ratio (TBR_{HGC}) and determined as follows:

$$TBR_{HGC} = \frac{ESAL'}{ESAL} \qquad \text{Eq. (10)}$$

and

$$\log(TBR_{HGC}) = \left(\frac{1}{0.40 + \frac{1094}{(SN'+1)^{5.19}}} - \frac{1}{0.40 + \frac{1094}{(SN+1)^{5.19}}}\right) G_t + 9.36 \log\left(\frac{SN'+1}{SN+1}\right) \qquad \text{Eq. (11)}$$

8.6.1.2. Reduced HMA thickness

Alternatively, a'_1 can be used to achieve the design objective of reducing asphalt thickness (for a given traffic volume). Specifically, for a given SN, using an equivalent (increased) layer coefficient for the HMA layer, facilitates adoption of a reduced HMA thickness and, therefore, the SN can now be defined as follows:

$$SN = a'_1 D'_{HMA} + a_2 D_2 m_2 + a_3 D_3 m_3 \qquad \text{Eq. (12)}$$

where, D'_{HMA} is the equivalent (reduced) HMA thickness. The SN and characteristics of the base and subbase layers (i.e., $a_2, a_3, D_2, D_3, m_2, m_3$) in Eq. (12) remain the same as those in the unreinforced road (Eq. 5). The SN of the geosynthetic-reinforced road (Eq. 12) will equal the SN of the unreinforced road (Eq. 5), for the following equivalent HMA layer thickness:

$$D'_{HMA} = \frac{a_1}{a'_1} D_{HMA} \qquad \text{Eq. (13)}$$

228

Also, the reduction in asphalt thickness (ΔD_{HMA}) can be obtained as follows:

$$\Delta D_{HMA} = (D_{HMA} - D'_{HMA}) = \left(\frac{a'_1 - a_1}{a_1}\right) D_{HMA} \qquad \text{Eq. (14)}$$

In summary, designing geosynthetic-reinforced asphalt roads using equivalent HMA-GS Composite modulus include following steps. First, assuming no geosynthetic, design the road for the traffic volume ($ESAL$) and determine the SN and characteristics of the subbase, base and HMA layers, including the HMA layer coefficient (a_1) and HMA thickness (D_{HMA}). Then, use α with the explained MLEA procedure to estimate the equivalent HMA-GS Composite modulus (E_{HGC}) and use the obtained E_{HGC} in Eq. (7) to determine the equivalent (increased) layer coefficient for the HMA layer (a'_1). If the design objective is to increase the traffic volume, use Eq. (8) to determine the equivalent (increased) structural number (SN') for the geosynthetic-reinforced asphalt road, and use SN and SN' in Eqs. (11) and (10) to determine the HMA-GS Composite Traffic Benefit Ratio (TBR_{HGC}) and the equivalent (increased) $ESAL$ for the geosynthetic-reinforced asphalt road ($ESAL'$). However, if the design objective is to reduce asphalt thickness, use Eq. (13) to determine the reduced HMA layer thickness (D'_{HMA}), or Eq. (14) to determine the asphalt thickness reduction (ΔD_{HMA}).

8.6.2. Equivalent HMA-GS Composite Axle Load Factor ($EALF_{HGC}$)

The equivalent axle load factor ($EALF$) is defined as the ratio between the number of repetitions of a standard single axle load and that of a non-standard axle load group to cause the same damage to the road. The $EALF$ depends on various parameters such as pavement type, thickness, structural capacity, and more importantly the definition of damage conditions. Using the AASHTO empirical equations (Eq. (3)) developed after AASHO Road Test is one of the most widely used methods to determine $EALF$. In this case, damage was defined by a certain loss in the serviceability index, determined empirically based on rating the road ride quality by a panel of experts. Accordingly, $EALF$ for axle load group 'i' (i.e., $EALF_i$) is determined as follows:

$$EALF_i = \frac{W_{t\,18}}{W_{t\,i}} \qquad \text{Eq. (15)}$$

where W_{t18} is the total number of standard single axle loads and $W_{t\,i}$ is the total number of axles with load 'i' that cause the same damage to a road section.

Alternative mechanistic methods have since been developed to determine EALF based on critical strains in the pavement (e.g., tensile strain at the bottom of HMA, vertical strain above subgrade) and the failure criteria defined either in terms of fatigue cracking or permanent deformations. In these methods, $EALF_i$ is determined as the ratio between the total number of load repetitions to failure, as follows:

$$EALF_i = \frac{N_{f18}}{N_{fi}} \qquad\qquad \text{Eq. (16)}$$

Where N_{f18} and N_{fi} are the number of load repetitions to failure by a load representing the standard single axle load and the axle load group 'i'. Depending on the test method and definition of failure, the EALF determined by various mechanistic methods may be slightly to largely different from one method to another. In this study, the well-established mechanistic model by Asphalt Institute is used. The Asphalt Institute model has been developed based on fatigue cracking created under laboratory beam-type testing. The Asphalt Institute model relies on the horizontal strain at the bottom of HMA layer and the elastic modulus of HMA, as follows:

$$N_f = f_1(\varepsilon_t)^{-f_2}(E_{HMA})^{-f_3} \qquad\qquad \text{Eq. (17)}$$

Where, N_f is the number of load repetitions to failure; ε_t is the elastic tensile strain at the bottom of the HMA layer under the applied load; and the coefficient f_1 and exponents f_2 and f_3 are constants. The Asphalt Institute model uses 0.0796, 3.291, and 0.854 for constants f_1, f_2 and f_3, respectively. Other studies have also adopted similar equations but with different constant values (e.g., Illinois DOT, Shell). Accordingly, using Eq. (17) into Eq. (16), $EALF_i$ for a certain asphalt mixture can be obtained as follows:

$$EALF_i = \left(\frac{\varepsilon_{ti}}{\varepsilon_{t\,18}}\right)^{f_2} \qquad\qquad \text{Eq. (18)}$$

Where $\varepsilon_{t\,18}$ and $\varepsilon_{t\,i}$ are the elastic tensile strains at the bottom of the HMA layer induced by a load representing the standard single axle and the axle load group 'i,' respectively.

Since the inclusion of a geosynthetic reinforcement results in the reduction of HMA tensile strains (as quantified by α), the damage due to a standard single axle load on the geosynthetic-reinforced asphalt road can be equated to the damage caused by an equivalent (reduced) axle load on the unreinforced road. Therefore, the concept of $EALF$ can be used to predict the reduced effect of a standard single axle load on the HMA-GS Composite. In this case, the $EALF_{HGC}$ can be defined as the ratio between the number of repetitions of a standard single axle load on the unreinforced road ($W_{t\,18}$) and that on the geosynthetic-reinforced asphalt road ($W_{t\,18\,GS}$) to cause the same damage (e.g., same loss in serviceability):

$$EALF_{HGC} = \frac{W_{t\,18}}{W_{t\,18\,GS}} \qquad\qquad \text{Eq. (19)}$$

Using the Asphalt Institute mechanistic model, from Eq. (18) $EALF_{HGC}$ can be expressed as follows:

$$EALF_{HGC} = \left(\frac{\varepsilon_{t\,18\,GS}}{\varepsilon_{t\,18}}\right)^{f_2} \qquad\qquad \text{Eq. (20)}$$

where, $\varepsilon_{t\,18\,GS}$ and $\varepsilon_{t\,18}$ are the elastic tensile strains at the bottom of the HMA under a load representing the standard single axle load in the geosynthetic-reinforced asphalt and unreinforced roads, respectively.

Using Eq. (1), $\frac{\varepsilon_{t\,18\,GS}}{\varepsilon_{t\,18}}$ in Eq. (20) can be replaced by α, as follows:

$$EALF_{HGC} = (\alpha)^{f_2}$$

Eq. (21)

Assuming $EALF$ definition from AASHTO empirical equations (Eq. (15)) for the geosynthetic-reinforced asphalt and unreinforced roads, the total number of standard single axle loads to failure of the geosynthetic-reinforced asphalt road ($W_{t\,18\,GS}$) can be expressed as follows:

$$W_{t\,18\,GS} = \frac{1}{EALF_{HGC}} W_{t\,18}$$

Eq. (22)

Similar to the Equivalent HMA-GS Composite Modulus approach, formulations were developed here for Equivalent HMA-GS Composite Axle Load Factor approach for the two common design objectives for incorporating geosynthetic reinforcements: increasing the traffic volume (for a given HMA layer thickness) or reducing the thickness of the HMA layer (for a given traffic volume). In the developed formulations, $EALF_{HGC}$ was used to determine the increased $ESAL$ for the geosynthetic reinforced asphalt road, $ESAL'$, for the objective of increasing the traffic volume. For the objective of reducing HMA thickness, $EALF_{HGC}$ was used to determine a reduced $ESAL$ used for the design of geosynthetic-reinforced asphalt road, $ESAL_{Design}$, which then is used to determine a reduced design SN and a reduced required HMA thickness.

An important aspect in the developed formulations for $ESAL'$ and $ESAL_{Design}$ is the reference number of axles used for defining $ESAL$. A simplified expression of $ESAL$ for unreinforced road in terms of $EALF_i$, n_i, and $W_{t\,18}$ is as follows:

$$ESAL = \sum_{i=1}^{m} EALF_i\, n_i W_{t\,18}$$

Eq. (23)

Where n_i is the percentage of total repetition for the axle load group 'i' and m is the total number of the axle load groups. In the unreinforced road, damage by any axle load group 'i' is referenced to that caused by a standard axle load. However, since the damage due to a standard single axle load is different for geosynthetic-reinforced asphalt and unreinforced roads, the reference for determining the $EALF$ in the two roads may also be considered different. Specifically, $EALF$ in a geosynthetic-reinforced asphalt road for any axle load group 'i' may be referenced to the number of repetitions of a standard single axle load on the geosynthetic-reinforced asphalt road ($W_{t\,18\,GS}$) (Eq. 24A) or to the number of repetitions of a standard single axle load on the unreinforced road ($W_{t\,18}$) (Eq. 24B):

$$EALF_{i\,GS} = \frac{W_{t\,18\,GS}}{W_{t\,i\,GS}}$$

Eq. (24A)

231

$$EALF_{i\,GS} = \frac{W_{t\,18}}{W_{t\,i\,GS}} \qquad\qquad \text{Eq. (24B)}$$

As further discussed below, Eq. (24A) was used in the formulation developed for the design objective of increasing traffic volume, and Eq. (24B) was used in the formulation developed for the design objective of reducing HMA thickness. It was assumed that $EALF_{i\,GS}$ from Eq. (24A) can be equated to $EALF$ in the unreinforced road (i.e., $EALF_i$):

$$\frac{W_{t\,18\,GS}}{W_{t\,i\,GS}} = \frac{W_{t18}}{W_{t\,i}} \qquad\qquad \text{Eq. (25)}$$

8.6.2.1. Increased Traffic Volume

For the objective of increasing traffic volume, $ESAL$ from Eq. (23) is expressed with reference to the increased number of standard single axle load on the geosynthetic-reinforced asphalt road ($W_{t\,18\,GS}$), as compared to that on the unreinforced road:

$$ESAL' = \sum_{i=1}^{m} EALF_{i\,GS}\, n_i W_{t\,18\,GS} \qquad\qquad \text{Eq. (26)}$$

Accordingly, $EALF_{i\,GS}$ is also expressed with reference to $W_{t\,18\,GS}$, as expressed in Eq. (24A).

Using Eqs. (15) and (25), $EALF_{i\,GS}$ in Eq. (26) can be replaced by $EALF_i$, and using Eq. (19), $W_{t\,18\,GS}$ can be replaced by $W_{t\,18}/EALF_{HGC}$:

$$ESAL' = \sum_{i=1}^{m} EALF_i\, n_i \frac{W_{t\,18}}{EALF_{HGC}} \qquad\qquad \text{Eq. (27)}$$

Comparing Eqs. (23) and (26), $ESAL'$ can be expresses in terms of $EALF_{HGC}$ and $ESAL$ as follows:

$$ESAL' = \frac{1}{EALF_{HGC}} ESAL \qquad\qquad \text{Eq. (28)}$$

Or the HMA-GS Composite Traffic Benefit Ratio (TBR_{HGC}) can be obtained as follows:

$$TBR_{HGC} = \frac{1}{EALF_{HGC}} \qquad\qquad \text{Eq. (29)}$$

8.6.2.2. Reduced HMA Thickness

Alternatively, $EALF_{HGC}$ can be used to achieve the design objective of reducing asphalt thickness (for a given traffic volume). For this objective, $ESAL$ from Eq. (23) should be expressed with reference to the same number of standard single axle load as that on the unreinforced road ($W_{t\,18}$), and accordingly, $EALF_{i\,GS}$ should also be expressed with reference to $W_{t\,18}$, as stated in Eq. (24B). The equivalent ESAL in this case is referred to as $ESAL_{Design}$, the design (reduced) number of equivalent standard single axle loads that can be used for the design of the geosynthetic-reinforced asphalt road:

$$ESAL_{Design} = \sum_{i=1}^{m} EALF_{i\,GS}\, n_i W_{t\,18} \qquad \text{Eq. (30)}$$

Using Eqs. (24B), (25) and (19), $EALF_{i\,GS}$ in Eq. (30) can be replaced by $EALF_i\, EALF_{HGC}$:

$$ESAL_{Design} = \sum_{i=1}^{m} EALF_i\, EALF_{HGC}\, n_i W_{t\,18} \qquad \text{Eq. (31)}$$

Comparing Eqs. (23) and (31), $ESAL_{Design}$ can be expresses in terms of $EALF_{HGC}$ and $ESAL$ as follows:

$$ESAL_{Design} = EALF_{HGC}\, ESAL \qquad \text{Eq. (32)}$$

The AASHTO empirical pavement design equation (AASHTO 1993) for an unreinforced road is expressed by Eq. (3). The geosynthetic-reinforced asphalt road can be treated as an unreinforced road with equivalent design parameters; thus, Eq. (3) can similarly be used for the geosynthetic-reinforced asphalt road. Accordingly, the AASHTO flexible pavement design equation can then be expressed for the geosynthetic-reinforced asphalt road as follows:

$$\text{Eq. (33)}$$

$$\log(ESAL_{Design}) = \frac{1}{0.40+\frac{1094}{(SN_{Design}+1)^{5.19}}} G_t + 9.36\log(SN_{Design}+1) - 0.2 + 2.32\log(M_R) - 8.07$$

where, SN_{Design} is the design (reduced) SN value when a geosynthetic reinforcement is adopted in the design. Replacing $\log(ESAL_{Design})$ with $\log(EALF_{HGC}\, ESAL)$, and using Eq. (3) to express $\log(ESAL)$, Eq. (33) can be reworked as follows:

$$\log\left(\frac{1}{EALF_{HGC}}\right) = \left(\frac{1}{0.40+\frac{1094}{(SN+1)^{5.19}}} - \frac{1}{0.40+\frac{1094}{(SN_{Design}+1)^{5.19}}}\right) G_t + 9.36\log\left(\frac{SN+1}{SN_{Design}+1}\right) \quad \text{Eq. (34)}$$

Given the other parameters (i.e., SN, G_t and $EALF_{HGC}$), the above equation can be solved for SN_{Design}. Considering the definition of structural number, SN can be expressed as in Eq. (5) , and SN_{Design} can be expressed as follows:

$$SN_{Design} = a_1 D'_{HMA} + a_2 D_2 m_2 + a_3 D_3 m_3 \qquad \text{Eq. (35)}$$

Since a smaller design structural number is required for the geosynthetic-reinforced asphalt road to support the same traffic volume as the unreinforced road, a reduced asphalt thickness (D'_{HMA}) can be adopted in the geosynthetic-reinforced asphalt road design. The reduction in asphalt thickness (ΔD_{HMA}) can be determined using Eq. (5) and (31 35) as follows:

$$\Delta D_{HMA} = (D_{HMA} - D'_{HMA}) = \frac{SN - SN_{Design}}{a_1} \qquad \text{Eq. (36)}$$

In summary, designing geosynthetic-reinforced asphalt roads using equivalent HMA-GS Composite axle load factor include the following steps. First, assuming no geosynthetic, design the road for the design traffic ($ESAL$) and determine the required SN and characteristics of the

subbase, base and HMA layers, including the HMA layer coefficient (a_1) and HMA thickness (D_{HMA}). Then, use Eq. (21) to obtain $EALF_{HGC}$. If the design objective is to increase traffic volume, use $EALF_{HGC}$ in Eqs. (28) and (29) to determine the equivalent (increased) $ESAL$ for the geosynthetic-reinforced asphalt road ($ESAL'$) and the HMA-GS Composite Traffic Benefit Ratio (TBR_{HGC}). However, if the design objective is to reduce the asphalt thickness, use SN and $EALF_{HGC}$ in Eq. (34) to solve for the design (reduced) SN when a geosynthetic reinforcement is used (SN_{Design}). Then, use Eq. (36) to determine the reduction in asphalt thickness (ΔD_{HMA}).

8.7. Development of Design Charts

In this section, the two design approaches developed were used along with reported ranges of α to quantify the benefits of geosynthetic reinforcement in the design of typical pavement sections. Specifically, the suitability of the proposed design approaches is illustrated using design charts that facilitate quantification of the design benefits of geosynthetic reinforcement. Material properties of pavement layers were selected to be consistent with typical values adopted by the Texas Department of Transportation (TxDOT), so that the α values obtained from field evaluation by Kumar et al. (2022) could be adopted. Although the design charts were developed for the specific pavement configurations, the same procedures can be implemented to generate design charts for any other pavement layer configurations. Nevertheless, for practical purposes, the range of α may remain independent from pavement configurations used.

8.7.1. Reference Unreinforced Road

The unreinforced road considered as reference includes subgrade, subbase, base and HMA layers, the design parameters of which are summarized in Table 8.1.

Table 8.1. Design parameters of pavement layers used to develop design charts.

Pavement Layer	Thickness, mm (in)	Modulus, MPa (ksi)	Poisson Ratio
HMA	$D_{HMA} = 229$ (9)	$E_{HMA} = 2,070{\sim}13,800$ (300${\sim}$2,000)	0.35
Base	$D_2 = 127$ (5)	$E_2 = 345$ (50)	0.35
Subbase	$D_3 = 254$ (10)	$E_3 = 345$ (50)	0.35
Subgrade	Semi-infinite	$M_R = 69$ (10)	0.40

The SN for unreinforced roadway was calculated by determining the structural layer coefficient for each pavement structural layer. The structural layer coefficients for the base (a_2) and subbase (a_3) was determined using correlations with their modulus values using Eqs. (6B) and (6C), respectively. The structural layer coefficient for the HMA layer was determined using correlations with its modulus. Figure 8.27 shows the data presented by Van Til et al. (1972) to estimate the layer coefficient of dense graded HMA using its modulus in semilogarithmic scale. The solid line shows the data presented by Van Til et al. (1972) and the dashed line is the

regression used in this study. As presented in this figure, a reasonably linear relationship can be obtained between the modulus of the HMA layer (E_{HMA}), in 10^5 psi, and its structural layer coefficient (a_1) as expressed in Eq. (6A).

Using Eq. (6A) for the range of HMA modulus values listed in Table 8.1 results a_1 ranging from 0.37 (for $E_{HMA} = 2,070\ MPa$) to 0.68 (for $E_{HMA} = 13,800\ MPa$). Accordingly, using Eq. (5), the SN for the unreinforced road used as reference in this evaluation ranges from 6.5 (for $E_{HMA} = 2,070\ MPa$) to 9.4 (for $E_{HMA} = 13,800\ MPa$). The drainage coefficients of the base (m_1) and subbase (m_2) layers were assumed to equal 1 in the SN calculation.
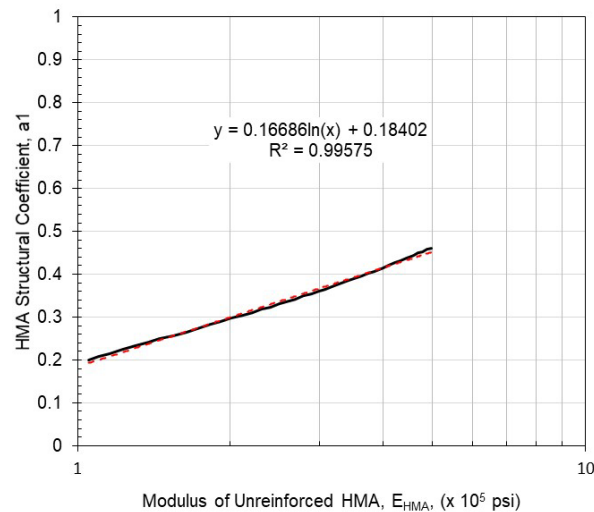
Figure 8.27. Correlation of HMA structural layer coefficient with modulus (after Van Til et al. 1972).

8.7.2. Geosynthetic-reinforced Asphalt Road Design

In this section, the abovementioned design for the reference unreinforced road was revised considering geosynthetic reinforcement in the HMA layer. While the characteristics of other layers remained the same, the design benefits from incorporating a geosynthetic reinforcement were evaluated by a parametric evaluation conducted by varying the relevant design parameters for the HMA layer. The effect of the geosynthetic was introduced by considering a suitable range for the elastic strain reduction factor (α) as defined in Eq. (1). For a wide range of geosynthetic products and pavement conditions, Kumar et al. (2022) found that α ranged from 0.8 (corresponding to a comparatively moderate performing geosynthetic reinforcement) to 0.4 (corresponding to a comparatively high performing geosynthetic reinforcement). This range was used in the development of the design charts presented next.

8.7.3. Design Charts for Equivalent HMA-GS Composite Modulus Approach

8.7.3.1. Equivalent HMA-GS Composite Modulus (E_{HGC})

Using the Equivalent HMA-GS Composite Modulus Approach, the increased asphalt modulus for the HMA-GS Composite (E_{HGC}) was determined using MLEA. Specifically, the pavement layer properties listed in Table 8.1 were used in the MLEA to determine the tensile strain at the bottom of the asphalt (ε_{HMA}) layer for different values of E_{HMA}. Table 8.2 shows the obtained tensile strains in the second column. Then, the elastic strain at the bottom of the geosynthetic-reinforced HMA (ε_{HGC}) was estimated using Eq. (2) for values of α ranging from 0.4 to 0.8. Lastly, the same layer properties from Table 8.1 were used in the MLEA, except that the HMA layer modulus was varied to back-analyze the elastic modulus that results ε_{HGC}. The obtained modulus values are presented as E_{HGC} for different values of α in Table 8.2.

Table 8.2. Results of MLEA for ε_HMA and E_HGC.

E_{HMA}	ε_{HMA}	E_{HGC} for $\alpha = 0.4$	E_{HGC} for $\alpha = 0.5$	E_{HGC} for $\alpha = 0.6$	E_{HGC} for $\alpha = 0.7$	E_{HGC} for $\alpha = 0.8$
(MPa)	--	(MPa)	(MPa)	(MPa)	(MPa)	(MPa)
2070	5.29E-05	7067	5240	4103	3344	2792
3450	3.61E-05	11804	8722	6861	5585	4668
6900	2.16E-05	22698	17120	13480	11101	9274
10350	1.59E-05	33193	25187	20030	16720	13893
13800	1.28E-05	43225	32937	26298	21685	18410

Figure 8.28 displays the ratio between E_{HGC} and E_{HMA} (i.e., E_{HGC}/E_{HMA}) for different values of α and E_{HMA}. As expected, decreasing 'α' values lead to increasing E_{HGC}/E_{HMA} ratios, indicating that the equivalent modulus for the HMA-GS Composite is higher if the geosynthetic reduces more significantly the strains in the asphalt layer. The analyses were conducted for values of E_{HMA} ranging from 2070 to 13800 MPa. As shown by the results presented in this figure, the E_{HGC}/E_{HMA} ratio was not significantly sensitive to E_{HMA}, with a limited range of variation for different E_{HMA} values. Accordingly, an average E_{HGC}/E_{HMA} value can be used for comparison as shown in Figure 8.28. Specifically, the average E_{HGC}/E_{HMA} ranges from 3.3 (for $\alpha = 0.4$) to 1.3 (for $\alpha = 0.8$), indicating the equivalent HMA-GS Composite modulus is 1.3 to 3.3 times higher than that of the unreinforced HMA.

α	E_{HGC}/E_{HMA} (AVG)
0.4	3.3
0.45	2.8
0.5	2.5
0.55	2.2
0.6	2.0
0.65	1.8
0.7	1.6
0.75	1.5
0.8	1.3
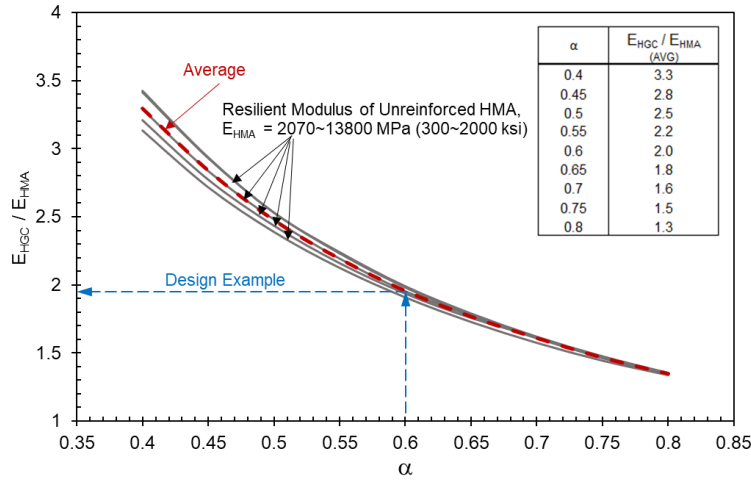
Figure 8.28. Ratio between equivalent HMA-GS Composite modulus and unreinforced HMA modulus using MLEA.

8.7.3.2. Equivalent HMA-GS Composite Layer Coefficient (a'_1)

The equivalent modulus of the HMA-GS Composite (E_{HGC}) was used in Eq. (6A) to estimate the equivalent (i.e., increased) structural layer coefficient for HMA-GS Composite (a'_1), as follows:

$$a'_1 = 0.384 \log(E_{HGC}) + 0.184 \qquad \text{Eq. (37)}$$

Using the E_{HGC}/E_{HMA} ratio, Eq. (37) can be reworked as follows:

$$a'_1 = 0.384 \log\left(\frac{E_{HGC}}{E_{HMA}} E_{HMA}\right) + 0.184 \qquad \text{Eq. (38)}$$

Or

$$a'_1 = a_1 + 0.384 \log\left(\frac{E_{HGC}}{E_{HMA}}\right) \qquad \text{Eq. (39)}$$

Considering the values obtained for E_{HGC}/E_{HMA} in Figure 8.28, the second term in Eq. (39) will be a constant value for each α. Accordingly, design lines to predict a'_1 are parallel to the line for estimating a_1. The design chart to estimate a'_1 for the various α values are shown in Figure 8.29 along with the original relationship to estimate a_1 in the unreinforced road. The input for all design lines (i.e., the horizontal axis in this chart) corresponds to the modulus of the unreinforced HMA (E_{HMA}).
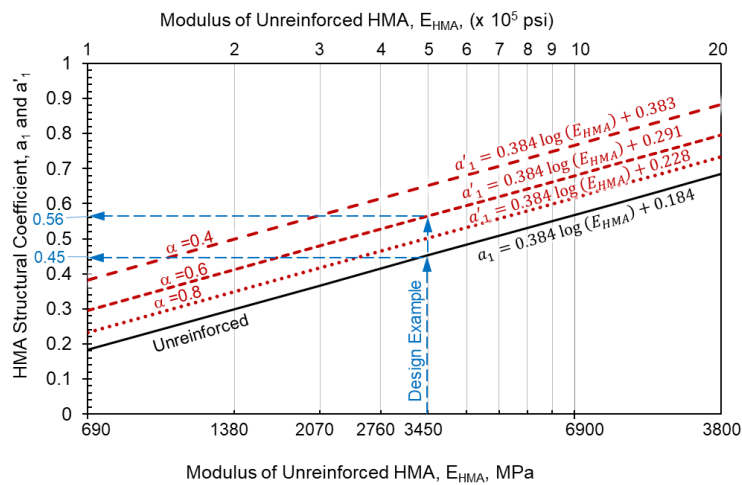
Figure 8.29. Design chart to predict the equivalent layer coefficient (⟦a'⟧ _1) for geosynthetic-reinforced HMA.

8.7.3.3. HMA-GS Composite Traffic Benefit Ratio (TBR_{HCR})

The increased HMA layer coefficient (a'_1) was used in Eq. (8) to estimate the increased structural number (SN') for the geosynthetic-reinforced asphalt road. Next, SN' and SN were used in Eq. (11) to estimate the HMA-GS Composite Traffic Benefit Ratio (TBR_{HGC}), the design chart for which can be seen in Figure 8.30.
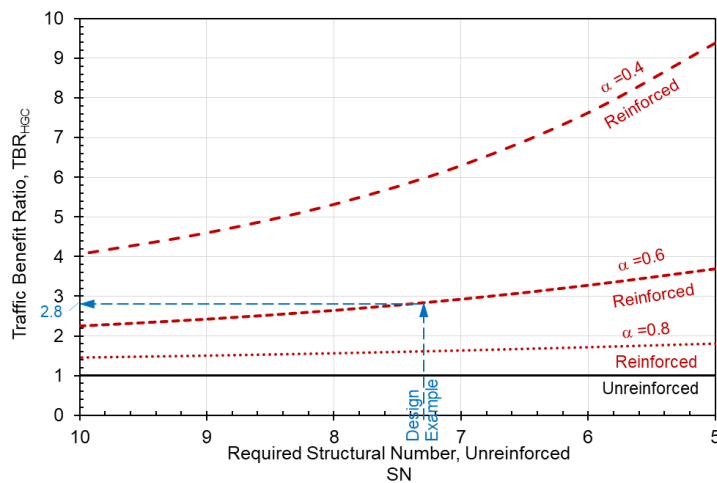
Figure 8.30. HMA-GS Composite Traffic Benefit Ratio (⟦TBR⟧ _HGC) in geosynthetic-reinforced asphalt road using equivalent HMA-GS Composite modulus.

238

8.7.3.4. Reduced HMA Layer Thickness (ΔD_{HMA})

Using the corresponding values of a'_1, a_1 and D_{HMA} into Eqs. (9) and (10), the equivalent (i.e., reduced) HMA thickness for the geosynthetic-reinforced asphalt road (D'_{HMA}) and reduced asphalt thickness (ΔD_{HMA}) can be estimated, respectively. Figure 8.31 shows the percentage decrease in HMA layer thickness for different values of 'α' and E_{HMA}. In all cases, the use of a geosynthetic reinforcement significantly reduced the required design thickness of the HMA layer. The percentage reduction in asphalt thickness ranged from approximately 23% to 35% for $\alpha = 0.4$ and 7% to 12% for $\alpha = 0.80$. The benefits from the geosynthetic reinforcement were found to diminish for comparatively stiff HMA layers.
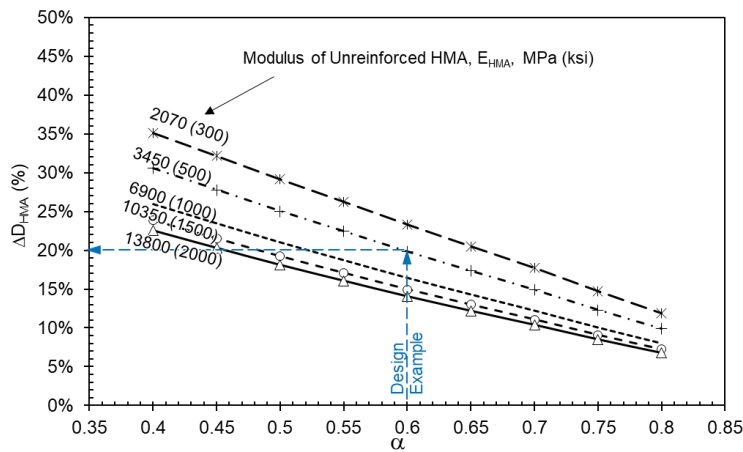
Figure 8.31. Percentage reduction in HMA layer thickness in geosynthetic-reinforced asphalt road using equivalent HMA-GS Composite modulus.

8.7.4. Design Charts for Equivalent HMA-GS Composite Axle Load Factor Approach

8.7.4.1. HMA-GS Composite Traffic Benefit Ratio (TBR_{HGC})

As derived in Eqs. (28) and (29), TBR_{HGC} expresses the ratio between the traffic volume of the geosynthetic-reinforced asphalt road and unreinforced road. As shown in Eq. (29), TBR_{HGC} is a function of α and f_2, which is the exponent for strain in transfer functions for fatigue cracking models. Among others, the values adopted for f_2 and f_3 by the Asphalt Institute (Shook et al. 1982) and Illinois Department of Transportation (DOT) (Thompson 1987) have commonly been used for roadway design, as follows:

Asphalt Institute: $f_2 = 3.291$ and $f_3 = 0.854$

Illinois DOT: $f_2 = 3.0$ and $f_3 = 0$

Using these values for f_2, TBR_{HGC} can be determined for various 'α' values as presented in Table 8.3 and Figure 8.32. As expected, comparatively greater benefits (i.e., higher traffic volume) were obtained for low α values. The expected traffic volume for the geosynthetic-reinforced asphalt road, with $\alpha = 0.4$, is estimated to be approximately 15 to 20 times that for the unreinforced HMA. Based on the values recommended by the two fatigue cracking transfer functions, predictions converge for higher values of α. At $\alpha = 0.8$, TBR_{HGC} is similar between the two methods (2.1 using the Asphalt Institute model versus 2.0 using the Illinois DOT model). The average TBR_{HGC} values in Figure 8.32 indicate that the traffic volume of the geosynthetic-reinforced asphalt road ranges from 2.0 (for $\alpha = 0.8$) to 18 (for $\alpha = 0.4$) times that of the unreinforced road.

Table 8.3. Traffic Benefit Ratio (〖TBR〗 _HGC) using equivalent HMA-GS Composite axle load factor.

α	TBR_{HGC} (Based on Asphalt Institute)	TBR_{HGC} (Based on Illinois DOT)	TBR_{HGC} (Average)
0.4	20.4	15.6	18.0
0.5	9.8	8.0	8.9
0.6	5.4	4.6	5.0
0.7	3.2	2.9	3.1
0.8	2.1	2.0	2.0
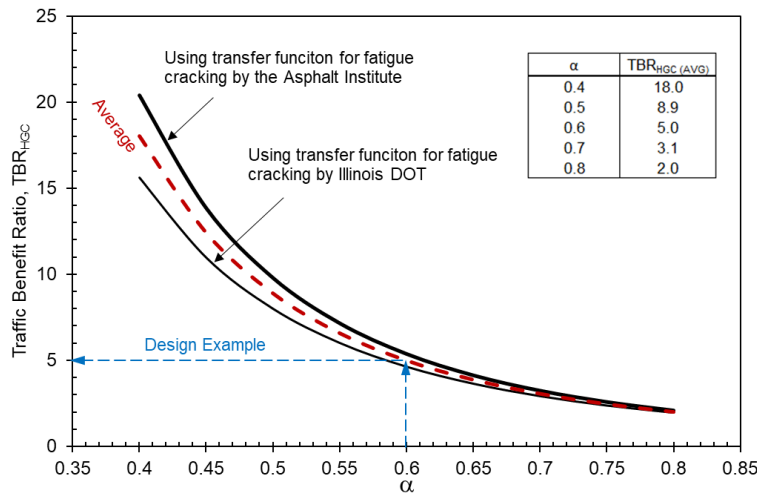
Figure 8.32. Traffic Benefit Ratio(〖TBR〗 _HGC) in geosynthetic-reinforced asphalt road using equivalent HMA-GS Composite axle load factor.

8.7.4.2. Design Structural Number (SN_{Design})

For the design objective of reducing asphalt thickness, the benefits from geosynthetic reinforcement can be expressed by solving Eq. (33) to obtain a reduced design structural number (SN_{Design}) for the same traffic volume and serviceability conditions. SN_{Design} can be obtained for any given $EALF_{HGC}$, G_t and SN values. Table 8.4 summarizes the SN_{Design} values solved from Eq. (33) for SN values ranging from 1.5 to 10 and α values of 0.4, 0.6 and 0.8. In this calculation, average $EALF_{HGC}$ values from Asphalt Institute and Illinois DOT were used. Also, assuming the initial and terminal serviceability as $p_{t\,0} = 4.2$ and $p_{t\,Terminal} = 2.7$, respectively, the serviceability loss and terminal loss of serviceability factors were used as $\Delta PSI = 1.5$ and $G_{t\,Terminal} = -0.26$, respectively.

Table 8.4. Design SN for geosynthetic-reinforced asphalt road.

SN (Unreinforced Road)	SN Design (Reinforced Road) for α = 0.4	SN Design (Reinforced Road) for α = 0.6	SN Design (Reinforced Road) for α = 0.8
10.0	7.0	8.2	9.2
9.0	6.3	7.4	8.3
8.0	5.5	6.5	7.3
7.0	4.7	5.7	6.4
6.0	3.9	4.8	5.4
5.0	3.1	3.9	4.5
4.0	2.4	3.0	3.6
3.0	1.8	2.3	2.7
2.0	1.2	1.5	1.8
1.5	0.8	1.1	1.3

Figure 8.33 illustrates the relationship between the design SN for an unreinforced and geosynthetic-reinforced asphalt road for different α values. Each design line in Figure 8.33 corresponds to a specific value of α. As expected, the data in Figure 8.33 confirms that the SN_{Design} decreased as 'α' decreased, suggesting greater benefits from geosynthetic reinforcement.
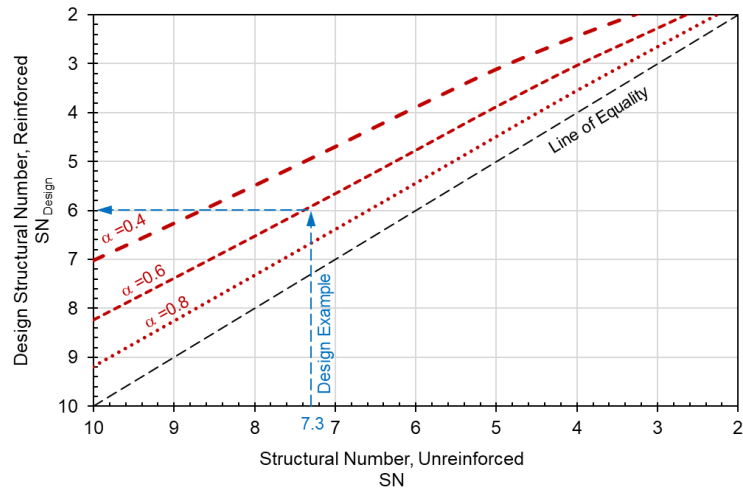
Figure 8.33. Design chart to estimate design SN for geosynthetic-reinforced asphalt road based on SN for unreinforced road, for same traffic volume.

8.7.4.3. Equivalent AASHTO 93 Design Chart

An alternative configuration of the design chart for the *SN* more consistent with the AASHTO 1993 design charts is presented in Figure 8.34. This figure shows the AASHTO 1993 design lines to estimate the required *SN* for unreinforced road along with the design lines considered in this study for various values of α to estimate the design *SN* for geosynthetic-reinforced asphalt road. The input for these design lines (on the vertical axis) is the same as that for the AASHTO 1993 nomographs. However, instead of using the design lines for unreinforced road, the design lines for reinforced road developed in this study can be used to estimate the design *SN*. An example demonstrating the use of this chart is presented in a subsequent section of this paper (see Design Example).

242
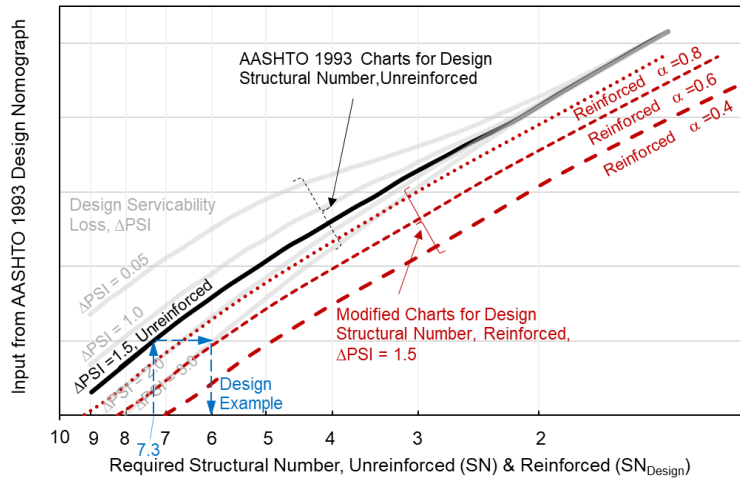
Figure 8.34. Equivalent AASHTO 1993 design chart to estimate design SN for geosynthetic-reinforced asphalt road.

8.7.4.4. Reduced HMA Layer Thickness (ΔD_{HMA})

The design SN for the geosynthetic-reinforced asphalt road can be used to reduce the HMA thickness. As expressed in Eq. (36), the reduction in HMA thickness (ΔD_{HMA}) can be obtained using SN, SN_{Design} and a_1. Since the asphalt layer coefficient (a_1) is a function of E_{HMA}, the absolute asphalt thickness reduction (ΔD_{HMA}) also changes for various E_{HMA} values. However, the percentage reduction in asphalt thickness will not directly depend on E_{HMA}, but it depends on SN, SN_{Design}, and characteristics of the base and subbase layers, as follows:

$$\frac{\Delta D_{HMA}}{D_{HMA}} = \frac{\frac{SN - SN_{Design}}{a_1}}{\frac{SN - a_2 D_2 m_2 - a_3 D_3 m_3}{a_1}} = \frac{SN - SN_{Design}}{SN - a_2 D_2 m_2 - a_3 D_3 m_3} \qquad \text{Eq. (40)}$$

Accordingly, using the values obtained above for SN and SN_{Design}, and characteristics of the base and subbase layers listed in Table 8.1, $\Delta D_{HMA}(\%)$ was calculated as presented in Table 8.5.

As an alternative presentation of the results in Table 8.5, Figure 8.35 presents a collective design chart showing both previously discussed design benefits from geosynthetic reinforcement (i.e., 1] modified design SN and 2] reduced HMA thickness):

- The design line shown by black solid line on the horizontal axis corresponds to the unreinforced road with SN ranging from 6 to 10.

243

- The red curves correspond to different α values and show the benefits from geosynthetic reinforcement:

  o On the horizontal axis, the range of SN values corresponding to the red curves indicates that geosynthetic reinforcement could reduce the range of design SN to 3.9 to 7.0 (for $\alpha = 0.4$), 4.8 to 8.2 (for $\alpha = 0.6$) and 5.4 to 9.2 (for $\alpha = 0.8$).

  o On the vertical axis, the red curves show the percentage reduction in HMA thickness, indicating that geosynthetic reinforcement could lead to a reduction in HMA thickness of 44% to 74% (for $\alpha = 0.4$), 26% to 45% (for $\alpha = 0.6$) and 12% to 20% (for $\alpha = 0.8$).

- For a given required SN for unreinforced road, the black dashed curves illustrate the benefits of using geosynthetic reinforcement with different α values. Reductions in the design SN are obtained by projecting these curves on the horizontal axis, and reductions in asphalt thickness are obtained by projecting these curves on the vertical axis.

Table 8.5. Design SN and percentage reduction in HMA thickness using equivalent HMA-GS Composite axle load factor.

α	SN = 6 (Unreinforced)		SN = 7 (Unreinforced)		SN = 8 (Unreinforced)		SN = 9 (Unreinforced)		SN = 10 (Unreinforced)	
	SN_{Design} (Reinforced)	ΔD_{HMA} (%)	SN_{Design} (Reinforced)	ΔD_{HMA} (%)	SN_{Design} (Reinforced)	ΔD_{HMA} (%)	SN_{Design} (Reinforced)	ΔD_{HMA} (%)	SN_{Design} (Reinforced)	ΔD_{HMA} (%)
0.4	3.9	77%	4.7	61%	5.5	53%	6.3	47%	7.0	44%
0.6	4.8	45%	5.7	36%	6.5	31%	7.4	28%	8.2	26%
0.8	5.4	20%	6.4	16%	7.3	14%	8.3	13%	9.2	12%
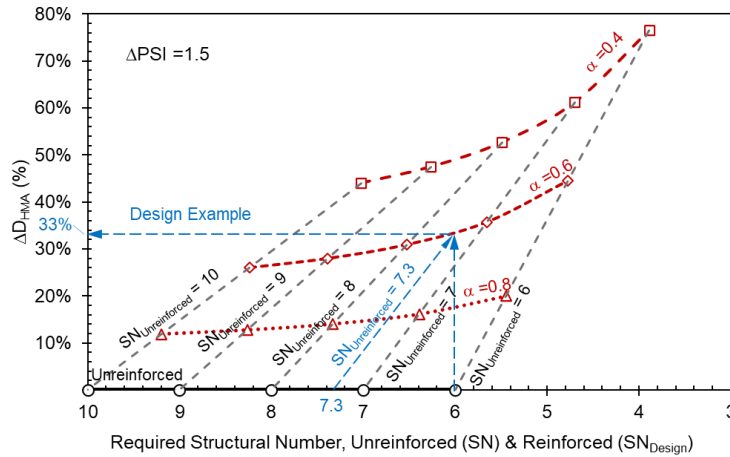
Figure 8.35. Collective design chart to estimate design SN and percentage reduction in HMA thickness using equivalent HMA-GS composite axle load factor approach.

8.8. Design Example

This section presents a design example to illustrate the proposed alternative designs for geosynthetic-reinforced asphalt road.

The unreinforced road section adopted in this example is considered to have the base and subbase course characteristics presented in Table 8.1. Considering a design traffic of 1020 million $ESAL$, the road design was established to require a SN of 7.3. Considering an HMA layer with a modulus of $E_{HMA} = 3,450\ MPa\ (500\ ksi)$ for unreinforced road, the structural layer coefficient for the HMA was obtained as $a_1 = 0.45$ using the information in Figure 8.29. Accordingly, the asphalt thickness is determined as $D_{HMA} = 229\ mm\ (9\ in)$.

Assume the designer considers using a geosynthetic reinforcement within the HMA layer that can reduce the elastic strain in the bottom of the HMA by 40% (i.e., $\alpha = 0.6$). Based on the design approaches and design charts presented in this study, alternative designs that can be adopted are as follows:

8.8.1. Adopting Equivalent HMA-GS Composite Modulus Approach:

- To achieve the design objective of increased traffic volume: Using $\alpha = 0.6$ and $SN = 7.3$:

245

- From Eq. (8), the equivalent (increased) SN for the geosynthetic-reinforced asphalt road is obtained as $SN' = 8.3$. From the design chart in Figure 8.30, the Traffic Benefit Ratio (TBR_{HGC}) is obtained as 2.8 and the traffic volume can be increased accordingly to $2.8 \times ESAL$.

- To achieve the design objective of reduced asphalt thickness: Using $\alpha = 0.6$ and $E_{HMA} = 3,450\ MPa$:

  - From the design charts in Figure 8.28 and Figure 8.29, the equivalent HMA-GS Composite modulus and modified layer coefficient for the geosynthetic-reinforced asphalt road are obtained as $E_{HGC} = 1.95 \times E_{HMA} = 6,728$ MPa, and $a'_1 = 0.56$.

  - From the design chart in Figure 8.31, the percentage reduction in HMA thickness can be obtained as $\Delta D_{HMA} = 20\%$; thus, the HMA thickness for the geosynthetic-reinforced asphalt road can be reduced to $D'_{HMA} = (1 - 0.20) \times D_{HMA} = 183\ mm$.

8.8.2. Adopting Equivalent HMA-GS Composite Axle Load Factor Approach:

- To achieve the design objective of increased traffic volume: Using $\alpha = 0.6$:

  - From the design chart in Figure 8.32, the Traffic Benefit Ratio (TBR_{HGC}) is obtained as 5.0 and the traffic volume can be increased accordingly to $5.0 \times ESAL$.

- To achieve the design objective of reduced asphalt thickness: Using $\alpha = 0.6$ and $SN = 7.3$:

  - From the design chart in Figure 8.33, the design (reduced) SN for the geosynthetic-reinforced asphalt road is obtained as $SN_{Design} = 6.0$. Alternatively, the design chart in Figure 8.34 could be used to obtain SN_{Design}. In this case, the point corresponding to $SN = 7.3$ can be mapped on the unreinforced road design line; the equivalent SN from the design line for $\alpha = 0.6$ can then be obtained, which results in the same SN_{Design} value of 6.0.

  - From the design chart in Figure 8.35, either $SN = 7.3$ or $SN_{Design} = 6.0$ can be used to find the percentage reduction in the HMA thickness ($\Delta D_{HMA}(\%)$). If $SN_{Design} = 6.0$ is used on the horizontal axis, the corresponding point on the design chart for $\alpha = 0.6$ can be obtained by extending a vertical line. If $SN = 7.3$

is used, the corresponding point on the design chart for $\alpha = 0.6$ can be obtained by interpolation between the lines corresponding to $SN = 7$ and $SN = 8$. Using either approach, $\Delta D_{HMA}(\%)$ is obtained as 33%; thus, the HMA thickness for the geosynthetic-reinforced asphalt road can be reduced to $D'_{HMA} = (1 - 0.33) \times D_{HMA} = 153\ mm$.

Table 8.6 summarizes the various alternative designs for the geosynthetic-reinforced asphalt road and compares them with the original design for the unreinforced road. Since the proposed design approaches follow different design concepts, the corresponding design outcomes will not be necessarily the same For example, the two design approaches suggest different reductions in HMA thickness and different traffic benefit ratios. Overall, the design example provided highlights the suitability of the design approaches and corresponding design charts presented in this study.

Table 8.6. Summary of design alternatives in design example.

	Design Approach		Design Parameters	Design Assumption	Predicted Geosynthetic Benefit
Unreinforced Road	AASHTO 1993 Empirical Design		$SN = 7.3$ $E_{HMA} = 3450\ MPa$ $a_1 = 0.45$ $D_{HMA} = 229\ mm$ $ESAL = 1020\ million$	-	-
Geosynthetic-Reinforced Asphalt Road (a = 0.6)	Equivalent HMA-GS Composite Modulus	Design Objective: Increase Traffic Volume	$SN' = 8.3$ $E_{HGC} = 6728\ MPa$ $a'_1 = 0.56$ $D_{HMA} = 229\ mm$ $ESAL' = 2.8 \times ESAL$	Asphalt thickness is the same as that in the unreinforced alternative	2.8 x traffic volume
		Design Objective: Reduce Asphalt Thickness	$SN = 7.3$ $E_{HGC} = 6728\ MPa$ $a'_1 = 0.56$ $D'_{HMA} = 183\ mm$ $ESAL = 1020\ million$	Traffic volume is the same as that in the unreinforced alternative	20% reduction in HMA thickness
	Equivalent HMA-GS Composite Axle Load Factor	Design Objective: Increase Traffic Volume	$SN = 7.3$ $EALF_{HGC} = 0.2$ $a_1 = 0.45$ $D_{HMA} = 229\ mm$ $ESAL' = 5.0 \times ESAL$	Asphalt thickness is the same as that in the unreinforced alternative	5.0 x traffic volume
		Design Objective: Reduce Asphalt Thickness	$SN_{Design} = 6.0$ $EALF_{HGC} = 0.2$ $a_1 = 0.45$ $D'_{HMA} = 153\ mm$ $ESAL = 1020\ million$	Traffic volume is the same as that in the unreinforced alternative	33% reduction in HMA thickness

8.9. Summary & Final Remarks

This chapter focuses on various activities completed under Task 7, specifically the synthesis and analysis of data collected from controlled traffic loading campaigns conducted before, during, and after the asphalt overlay construction at SH21. The effect of asphalt type, thickness, ambient air temperature, and time since construction (i.e., asphalt aging and degradation) on the performance of geosynthetic-reinforced asphalt overlay sections and quantification of increased roadway structural capacity has been summarized in detail. Additionally, design of roadways comprising geosynthetic-reinforced asphalt layers together with the development of design charts to quantify the increased roadway structural capacity in terms of increased traffic volume and decreased asphalt thickness has been discussed. A design example demonstrating such benefits due to the increased roadway structural capacity has also been presented.

Chapter 9. Characterization of Milling, Reuse and Recycling of Geosynthetic-Reinforced Asphalt

9.1. Introduction

This chapter reports the activities that have been completed in Task 12 of TxDOT Project 0-7002. The primary objective of Task 12 is to characterize the milling, reuse, and recycling of asphalt layers reinforced with paving interlayers to understand if the asphalt layers reinforced with paving interlayers are millable or not. Additionally, if millable, the subsequent characterization includes evaluating if the milled asphalt comprising paving interlayers are reusable and recyclable within the roadway base or surface courses. This technical memorandum elaborates specifics of the various laboratory tests conducted on the collected milled asphalt containing paving interlayer (geotextile) fragments. Specifically, the following laboratory tests were conducted:

1. Base course characterization

    o   Compaction tests

    o   Water absorption tests

    o   Abrasion resistance tests

    o   Hydraulic conductivity tests

    o   Resilient modulus tests

2. Surface course characterization

    o   Indirect tensile strength (IDT) tests

    o   Moisture susceptibility tests

In addition to geotextile interlayers, this report explains the milling of polyester (PET) and fiberglass (FG) geogrids.

9.2. Background

A conventional flexible pavement rehabilitation program adopted to restore roadway serviceability includes milling the existing old and oxidized asphalt surface and replacing it with a structural asphalt overlay (Kumar et al. 2021). Such rehabilitation programs involve milling operations that result in the generation of large quantities of asphalt millings, also referred to as

Reclaimed Asphalt Pavement (RAP). Specifically, about 138 million tons of RAP were stockpiled in the US in 2019, which is about 20% higher than that stockpiled in 2018 (NAPA 2019). The significant accumulation of RAP stockpiles necessitates developing sustainable construction techniques that can utilize RAP as a construction material in large quantities. Such sustainable construction techniques would ultimately reduce the burden on landfills and raw materials required for construction. Accordingly, use of RAP in the construction of roadway base, subbase and surface layers has become an integral part of the pavement industry (Mousa et al. 2021). The sustainable geotechnical use of RAP may also include their incorporation as backfill material in structures such as retaining walls and embankment fills. Soleimanbeigi et al. (2022) reported that the effective friction angle of compacted RAP was 39°, which is similar to that of a densely compacted sand, suggesting the possibility for use of RAP as an alternative to densely compacted sand. Additionally, Soleimanbeigi et al. (2022) reported that the hydraulic conductivity of RAP mixtures can be comparable to that of natural or other recycled aggregates, thus making it a good candidate for use in the embankment/fill applications. However, while RAP mixtures can potentially add ability of the backfill to freely drain, minimizing the possibility to development of excess pore pressures, the thermal sensitivity due to the asphalt binder coatings on other geotechnical properties requires more attention.

In addition, the manufacture of new asphalt mixes incorporating RAP has been a major application in sustainable roadway construction practice. Several researchers (Daryaee et al. 2020; Guo et al. 2014; Huang et al. 2005; Marin-Uribe and Restrepo-Tamayo 2022, Singh et al. 2017; Zhao et al. 2013) have evaluated the potential of incorporating RAP into Hot Mix Asphalt (HMA) layers. Specific mix design concerns have been addressed by evaluating the cracking resistance potential, rutting resistance and resistance to moisture damage of the asphalt mixtures containing RAP material. Moreover, RAP can also be used as granular base material in parking areas, shoulders, residential driveways as well as fill in trench drains. In addition, researchers (Guduru et al. 2022; Gupta et al. 2009; Kim et al. 2007; Locander 2009; Mousa et al. 2021; Plati and Cliatt 2018) have evaluated the possibility of adopting RAP in the construction of base and subbase layers, suggesting that high-quality base can be produced by blending RAP with virgin aggregates or treating RAP with chemical additives such as lime or cement. Specifically, an evaluation of RAP blends should account for variations in the type of aggregate, particle size distribution and binder content, as well as the resulting differences in mechanical and hydraulic properties.

The adoption of sustainable practices to extend pavement service life includes incorporating paving interlayers in the form of geotextiles, geogrids and geocomposites within asphalt layers to minimize reflective cracks and enhance pavement structural capacity (Canestrari et al. 2022; Correia and Zornberg 2016; Kumar et al. 2022; Saride and Kumar 2019; Solatiyan et al. 2020). The widespread adoption of paving interlayers as a sustainable technique has significantly

increased the likelihood of overlay projects in which the asphalt layers to be milled already include paving interlayers. Hence, experimental programs are needed to evaluate the characteristics and behavior of the RAP collected from such millings with paving interlayers. In addition, the current question within the asphalt pavement community on whether geosynthetics are indeed "millable" has remained largely unanswered because the existing literature on this topic is unfortunately very limited. The only available studies (Button and Lytton 2003; Marienfeld 2020) have focused on evaluating the millability of geosynthetic-reinforced asphalt layers where large and strong pieces of fabrics obtained from milling operations have been observed to clog milling drums and make the RAP unfit for recycling back into asphalt concrete. On the other hand, Tran et al. (2012) investigated the problem of milling geosynthetic-reinforced asphalt layers and found that the asphalt layers reinforced with paving mat were millable without any issues. In addition, Tran et al. (2012) evaluated asphalt mixtures prepared with 30% RAP (both with and without milled geosynthetic) and reported minor differences in terms of tensile strength properties, rutting performance, moisture susceptibility and thermal cracking analyses of the evaluated asphalt mixtures. Recently, Gu et al. (2021) reported that use of RAP with up to 30% geosynthetic fragments in the new asphalt mixtures showed excellent performance in terms of rutting resistance and moisture susceptibility.

In summary, only limited research has been carried out on the millability and recyclability of asphalt layers with interlayer fragments. As such, this requires a systematic evaluation that involves initially evaluating the millability of asphalt layers with paving interlayer, followed by evaluations for identification and characterization of asphalt millings containing geosynthetic (geotextile) fragments, or Geosynthetic RAP (GRAP) in the preparation of new asphalt mixtures as well as in the construction of base and subbase materials. This study aims at determining whether the asphalt layers with paving interlayer (geotextile/geogrid) are millable or not, followed by determining whether the presence of interlayer (geotextile) fragments in RAP blends has any impact on base course or asphalt surface course characteristics. An evaluation of base course blends incorporating GRAP and RAP materials included determination of particle size distribution, binder content, compaction characteristics, abrasion resistance, hydraulic conductivity, and resilient modulus. In addition, the actual asphalt mixtures comprising GRAP and RAP materials were evaluated via determination of particle size distribution, indirect tensile strength and moisture susceptibility characteristics.

9.3. Millability Evaluation of Asphalt with Geotextile Interlayer

The millability evaluation conducted under this task (Task 12) involved the milling of asphalt layers with and without paving (geotextile) interlayers separately using a cold milling machine. Specifically, asphalt layers with and without paving interlayers were milled as part of the rehabilitation program of an in-service highway (US 70/84) in Muleshoe, Texas. The

rehabilitation program included milling the pre-existing asphalt layer partially or completely (i.e., a fraction or the entire depth of the asphalt layer), installing a level-up course, applying tack coat, installing the new paving interlayer, and finally placing and compacting a 50-mm-thick asphalt overlay. Among these multiple field construction stages, this study focuses only on a field evaluation of the milling operations conducted as part of the rehabilitation program, which will be complemented with a subsequent experimental evaluation of the reuse and recyclability of the milled materials in roadway base and surface courses. Figure 9.1a shows the typical pre-existing roadway profile (cross-section) comprised of a sandy loam subgrade, 300-mm-thick granular base layer, and 110-mm-thick dense-graded asphalt layer with a paving interlayer. The uppermost 110-mm-thick asphalt layer depicted in Figure 9.1a consisted of a 50-mm-thick dense-graded asphalt layer, referred to as TY-C, overlain by a paving interlayer and a 60-mm-thick TY-C layer. The paving interlayer was a nonwoven geotextile manufactured using 60 to 80% polypropylene and 20 to 40% recycled polyester fibers with a mass per unit area of 139 g/m^2. This interlayer had been originally adopted to provide stress relief and moisture barrier functions and, therefore, had an ultimate grab tensile strength of only 0.45 kN at an elongation of about 50%, and an asphalt retention capacity of 0.91 l/m^2.
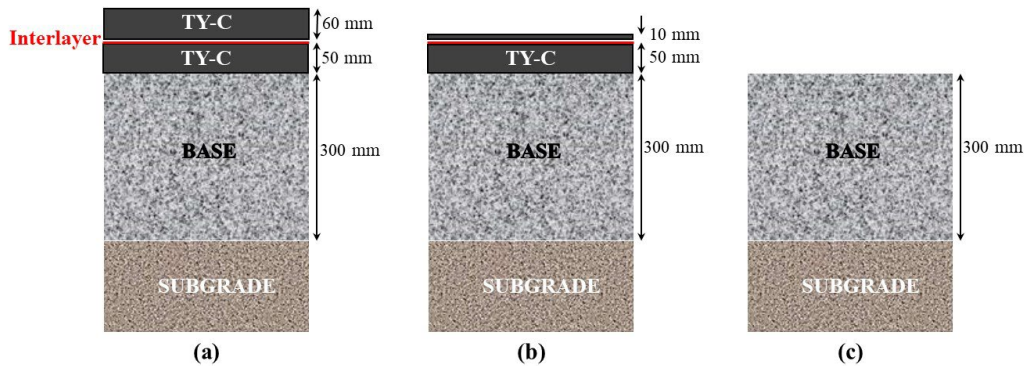
Figure 9.1. Cross-sections of typical roadway profiles: (a) pre-existing roadway; (b) after first stage of milling; and (c) after second stage of milling.

As part of the rehabilitation of the pre-existing asphalt, the milling operation for the 110-mm-thick asphalt layer was conducted in two stages. The first stage involved milling the top 50 mm to evaluate the millability of the asphalt layer without a paving interlayer (see Figure 9.1b). In the second stage, the rest of the asphalt layer, comprising a 50-mm-thick TY-C layer overlain by a paving interlayer and a remaining 10-mm-thick TY-C layer, was milled (see Figure 9.1c) to carry out the millability evaluation of asphalt layers with a paving interlayer. Figure 9.2a shows different views of the asphalt millings from the first (RAP) and second (GRAP) stages of milling operations, which were collected separately by dump trucks and transported to the stockpile location. Notably, the presence of a paving interlayer between asphalt layers did not affect milling operations and no traces of interlayer fragments were detected on the milling drum (see Figure 9.2b) after conducting milling operations. In other words, no difference was found

between the milling operations conducted on asphalt layers with and without paving interlayers. However, the RAP and GRAP materials visibly showed relevant differences in their particle sizes. Figure 9.3 displays representative samples of the RAP and GRAP materials collected from their respective stockpiles. As shown in the figure, the GRAP sample had comparatively larger particles compared to those in the RAP sample due to the presence of interlayer fragments and asphalt coating on the aggregates. However, due to their larger particle sizes, neither the RAP nor the GRAP samples were directly reused in the project as base or surface course, requiring additional processing to achieve the required gradations.

Figure 9.2. Milling operation to collect RAP and GRAP samples: (a) view of equipment during operations; and (b) detail of milling drum.

253
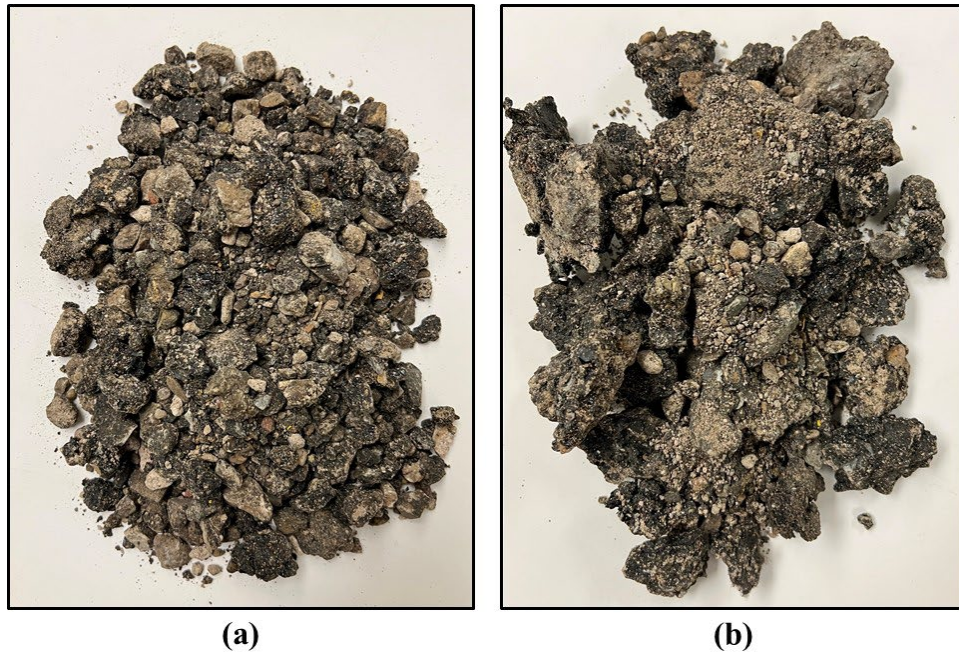
Figure 9.3. Representative samples of: (a) RAP; and (b) GRAP.

The RAP and GRAP sample processing procedure adopted in this study included crushing the samples in different batches using a modified Proctor compaction hammer. Specifically, GRAP samples weighing approximately 3 kg were placed in a modified Proctor mold and crushed by a 4.5-kg modified Proctor compaction hammer dropped about 100 times from a height of 450 mm. The RAP and GRAP samples are presented in Figure 9.4 and Figure 9.5, respectively both before and after crushing. The crushing process reduced the particle sizes of both RAP and GRAP samples to less than 37.5 mm. The RAP and GRAP samples were determined to have a specific gravity of 2.38 and 2.22; and water absorption values of 1.71% and 2.01%, respectively. The asphalt content of the RAP and GRAP samples was established according to a binder extraction test defined in AASHTO T164-22, and determined to be 4.92% and 5.87%, respectively. The higher asphalt content in the GRAP sample is attributed to the application of tack coat that is conducted during installation of the paving interlayers.

(a)   (b)
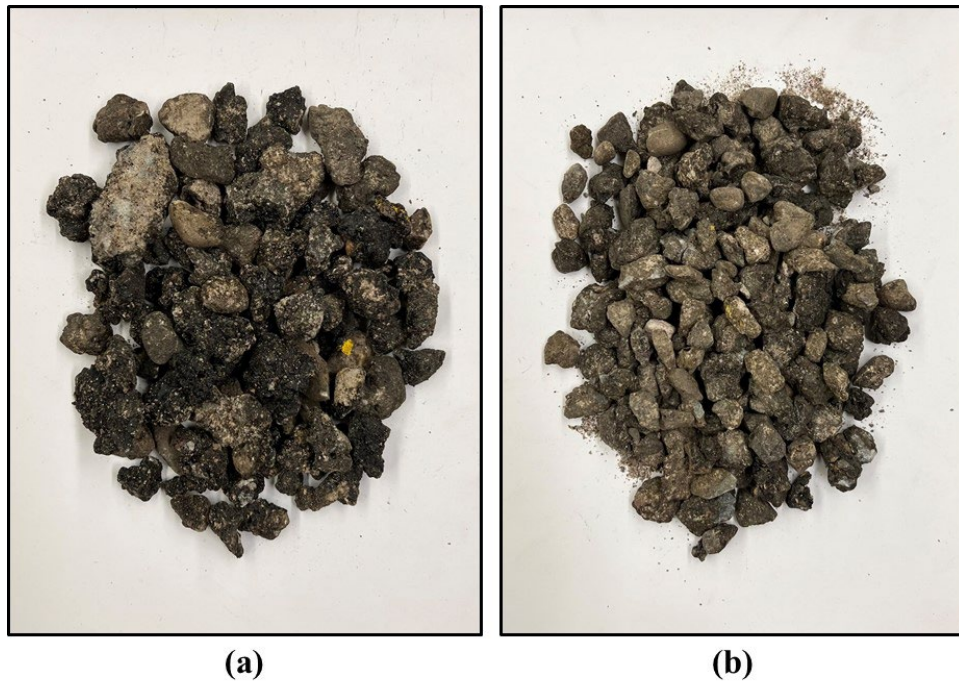
Figure 9.4. RAP samples: (a) before processing; and (b) after processing.

(a)   (b)
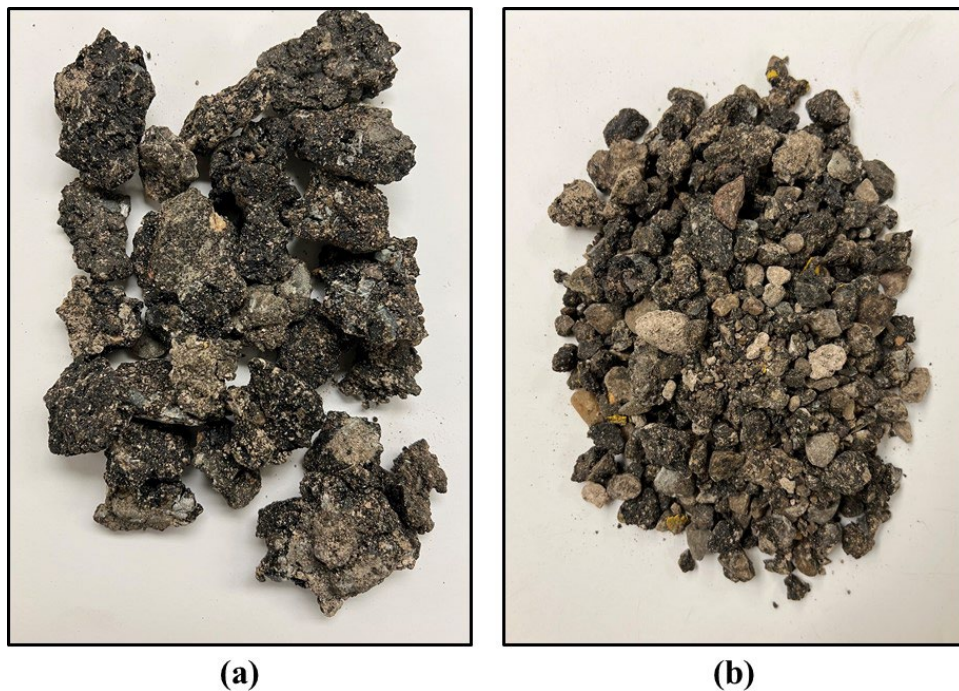
Figure 9.5. GRAP samples: (a) before processing; and (b) after processing.

Table 9.1 presents the particle size distribution of crushed GRAP and RAP samples. As indicated in the table, both samples had comparatively similar particle size distributions, although RAP

255

samples showed slightly finer particle sizes. The particle size distribution of the crushed GRAP sample revealed the presence of paving interlayer fragments that were greater than 12.7 mm and of 0.02% of particles that were finer than 0.075 mm. For the crushed RAP sample, the percentage of particles finer than 0.075 mm was determined to be 0.32%, which is also very low in relation to that conventionally required for base or surface courses. This condition necessitates blending the RAP and GRAP samples with Virgin Aggregate (VA) individually to achieve the gradation required for each blend (mixture) to be used as base and surface courses in roadway construction. The various RAP-VA and GRAP-VA blends prepared for this investigation as representative of those used in base and surface courses are detailed next.

Table 9.1. Particle size distribution of crushed GRAP and RAP samples.

Sieve size (mm)	Percentage passing (%)	
	GRAP	RAP
37.50	100.00	100.00
25.00	90.49	99.16
19.00	73.31	90.32
12.70	53.25	66.58
9.50	28.34	42.11
4.75	8.31	15.17
2.38	3.93	7.60
0.60	1.19	3.60
0.30	0.43	1.72
0.075	0.02	0.32

9.4. Recyclability Evaluation of Asphalt with Geotextile Fragments: Experimental Program

The recyclability evaluation conducted under this task (Task 12) involved the characterization of various RAP-VA and GRAP-VA blends as potential base and surface courses.

9.4.1. Base Course Characterization

Five different blends were prepared to evaluate the suitability and recyclability of GRAP material as a potential roadway base course. These blends consisted of 50% GRAP:50% VA (referred to as 50-50 GRAP), 50% RAP:50% VA (referred to as 50-50 RAP), 25% GRAP:75% VA (referred to as 25-75 GRAP); 25% RAP:75% VA (referred to as 25-75 RAP); and conventional Base Course (referred to as BC). The characteristics of the RAP and BC blends were evaluated and compared to those of the GRAP blends to assess the effects and suitability of incorporating GRAP as base course material. Specimens containing up to 50% RAP/GRAP were prepared based on the mix proportions used in the previous studies (Cavalli et al. 2017;

MacGregor et al. 1999). Moreover, the existing literature indicates that 100% RAP could not produce a high-quality base course due to its high deformation and creep (Dong and Huang 2014). Preparation of the GRAP and RAP blends entailed mixing the target proportions (by weight) of VA with crushed GRAP material and RAP material separately. Table 9.2 shows the particle size distribution of the five base course blends, including the 50-50 GRAP, 50-50 RAP, 25-75 GRAP, 25-75 RAP and conventional BC blends, evaluated herein, as well as Texas Department of Transportation (TxDOT) specifications (TxDOT, 2014) aggregate size limits for base course. As shown in the table, the particle size distributions for the three blends (25-75 GRAP, 25-75 RAP, and BC) were well within the gradation requirements for granular base course per TxDOT specifications (TxDOT, 2014). While a few particle sizes of 50-50 GRAP and 50-50 RAP were determined to be beyond the TxDOT specifications for base course. Such particle size gradations were obtained due to the presence of coarser particles of RAP and GRAP in a given blend which now occupied 50% weight of the total blend. The characterization of the base course blends to evaluate their suitability as base course material included compaction, water absorption, abrasion resistance, hydraulic conductivity, and resilient modulus tests, as detailed next. Please note that all the tests detailed next were repeated twice to confirm their repeatability and it was determined the tests were deemed repeatable, as the maximum variation in results was approximately 5%.

Table 9.2. Particle size distribution of base course blends.

Sieve size (mm)	Percentage passing (%)					
	50-50 GRAP	50-50 RAP	25-75 GRAP	25-75 RAP	VA	TxDOT Specification
37.50	100.0	100.0	100.0	100.0	100.0	100-98
25.00	89.2	95.0	90.3	92.1	90.0	94-78
19.00	74.1	88.5	79.7	83.2	82.0	85-64
12.70	52.3	67.3	61.8	64.3	65.0	70-50
4.75	27.1	32.4	37.7	38.8	48.0	50-30
2.36	20.3	23.4	26.1	26.5	34.0	36-22
0.60	18.1	18.3	15.6	16.0	21.0	23-8
0.30	9.6	10.2	12.6	12.6	17.0	19-3
0.075	1.3	1.8	4.6	4.2	6.0	7-2

9.4.2. Compaction Testing Program

Modified Proctor compaction tests were conducted per ASTM D1557 (ASTM D1557, 2021) on the five base course blends to determine their moisture-unit weight characteristics. The test procedure involved adding a molding water content to the blends and mixing before placing them in a compaction mold in five equal layers. Each layer was compacted by dropping a 0.04 kN rammer from a height of 457 mm about 56 times, which applied a total compactive effort of

2700 kN-m/m^3 for all five layers. The total weight of the compacted sample and volume of the compaction mold was measured to calculate the corresponding bulk unit weight of the compacted sample. Additionally, a portion of the compacted sample was collected, weighed and placed in a hot air oven to obtain the sample's moisture content as well as its bulk unit weight to determine the sample's dry unit weight. The test was repeated for different molding moisture content values, and the dry unit weight and moisture content corresponding to each was obtained for the compacted sample. The variations in dry unit weight with molding moisture content were then plotted to determine the maximum dry unit weight and optimum moisture content of the base course blends evaluated in this study.

9.4.3. Water Absorption Testing Program

Water absorption tests were conducted per AASHTO T85 (AASHTO T85, 2022) on all five base course blends to determine their ability to absorb moisture under specific conditions, which in turn showed the material's internal structure (e.g., if the material is porous or comparatively impervious). The test procedure involved oven-drying a sample of about 3 kg in a hot air oven, and then cooling it at room temperature for one to three hours and recording the sample weight. The samples were subsequently immersed in room temperature water for about 24 hours. The samples were then removed from the water bath and weighed after surface drying by rolling the samples on an absorbent cloth until no visible traces of water remained. The water absorption value was ultimately determined using the relationship between the oven-dried mass and saturated surface dry mass of the samples.

9.4.4. Abrasion Resistance Testing Program

The Los Angeles (LA) abrasion test was conducted per ASTM C131 (ASTM C131, 2020) to determine the toughness of the base course material evaluated herein, which in turn establishes the material's resistance to mechanical degradation. The test procedure involved oven-drying a sample of about 10 kg, and then cooling it at room temperature for one to three hours and recording the sample weight. The sample was then placed together with 12 steel spherical balls in the drum of an LA abrasion machine rotating at a speed of 30 to 33 revolutions/minute for about 500 revolutions. The samples were then removed from the rotating drum, sieved through a 1.6-mm sieve and the retained sample weighed. The abrasion resistance value was ultimately determined using the relationship between the oven-dried and retained mass of the samples.

9.4.5. Hydraulic Conductivity Testing Program

The drainage characteristics of a base course material play a crucial role in pavement performance. Specifically, moisture entrapped in the base layer can lead to severe deterioration of the base and subgrade layers, thereby compromising pavement performance. Constant head

hydraulic conductivity tests were conducted according to ASTM D2434 (ASTM D2434, 2022) on the five base course blends to determine their hydraulic characteristics. The test procedure involved compacting samples of each blend at its maximum dry unit weight and optimum moisture content in five equal layers in a mold measuring 152 mm in diameter and 254 mm in height. The compacted samples were fully saturated via a constant pressure head and the hydraulic conductivity was thereby obtained for the different blends evaluated in this study.

9.4.6. Resilient Modulus Testing Program

The stiffness of the five different base course blends evaluated herein were determined by conducting resilient modulus tests per AASHTO T307 (AASHTO T307, 2021). Specifically, a triaxial cell was used to maintain a constant confining pressure while simultaneously applying cyclic axial loading. Specimens for the resilient modulus tests were prepared at their respective maximum dry densities and optimum moisture contents in a cylindrical mold that had diameter and height of 100 mm and 200 mm, respectively. For a typical Type 1, or compacted specimens of Type 2 base course materials, the diameter of molded specimens should be equal to five times the size of the maximum particle, per AASHTO T307 recommendations. In this study, since cylindrical specimens of 100 mm diameter and 200 mm height were used, the particles greater than 19 mm were replaced with equivalent weight of particles having size less than 19 mm. Similar specimen preparation procedures have been previously adopted by Dong and Huang (2014) and Wu et al. (2012). The test procedure adopted in this study involved placing the specimen assembly that required use of porous stones, specimen caps, membrane, and O-rings, inside the triaxial cell. The axial loading piston and triaxial cell were positioned so that the loading piston came into contact with the specimen. The confining pressure applied to the specimen was controlled via cell pressure and back pressure valves before the axial load was applied. The testing program involved pre-conditioning the specimen by applying haversine load pulses for about 500 cycles at a frequency of 1 Hz, with each load cycle consisting of 0.1 seconds of loading followed by a rest period of 0.9 seconds. Following the specimen pre-conditioning, about 15 sequences of 100 load cycles each were applied with increasing confining pressure and axial loads. The resilient modulus was calculated as the average value obtained from the last five cycles of each sequence.

9.5. Surface Course Characterization

To evaluate the suitability and recyclability of GRAP material as a potential dense-graded asphalt surface course, five different asphalt mixtures were prepared. These mixtures included 30% GRAP:70% VA (referred to as 30-70 GRAP); 30% RAP:70% VA (referred to as 30-70 RAP); 15% GRAP:85% VA (referred to as 15-85 GRAP); 15% RAP:85% VA (referred to as 15-85 RAP); and a conventional dense-graded Asphalt Course mix (referred to as AC). Item 340 of

TxDOT specifications (TxDOT, 2014) suggests that not more than 30% of RAP should be used in the surface course. Moreover, Singh et al. (2017) reported that moisture damage of asphalt mixtures containing RAP improved until 30 % RAP content, and further increase in RAP content made the asphalt mixture vulnerable to moisture damage. In this study, the characteristics of the RAP and AC mixtures were evaluated and compared to those of the GRAP mixtures to assess the effects and suitability of incorporating GRAP into dense-graded hot mix asphalt. Preparation of the GRAP and RAP mixtures consisted of separately blending about 30% and 15% crushed GRAP material (by weight) respectively with 70% and 85% VA, and 30% and 15% crushed RAP material (by weight) respectively with 70% and 85% VA. Table 9.3 shows the particle size distribution of the aggregates in the five dense-graded surface course mixtures, including the 30-70 GRAP, 30-70 RAP, 15-85 GRAP, 15-85 RAP and AC mixtures, evaluated in this study. As shown in the table, the particle sizes for all the five mixtures were well within the dense-graded asphalt surface course requirements per TxDOT specifications (TxDOT, 2014). A Performance Grade (PG) 64-22 binder was used in the preparation of all five asphalt mixtures. An optimum binder content corresponding to a target air void content of 7% was determined to be 3.55% (30-70 GRAP), 3.7% (30-70 RAP), 4% (15-85 GRAP), 4.10% (15-85 RAP), and 4.45% (AC) per ASTM D6925 (ASTM D6925, 2015). As expected, the binder content of the AC mixture was higher than that of the RAP and GRAP mixtures due to the presence of binder in the RAP and GRAP materials. A Superpave gyratory compactor was used to compact all specimens prepared for the evaluation of asphalt mixtures containing GRAP and RAP materials. Specimen preparation involved heating the aggregates and binder to temperatures of 110 °C and 150 °C, respectively, after which the aggregates and binder were mixed at a temperature of 160 °C and then compacted at a temperature of about 145 °C. Multiple specimens of the five different asphalt mixtures were prepared to determine the optimum binder content. In addition to the tests described to characterize the base course materials, characterization of the dense-graded asphalt mixtures, including indirect tensile strength and moisture susceptibility tests, are detailed next. Please note that all the tests detailed next were repeated at least twice to confirm their repeatability and it was determined the tests were repeatable with variations of less than 5% between them.

Table 9.3. Particle size distribution of asphalt mixtures.

Sieve size (mm)	Percentage passing (%)					
	30-70 GRAP	30-70 RAP	15-85 GRAP	15-85 RAP	AC	TxDOT Specification
19.00	100.0	100.0	100.0	100.0	100.0	100
12.70	98.4	98.6	98.5	98.4	98.0	100-98
9.50	94.7	92.6	94.8	94.0	94.3	100-85
4.75	69.2	66.6	69.1	68.6	67.0	70-50
2.36	40.2	39.9	40.2	40.1	38.0	46-35
0.60	27.5	25.2	27.5	27.1	20.0	29-15

0.30	13.3	14.2	14.1	14.6	11.0	20-7
0.075	4.7	3.7	4.8	6.0	5.3	7-2

9.5.1. Indirect Tensile Strength Testing Program

The indirect tensile strength test (herein referred to as IDT) was used to characterize the tensile strength and viscoelastic properties of the asphalt mixtures, and evaluate their rutting and cracking potential. The IDT was conducted per ASTM D6931 (ASTM D6931, 2017) to obtain the indirect tensile strength of the five different asphalt mixtures evaluated herein. Specifically, a cylindrical specimen was loaded vertically in its diametrical position so that uniform tensile stresses were generated perpendicular to the load along the diameter of the specimen (see Figure 9.6a). The cylindrical specimens were prepared to a target air void content of 7% using the Superpave gyratory compactor, resulting in dimensions of 150 mm in diameter and 95 mm in thickness. Three specimens were prepared and tested from each of the five different asphalt mixtures. The IDT test procedure involved conditioning the specimens at a constant temperature (25 °C) for about 2 hours, followed by placement in the loading frame (see Figure 9.6b) after which the load was applied at a displacement rate of 50 mm/min until failure (see Figure 9.6c). The load and displacements are recorded so that the maximum load and corresponding displacement are determined for each test to calculate the indirect tensile strength, as follows (ASTM D6931, 2017):

$$\sigma_{IDT} = \frac{2000 P_{max}}{\pi t d} \qquad\qquad (1)$$

where, σ_{IDT} is the indirect tensile strength, in kPa; P_{max} is the ultimate load applied, in N; and t and d are the thickness and diameter of the specimen, respectively, in mm.

(a)   (b)   (c)
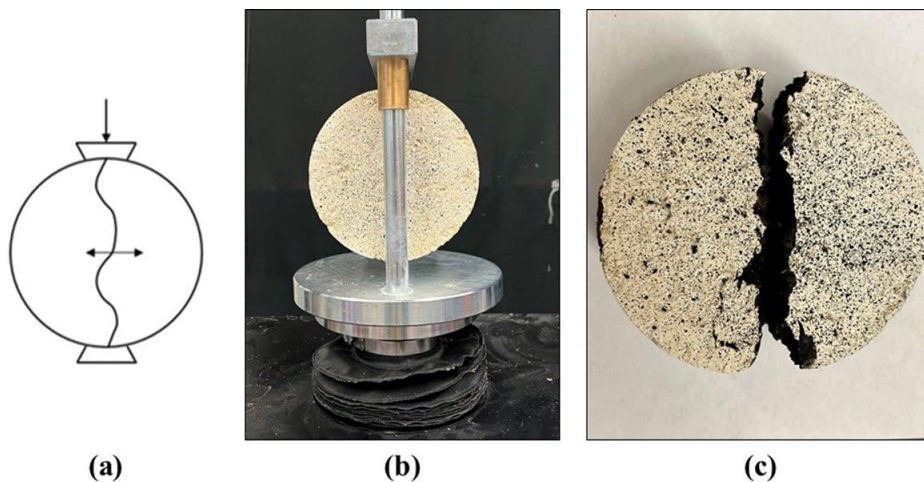
Figure 9.6. Indirect Tensile Strength Test (IDT): (a) schematic view; (b) IDT specimen before testing; and (c) IDT specimen after testing.

9.5.2. Moisture Susceptibility Testing Program

Moisture susceptibility tests are performed to determine the potential for moisture damage to the asphalt mixtures subjected to the presence of moisture over prolonged periods of time. The test procedure per ASTM D4867 (ASTM D4867, 2022) involves conducting IDT to determine the moisture susceptibility in terms of tensile strength ratio. Six specimens were prepared for each of the five different asphalt mixtures to a target air void content of 7% using the Superpave gyratory compactor. The specimens were then tested under both dry and wet conditions. The dry condition test series involved conditioning the specimens at 25 °C for about 2 hours, while the wet condition test series involved partially saturating the specimens (to a degree of saturation of 70 to 80%) and then immersing them in a 60 °C water bath for about 24 hours. IDT tests were conducted using the dry and wet specimens by loading them at a displacement rate of 50 mm/minute under a temperature of about 25 °C, ultimately resulting in the dry and wet indirect tensile strengths of the asphalt mixtures. The ratio of the wet and dry indirect tensile strengths is referred to as the Tensile Strength Ratio (TSR), which is determined as follows:

$$TSR = \frac{\sigma_{IDT,wet}}{\sigma_{IDT,dry}} \qquad (2)$$

where, $\sigma_{IDT,wet}$ and $\sigma_{IDT,dry}$ are the indirect tensile strengths at wet and dry conditions, respectively, in kPa. The TSR is a measure of the asphalt mixtures' potential for moisture damage, i.e., a greater TSR value results in the least moisture damage and vice versa.

9.6. Recyclability Evaluation of the Base Course: Discussion of the Experimental Results

9.6.1. Compaction Characteristics

The moisture-unit weight characteristics of the five base course blends evaluated herein were determined following the procedures described previously. Specifically, the relationships between dry unit weights and molding moisture contents were determined, with the results presented in Figure 9.7. As the results in this figure indicate, the trends that are typical of soils were also observed in the GRAP and RAP blends. That is, the compaction curves for all base course blends show an initially increasing dry unit weight with increasing molding moisture content up to a peak value, subsequently showing a decreasing unit weight with further increase in moisture content. The Maximum Dry Unit weight (MDU) and Optimum Moisture Content (OMC) values obtained for the five blends evaluated in this study were 21.4 kN/m³ and 4.43% (50-50 GRAP); 22.1 kN/m³ and 5% (50-50 RAP); 22.5 kN/m³ and 5.07% (25-75 GRAP); 22.9 kN/m³ and 5.21% (25-75 RAP); and 24.1 kN/m³ and 5.5% (VA), respectively. The MDU inclines to decrease with increase in RAP/GRAP content in the blends. Moreover, OMC also decreases with an increase in RAP/GRAP content in the blends. From Figure 9.7, it can be

observed that MDU of 50-50 GRAP, 50-50 RAP, 25-75 GRAP, and 25-75 RAP is about 11.2%, 8.3%, 6.6%, and 5% respectively, lower than that of the BC blend. Additionally, the OMC of 50-50 GRAP, 50-50 RAP, 25-75 GRAP, and 25-75 RAP is about 19.45%, 9.09%, 7.81%, and 5.27% respectively, lower than that of the BC blend. Such a condition may be due to the fact that moisture holding capacity of RAP is lower than that of BC, since RAP material has less fines (passing 0.075 mm sieve) than BC, and most of the RAP/GRAP particles are coated with asphalt, which reduces the moisture absorption capacity of the blends (Mousa et al. 2021). Among the GRAP and RAP blends, the MDU and OMC of the 50-50 GRAP blend were lower than those for the 50-50 RAP blend, which were in turn lower than those for the 25-75 GRAP blend, followed by the 25-75 RAP blend. These reductions in MDU and OMC may be attributable to the presence of asphalt in the GRAP and RAP material, while the presence of interlayer fragments may account for the additional reductions in the 50-50 GRAP and 25-75 GRAP blends in comparison with 50-50 RAP and 25-75 RAP blends, respectively. Similar trends showing a reduction of about 11% in the MDU of RAP as compared to that for conventional base were reported by Mousa et al. (2021). Additionally, Saride et al. (2016) reported that the OMC of RAP bases were lower than those for conventional bases.
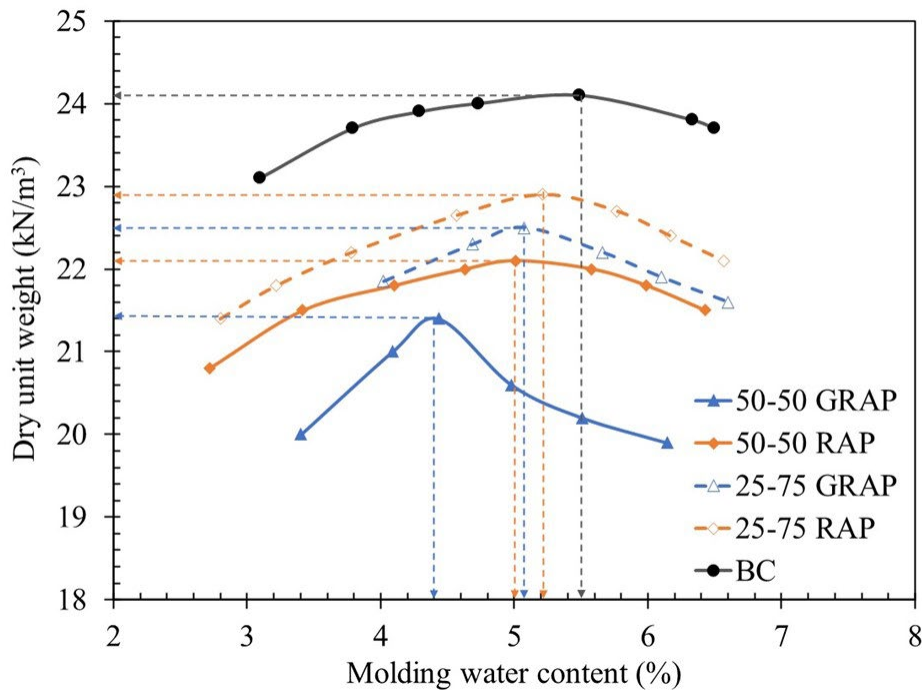
Figure 9.7. Compaction curves of the different base course blends.

9.7. Water Absorption Capacity

The water absorption capacity of the five base course blends evaluated herein were determined to be 2.51% (50-50 GRAP), 2.06% (50-50 RAP), 2.64% (25-75 GRAP), 2.53% (25-75 RAP) and

2.82% (VA). The lower water absorption capacity values of the GRAP and RAP blends in relation to that of the BC blend can be attributed to the presence of asphalt in the RAP and GRAP blends. Specifically, the asphalt in the RAP and GRAP blends would fill the pores of aggregates and thereby reduce their ability to absorb moisture, while the pores of the VA are comparatively less impeded to absorb moisture. However, of the GRAP and RAP blends evaluated herein, both the 50-50 and 25-75 GRAP blends showed higher water absorption capacity compared respectively to 50-50 RAP and 25-75 RAP blends possibly due to the presence of interlayer fragments that may absorb additional moisture. Saride et al. (2016) also reported lower water absorption capacities for RAP blends compared with those for conventional base, suggesting the hydrophobic nature of the asphalt coating is responsible for the lower water absorption capacities of RAP material in comparison with conventional road base. It is also important to note that lower water absorption capacity can result in a comparatively better resistance against moisture degradation of the roadway base.

9.8. Abrasion Resistance Characteristics

The abrasion resistance characteristics of the five base course blends tested in this study were evaluated using the LA abrasion test. Abrasion values were determined to be 9.5%, 17.2%, 17.66%, 21.12% and 25.4% for the 50-50 GRAP, 50-50 RAP, 25-75 GRAP, 25-75 RAP and VA blends, respectively. It should be noted that the limiting value of abrasion obtained via the LA abrasion test for coarse aggregate particles to be used as road base is 50% per AASHTO M147 (AASHTO M147, 2021). The abrasion values for the GRAP and RAP blends were determined to be lower than that for the BC blend, which suggests that the RAP and GRAP material exhibits greater resistance to abrasion and impact loading. Specifically, the impact energy is expected to be more efficiently absorbed by the asphalt and interlayer fragments in the GRAP blends, resulting in reduced particle breakage as compared to that for the RAP blends. Amongst the GRAP and RAP blends evaluated herein, the 50-50 GRAP blend had the lowest abrasion value followed by 50-50 RAP, 25-75 GRAP, and finally 25-75 RAP blends. Such resistance against abrasion may be due to the presence of interlayer fragments that allow additional capacity to absorb the impact energy and reduce damage to aggregate particles in GRAP mixtures. Additionally, the asphalt on RAP surface absorbs the impact energy and dissipates, which results in lesser separation of the agglomerated fine aggregate, thus leading to reduction in fragmentation value (particle breakage value) (Guduru et al. 2022).

9.9. Hydraulic Characteristics

The saturated hydraulic conductivity values were determined for all five blends investigated in this study via the constant head permeability test. The results, plotted in Figure 9.8, show that the hydraulic conductivity was lowest in the BC blend, followed by the 25-75 RAP and 50-50 RAP

blend, and finally the 25-75 GRAP and 50-50 GRAP blend, which had the highest hydraulic conductivity. The higher hydraulic conductivity values in the GRAP and RAP blends compared to BC blends can be attributed to the lower unit weight (i.e., higher void) achieved during preparation of the specimens, compacted to the same compaction energy. Additionally, the higher permeability determined for the GRAPs blend as compared to that for the corresponding RAPs blend can be attributed to the presence of interlayer fragments that absorb moisture. Similar hydraulic conductivity values for the RAP and BC blends were reported by Gupta et al. (2009). In contrast, Locander (2009) and Mousa et al. (2021) reported comparatively lower permeability values for RAP blends in comparison with conventional road base material, suggesting that the presence of RAP reduced the porosity of the blends. Additionally, they reported that the interlocking between the RAP and VA particles resulted in reduced permeability due to the aggregation of RAP particles during compaction of the blends. However, it should be noted that the percentage of particles finer than 0.075 mm was lower in the GRAP and RAP blends than that in the BC blend (see Table 9.2). This is consistent with the comparatively higher permeability values that were determined for the GRAP and RAP blends tested herein. The differences in permeability values reported in the aforementioned studies could be due to variability in the properties of the VA and RAP materials used.
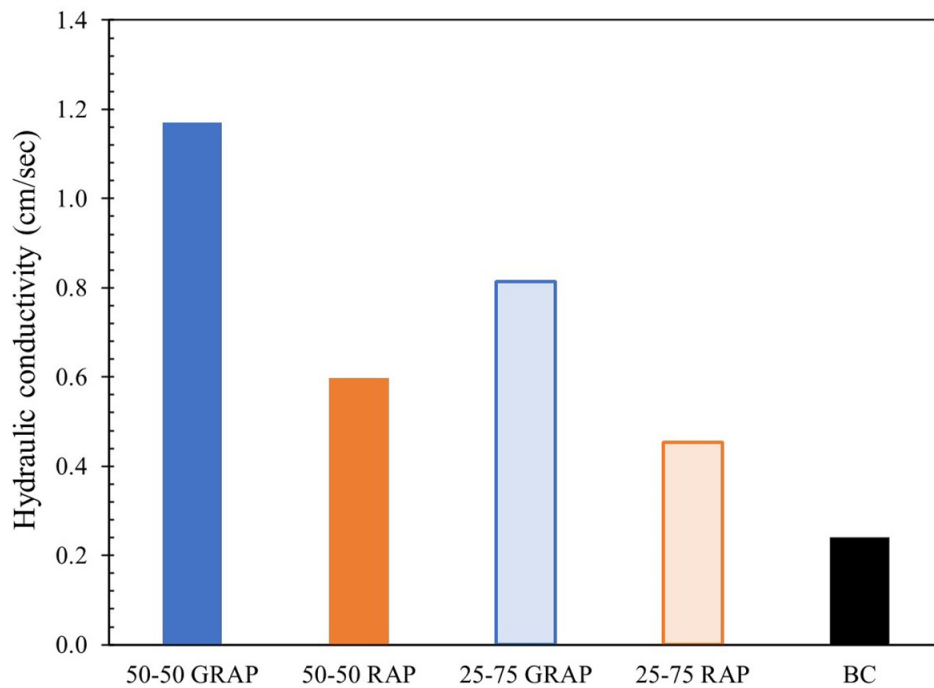
Figure 9.8. Saturated hydraulic conductivity of base course blends.

9.10. Resilient Modulus Characteristics

Figure 9.9 shows the resilient modulus test results obtained for the five base course blends evaluated herein, presented as a function of the bulk stress. The cyclic testing program involved application of three different amplitude loadings for each confining pressure. That is, three different deviatoric stresses were applied for each of the five confining pressures considered in the testing program, which resulted in three resilient moduli at a given confining pressure for each one of the five blends investigated in this study. Subsequently, the bulk stress (Θ), which is the summation of confining stresses acting in three different directions on the specimens and deviatoric stress acting in vertical direction on the specimen, was determined. As expected, the resilient modulus increased with increasing bulk stress for all the blends evaluated herein. In addition, resilient modulus values increased with the increase in the percentage of RAP/GRAP in the blends. It can be observed from Figure 9.9 that the 50-50 RAP blend has higher resilient modulus followed by 50-50 GRAP, 25-75 RAP, 25-75 GRAP, and finally BC blend. This is due to the fact that the blending of RAP/GRAP with the VA to constitute RAP/GRAP blends enhance the cohesion between particles because of the existing asphalt that coats the VA in RAP/GRAP blends that leads to a stiffer blend. The resilient modulus values obtained in this study for 50-50 RAP and 25-75 RAP complies with the findings from studies conducted by Kim et al. (2007), MacGregor et al. (1999), and Mousa et al. (2021). However, it should also be noted that different studies have reported different amplitudes of resilient modulus, which may be due to the variation in the RAP source, aged binder on RAP, RAP gradation. Moreover, the results also indicate that the resilient moduli of the BC blend are the highest at low bulk stress but increases gradually as bulk stress increase. In contrast, the resilient moduli of the 50-50 GRAP, 50-50 RAP, 25-75 GRAP and 25-75 RAP blends were comparatively lower than that of the BC at low bulk stress but they increased significantly with increasing bulk stress. For instance, at a bulk stress of 81 kPa, the resilient moduli of 50-50 GRAP, 50-50 RAP, 25-75 GRAP, 25-75 RAP and BC blends were on the order of 12.22 MPa, 18.23 MPa, 18.56 MPa, 21.34 MPa and 32.43 MPa, respectively. While at bulk stress of around 665 kPa, these values increased to 299.63 MPa, 405.85 MPa, 224.04 MPa, 255.40 MPa and 179.18 MPa respectively for 50-50 GRAP; 50-50 RAP, 25-75 GRAP, 25-75 RAP and BC blends. These trends suggest that the particles in the GRAP and RAP blends may have been rearranged with increasing bulk stress resulting in stiffer configurations. On the other hand, the BC blend had a well-graded particle size distribution that resulted in comparatively higher moduli at low confining pressures and increased comparatively more gradually with increasing confining pressures. Kim et al. (2007) reported similar trends, which highlighted that 50-50 RAP blends develop stiffness equivalent to that of conventional base blends at lower confining pressures, which increases with increasing confining pressures. Among the RAP/GRAP blends, the 50-50 RAP blend shows the highest resilient modulus followed by 50-50 GRAP, 25-75 RAP, and finally 25-75 GRAP blends. Such a performance in

GRAP blends may be attributed to the presence of interlayer fragments that may have been resulted in higher expansion and contraction when subjected to cyclic loading.
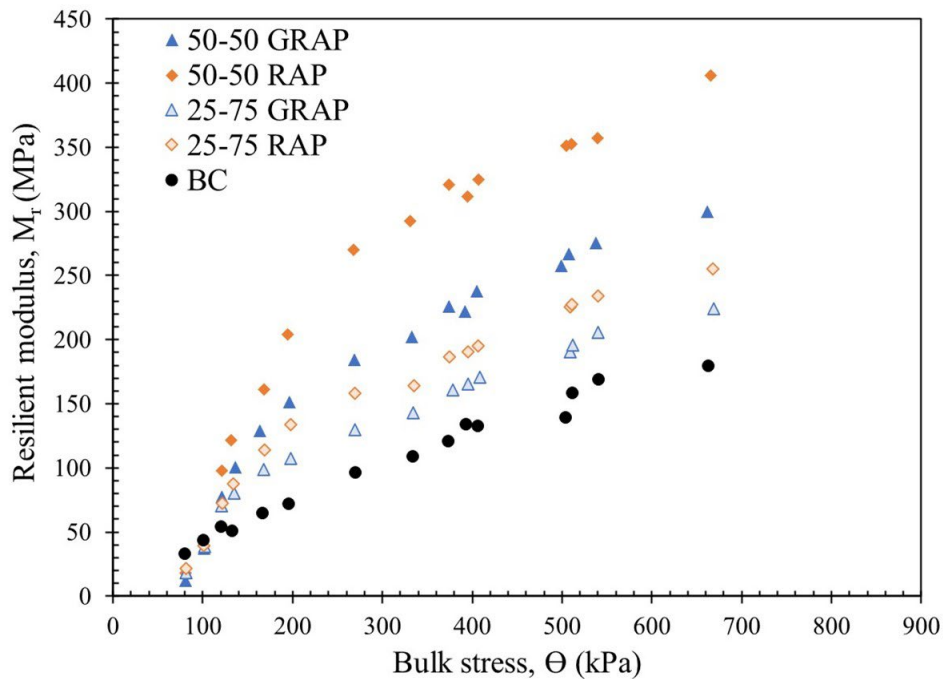
Figure 9.9. Relationship between resilient modulus and bulk stress.

9.11. Recyclability Evaluation of the Surface Course: Discussion of the Experimental Results

9.11.1. Indirect Tensile Strength Characteristics

The IDT results for all specimens tested in this study are presented in the form of load-displacement trends, as shown in Figure 9.10. As the figure shows, for all the specimens, the applied load increased with increasing displacements until a peak value was reached, and decreased thereafter as displacements increased further. The peak load and corresponding displacement along with the specimen dimensions were noted for all specimens tested. As can be seen in the Figure 9.10, incorporation of RAP and GRAP increased the strength of HMA mixtures. However, due to the increase in the brittleness (decreased failure displacement), the fatigue life of HMA mixtures may be compromised. This increase in load carrying capacity and decrease in failure displacement can be attributed to the stiffening effect of the aged asphalt in RAP and GRAP blends. Although the specimens observed to fail at lower strain value for the asphalt mixtures with GRAP/RAP material, higher load was required to initiate the crack in the specimen. Finally, the average indirect tensile strengths for all specimens were determined and plotted in Figure 9.11. The average indirect tensile strength value was observed to be highest for

the 30-70 RAP specimen, followed by the 30-70 GRAP, 15-85 RAP, 15-85 GRAP, and finally AC specimens. The higher indirect tensile strength and lower displacement values for the 30-70 RAP and 30-70 GRAP specimens compared respectively to those for the 15-85 RAP, 15-85 GRAP and AC specimens can be attributed to the comparatively stiffer and more brittle behavior of the aged asphalt and the amount of GRAP/RAP present in the 30-70 GRAP and 30-70 RAP mixtures. Notably, the indirect tensile strength of the AC specimen was 38%, 31%, 20%, and 18% lower than that of the 30-70 RAP, 30-70 GRAP, 15-85 RAP, and 15-85 GRAP specimens, respectively. However, there was no significant difference between the indirect tensile strength and corresponding displacement values observed for the 30-70 GRAP and 30-70 RAP specimens, or the 15-85 GRAP and 15-85 RAP specimens. Similar observations between RAP and GRAP specimens were reported by Tran et al. (2012), which indicated that no appreciable differences in tensile strength were recorded between specimens with only 30% RAP and those with 30% RAP with geosynthetic fragments. On the other hand, 15-85 GRAP had lower indirect tensile strength values at higher strains at failure compared to those for 15-85 RAP specimens, followed by the 30-70 GRAP specimens and finally, 30-70 RAP specimens with the highest indirect tensile strength at lower strains at failure. Such responses may be due to the amount of GRAP/RAP and the presence of interlayer fragments that reduce the stiffness of the specimen.
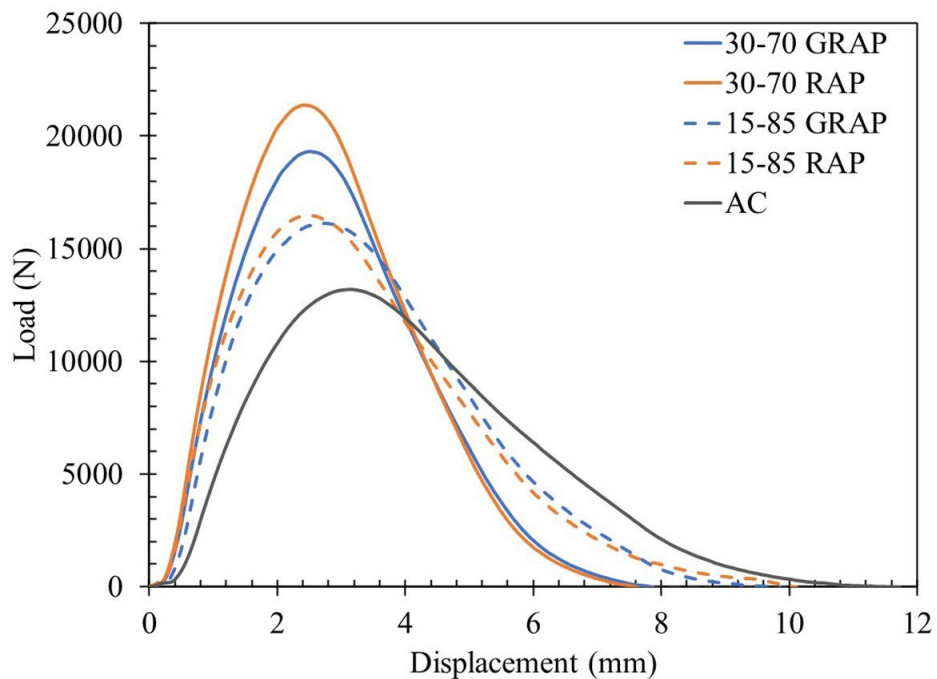
Figure 9.10. IDT load-displacement curves of different asphalt mixtures.
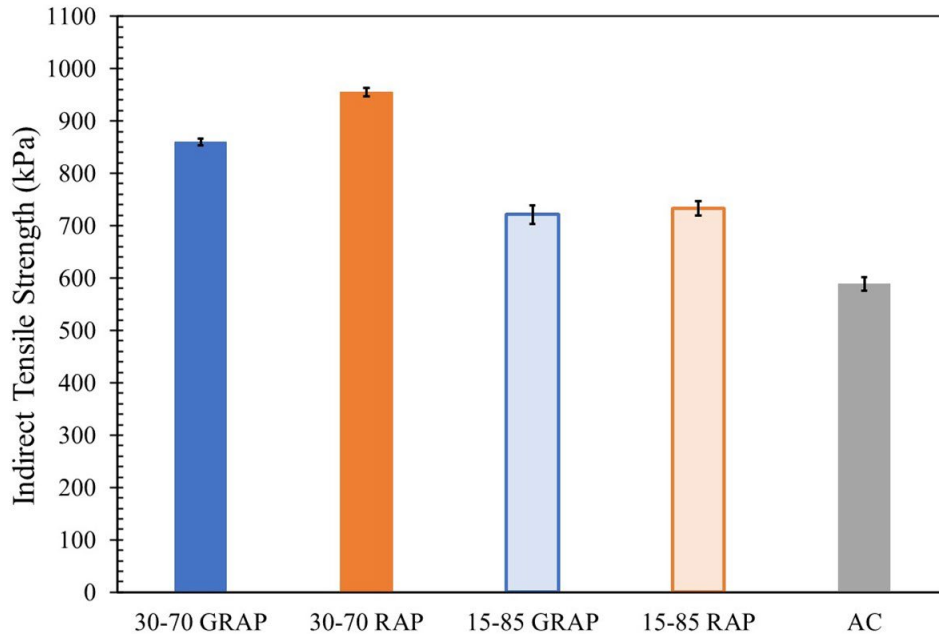
Figure 9.11. IDT characteristics of asphalt mixtures.

9.12. Moisture Susceptibility

The moisture susceptibility of the five asphalt mixtures tested herein was evaluated by determining the TSR of the specimens. The TSR values were calculated using the indirect tensile strength values obtained for the specimens tested under both dry and wet conditions (see Equation 2). Figure 9.12 shows the TSR values obtained for the 30-70 GRAP, 30-70 RAP, 15-85 GRAP, 15-85 RAP and AC specimens. As shown in the figure, the 30-70 RAP specimens had the highest TSR value of 0.90 followed by the 30-70 GRAP specimens with a TSR of 0.87, 15-85 RAP specimens with a TSR of 0.85, 15-85 GRAP specimens with a TSR of 0.82, and finally, the AC specimens with the lowest TSR value of 0.81. However, it is important to note that the minimum required TSR value for an asphalt mixture is about 0.80, per India's Ministry of Road Transport and Highways (MoRTH) specifications (MoRTH 2013). Accordingly, all the asphalt mixtures evaluated in this study including those with GRAP/RAP are acceptable. In addition, the TSR values indicate that the RAP or GRAP present in the asphalt mixture effectively resists moisture damage as compared to conventional asphalt mixtures. Specifically, the aged asphalt may have resulted in mechanisms of interlocking and bonding with the aggregates that may not be present for specimens with VA mixtures (Shu et al. 2012). Additionally, Huang et al. (2005) reported that the aged asphalt in the RAP mixture increase the stiffness of the mixture that improves the performance of asphalt mixtures against moisture damage. The TSR for the 15-85 GRAP specimen was found to be slightly lower than that for the 15-85 RAP specimen, followed by the 30-70 GRAP specimen, and finally the 30-70 RAP specimen. Such a response maybe

because of the amount of RAP/GRAP and the presence of interlayer fragments in GRAP specimens that may absorb moisture. However, all the GRAP and RAP mixtures exhibited better resistance to moisture damage compared to that of the conventional asphalt mixture evaluated in this study. Similar observations were reported by Tran et al. (2012) and Gu et al. (2021).
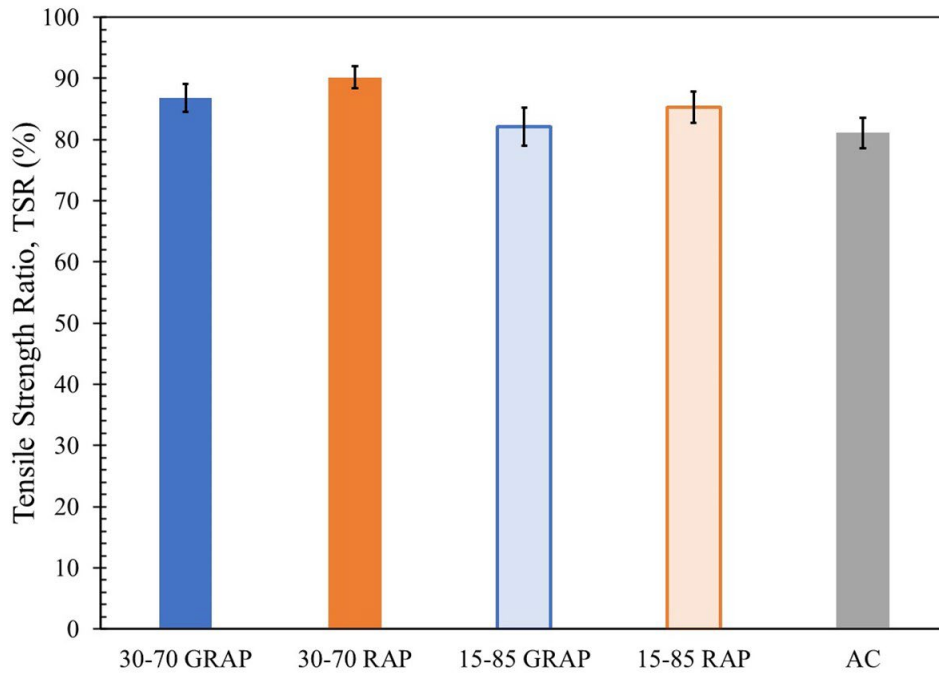
Figure 9.12. Moisture susceptibility characteristics of asphalt mixtures.

9.13. Additional Remarks on Millability

9.13.1. Millability Evaluation of Asphalt with Polyester (PET) Geogrid Interlayer

The milling operation employed at the Bastrop site (second site chosen to evaluate millability of paving interlayers) encompassed the sequential milling of asphalt layers, both with and without the presence of paving interlayer. Figure 9.13 shows the initial configuration of roadway, comprising subgrade, subbase and hot mix asphalt (HMA) layer. The asphalt layer shown in Figure 9.13 consisted of a 150 mm thick asphalt layer, overlain by a paving interlayer and 50 mm thick TY-D asphalt layer at the surface. The geosynthetic incorporated at the site was a polyester (PET) geogrid, characterize by high-modulus polyester yarns interwoven with an ultra-light non-woven fabric. This geosynthetic reinforcement was integrated into the asphalt layer to encounter sustained dynamic vehicular loads by enhancing the system's structural integrity. The geosynthetic had a mass per unit area of 270 g/m^2 and a tensile strength of 12 kN/m at 3% strain level. Notably, its asphalt retention capacity stood at 0.47 l/m^2. Similar to the approach adopted

at the Muleshoe site, the rehabilitation of the existing asphalt layer at Bastrop site was executed through a two-stage milling process. Figure 9.14 shows the milling operation performed at the site (see Figure 9.14a) and presence of PET geogrid fibers at the site (see Figure 9.14b). The milling process commenced with the removal of 38 mm thick topmost layer of asphalt (see Figure 9.13b), aimed to extract RAP without any geosynthetic fibers (denoted as RAP_PET). Subsequently, a 25 mm thick asphalt layer containing geosynthetic, positioned 12 mm beneath the milled surface, was milled (see Figure 9.13c) to collect RAP with geosynthetic fibers (denoted as GRAP_PET). The milling operation conducted at the Bastrop site was visually documented, revealing instances where PET geogrid was milled without any damage to the milling machine.
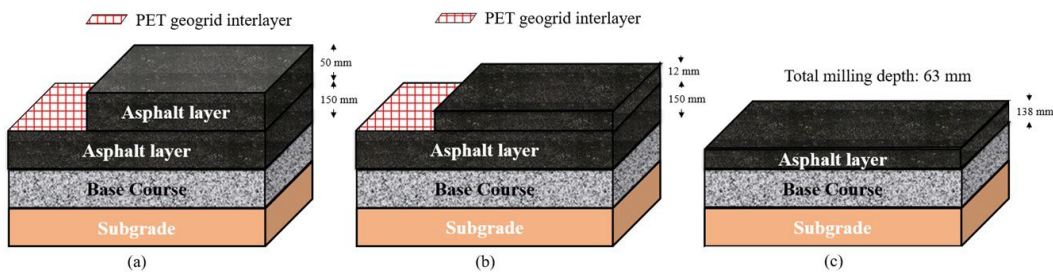
Figure 9.13. Cross-section of site: (a) before milling; (b) after collection of RAP_PET; and (c) after collection of GRAP_PET.

Figure 9.14. Milling of asphalt layer that had polyester (PET) geogrid: (a) milling operation performed at site; and (b) presence of PET geogrid fibers at the site.

9.14. Millability Evaluation of Asphalt with Fiberglass (FG) Geogrid Interlayer

The third site chosen to evaluate the millability of geosynthetic-reinforced asphalt layers was located in Laredo. Here, the focus was on the investigation of millability of a fiberglass geogrid integrated within the asphalt layers. The schematic representation in Figure 9.15 showcases the cross-sectional configuration of the roadway, comprising of subgrade, base course and asphalt layer. The asphalt layer comprised of a 50 mm thick TY-D asphalt layer underlying a geosynthetic interlayer, and ultimately covered by an additional 50 mm thick TY-D asphalt layer. The fiberglass geogrid consisted of fiberglass strands coated with an elastomeric polymer, arranged into a grid-like configuration. This geosynthetic was employed to mitigate the vertical crack stresses inherent to roadways, by redirecting them horizontally between the levelling course and surface course in asphalt overlays. Notably, the geosynthetic exhibited a mass/area ratio of 405 g/m^2 and tensile strength of 80 kN/m at 2% elongation. In alignment with the milling methodology applied at the Muleshoe and Bastrop sites, the milling procedure at Laredo site was executed in two distinct stages. Firstly, a 38 mm thick asphalt layer was milled (see Figure 9.15b) to obtain RAP without geosynthetic fiber (denoted as RAP_FG), followed by subsequent milling of 25 mm thick asphalt layer (see Figure 9.15c) to procure RAP with geosynthetic fibers (denoted as GRAP_FG). Figure 9.16 shows the milling activity conducted at the Laredo site. Notably, the asphalt layer reinforced with fiberglass geogrid exhibited a seamless milling, with no observable adverse impact on the milling machinery. This implies that asphalt layers with fiberglass geogrids can be effectively milled in the field with the currently available milling equipment.
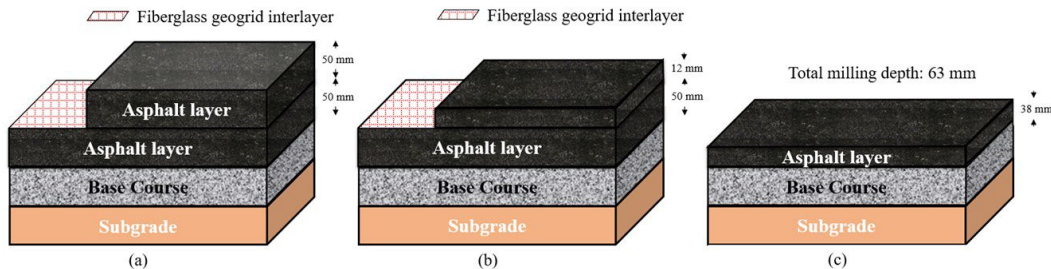
Figure 9.15. Cross-section of site: (a) before milling; (b) after collection of RAP_FG; and (c) after collection of GRAP_FG.

Figure 9.16. Milling of asphalt layer that had fiberglass (FG) geogrid.

9.15. Summary and Final Remarks

The millability of asphalt layers with paving interlayers were evaluated by milling asphalt layers with and without paving interlayers as part of Task 12. In addition, asphalt millings with and without geotextile fragments, known as GRAP and RAP, respectively, were collected and used together with VA to constitute five different blends for base course (50-50 GRAP, 50-50 RAP, 25-75 GRAP, 25-75 RAP, and BC) and five different asphalt mixtures (30-70 GRAP, 30-70 RAP, 15-85 GRAP, 15-85 RAP, and AC). Their suitability and performance as potential base and surface course materials were evaluated and the following conclusions were drawn from this study:

- Millability of asphalt layers remained unaffected by the presence of non-woven geotextile, PET geogrids and fiberglass geogrids.

- The Maximum Dry Unit weight (MDU) and Optimum Moisture Content (OMC) of the 50-50 GRAP blend were found to be lower than those for the 50-50 RAP blend, which were in turn lower than those for the 25-75 GRAP, 25-75 RAP, and BC blend. The decreased MDU and OMC values for the RAP and GRAP blends could be attributed respectively to the lower unit weight and hydrophobic nature of asphalt available on the surface of RAP and GRAP materials.

- The asphalt coated on the RAP particles were found to reduce the water absorption capacity in the RAP and GRAP blends, while interlayer fragments may have absorbed

273

moisture, thus increasing the water absorption capacity of the 50-50 GRAP and 25-75 GRAP blends compared to that of 50-50 RAP and 25-75 RAP blends, respectively.

- The presence of asphalt was found to increase the abrasion resistance of the RAP and GRAP blends, while further increased abrasion resistance was observed for the GRAP blend, possibly due to the presence of interlayer fragments, which might have resulted in dissipation of the impact energy.

- The saturated hydraulic conductivity of the specimens containing GRAP/RAP materials was found to be higher than BC blends. Among the GRAP and RAP materials, specimens prepared with GRAP material have resulted in higher hydraulic conductivity. The higher permeability determined for the GRAP blends as compared to that for the RAP blends can be attributed to the presence of interlayer fragments that absorb moisture.

- The resilient moduli of the BC blend were higher than those in the GRAP and RAP blends at low bulk stress, which gradually increased with increasing bulk stress. In contrast, the resilient moduli of the GRAP and RAP blends were lower at low bulk stress and increased significantly with increasing bulk stress.

- The incorporation of RAP and GRAP materials into the asphalt mixture was found to improve the indirect tensile strength and resistance against moisture damage compared to the conventional asphalt mixture tested in this study. The improved performance observed for asphalt mixtures with RAP and GRAP material could be attributed to the presence of aged asphalt that increases the stiffness of the mix.

Overall, it may be concluded that the millability and recyclability of asphalt layers with and without a paving interlayer is similar. Additionally, the results of this investigation suggest that up to 30% GRAP and 50% GRAP can be incorporated into asphalt mixtures (surface course) and granular base courses, respectively, thus leading to sustainable roadway construction practices. The future scope of this research study may be focused on the evaluation of millability of asphalt layers with different paving interlayers to confirm that the asphalt layers with paving interlayers are indeed millable with the existing milling equipment and techniques. Additional scope includes working towards the development of an ASTM specification for the evaluation of suitability of GRAP material in transportation geotechnical applications including backfill material in retaining walls and embankment fills, roadway base and surface courses, slope protection, and landfill capping systems.

References

AASHTO. 2021. Standard Method of Test for Determining the Resilient Modulus of Soils and Aggregate Materials. AASHTO T307 (2021). Washington, DC: American Association of State and Highway Transportation Officials.

AASHTO. 2021. Standard Specification for Materials for Aggregate and Soil-Aggregate Subbase, Base and Surface Courses. AASHTO M147 (2021). Washington, DC: American Association of State and Highway Transportation Officials.

AASHTO. 2022. Standard Method of Test for Specific Gravity and Absorption of Coarse Aggregate. AASHTO T85 (2022). Washington, DC: American Association of State and Highway Transportation Officials.

AASHTO. 2022. Standard Method of Test Quantitative Extraction of Asphalt Binder from Asphalt Mixtures. AASHTO T164 (2022). Washington, DC: American Association of State and Highway Transportation Officials.

ASTM International. 2015. Standard test method for preparation and determination of the relative density of asphalt mix specimens by means of the superpave gyratory compactor. ASTM D6925 (2015). West Conshohocken, PA: ASTM International, approved January 1, 2015.

ASTM International. 2017. Standard Test Method for Indirect Tensile (IDT) Strength of Asphalt Mixtures. ASTM D6931 (2017). West Conshohocken, PA: ASTM International, approved July 1, 2017.

ASTM International. 2020. Standard Test Method for Resistance to Degradation of Small-Size Coarse Aggregate by Abrasion and Impact in the Los Angles Machine. ASTM C131 (2020). West Conshohocken, PA: ASTM International, approved February 15, 2020.

ASTM International. 2021. Standard Test Methods for Laboratory Compaction Characteristic of Soil Using Modified Effort. ASTM D1557 (2021). West Conshohocken, PA: ASTM International, approved July 1,2021.

ASTM International. 2022. Standard Test Method for Effect of Moisture on Asphalt Concrete Paving Mixtures. ASTM D4867 (2022). West Conshohocken, PA: ASTM International, approved November 1, 2022.

ASTM International. 2022. Standard Test Methods for Measurement of Hydraulic Conductivity of Coarse-Grained Soils. ASTM D2434 (2022). West Conshohocken, PA: ASTM International, approved March 15, 2022.

Button, J.W., Lytton, R.L. (2003). Guidelines for Using Geosynthetics with HMA Overlays to Reduce Reflective Cracking. Report 1777-P2, Project Number 0-1777, Texas Department of Transportation, Austin, TX, 2003.

Canestrari, F., Cardone, F., Gaudenzi, E., Chiola, D., Gasbarro, N., Ferrotti, G. (2022). Interlayer bonding characterization of interfaces reinforced with geocomposites in field applications. Geotextiles and Geomembranes, 50 (1), 154-162.

Cavalli, M. C., Partl, M. N., and Poulikakos, L. D. (2017). Measuring the binder film residues on black rock in mixtures with high amounts of reclaimed asphalt. Journal of Cleaner Production, 149, 665-672.

Correia, N. S., and Zornberg, J. G. (2016). Mechanical response of flexible pavements enhanced with geogrid-reinforced asphalt overlays. Geosynthetics International, 23 (3), 183.

Daryaee, D., Ameri, M., and Mansourkhaki, A. (2020). Utilizing of Waste Polymer Modified Bitumen in Combination with Rejuvenator in High Reclaimed Asphalt Pavement Mixtures. Construction and Building Materials, 235, 117516.

Dong, Q., and Huang, B. (2014). Laboratory Evaluation on Resilient Modulus and Rate Dependencies of RAP Used as Unbound Base Material. Journal of Materials in Civil Engineering, 26(2), 379-383.

Gu, F., Andrews, D., and Marienfeld, M. (2021). Evaluation of Bond Strength, Permeability, and Recyclability of Geosynthetic Products. Proceedings of Geosynthetics Conference, February 2021, 362-373.

Guduru, G., Tavva, T. L., and Kuna, K. (2022). Estimation of Reclaimed Asphalt Pavement (RAP) Characteristics Using Simple Indicative Tests. Road Materials and Pavement Design, 23 (4): 822-848.

Guo, N., You, Z., Zhao, Y., Tan, Y., and Diab, A. (2014). Laboratory Performance of Warm Mix Asphalt Containing Recycled Asphalt Mixtures. Construction and Building Materials, 64, 141-149. https://doi.org/10.1016/j.conbuildmat.2014.04.002.

Gupta, S., Kang, D. H., and Ranaivoson, A. (2009). Hydraulic and Mechanical Properties of Recycled Materials. Final Report No. 2009-32, Minnesota Department of Transportation, Research Service Section, Saint Paul, MN, October 2009.

Huang, B., Li, G., Vukosavljevic, D., Shu, X., and Egan, B. K. (2005). Laboratory Investigation of Mixing Hot-Mix Asphalt with Reclaimed Asphalt Pavement. Transportation Research Record: Journal of Transportation Research Board, 1929, 37-45.

Kim, W., Labuz, J. F., and Dai, S. (2007). Resilient Modulus of Base Course containing Recycled Asphalt Pavement. Transportation Research Record: Journal of Transportation Research Board, 2005, 27-35.

Kumar, V. V., Roodi, G. H., Subramanian, S., and Zornberg, J. G. (2022). Influence of asphalt thickness on performance of geosynthetic-reinforced asphalt: Full-scale field study. Geotextiles and Geomembranes, 50 (5): 1052-1059.

Kumar, V. V., Saride, S., and Zornberg, J. G. (2021). Mechanical response of full-scale geosynthetic-reinforced asphalt overlays subjected to repeated loads. Transportation Geotechnics, 30, 100617.

Locander, R. (2009). Analysis of using Reclaimed Asphalt Pavement (RAP) as a Base Course Material. Report No. CDOT-2009-5, Colorado Department of Transportation, DTD Applied Research and Innovation Branch, February 2009.

MacGregor, J. A., Highter, W. H., and DeGroot, D. J. (1999). Structural numbers for reclaimed asphalt pavement base and subbase course mixes. Transportation research record, 1687(1), 22-28.

Marienfeld, M. (2020). Trends and Advances in Geosynthetic Interlayers. Purdue Road School 2020.

Marin-Uribe, C. R., and Restrepo-Tamayo, L. M. (2022). Experimental Study of the Tensile Strength of Hot Asphalt Mixtures Measured with Indirect Tensile and Semi-circular Bending Tests. Construction and Building Materials, 339, 127651.

MoRTH (2013). Specifications for Roads and Bridge Works. Fifth revision. Ministry of Road Transport and Highways, Indian Road Congress, New Delhi, India.

Mousa, E., El-Badawy, S., and Azam, A. (2021). Evaluation of Reclaimed Asphalt Pavement as Base/Subbase Material in Egypt. Transportation Geotechnics, 26, 100414. https://doi.org/10.1016/j.trgeo.2020.100414

NAPA. (2019). Asphalt Pavement Industry Survey on Recycled Materials and Warm-Mix Asphalt Usage: 2018–2019. Washington, DC: National Asphalt Pavement Association, 2019 Mix Production Survey.

Plati, C., and Cliatt, B. (2018). A Sustainability Perspective for Unbound Reclaimed Asphalt Pavement (RAP) as a Pavement Base Material. Sustainability, 11 (1): 78.

Saride, S., and Kumar, V. V. (2019). Reflection Crack Assessment using Digital Image Analysis. In: Frontiers in Geotechnical Engineering, Developments in Geotechnical Engineering (ed. G. M. Latha). Springer, Singapore, 139-156.

Saride, S., Avirneni, D., and Javvadi, S. C. P. 2016. Utilization of Reclaimed Asphalt Pavements in Indian Low-Volume Roads. Journal of Materials in Civil Engineering, 28 (2): 04015107.

Shu, X., Huang, B., Shrum, E. D., and Jia, X. 2012. Laboratory Evaluation of Moisture Susceptibility of Foamed Warm Mix Asphalt Containing High Percentages of RAP. Construction and Building Materials, 35: 125-130.

Singh, D., Chitragar, S. F., and Ashish, P. K. (2017). Comparison of Moisture and Fracture Damage Resistance of Hot and Warm Asphalt Mixes Containing Reclaimed Pavement Materials. Construction and Building Materials, 157, 1145-1153.

Solatiyan, E., Bueche, N., Carter, A. (2020). A review on mechanical behavior and design considerations for reinforced-rehabilitated bituminous pavements. Construction and Building Materials, 257, 119483.

Soleimanbeigi, A., Ozocak, A., Li, B., Akmaz, E., Dayioglu, A. Y., Tanyu, B. F., Aydilek, A. H., and Likos, W. J. (2022). Mechanical and hydraulic compatibility of RAP with geosynthetics used in MSE walls. Geosynthetics International, 29(1), 1-18.

Tran, N. H., Julian, G., Taylor, A. J., Willis, R., and Hunt, D. (2012). Effect of Geosynthetic Material in Reclaimed Asphalt Pavement on Performance Properties of Asphalt

Mixtures. Transportation Research Record: Journal of Transportation Research Board, 2294, 26-33.

TxDOT. 2014. Standard Specifications for Construction and Maintenance of Highways, Streets, and Bridges. Item 341 TxDOT (2014). Texas Department of Transportation (TxDOT), Austin, Texas, USA.

Wu, M., Wen, H., Balasingam, M., and Manahiloh, K. N. (2012). Influence of Recycled Asphalt Pavement Content on Air Void Distribution, Permeability, and Modulus of Base Layer. Transportation research record, 2267(1), 65-71.

Zhao, S., Huang, B., Shu, X., and Woods, M. (2013). Comparative Evaluation of Warm Mix Asphalt Containing High Percentages of Reclaimed Asphalt Pavement. Construction and Building Materials, 44, 92-100.

Chapter 10: Conclusions

TxDOT project 0-7002 involved the sensor-instrumentation and performance monitoring of full-scale field sections of an in-service Texas State Highway (SH) 21 in Lee County, Austin, TX. The following are key conclusions from the research project.

- A comprehensive full-scale field monitoring program involving different types of geosynthetic reinforcement products, including various sensors such as asphalt strain gauges, thermocouples, geophones, and moisture sensors were successfully implemented.

- All the asphalt overlay sections reinforced with geosynthetic reinforcements performed better than the control section in terms of minimizing the tensile strains under the controlled traffic loads, thereby improving the roadway structural capacity.

- The tensile strains decreased with increasing asphalt overlay thickness, irrespective of presence or absence of geosynthetic reinforcements below the asphalt overlays.

- The benefit from incorporating geosynthetic reinforcements below the asphalt overlays is significantly higher in thin asphalt overlays compared to that in thick asphalt overlays. In other words, lower the thickness of the asphalt layer, greater the benefit from incorporating geosynthetic reinforcements.

- The tensile strains increased with increasing ambient air temperatures, irrespective of the presence or absence of geosynthetic reinforcements below the asphalt overlays.

- The benefit from incorporating geosynthetic reinforcements below the asphalt overlays is significantly higher in hot temperatures compared to that in cold temperatures. In other words, higher the ambient air and the asphalt temperature, greater the benefit from incorporating geosynthetic reinforcements.

- The tensile strains increased with increasing time since construction (i.e., asphalt aging and degradation), irrespective of the presence or absence of geosynthetic reinforcements below the asphalt overlays.

- The benefit from incorporating geosynthetic reinforcements below the asphalt overlays is significantly higher as asphalt ages and degrades compared to the fresh asphalt layer. In other words, larger the time since asphalt overlay construction, greater the benefit from incorporating geosynthetic reinforcements.

- The reductions in tensile strains with the inclusion of geosynthetic reinforcements suggest an increase in the roadway structural capacity. Such benefits could be incorporated into the design via two approaches:

    o Approach 1: Apparent Increased Asphalt Modulus

    o Approach 2: Reduced Fatigue Damage.

- The two design approaches would eventually lead to the following benefits:

    o Increased service life (ESALs)

    o Decreased asphalt thickness.

Appendix A: Introduction

This technical memorandum summarizes work conducted in Task 10 for Project 0-7002: Evaluation of Geogrids of Asphalt Pavement Construction. Unlike the common objective of using paving interlayers to mitigate the development of reflective cracks, the primary objective of this project for adopting geosynthetics was to render an increased roadway structural capacity.

The main focus of the project was on supporting TxDOT on the ongoing reconstruction of segments of SH21 near Bastrop, designing pavement test sections using all classes of geogrids within the asphalt layers, designing instrumentation and monitoring plans for pavement test sections, supporting TxDOT on procurement, testing, and installation of sensors, and collecting and interpreting performance data (collected by sensors and other components of the monitoring program) from the pavement test section.

As part of Task 10, the research team considered qualitative and economic benefits of research according to Table 1 shown below. The functional areas listed in this table were identified by the sponsoring agency to be specifically considered for Project 0-7002.

Table 1.10. Applicable focus areas for Value of Research (VoR) for Project 0-7002.

Selection	Benefit Areas	QUAL	ECON	Both	TxDOT	State	Both
X	Level of Knowledge	X			X		
X	Environmental Sustainability	X					X
X	System Reliability		X		X		
X	Increased Service Life		X		X		
X	Improved Productivity and Work Efficiency		X		X		
X	Expedited Project Delivery		X		X		
X	Reduced Construction, Operations, and Maintenance Cost		X		X		
X	Materials and Pavements		X		X		
X	Infrastructure Condition		X				X
X	Engineering Design Development/ Improvement			X			X

Qualitative Benefits

Functional Area 1: Level of Knowledge

In this study, a research program involving evaluation of the structural performance of full-scale instrumented field sections was implemented to quantify the structural benefits expected from geosynthetics placed below the asphalt overlay, but not necessarily benefits against reflective cracking. Specifically, the field study presented in this research provides an evaluation of the

influence of two different asphalt thickness with different asphalt types, on the performance of full-scale highway sections with unreinforced and geosynthetic-reinforced asphalt overlays under a series of controlled traffic loadings. Moreover, the research explains the benefits provided by geosynthetics over a large period of time compared to control sections. The performance of each geosynthetic-reinforced section is compared against that of the control section, allowing quantification of the structural benefits derived from geosynthetic reinforcement. The influence of overlay types is also qualitatively evaluated. Field loading campaigns were conducted as part of this study at locations where the pre-existing asphalt was intact. Consequently, rather than focusing on the impact of mitigating reflective cracking, the differences in performance between reinforced and control sections allow quantification of the impact of the geosynthetic reinforcements on the roadway structural capacity. Outcomes of this project will provide valuable data relevant to the performance under traffic and environmental loads of geosynthetic-reinforced roadways. This information is collected over a long period of time and for control pavement test sections (i.e., sections without geosynthetic) as well as pavement test sections that were constructed using different classes of geogrid. Interpretation of this data will be particularly useful in the future design of geosynthetic-reinforced overlays. Specifically, the outcomes of this project will provide insight on the following aspects of the future design:

1. benefits from geosynthetic reinforcement of overlays subjected to traffic loads

2. benefits from geosynthetic reinforcement of overlays subjected to environmental loads

3. structural benefits in the hot mix asphalt layer from geosynthetic reinforcement of overlays

4. difference between the expected benefits from various types of geogrids

Functional Area 2: Environmental Sustainability

Outcomes of this project allows TxDOT to enhance environmental sustainability by extending pavement life and reducing maintenance frequency, thus conserving raw materials and lowering greenhouse gas emissions. Optimized material usage and reduced virgin material extraction improve resource efficiency. More specifically, documentation and interpretation of the performance of the pavement test sections in this project will help TxDOT to determine economic and mechanical advantages and disadvantages of using geosynthetic reinforcement while reducing the thickness of the overlays. This insight will be crucial in the future decision-making of TxDOT managers and policy makers to adopt (or not) geosynthetic-reinforced reduced overlays. Additionally, these practices minimize construction waste and energy consumption, and promote innovative sustainable practices. Overall, such testing supports sustainable infrastructure by reducing environmental impacts and promoting efficient resource utilization in pavement construction and maintenance.

Functional Area 3: Engineering Design Development/Improvement

In the lack of a proper design procedure for geosynthetic-reinforced roadways, TxDOT as well as other U.S. state transportation departments have often relied on design recommendations provided by geosynthetic manufacturers. This project will provide valuable information to advance current TxDOT design procedures to include geosynthetic reinforcement in the asphalt overlays. The adoption of such design will be advantageous in all districts of Texas, and will also reduce reliance of TxDOT to empirical and/or non-verified designs that may otherwise suggested by geosynthetic manufacturers.

Economic Benefits

Overall Approach

Economic benefits are expected to realize in the following functional areas:

System Reliability

Increased Service Life

Improved Productivity and Work Efficiency

Expedited Project Delivery

Reduced Construction, Operations, and Maintenance Costs

Materials and Pavements

Infrastructure Conditions

Engineering Design Development/Improvement

Although each factor will provide individual economic benefits, the financial calculations conducted as part of this report was aimed at evaluating the most important economic benefit that may overshadow other marginal benefits.

Assumptions

Since the focus of this project is on the improvement of structural capacity of roadway resulting in reduced asphalt overlay thickness while installing geogrids, it was envisioned that the most significant change in TxDOT construction approach after completion of this project would be

adoption of geosynthetic-reinforced reduced overlay thickness roadways as a common design and construction practice. Therefore, the most important economic benefit would be expected to result from replacing a portion of the asphalt overlay layer by the geosynthetic layer. The main assumptions adopted to calculate this benefit are as follows:

Use of geosynthetic reinforcement can result in reduction of 20 % in the overlay thickness

TxDOT adopts the new approach (i.e., replacing 20 % of the overlay course by the geosynthetic layer) only in highway construction projects

TxDOT adopts the new approach in all highway construction projects that involves rehabilitation (i.e. construction of asphalt overlay on top of cracked surfaces)

The economic benefit from this project will be realized in the fifth (i.e., last) year of the project, when the accumulated performance data will provide compelling evidence to TxDOT on the suitable performance of this technique

An expected value duration of 15 years from the beginning of the project was adopted

A discount rate of 5 % was adopted

Calculation was conducted based on TxDOT projects letting and bids information in the past twelve months ending in December 31st 2023

To best estimate the economic benefits detailed above, the TxDOT statewide average low bid unit price website was heavily utilized. Specifically, using the information published for the past twelve months as of December 31, 2023, annual costs for construction of asphalt layer were estimated. Detailed calculations of the economic benefit are presented in the subsequent section of this technical memorandum.

Calculations

The total 12-month cost of various types and thicknesses of compacted-in-place asphalt layers in TxDOT Highway Construction Projects was found as follows:

Total Cost of Asphalt layer Construction = **$267,871,636**

Assuming a 20 % reduction in the asphalt overlay thickness due to the use of geosynthetic reinforcement in asphalt layers, the total annual saving was estimated:

Total Estimated Saving Due to Reduction of Overlay Thickness = **$53,574,327**

Using the TxDOT statewide average low bid unit price website for the past twelve months, it was found that the average bid price for a square yard of geogrid for asphalt reinforcement ranged approximately from $1.3 to $3.03. The total square yard of asphalt layer construction was then estimated:

Total Asphalt layer Construction = 594937 cy / 0.1 y = **5,949,373 sy**

In this estimation, an average thickness of 0.1 yard (3.6 inch) was assumed for the asphalt layer volume that was available in cubic yard.

The total additional cost for procurement and installation of the geogrid was then estimated to vary in the following range:

Total Estimated Cost of Geogrids = 5,949,373 sy × $1.3 ~ $3.03 = **$7,734,184** to **$18,026,600**

Therefore, the expected annual benefit for adopting the geosynthetic-reinforced asphalt layers is expected to be in the following range:

Scenario 1:

= **$53,574,327** (Saving) - **$7,734,184** (Additional Cost) = **$45,840,143** (Benefit) per year

Scenario 2:

= **$53,574,327** (Saving) - **$18,026,600** (Additional Cost) = **$35,547,727** (Benefit) per year

Note that Scenario 1 assumes a 20 % reduction in the asphalt layer thickness while a cheaper geogrid (i.e., $1.3 /sy) is used, and Scenario 2 assumes a 20 % reduction in the asphalt thickness while a more expensive geogrid (i.e., $3.03 /sy) is used.

Net Present Value

The calculations presented in the previous section was used in the RTI VoR template to compute the Net Present Value. As stated in Section 1.3.2, this analysis was conducted assuming a 5-percent discount rate and a 15-year expected value duration. Figures 1 and 2 on the following pages show the completed VoR templates for the two scenarios explained in Section 1.3.3. The estimated net present value of this research was found to range approximately from $260 to $340 million and the cost benefit ratio of investing in this project was estimated to range from 219 to 283.

	Project #	0-7002		
	Project Name:			
Texas Department of Transportation		Evaluation of Geogrids of Asphalt Pavement Construction		
	Agency:	University of Texas (CTR)	Project Budget	$ 1,194,503
	Project Duration (Yrs)	5.0	Exp. Value (per Yr)	$ 45,840,143
	Expected Value Duration (Yrs)	15	Discount Rate	5%

Economic Value			
Total Savings:	$ 411,366,784	Net Present Value (NPV):	$ 338,051,233
Payback Period (Yrs):	0.026058	Cost Benefit Ratio (CBR, $1 : $___):	$ 283

Years	Expected Value
0	$44,645,640
1	$0
2	$45,840,143
3	$45,840,143
4	$45,840,143
5	$45,840,143
6	$45,840,143
7	$45,840,143
8	$45,840,143
9	$45,840,143
10	$45,840,143
11	$45,840,143
12	$45,840,143
13	$45,840,143
14	$45,840,143
15	$45,840,143

Value of Research: NPV — Project Duration (Yrs)
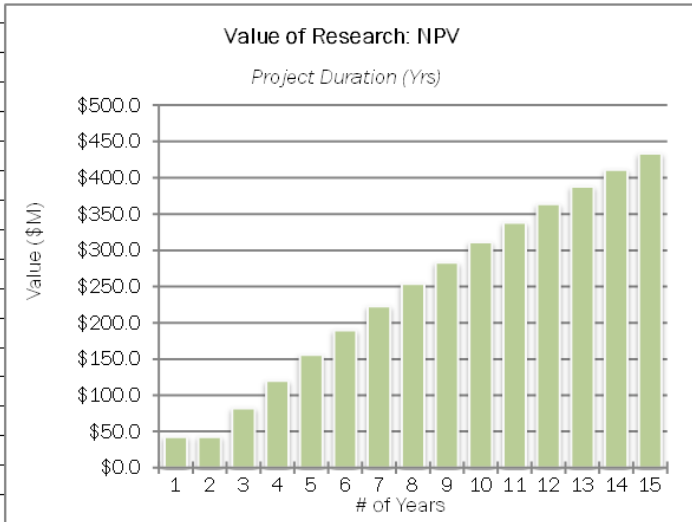
Years	Expected Value	Expected Value	Expected Value	NPV
0	$44,645,640	$44,645,640	$44.65	$42.52
1	$0	$44,645,640	$44.65	$42.52
2	$45,840,143	$90,485,783	$90.49	$82.12
3	$45,840,143	$136,325,926	$136.33	$119.83
4	$45,840,143	$182,166,069	$182.17	$155.75
5	$45,840,143	$228,006,212	$228.01	$189.95
6	$45,840,143	$273,846,355	$273.85	$222.53
7	$45,840,143	$319,686,498	$319.69	$253.56
8	$45,840,143	$365,526,641	$365.53	$283.11
9	$45,840,143	$411,366,784	$411.37	$311.25
10	$45,840,143	$457,206,927	$457.21	$338.05
11	$45,840,143	$503,047,070	$503.05	$363.58
12	$45,840,143	$548,887,213	$548.89	$387.89
13	$45,840,143	$594,727,356	$594.73	$411.04
14	$45,840,143	$640,567,499	$640.57	$433.09
15	$45,840,143	$686,407,642	$686.41	$454.09

Figure 1: Results from completed VoR template in Scenario 1

		Project #		0-7002	
		Project Name:			
				Evaluation of Geogrids of Asphalt Pavement Construction	
		Agency:	University of Texas (CTR)	Project Budget	$ 1,194,503
		Project Duration (Yrs)	5.0	Exp. Value (per Yr)	$ 35,547,727
		Expected Value Duration (Yrs)	15	Discount Rate	5%
Economic Value					
	Total Savings:	$ 318,735,040		Net Present Value (NPV):	$ 261,893,687
	Payback Period (Yrs):	0.033603		Cost Benefit Ratio (CBR, $1 : $___):	$ 219

Years	Expected Value
0	$34,353,224
1	$0
2	$35,547,727
3	$35,547,727
4	$35,547,727
5	$35,547,727
6	$35,547,727
7	$35,547,727
8	$35,547,727
9	$35,547,727
10	$35,547,727
11	$35,547,727
12	$35,547,727
13	$35,547,727
14	$35,547,727
15	$35,547,727

Value of Research: NPV
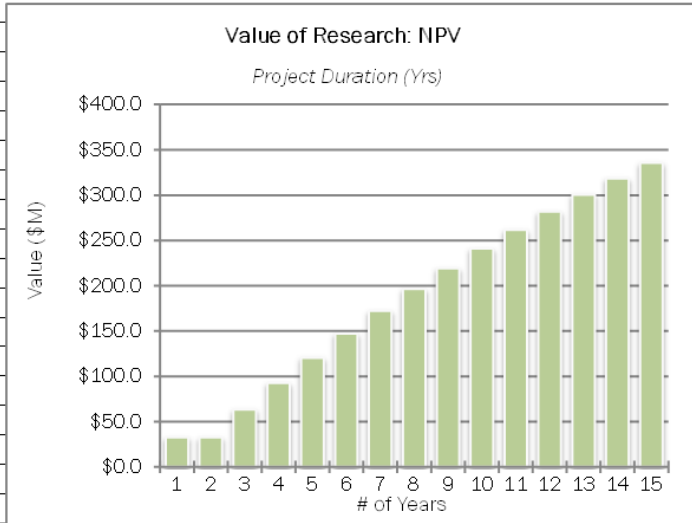
Years	Expected Value	Expected Value	Expected Value	NPV
0	$34,353,224	$34,353,224	$34.35	$32.72
1	$0	$34,353,224	$34.35	$32.72
2	$35,547,727	$69,900,951	$69.90	$63.42
3	$35,547,727	$105,448,678	$105.45	$92.67
4	$35,547,727	$140,996,405	$141.00	$120.52
5	$35,547,727	$176,544,132	$176.54	$147.05
6	$35,547,727	$212,091,859	$212.09	$172.31
7	$35,547,727	$247,639,586	$247.64	$196.37
8	$35,547,727	$283,187,313	$283.19	$219.29
9	$35,547,727	$318,735,040	$318.74	$241.11
10	$35,547,727	$354,282,767	$354.28	$261.89
11	$35,547,727	$389,830,494	$389.83	$281.69
12	$35,547,727	$425,378,221	$425.38	$300.54
13	$35,547,727	$460,925,948	$460.93	$318.49
14	$35,547,727	$496,473,675	$496.47	$335.59
15	$35,547,727	$532,021,402	$532.02	$351.88

Figure 2: Results from completed VoR template in Scenario 2

Discussion

This VoR estimate was developed by the research team based on a preliminary understanding of the VoR functional areas. It should be noted that this preliminary estimate was based on the assumptions listed in Section 1.3.2, and final values may not reflect actual savings that will be realized by TxDOT. In the future, a better understanding of the functional areas and the economic benefits of the research will be developed. In turn, this estimate can be revised. Additionally, the research team intended to work with the TxDOT project advisors and RTI throughout the duration of the research project to provide continual updates to the value of research estimate.